MATERIAL DESIGN, PROCESSING, AND ENGINEERING REQUIREMENTS FOR

MAGNETIC SHAPE MEMORY DEVICES

by

Andrew Armstrong

A dissertation

submitted in partial fulfillment

of the requirements for the degree of

Doctor of Philosophy in Materials Science and Engineering

Boise State University

August 2020

BOISE STATE UNIVERSITY GRADUATE COLLEGE

DEFENSE COMMITTEE AND FINAL READING APPROVALS

of the dissertation submitted by

Andrew Armstrong

Dissertation Title: Material Design, Processing, and Engineering Requirements for Magnetic Shape Memory Devices

Date of Final Oral Examination: 30 July 2020

The following individuals read and discussed the dissertation submitted by student Andrew Armstrong, and they evaluated their presentation and response to questions during the final oral examination. They found that the student passed the final oral examination.

Peter Müllner, Ph.D.   Chair, Supervisory Committee

Paul Simmonds, Ph.D.   Member, Supervisory Committee

Joseph Guarino, Ph.D.   Member, Supervisory Committee

Ladislav Straka, Ph.D.   External Committee Member

The final reading approval of the dissertation was granted by Peter Müllner, Ph.D., Chair of the Supervisory Committee. The dissertation was approved by the Graduate College.

DEDICATION

It takes a village to raise a person.

I dedicate this to the village.

ACKNOWLEDGMENTS

ABSTRACT

For magnetic shape memory (MSM) alloys, a magnetic field stimulates a shape change. We use the shape change to build devices such as micro-actuators, sensors, and microfluidic pumps. Currently, (as a novel technology,) devices suffer from some material and magnetic driver shortcomings. Here we address the issues related to operating temperature, repeatability, failure, and magnetic driver development. To increase the operating temperature of the MSM material, we alloyed Fe and Cu to Ni-Mn-Ga. We showed that the element-specific contribution to the valence electron density as parameter systematically determines the effect of each element on the variation of the martensite transformation temperature of the 10M phase. To stabilize the material, we developed a micro-shotpeening process that adds stresses to the material surface, thereby inducing a fine twin microstructure. The treatment allowed nearly full magnetic-field-induced strain, and extended fatigue life of the material from only one thousand cycles in the electropolished state to more than one million cycles in the peened state. We measured the effect of the peening process on material actuation when in MSM pump configuration. In the polished state, the deformation was stochastic, with a sharp-featured, faceted shrinkage. In the treated state, the deformation was smooth and repeatably swept along the surface akin to a wave.

To actuate the MSM micropump without electromotor, we developed a linear electromagnetic actuation device and evaluated its effectiveness in the switching mechanism of the material. By compressing the magnetic field between opposing coils,

we generated a strong magnetic field, which caused a localized region to switch at selected poles. In the next iteration of the drive, we inserted the MSM sample between two linear pole arrangements of high pitch density to approximate a moving vertical field. The incremental stepping of the vertical field between poles caused translation of the switched region. The results of this dissertation demonstrate the suitability of MSM alloys for high-precision, persistent, and reliable actuators such as micropumps.

TABLE OF CONTENTS

LIST OF TABLES

LIST OF FIGURES

expanded, creating the left slope of shrinkage. At 90° the twin slightly thickened and moved along the element. At 136°, the primary twin broke apart into thinner twins and moved along the element. At 180°, the primary twin further thinned into multiple finer twins and moved along the element. The arrows point to leading twins which create the right slope of shrinkage. (b) the sequence for the micropeened sample. The twin lamellar is oriented along the white line in the bottom micrograph. 116

CHAPTER ONE: INTRODUCTION

The phenomenon of magnetic-field-induced strain (MFIS) by twinning causing large plastic deformation was discovered in the late 1960s in Dy and other rare earth elements at cryogenic temperatures [1, 2]. In 1984, Webster *et al.* published work on Ni2MnGa [3]. Chernenko and Kokorin and Vasilev studied Ni-Mn-Ga in the 1980s and 1990s but did not refer to MFIS in their publications [4-9]. Ullakko re-introduced the idea of magnetic-field-induced twinning in 1995 [10]. He did not mention, though, the early work on Dy, although it is the same effect. The essential difference and innovation was that Ni-Mn-Ga is an alloy that exhibits MFIS near room temperature, unlike Dy, which has a Curie temperature of 85 °C. Further, the Ni-Mn-Ga shows large magnetoplasticity of up to 7% in its most commonly used 10M phase [11] MFIS. Since that discovery, magnetoplasticity has been studied intensely for off-stoichiometric Ni_2MnGa Heusler alloys [12-16]. MFIS values up to 12% are now possible by magnetic field reorientation in a magnetic field [16].

Ni-Mn-Ga is of interest in the design of small, mesoscale, and microscale machines and actuators. Magnetic Shape Memory (MSM) alloy is a smart material, capable of transmitting magnetic energy into material motion. The fast actuation and large stroke give MSM alloys potential for application in actuators [10, 17, 18] sensors, [19-21] energy harvesting [19, 22], and MSM micropumps [23-26].

The first report of an MSM pump using localized actuation to transport fluid was published in 2012 [23]. The pump deviates from other MSM actuators, as it uses motion

more akin to a locally deforming muscle rather than a piston's uniform push-pull stroke. A local magnetic field actuates confined regions and allows for complex deformation patterns. The MSM micropump transports small volumes (about 100 nL per gulp) [24] at pressures up to about 10 bar [26]. Compared to conventional micropumps, such as found in infusion pumps for medical devices, the MSM pump has demonstrated higher pressure generation. Other advantages include bidirectional actuation, operation without valves, a large dynamic range, and precise stop-and-go functionality. These properties make the MSM micropump useful for microfluidic devices for biomedical applications such as the lab-on-a-chip.

To build a precision actuator out of a smart material, that material must meet several conditions:

- The operational temperature must meet the range imposed by the environment.

- The material must be durable, resistant to fatigue.

- The material must actuate in a repeatable and reliable manner.

- The actuation motion must be defined.

- For miniaturized devices, the driver of the functional material must be small and energy-efficient.

This dissertation addresses solutions to these tasks with the goal to advance the state of the art in MSM micropumps. Results inform the design of MSM micropumps and other MSM actuators.

The martensite transformation temperature, i.e. the maximum operating temperature of the magnetic shape memory effect depends on the alloy composition. For the most commonly studied Ni-Mn-Ga alloy with 10M martensite, the maximum

operation temperature is about 80 °C [11, 27]. This suffices for many in-door applications. Many situations, however, require higher operation temperatures. Towards this, we studied an alloy system with the goal to increase the martensite transformation temperature (Chapter 4).

MSM elements have poor fatigue life when locally actuated in the manner of the micropump. Elements develop cracks upon the surface, which can propagate by the cyclic magnetic field to fracture after only 1000 cycles. We developed a surface treatment process, which hardens the material against fatigue to at least 1 million cycles. The surface treatment also changes material elasticity and plasticity, resulting in changes to material behavior (Chapter 5).

A localized rotating magnetic field imparts a traveling constriction (or shrinkage) on the element surface. We capture this moving constriction in the micropump to transport fluid. This surface profile has seen little study, beyond that of simply measuring the volumetric flowrate of micropumps. It is hard to design actuators around an ill-defined mechanism. Here we report a systematic characterization of the surface profile, before and after the surface treatment. Information such as stroke width, stroke amplitude, stroke envelope, a correlation of shape to magnetic field position, and measurements of profile repeatability yields parameters necessary to building reliable devices (Chapter 6).

We finally describe two miniaturized drive systems. Rather than spinning a permanent magnet to generate the rotating magnetic field, we used a series of magnetic poles, stationary permanent magnets, and coils to generate and manipulate the local magnetic field, thus providing a motionless driver of compact design. In Chapter 7, we

study an electromagnetic drive, which uses electrical coils to generate compressed

magnetic fields and to actuate an MSM element at two pole locations. Chapter 8 reports

on a drive which has a tighter pitch density, with linear yokes on two sides of the MSM

element. We draw the flux from pole to pole through the element. By switching actuation

from one pole pair to the next, a confined vertical field moves through the device.

CHAPTER TWO: BACKGROUND

2.1 Smart materials

Back in 1847, James Prescott Joule found that in iron exposed to magnetic field,

"the elongation is, for the same intensity of magnetism, greater in proportion to the

softness of the softness of the metal" [28]. This magnetostriction of iron was one of the

very early reports on converting external stimuli into mechanical work by a material. A

smart material converts the stimuli, be it electrical, magnetic, thermal, etc. into action, for

example, mechanical strain. The class of smart materials includes piezo, shape memory,

magnetostrictive, electrostrictive, electrorheological, magnetorheological, and

photomechanical materials [29]. Some smart materials are already fully commercialized.

Piezoelectric devices make up much of modern scientific instrumentation's many micro-

positioners and focusing contraptions for lenses. Some of us have worn shape memory

alloys to correct our teeth in the form of the arch-wire of braces. Shape memory alloys

(SMA) find other application in braces and eyeglass nosepieces, but also include

important applications like surgical arterial stents and orthopedic stapes, having high

biocompatibility [30]. SMA holds especial promise in aerospace applications as it can

make lightweight actuators [31].

2.1.1 Shape memory alloys

Shape memory alloys are thought of as smart materials able to "remember"

shapes. In the West it was first observed by Arne Ölander studying the pseudoelastic

behavior Au-Cd alloy [32], then developed upon by Chang and Read who in 1951

describe a rubber-like effect in the martensite due to variant reorientation [33]. The Soviet scientist Kurdyumov described martensitic "elastic crystals" in Cu-Al 1949 [34].

However, the effect was faint. In the 1960s, the United States Naval Ordnance Laboratory developed practical SMA studying Ni-Ti [35-37]. Ni-Ti based alloys are now the main thermal (responding to temperature as stimuli) SMA metal. Other shape-memory materials are common such as polymeric shape memory plastics, (e.g. the material of heat shrink tubing), but these are outside the scope of this dissertation.

In metallic alloys, the shape memory effect (SME) stems from a diffusionless, displacive phase transformation between a high symmetry, high-temperature phase (austenite), and a low symmetry, low-temperature phase (martensite). Figure 2-1 schematically illustrates the martensitic transformation and SME. Upon heating, the material assumes the austenite phase which often has a cubic lattice. Upon cooling, it transforms martensitically by shearing into a low symmetry (such as tetragonal or monoclinic) lattice. Following group theory, the reduction of symmetry leads to the creation of martensite variants. The variants are separated by variant boundaries. Applying stress causes the transformation of one variant to another, generating the high strains. Upon reheating the material transforms back to the austenite phase and recovers the original shape.
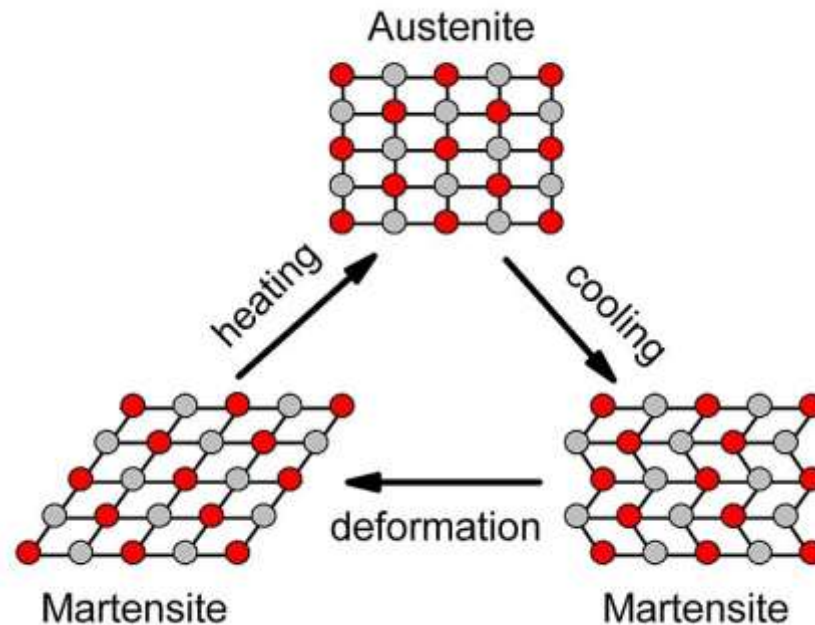
Figure 2-1: **The shape memory effect. Cooling causes the forwards martensitic transformation. Stress drives twin boundary motion and martensite variant reorientation, which causes a shape change. The original shape recovered upon heating. Reprinted from wikicommons [38].**

Drawbacks however exist for SMA. Most applications use the two-way effect, in which transformation strain is at most half of the one-way effect. Another drawback is that thermal actuation is a slow process. SMA actuators typically run an electrical current through the SMA element to produce Joule heating and obtain the cooling by convective heat transfer to the environment. While heating can be fast, the cooling process is quite slow. The fatigue life is typically up to tens of thousands of switching cycles and is rather low [39].

2.1.2 Magnetic shape memory alloys

A distinguishing feature of *magnetic* shape memory (MSM) alloys is a macroscopic shape change when exposed to a magnetic field. The shape change is divided into magnetoplastic and magnetoelastic strain [40]. During magnetoelastic deformation, the initial shape is restored when the applied magnetic field is removed.

During magnetoplastic deformation, the shape change is reversible by reorientation of a magnetic field. Akin to mechanical stress, the magnetostress caused by the magnetic field induces the deformation. The strain resulting from the macroscopic shape change by the magnetic field is called the magnetic-field-induced strain (MFIS). The stress necessary to initiate twin boundary motion is the twinning stress.

MSM alloys combine features of SMA and typical magnetostrictive materials such as Terfenol-D. They have a large strain and are not limited by kinetics of heat transfer as in thermally activated SMA. MFIS can occur at kHz frequencies [41-43]. The material has been demonstrated to sustain up to two billion mechanical cycles. SMA has a fatigue life of only tens of thousands of cycles. Figure 2-2 shows the work output of MSM compared to other actuator technologies. MSM alloys have the distinction of having both fast actuation frequency and high strains, i.e. high power density.
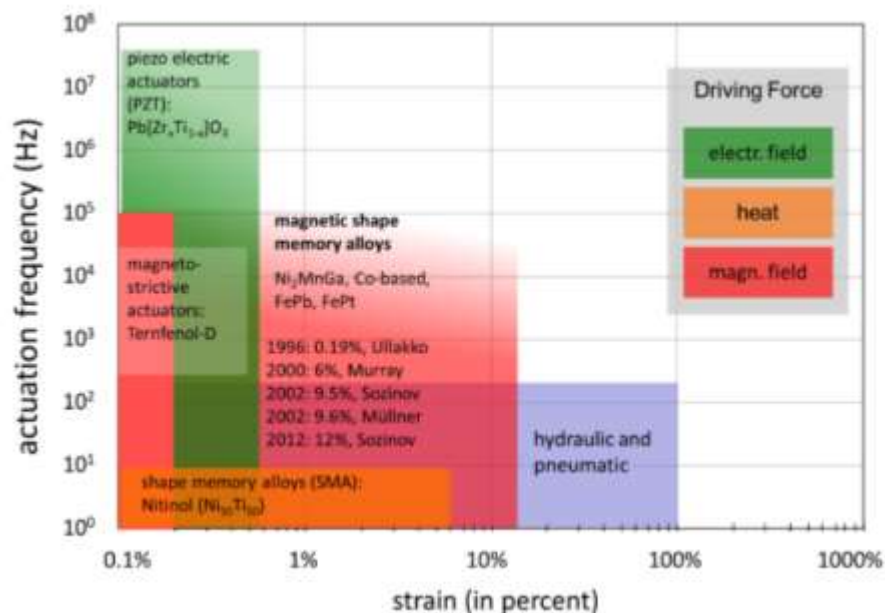
Figure 2-2: **Work output of various actuators. Piezoelectrics have low strains but actuate at high frequency. Shape memory alloys are slow but have a high strain. Magnetic shape memory alloys have high strain at high frequencies and thus have high work density.**

2.2 Magnetism

Magnetic fields permeate our world on earth, from superconductors used for magnetic resonance imaging machines (MRI) to the impulse of a heartbeat, to the fine EMF of the Human brain. Earth's magnetic flux shields our world from ionizing radiation and allows for the magic of Life.

<u>2.2.1 Fundamentals</u>

This section is based on the contents of Callister [44], and Jiles [45]. Magnetic field is produced whenever there is electrical charge in motion. Magnetic field sources exist as a magnetic dipole, analogous to an electrical dipole. When charges in a material are at rest, the only interaction between them is the electrostatic Coulomb force. If the charges are in motion, they cause an additional interaction force, the Lorenz force, which we commonly call magnetic field.

Equation (1) describes the vector of the magnetic field (H) produced by a circular current, with N being the number of turns, l the length, and I the induced current.

$$H \ = \ \frac{NI}{l} \ (1)$$

The magnetic flux density (B) is the magnetic field multiplied with the magnetic permeability μ of the medium:

$$B = \mu H, \text{ in vacuum } B = \mu_0 H \ (2)$$

Where μ_0 is the permeability of free space in a vacuum, 4π x 10^{-7} H/m. Commonly, permeability is reported as the relative permeability μ_r, which compares the ratio of the matter's magnetic permeability to the permeability of free space:

$$\mu_r \ = \ \frac{\mu}{\mu_0} (3)$$

We describe the magnetic field induced in matter as magnetization M:

$$\boldsymbol{B} = \mu_0\boldsymbol{H} + \mu_0\boldsymbol{M} \text{ (4)}$$

In the presence of $\boldsymbol{H}$, the magnetic momenta, the sum of the individual magnetic moments of the constituent atoms, align with the applied magnetic field and reinforce the field by the amount $\mu_0\boldsymbol{M}$. The magnetic moment is the strength and orientation of the material's magnetic dipole.

2.2.2 Magnetism in materials

Magnetization $\boldsymbol{M}$ is the sum of magnetic moments of atoms in the matter. Electrons have a spin. The net magnetic moment of an atom is the sum of all electron spins and moments resulting from the electron "orbit". A magnetic field interacts with each individual moment. The type of alignment gives rise to the behaviors we label diamagnetism, paramagnetism, ferromagnetism, ferrimagnetism, and anti-ferromagnetism.

Ferromagnetic materials are strongly magnetic due to the quantum mechanical interaction called the exchange interaction. In ferromagnetic materials, the exchange energy has a minimum when the moments align parallel. The parallel alignment of magnetic moments extends across large regions of the material. If $\boldsymbol{H} << \boldsymbol{M}$ we can neglect $\boldsymbol{H}$, thus:

$$\boldsymbol{B} \simeq \mu_0\boldsymbol{M} \text{ (5)}$$

Ferromagnetism is associated with unpaired electrons, as pairing cancels the magnetic moments. Therefore, the elements which show ferromagnetism are in the center of the transition metals block in the periodic table (Fe, Ni, Co), and include several of the lanthanides (e.g. Dy, Nd, Sm).

When all magnetic moments are fully aligned with the magnetic field, magnetization has its maximum. The maximum possible magnetization of a ferromagnet is the saturation magnetization (M_S). Temperature has a significant influence on magnetization, as shown in Figure 2-3(a). Thermal energy in form of entropy counteracts the stabilizing effect of the exchange interaction. At the Curie temperature T_C, the thermal energy exceeds the exchange energy. At 0 K, the saturation magnetization is maximal. With increasing temperature, M_S decreases until reaching T_C. Above T_C, the material is paramagnetic.

2.2.3 Magnetocrystalline anisotropy

The exchange interaction varies according to the crystallographic direction. Having a non-spherical magnetic anisotropy energy surface is a characteristic of all ferromagnets. Magnetocrystalline anisotropy is found to some extent in all crystalline magnets but is macroscopically relevant predominantly in single crystals and textured polycrystals. In single crystals, the material expresses its full anisotropy, and the different axes magnetize according to their anisotropy energy surface. The randomization of crystallographic orientations in a polycrystal cancels out net magnetocrystalline anisotropy. In Figure 2-3(b), magnetized along an easy direction, the material quickly saturates. Magnetized along a hard axis, the material slowly magnetizes, reaching saturation at the anisotropy field (H_A). The area between the easy and hard magnetization curves and below M_S is the magnetocrystalline anisotropy energy K_U. A large K_U is an important condition for the MSM effect. The commonly used 10M phase of Ni-Mn-Ga has nearly uniaxial anisotropy with a first order uniaxial constant of $K_1(283K) = 2.0$ x $10^5 J/m^3$ [46]
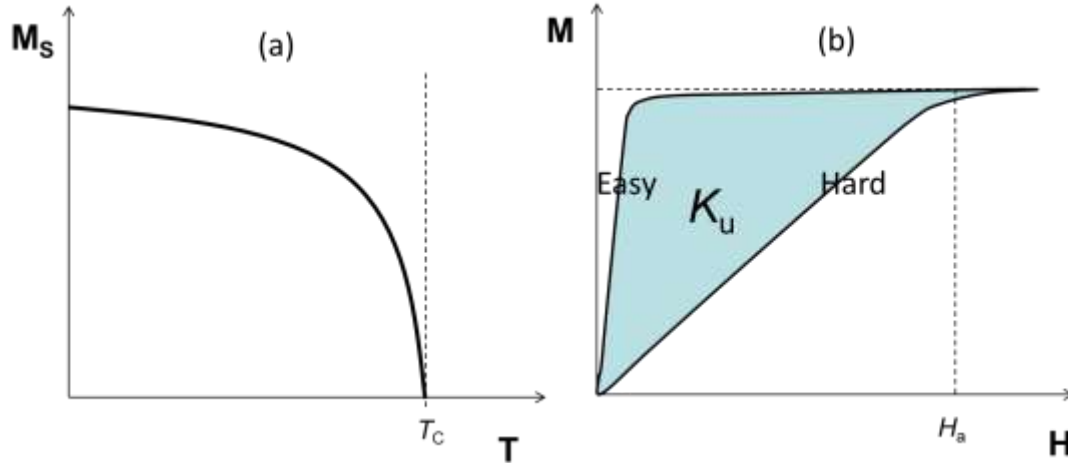
Figure 2-3: **(a) Decreasing magnetization with increased temperature in a ferromagnet. With increasing temperature, phonons counteract the exchange interaction, until canceling it, at T_C (b) Magnetization along the easy and hard magnetization axes in a material exhibiting uniaxial anisotropy. The maximum area available to do work is a function of the anisotropy energy (K_U). The anisotropy field H_A refers to the point of magnetic saturation for the easy and hard axes, respectively.**

2.2.4 Stray field

The magnet shown in Figure 2-4 is fully magnetized, i.e. it is magnetically saturated such that all the magnetic domains aligned in a parallel arrangement, and the exchange energy is at the lowest value. North and south poles are generated in the magnet, which create a magnetic field around the magnet, the stray field. Inside the magnetized material, the stray field acts opposite to the direction of magnetization. The internal demagnetization reduces the effective magnetic field by the demagnetization factor N_D and depends on the sample shape. The effective field, (H_{EFF}) is:

$$H_{EFF} = H_{APP} - N_D M \quad (6)$$

Applying a magnetic field parallel to an infinite rod, the demagnetization factor is zero. Applying a magnetic field perpendicular to an infinite plate results in a demagnetization factor of one, and an $H_{EFF} = 0$, i.e. it is impossible to magnetize the infinite plate. In effect, thin sheets do not magnetize as well as long elements.

A magnetic circuit is analogous to an electrical circuit. As an electric field causes an electric current to flow across the resistance, a magnetic field generates magnetic flux, and rather than using electrical energy, it stores magnetic energy. Analogous to electric resistors, are air gaps, which have high reluctance and store magnetic energy, rather than heat in the case of resistor. The total circuit reluctance is the sum of the reluctance of each component in the magnetic circuit. The lowest energy state is that with the lowest reluctance. A material may change its magnetic structure to reach the lowest energy state.
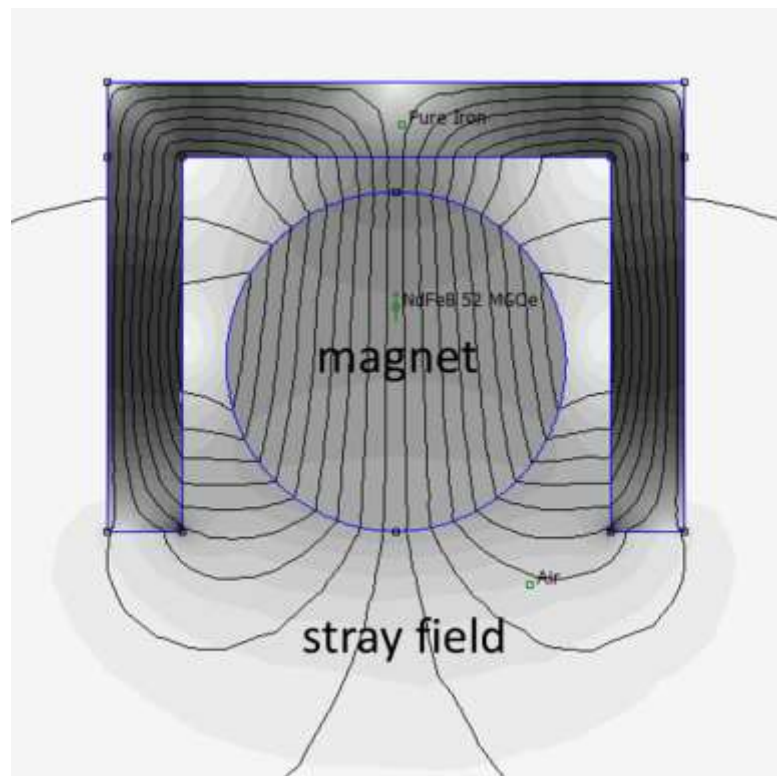
Figure 2-4:   FEMM simulation of a NdFeB magnet interacting with an iron yoke. The stray field outside of the magnet takes the path of least reluctance. Therefore, it enters the ferromagnetic yoke. The stray field is the total field energy outside of the magnet. The flux enters the yoke to reduce the total stray field energy.

Air, unlike in electricity, is however still a reasonable conductor of flux. Some of the flux shorts through the air, and is lost as leakage flux. A high-efficiency magnetic circuit has

a low reluctance and minimal air gaps, as the areas of high reluctance (such as air gaps) store more energy.

Much energy can be stored in the stray field, which, if generated electrically makes the switching motion of actuators inefficient. If the stray field is created by a permanent magnet, high-speed rotation leads to an electromotive force that affects nearby conductors. For high-speed actuation, the stray field energy should be low. The design of a magnetic actuator should avoid large air gaps, as these leak stray field.

2.3 Finite element method magnetics (FEMM)

Magnetostatics calculation software use solutions of Maxwell equations to model magnetic circuits. Figure 2-4 shows the results of a simulation of an N52 grade magnet interacting with a pure iron yoke in air. The stray field enters the iron yoke to reduce the magnetic circuit's reluctance. The stray field tends to permeate out if not contained by low reluctance materials.

Finite element analysis (FEA) is a numerical method of calculating magnetic fields at each node of the generated mesh of the model. We use the software created by D. Meeker, Finite Element Method Magnetics (FEMM) [47]. We additionally use relative permeabilities of 2 and 40 from Suorsa *et al*. [21] to model Ni-Mn-Ga variants introduced. The software does not allow for full description of Ni-Mn-Ga material, as it does not allow for modeling of an anisotropic magnetizations to include non-linear magnetization.

We include both permanent magnets and electrical coils in the simulations. The energy of the permanent magnet is determined by its location on the 2nd quadrant demagnetization curve, which is nearly linear in rare-earth magnets [45, 47]. The stored energy in the magnet is the energy stored in the magnet's internal reluctance:

$$W_m = \frac{1}{2} R_m \Phi_d^2$$

For a uniformly magnetized magnet is the energy is approximately:

$$w_m = \frac{1}{2} \mu \boldsymbol{H^2}$$

The flux for a magnetic circuit using both coils and magnets is modeled using the Thévenin circuit, which considers a constant flux source and parallel reluctance. Interaction with electromagnetic fields, induced by coils, act to change the position of the operating point of the magnet in the 2nd quadrant demagnetization [48, 49]. The fluxes and energies calculated in FEMM use these principles and calculate over a finite element mesh.

<div align="center">

2.3 Ni-Mn-Ga

</div>

2.3.1 Heusler alloys

In 1903, German chemist Friedrich Heusler discovered that the alloy Cu_2MnSn was ferromagnetic, even though none of the constituent elements were magnetic[50]. The Heusler alloys can be highly magnetic; Cu_2MnSn has a saturation magnetization higher than even the ferromagnetic Ni. Heusler alloys are ferromagnetic materials which exhibit the $L2_1$-ordered face-centered cubic structure. The $L2_1$ structure has a composition X_2YZ where X and Y are typically transition metals, while Z is a intermetallic or non-metal. For Ni_2MnGa, despite having ferromagnetic Ni, most of the magnetism comes from Mn [51].

2.3.2 Crystal structures

In the cubic Heusler austenite phase, the manganese occupies the eight corners of the unit cell and the six face centers resulting in a face-centered cubic structure (FCC) shown in Figure 2-5. Gallium resides in between the manganese atoms and forms an FCC

sub-lattice. Nickel atoms take the ¼, ¼, ¼ sites of the unit cell and form a simple cubic

sub-lattice.
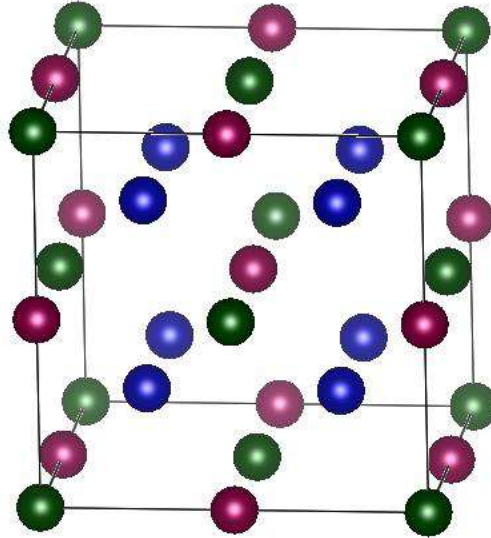
Figure 2-5:   Heusler L2₁ Ni-Mn-Ga. The Ni takes blue sites. Mn and Ga take the FCC sublattice sites.

In the martensitic transformation, cubic austenite distorts into a tetragonal or

monoclinic martensite. Three martensitic phases exist for Ni-Mn-Ga: (NM), (14M), and

(10M). Cooling from austenite, the martensite can have either 10M, 14M, or NM

structure, depending upon alloy composition.

NM martensite has a tetragonal unit cell with $c/a >1$. This martensite has

relatively high twinning stress and in most cases does not exhibit shape changes in

magnetic field. The twinning strain is up to 20%. A 12% MFIS was demonstrated for Ni-

Mn-Ga-Co-Cu NM martensite [16]. The 14-layer modulated (14M) martensite has an

approximately orthorhombic structure with $c/a <1$, modulated by a seven layer-periodic

shuffling. The MSM effect has been demonstrated in 14M with MFIS of about 10% [15,

18].

The lattice of 10 layer modulated (10M) martensite has an approximately tetragonal unit cell with a modulation of 5 layers that repeats twice for a full period. The approximately tetragonal cell has a ratio c/a <1. 10M martensite has extraordinarily low twinning stress. 10M shows full theoretical MFIS around 6-7% [12, 27] and is the prototype material for most MSM actuators and also the phase of study in this dissertation.

The stoichiometric form X_2YZ refers to an intermetallic compound with exact composition 50 at.% X, 25 at.% Y, and 25 at.% Z and each element occupying the positions as described in Figure 2-5. Some Heusler alloys have a large solubility range and different species occupy different sites. In such a case, the form X-Y-Z (e.g. Ni-Mn-Ga) is used.

2.3.3 Martensitic transformation

Figure 2-6 is a low field (100 Oe) temperature scan of magnetization. We find the transformation temperatures from such scans. In the forward transformation, the transformation to martensite begins at M_S and finishes at M_F. A sharp decrease in the low-field magnetization occurs at the transformation. In the reverse transformation, the austenite phase begins to form at A_S and fully transforms into martensite at A_F.

The martensitic transformation exhibits a thermal hysteresis. The average martensitic transformation temperature is usually reported as the center of the transformation, or $(A_S + M_S)/2 = T_M$.
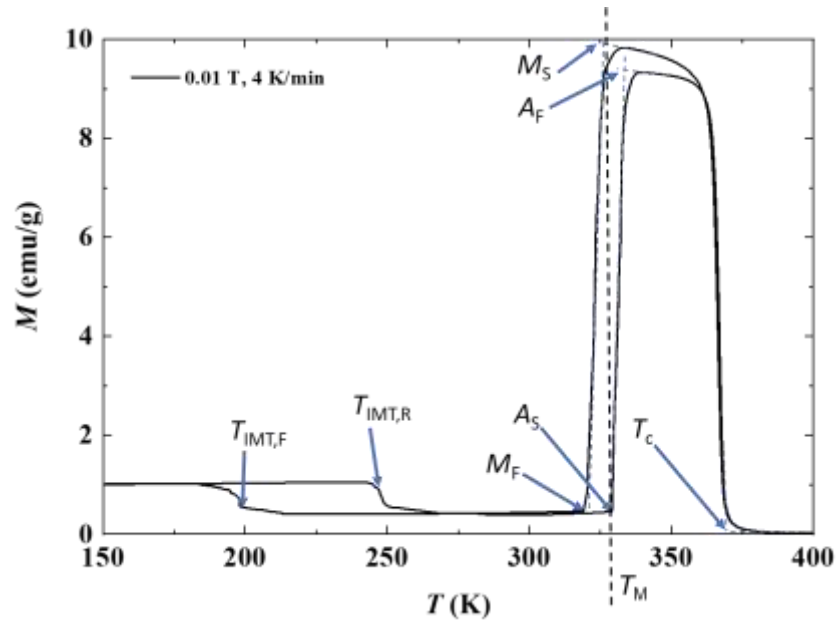
Figure 2-6: Phase transformations identified by measuring the magnetization of Ni-Mn-Ga in a low magnetic field of 0.01 T. Heating the material from 150 K, the 14M phase experiences an intermartensitic transformation to 10M phase at $T_{IMT, R}$. Further heating in the 10M phase induces a reverse martensitic transformation beginning at temperature A_S. The transformation ends at A_F. With heating, ferromagnetic ordering vanishes at T_C. Cooling again, the sample experiences a forward martensitic transformation, from M_S to M_F, and then the forwards intermartensitic transformation ($T_{IMT, F}$).

In Figure 2-6, an intermartensitic transformation occurs as the 10M structure

transforms to 14M. The forwards transformation occurs upon cooling at $T_{IMT, F} \sim 200K$,

and the reverse transformation upon heating at $T_{IMT, R} \sim 250$ K. The transition is sensitive

to composition and external forces [8, 52, 53]. Cooling further, the 14M martensite

transforms into non-modulated martensite (NM). For Ni_2MnGa, NM is the ground state

[54-56].

2.3.4 Tailoring *Tm* by composition

The martensitic transformation temperatures of Ni-Mn-Ga are quite sensitive to

the composition. Changing the compositions by 5%, the austenite/martensite equilibrium

temperature varies from 154 to 458 K [52]. Chernenko first found the transformation

temperatures of Ni-Mn-Ga were, akin to other Heusler β-alloys, dependent upon the

Hume-Rothery mechanism, the e/a measuring the decrease of the electron energy. The

electron concentration (e/a) gives the electrons outside the core, e.g Ni is core $+ 3d^8 4s^2$,

which is 10 electrons. For Ni2MnGa, a unit cell contains 8 Ni atoms with 10 valence

electrons each, 4 Mn atoms with 7 valence electrons each, and 4 Ga atoms with 3 valence

electrons each. Thus, for stoichiometric Ni2MnGa, the e/a ratio is 7.5.
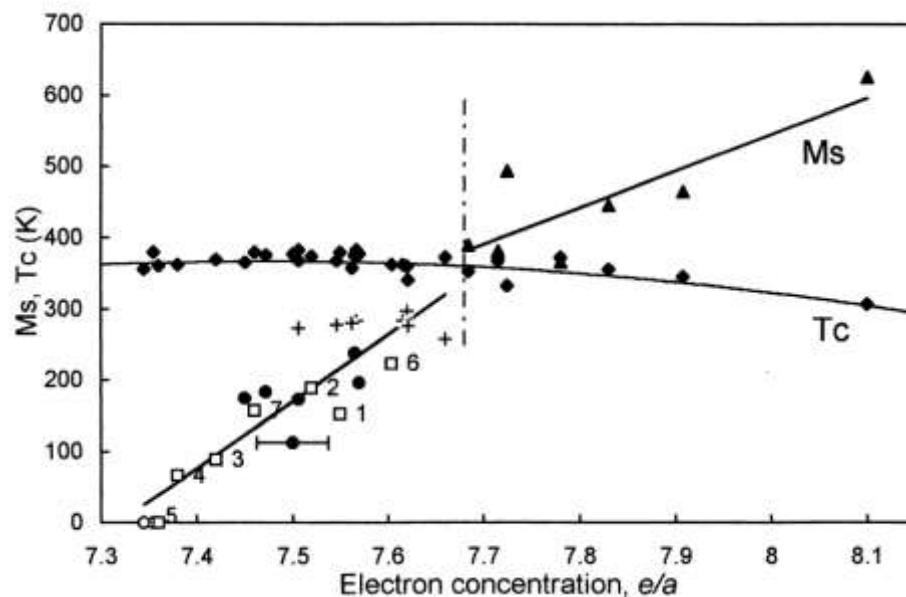
Figure 2-7: **Chernenko first described the dependence of M_S and T_C upon the valence electron ration. Continued research showed that the e/a ratio is a good predictor for many of the functional properties of Ni-Mn-Ga [57]. The discontinuity at e/a about 7.7 is the transition accommodated by 14M phase. Reprinted from Scripta Materialia, 40, V.A. Chernenko, Compositional instability of β-phase in Ni-Mn-Ga alloys, 523-527. Copyright (1999), with permission from Elsevier.**

The e/a ratio increases with increasing Ni content, or by substituting Mn for Ga.

The martensite transformation and Curie temperatures are given as a function of e/a ratio

in Figure 2-7 reprinted from Chernenko *et al.* [57]. The solid lines give the Curie

transformation, and the martensite start (M_S) temperatures. The dashed vertical line is a

transition suggested by Chernenko to be accommodated by the 14M intermediate

martensite phase. Further analysis has shown that the *e/a* ratio is a useful metric for

analyzing the twinning stress, and magnetization saturation of Ni-Mn-Ga based MSM

alloys [58]. The curie temperature is less dependent upon phase, only slightly decreasing

with increased *e/a*.

2.3.5 Twinning

      The mechanism of deformation in Ni-Mn-Ga is twinning. The transformation

from higher symmetry cubic to lower symmetry tetragonal causes multiple orientations.

These are called twin domains. Twin domains are related by rotation about a common

direction or reflection across a common plane. In Figure 2-8a, a twin boundary separates

two twin domains. The twin boundary advances by the motion of twinning dislocations

across the twin boundary as shown in Figure 2-8b. The ease of movement of the

dislocations defines the twinning stress.
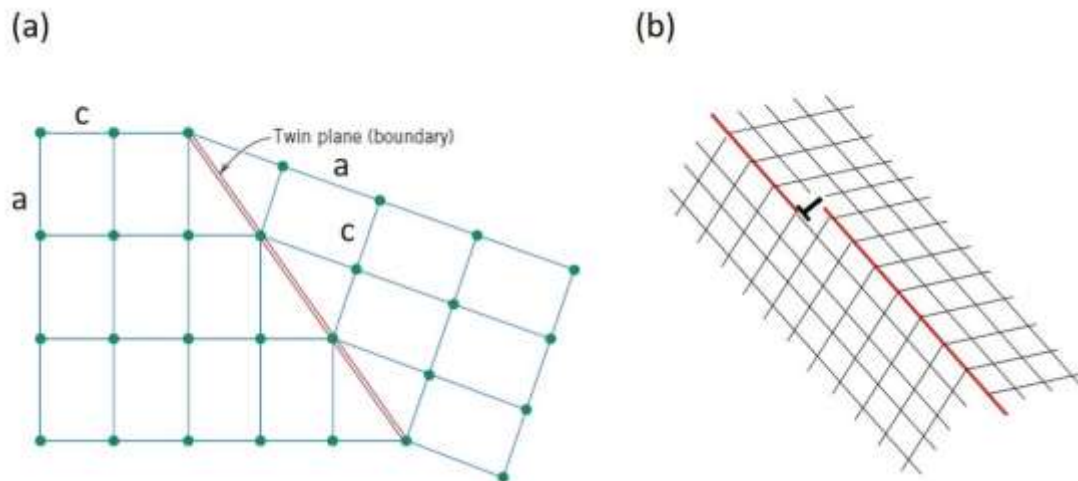
Figure 2-8: In (a) a twin boundary separates the tetragonal martensite, the short *c*-axis, and long *a*-axis. In (b) a twinning dislocation moves along the twin boundary, the mechanism of "twin boundary motion"

When the MSM alloy is strained, twin boundaries move through the material and flip the orientation of the *c*-axis. Figure 2-9 shows the process of magnetically induced reorientation (MIR). The red twin domain with vertical *c* consumes the unfavorably aligned yellow domain. The twin boundaries move and transform one martensite variant into another.

A characteristic of 10M martensite is its very low twinning stress of below about 1 MPa enabling the actuation of twinning by a magnetic field. The twinning stress is affected by the twin microstructure, type of twins, and crystalline defects.
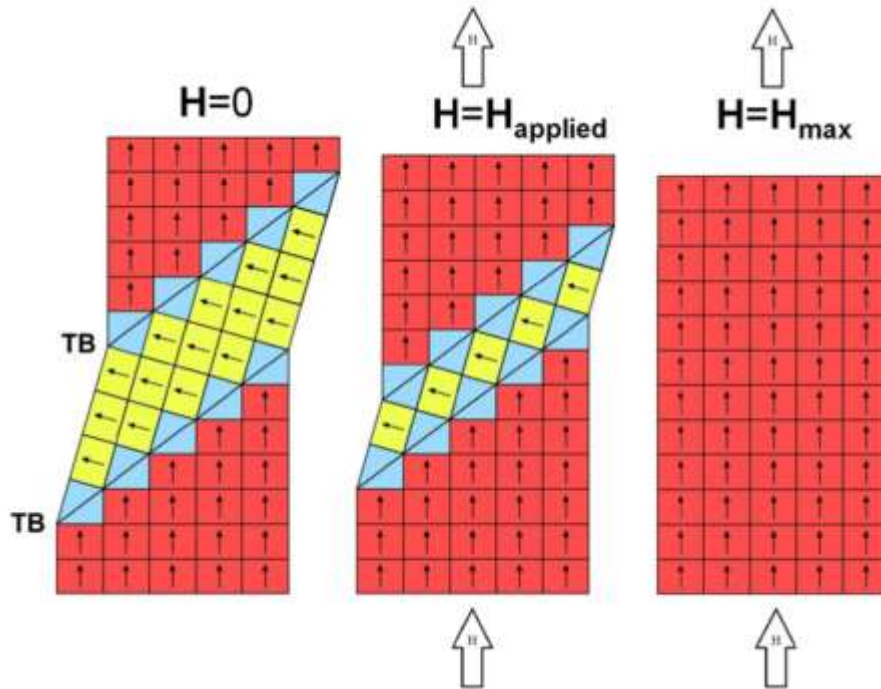
Figure 2-9:   Mechanism of MFIS. The c axis of the variant will align with the magnetic field by the motion of twin boundaries transforming the volume fraction. The energetically unfavorable variant (yellow) disappears, transformed into red, causing contraction in the vertical direction.

The twins of interest in this dissertation are type I and type II twins, which carry the deformation in the 10M martensite. The twins are distinguished by the type of orientation relationship, which leads to slightly different orientations of the twin

boundary. Ref. [59] gives a detailed overview of twinning in Ni-Mn-Ga. The orientation,

and thus the type of the twin, can be identified with optical microscopy through the

direction of the trace of the twin boundary plane on the sample surface, as shown in

Figure 2-10 [60, 61]. Type I twins have a twinning stress of about 1.0MPa near the

martensitic transformation. The twinning stress increases at $\sim$ 0.04 MPa K^{-1} upon cooling

[60]. Below about 40 K under A_S, the twinning stress of the Type I boundary is greater

than the available magnetostress [62, 63]. Therefore, the operating temperatures range of

the Type I twinned MSM device is from below 40 K under the martensitic transformation

up to the austenite start temperature.
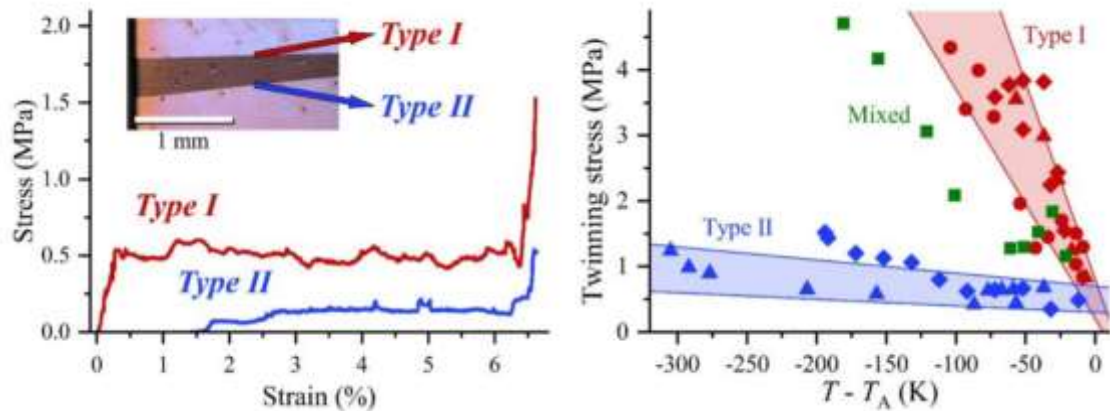
Figure 2-10: (a) The mobility of the Type I and Type II twin boundary in the same crystal. (b) Type I twin boundaries are thermally activated, whereas, the Type II twins are nearly athermal. From SSRN published paper [61]

Type II twins have very mobile twin boundaries in Ni-Mn-Ga [64, 65]. The

twinning stress is often lower than 0.1 MPa and does not substantially depend on

temperature down to 1.7K [66]. An actuator using type II twins might have a range from

cryogenic temperatures up to A_S. The highest A_S reported for 10M Ni-Mn-Ga is 353 K

[27]. Often both twin types occur simultaneously. This is seen in the green lines of the

Mixed in Figure 2-10, where the twin boundary mobility and temperature dependence take a value in between the Type I and Type II behaviors.

2.3.6 Magnetically induced twinning

The twinning stress is important to the functional properties of MSMA. Figure 2-11 shows a typical M-H loop for a 10M sample (blue curves). Applying the magnetic field parallel to the hard axis results in magnetization along a shallow slope. At the switching field H_S, twin boundaries start moving and transform between martensitic variants. The switching field H_S corresponds to a twinning stress according to conversion models [67, 68]. Decreasing the field, the sample demagnetizes along the easy axis. The work done on the MSM alloy is the area indicated in Figure 2-11. This is a dissipative work and results in heating of the sample. With a higher H_S, the work done on the MSM sample is greater, and the energy output (green area) is less. By decreasing the switching field to 0.05 MA/m, as for a type II twin, the work done on the sample is low, and the energy output is high, giving high power conversion efficiency. Therefore, type II are preferred over type I twins for practical application.
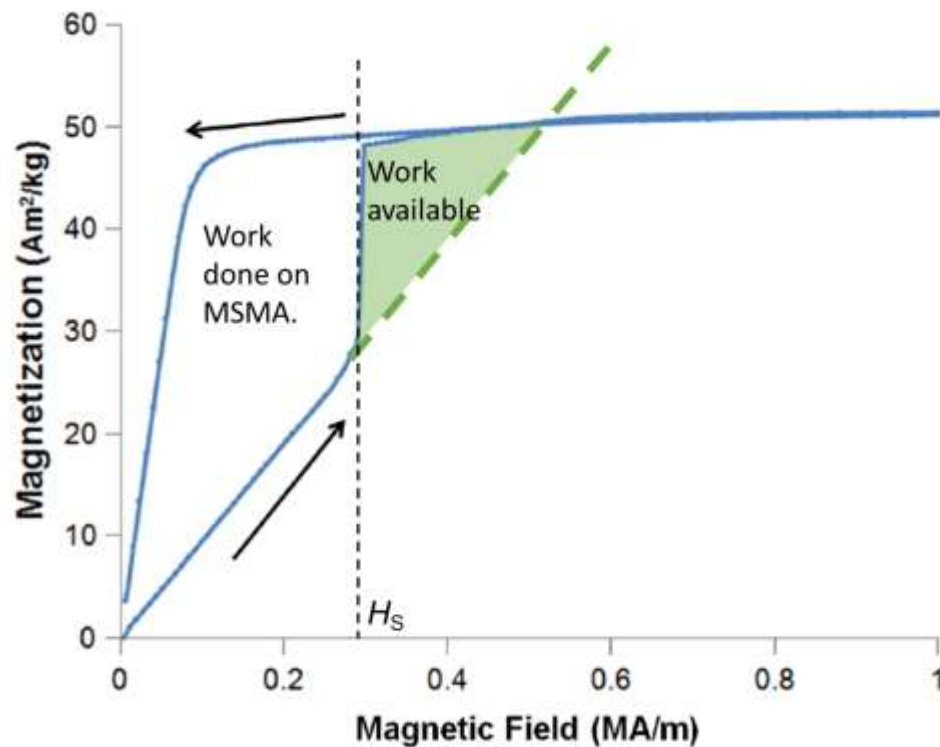
Figure 2-11: Switching field graph recorded for a 10M element. Beginning with the magnetic field orthogonal to the *c*-axis, the material magnetizes along the hard axis. The magnetization jumps to saturation as the material quickly switches from one orientation to another. If the switching occurs at low fields, the work done on the MSMA is low, and the work available high, giving high efficiency. If the twinning stress is high, the available work density is lower.

2.3.7 Twin microstructure

At this point, it is useful to define an MSM element. A single crystal is grown,

and then a small section is cut from the boule, and the surface prepared according to

required experiment, usually with all faces parallel {100}. From here, the element begins

its thermomechanical history. The element is heated, and twinned, and exposed to a

pattern of mechanical stress and magnetic field variations. Each causes a small effect

upon the motion of the many twin boundaries. The history can take many paths. Thus, an

MSM element is not just a piece of metal, it is the metal plus the history. We call this

history training. One effect of this training is that it promotes the selection of the most

favored (i.e. lowest energy) twin domains, which consume the weaker. This leads to a coarse twin structure, where the entire sample deformation may be carried by a single moving twin boundary.

Self-accommodated martensite (SA)

Cooling from the parent austenite, the martensite phase takes a great many martensite domains on several length scales. This is called the self-accommodated (SA) martensite microstructure. The misoriented twin boundaries serve as obstacles to the motion of other twin boundaries. This self-accommodated twin microstructure shows a substantially reduced MFIS of about 0.1% but has long fatigue life [69].

Single-variant martensite (SV)

By rotating the single crystal element back and forth ~ 20 times in a strong magnetic field, twin boundaries migrate out to the surface and disappear. When removed from the magnetic field with one variant being aligned predominantly, the element takes a single martensite variant (SV) structure. SV elements deform by the motion of a single twin boundary through the element [70]. The SV microstructure exhibits the full MFIS of up to 7% for 10M structure and has a very low twinning stress of 0.1 MPa for type II twins. The single variant structure has critical disadvantages though, such as poor fatigue life, and stochastic, unstable actuation [69, 71]. The twin boundary mobility is a function of its location in the material. The twinning stress of a single type II twin boundary in Figure 2-12 is indicated as "single boundary".

Fine twin

The optical micrographs in Figure 2-12, show an oriented *two domain* fine twin microstructure [72]. The two twin domains are distributed into a pattern, or *lamellar*, of

the two variants. During actuation, the energetically preferred domain expands into the other domain, resulting in strain in the lamellar. The strain increases smoothly with stress, at modest twinning stress of 0.8 MPa. The fine twin structure strains less, only 3%, as both twin variants are present initially. This fine twin structure was trained into the element by bending over a radius, plastically inducing the equal twin volume fraction. The fine twin structure created by bending is impermanent and transforms into an SV structure rapidly upon cycling.
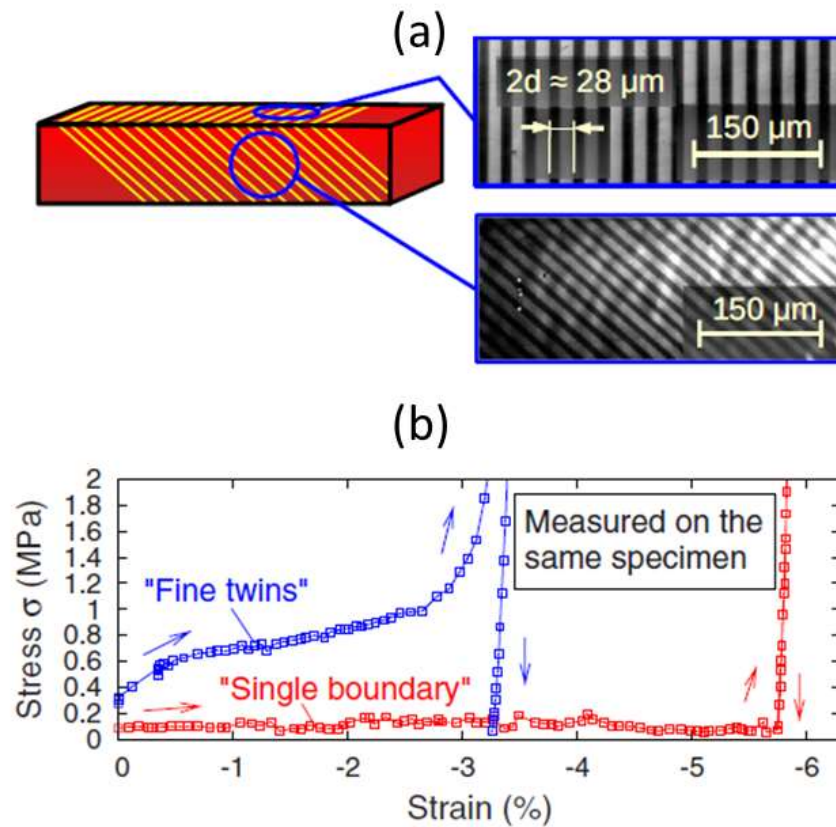
Figure 2-12: (a) microstructure of fine twins created by bending, viewed from the top, and the side under polarized light. (b) The influence of twin microstructure upon superplasticity. The single twin boundary has very low twinning stress and full strain. The fine twin structure has a smoothly increasing twinning stress and strains about 3%. L. Straka, N. Lanska, K. Ullakko, and A. Sozinov, Twin microstructure dependent mechanical response in Ni – Mn – Ga single crystals, Appl. Phys. Lett. 96, 2010], with the permission of AIP Publishing [72]

<u>2.3.8 Modes of actuation</u>

The sample can actuate longitudinally, in the manner of a traditional push-pull actuator as shown in Figure 2-13(a) and 2-13(b) reprinted from [73]. In this process, the twin boundaries are mutually parallel.

The two domains can assume interlaced triangles to accommodate the bending strain [74]. In Figure 2-13(c) the bottom is compressed, as it is fully blue with c horizontal; the top is extended and is orange with c vertical. Kucza *et al.* demonstrated that reversible bending can be caused by a magnetic field in high aspect ratio beams [73]. They found that samples both extended and bent. This is possible by changing the microstructure to have an unequal twin variant fraction as in Figure 2-13(d). A sample subject to torque in a magnetic field exhibits a mixture of bending strains and longitudinal strains.
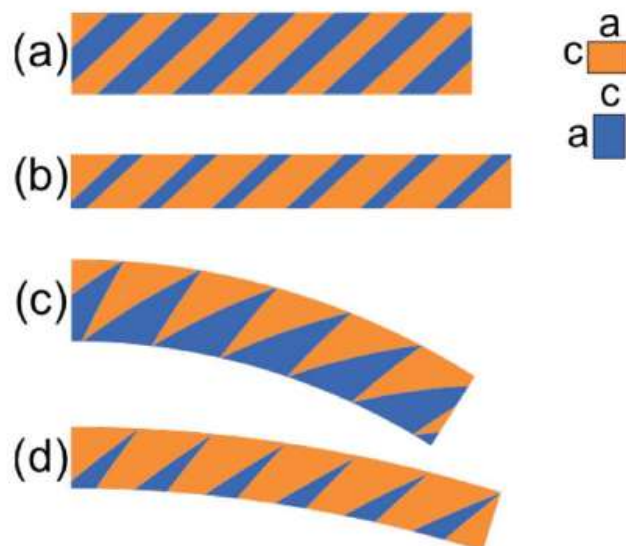
Figure 2-13:   Modes of MSM actuation. (a) the sample compresses axially and (b) expands axially. The element can bend via tapered wedge twins in response to bending stress. In (d) the sample can extend both bends and axially extend simultaneously. Reprinted from Acta Materialia, 95, N. Kucza *et al,* Magnetic-field-induced bending and straining of Ni-Mn-Ga single crystal beams with high aspect ratios, 284-290, Copyright (2015), with permission from Elsevier.

2.3.9 Fatigue and fracture

Fatigue is the accumulation of damage over cyclic loading. Accumulation of damage leads to hardening, crack nucleation, crack growth, and fracture. Fatigue determines the performance over the lifespan of the actuator. Müllner *et al.* studied fatigue on "effectively trained" (SV) and an "ineffectively trained" (SA) MSMA [71]. The single variant (SV) samples showed nearly full theoretical MFIS but fractured quickly. The self-accommodated (SA) samples had low MFIS ($< 1\%$) but did not fracture until more than 10^7 cycles. The authors explained the different fatigue life as related to blocked twinning dislocations, which pile up and lead to high-stress concentration and crack nucleation. In the self-accommodated structure, the dislocations do not move far, and thus don't pile up at defects. The reduced dislocation pile-up concentrates stresses less effectively. The reduction of stress concentration avoids the nucleation of cracks and

results in long fatigue life. Cycling the element has the effect of training a coarser microstructure. Chmielus *et al.* extended the study, to follow the SA turn into an SV microstructure over a high number of magneto-mechanical cycles [69]. The strain occurred in 3 stages. Up to 10^3 cycles, the strain was uniform at 0.2%. Between 10^3 and 10^5 - 10^6 cycles the strain gradually increased to 0.75 %. Abruptly, the strain jumped to 2%, then decreased back to 1% at 10^8 cycles before fracturing. The jump was due to a large training event that coarsened twins. The authors found that the constraints at the sample ends due to fixturing resulted in fine twins at the constraint, which transition to coarse twins near the center, in the bulk.

Aaltio *et al.* found that actuated mechanically, some SV 10M samples endured greater than 2 x 10^9 cycles at 2% strain range [75]. The strain occurred in a region that had twins approximately 100 μm thick. The coarser twins were blocked in their motion by the end fixturing, giving the large fatigue life. Straka *et al.* reported on the fatigue life of 10M elements treated with a surface modification technique which created a fine twin microstructure and allowed up to 5% MFIS [76]. The samples all sustained at least 10^8 cycles in push-pull mode and began to experience a reduction in MFIS after 10^7 cycles, to only half of the initial MFIS.

In 2016, Lawrence *et al*. tested sixty unconstrained 10M samples in a rotating magnetic field [77]. Most samples fractured before 10^5 cycles. Unconstrained crystals, it seems, have especially low fatigue life. The samples which were most resistant against fatigue had finely polished surfaces. Surfaces with deeper scratches, as induced by grinding [78] experienced rapid crack nucleation and fracture. Crystal defects, such as small-angle grain boundaries somewhat blocked twin dislocations, leading to dislocation

pile-up and fracture, demonstrating the importance of crystal quality upon fatigue properties.

2.3.10 Effect of surface properties and constraints

Surface damage stabilizes a fine twin structure, as shown by Chmielus *et al.* [79] and Ezer *et al.* [80]. Figure 2-14 shows changes to the material's superelasticity with increasing surface damage. The pressures refer to the pressure of the air which carries the stream of small particles. Increased damage increased the twinning stress and caused a smoother deformation curve. Plastic deformation on the surface layer created a dense layer of pinning sites for twin boundaries. Other surface damage techniques have been studied as a way to stabilize a fine twin structure. In [81], Nb^+ ions were implanted into the surface. The ion implantation smoothened the actuation, but only allowed for about 3 % MFIS. Coating the MSM element imposes a constraint against motion which creates fine twins. After applying a coating of TiN in the austenite phase and subsequent cooling, the sample took a fine twin structure. The MFIS, however, was only 1% [81]. In the same study, constrained by a soft silicone elastomer, the element took a mesoscopic twin structure of 100 μm periodicity. In [82] Musiienko *et al.* applied an amorphous diamond coating which allowed MFIS of 4%.

a)
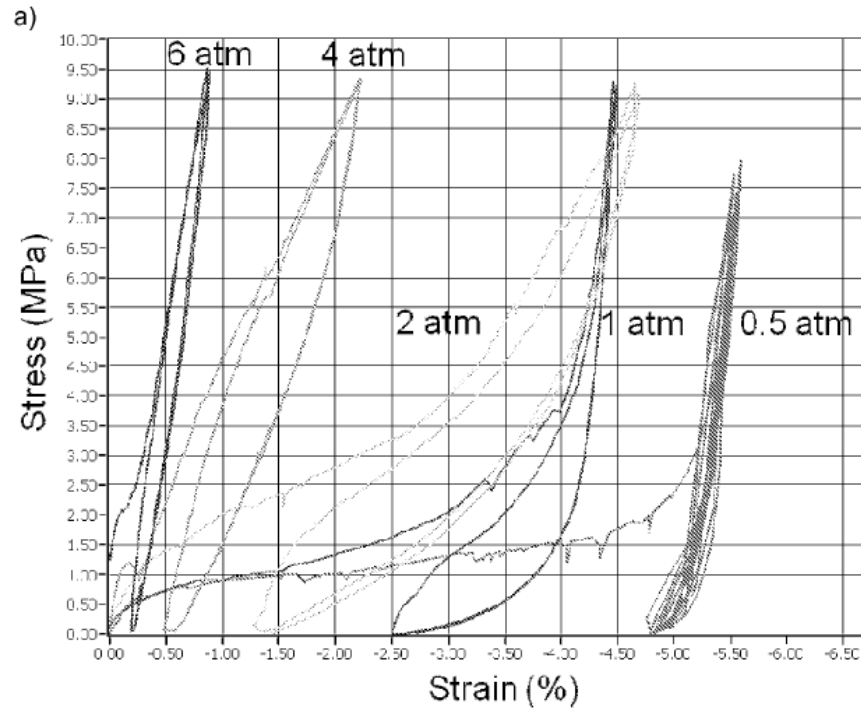
Figure 2-14:   Changes to superplasticity and superelasticity due to change in surface treatment pressure described in [80]. With low damage (0.5 atm), the superplasticity strain is about 5%, slightly less than theoretical MFIS, but increasing and still serrated. At 1 atm, the deformation is smoother. In the unloading, almost 1.5% of the strain is recovered, the superelastic response. With increasing pressure, the actuator becomes hard, with decreased available work density.

10M samples with fine twin structure, whether oriented or lamellar, exhibits good

fatigue life [71, 83]. In [76], Straka *et al.* propose a phenomenological model, which

describes the mechanism of reducing fatigue. According to that model, the sample

develops many microcracks in the active volume. The active twin volume is separated by

twin volumes which do not actuate. The passive regions do not accumulate fatigue and

block microcracks from propagating through the undamaged region.

2.4 MSM micropump

2.4.1 Local actuation

      Until here we have considered MSMA elements actuated by a uniform magnetic field. Now we discuss an element that has a localized strain in a heterogeneous magnetic field. With a sufficiently strong local magnetic field, the c axis of a region aligns with the magnetic field generating magnetic pole and causes a vertical contraction immediately above the pole. We call this contraction a shrinkage. Figure 2-14(a) shows the top surface of a locally actuated MSM element in a microscope equipped with polarized light. A series of twins (dark color) causes a local vertical shrinkage in the parent variant (light color). When the region shrinks vertically in the direction of the magnetic field the sample expands horizontally along the shrinkage to conserve volume.

      Figure 2-15(b) is a schematic side view of the MSM element shown in Figure 2-15(a). When the magnet in Figure 2-15(b) rotates, the strained region travels along the element length. The element actuates twice (once with the north pole and once with the south pole) in each magnetic field revolution. With clockwise magnet rotation, a shrinkage forms on the left then travels along the element and disappears on the right.
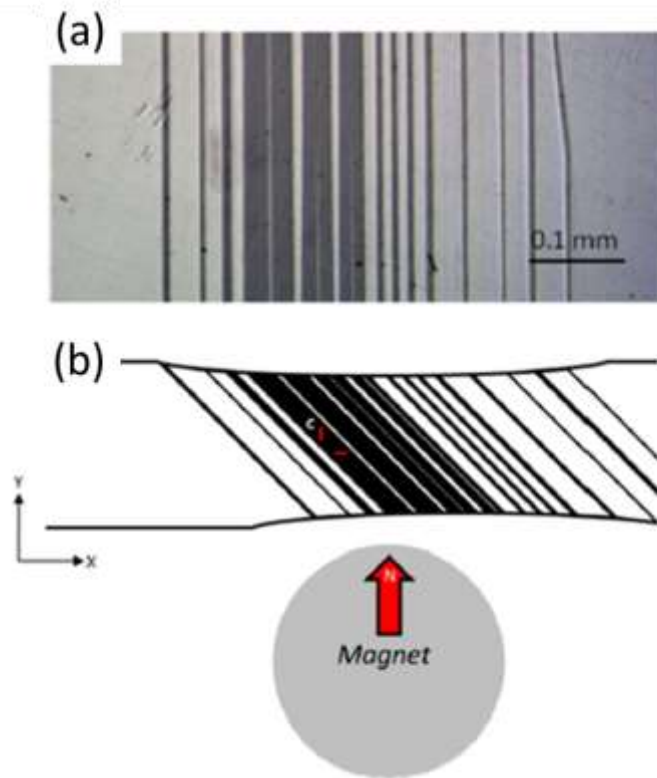
Figure 2-15:   A localized region is created by the pole of a rare earth magnet. The shrinkage is composed of two variants, the dark and light variant, seen by the polarization of reflected light on the element top surface (a). In (b), the twin structure along the side of the element. The central region is mostly black, then tapers back up to the white variant [23]. © IOP Publishing. Reproduced with permission. All rights reserved.

2.4.2 Pump mechanism

To make a pump we encapsulate the element in an elastomer, such as to seal the bottom and sides. We then place a top plate on the top surface, with an inlet and outlet port at about ± 2 mm from the center of the element. We can capture a bit of fluid with the shrinkage below the inlet, then rotate the magnet to transfer the fluid packet to the outlet. In essence, the pump consists of a single mechanical and stationary component, the MSM element, which transports the fluid. While the pump element itself deforms, there are no moving parts. A typical MSM pump module is shown in Figure 2-16.

Model P1.2
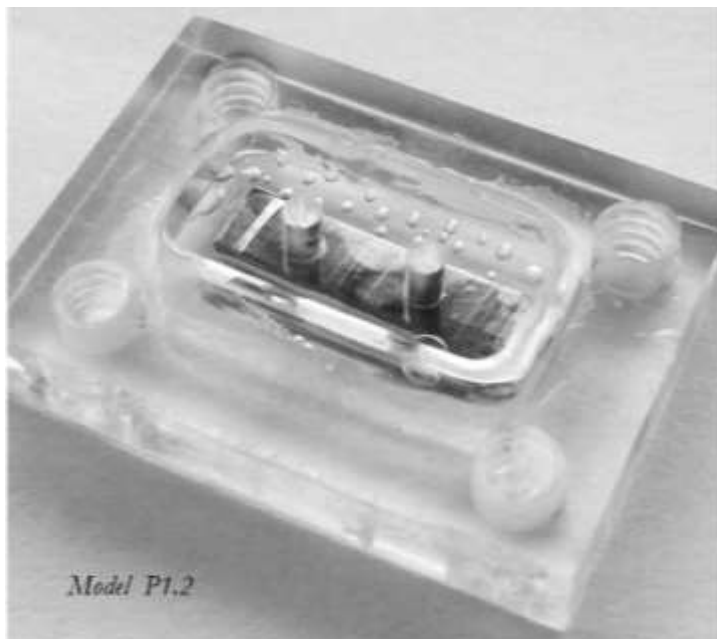
Figure 2-16:   The MSM micropump: The MSM element is the metallic bar suspended in the center of the plastic housing. The various white lines across the element surface are the twins. Two ports allow for the insertion and withdrawal of pumping media.

The MSM pump has a mechanism which is quite beneficial to microfluidics, allowing for greater pressure generation. Common micropumps are made of either piezoelectric or a micro-peristaltic mechanism. Such pumps are capable of pumping against relatively low pressure up to 55 kPa, though usually much less [84-86]. Often, requirements exist for pressures greater than this. The input pressure at the tip of the 16-gauge needle administering the flu shot can be 1 MPa [87, 88]. The maximum theoretical pressure of the MSM micropump determined by the blocking stress, 3 MPa in Ni-Mn-Ga, the pressure of a 300-meter column of water.

The MSM micropump presents the opportunity of a high pressure, high precision micropump. In the first presentation of an MSM pump, Ullakko *et al.* [23] described the pump, its basic mechanism, and some early simulation of magnetic flux pattern. The

authors used the pump to perform a polymerase chain reaction, finding that the pump was compatible with the PCR process. Smith *et al.* [24] measured the pump flowrate and generated pressures up to 150 kPa. Saren *et al.* [26] built a pump, which operated at pressure up to 1.0 MPa. In Ullakko *et al.* the MSM element surface was measured with a laser profilometer. A shrinkage formed in the MSM element (Figure 2-17), then moved along the element. The depth of the shrinkage was approximately 50 μm. The shrinkage slopes were asymmetrical and serrated, and do not appear to be systematic.
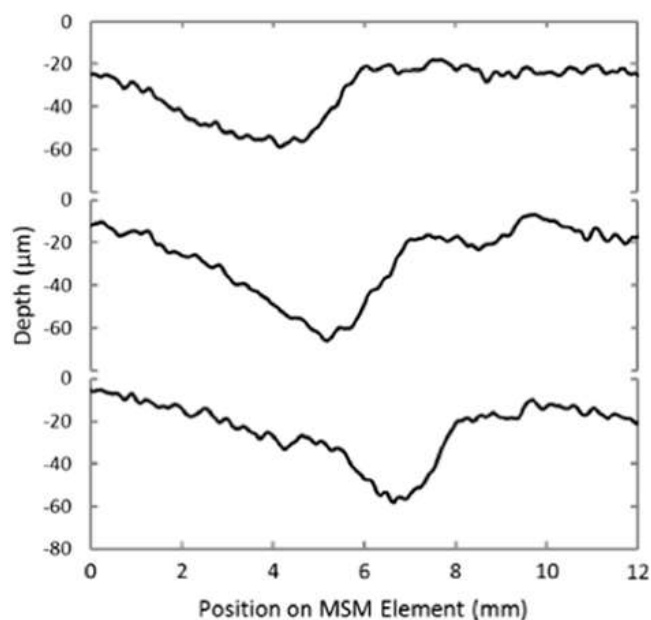
Figure 2-17: The shrinkage measured at three locations along the element, created by the rotation of a magnetic field beneath the element. The surface was measured by a laser profilometer. Non-contact profilometry is preferred, due to the large stray field of the rare earth magnet [23]. © IOP Publishing. Reproduced with permission. All rights reserved.

2.4.3 Electromagnetic driver

The simplicity of the MSM micropump - a pump which requires no moving parts - is one of its key attributes providing opportunity for miniaturization. Actuating the pump with an electromotor confounds this aspect. The micromotor is many times larger than the MSM pump element. Small precision motors are expensive. The possibility of an

electromagnetic driver was proposed in the first pump paper [26]. Such a driver would eliminate any rotating parts, which is a requirement for miniaturizing the entire pump system.

In 2014, Smith *et al.* [89] studied controlling the twin domain configuration in a constrained Ni-Mn-Ga sample using local magnetic fields. The authors showed that local twinning can be created at a specific location by the use of a focused magnetic field generated by an electromagnet. The authors determined that the twin volume fraction was constant, i.e. independent of position. Figure 2-18 shows the modeled magnetic flux with and without the presence of a stack of twins. Two poles were oriented facing each other orthogonal to the element. The authors physically moved the poles to cause a new twin to switch.
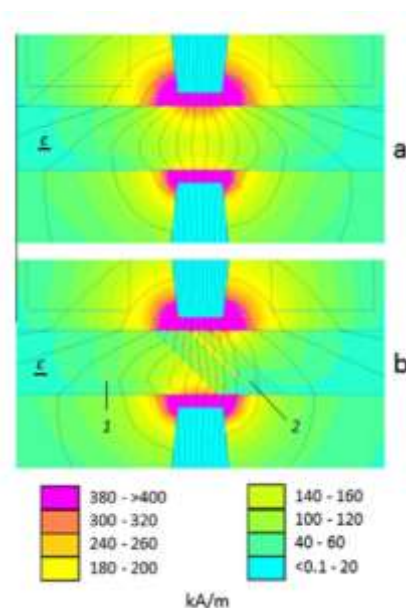
Figure 2-18: **FEA simulation of the focused magnetic field used by Smith *et al.* to create local twinning between the poles. In (a) the element was a single variant, subject to a ~300 mT field. In (b) the sample has twinned in response to the field, now taking a different field pattern, the field lines slightly deflected by twin boundaries [89]. Reprinted from Scripta Materialia, 77, A. Smith *et al.,* Controlling twin variant configuration in a constrained Ni-Mn-Ga sample using local magnetic fields, 68-70, Copyright (2014), with permission from Elsevier.**

Movement of the magnetic field in a motionless drives system would be desirable, such as made using a plurality of coils and ferromagnetic yokes cause an advancing vertical field, carrying along the shrinkage region. In a patent, Müllner *et al.* [90] envision the advancement of flux across a series of poles using the magnetic field compressed between adjacent opposing coils. The addition of permanent magnets was also noted as a method of adding increased flux to the system.

The electrical driver is an additional requirement. Solid state switching of high currents is fast and performed by transistors and thyristors. The material's switching rate is fast, and the rate of induction being the limiting factor. Switching via relays is slower, about 5 ms, though cheap and reliable.

Unfortunately, there is no easy way to measure the flux of some magnetic circuits, as the hall sensor has substantial width (0.9-3.0 mm in this study) of which is paramagnetic. Introducing the hall sensor thus has large effect upon the flux in most circuits, which are designed to have small airgaps to maximize efficiency. Our best measurement is actually well calibrated simulations which use other simulations to verify accuracy of the model to the physical device.

The switching may be done considering incremental steps between poles by switching DC power, by three phase power, or by slowly modulated DC systems. This dissertation considers only the switching of DC power methods.

CHAPTER THREE: MOTIVATION, OVERVIEW, AND CONTRIBUTIONS

In Chapter 1, we listed requirements for devices operated with an MSM element. Those requirements motivate this study. We evaluate methods to improve the MSMA element in a manner making it more suitable for application in an MSM micropump. Below is an outline of the content of the papers and manuscripts, which constitute this dissertation and my contribution to each paper. I presented some of these results at the 16th International Conference on New Actuators, June 25-27, 2018 in Bremen, Germany, and at the International Conference on Ferromagnetic Shape Memory Alloys, June 2-7, 2019 in Prague, Czech Republic.

Chapter 4 (i.e. "Systematic Trends of Transformation Temperatures and Crystal Structure of Ni-Mn-Ga-Fe-Cu Alloys" published February 2020 in Shape Memory and Superelasticity), evaluates the alloy system Ni-Mn-Ga-Fe-Cu and identifies strategies for increasing the martensitic transformation temperature (T_M). My contributions to this study were the design of the alloy, the synthesis of alloys, the measurements of phase transformation temperatures, saturation magnetization, and Curie temperatures, the data evaluation, and authorship. I performed this research while visiting the Institute of Physics of the Czech Academy of Sciences in Prague, Czech Republic, from June to December 2018.

Chapter 5 (i.e. "Effects of surface modifications on the fatigue life of unconstrained Ni-Mn-Ga single crystals in a rotating magnetic field" published June 2018 in Acta Materialia) evaluates "micropeening" as a method to introduce surfaces

stresses for increasing the fatigue resistance of MSM transducers. My contribution to this study was the design and construction of the micropeening apparatus, selection of process parameters, assistance with experiments, and co-authorship and revisions in the paper.

Chapter 6 (i.e. "Traveling surface undulation on a Ni-Mn-Ga single crystal element" to be submitted), evaluates the effect of micropeening upon the mechanical response of the MSM micropump element. My contributions to the study are in the design/build of the experimental apparatus, the collection and evaluation of data, and authorship of the manuscript.

Chapter 7 (i.e. "A motionless actuation system for magnetic shape memory devices" published June, 2017 in Smart Materials and Structures), evaluates a compressed magnetic field generated by two electrical coils of opposed polarity as a method for driving an MSM micropump. My contribution to the study was in the design/ build of the electrical driver, the data collection, and the authorship of the paper.

In Chapter 8 (i.e. "Actuating a magnetic shape memory element locally with a set of coils" to be submitted), we report on a juxtaposed pole design for the magnetic driver and the twin structures which result from the pattern of magnetic field switching between poles. My contribution is in the design/build of the device, the testing of the device, the simulations, and the authorship of the paper.

Appendix A gives a description of the micropeening apparatus, some characterization of the peening parameters, and also the operating procedure of the device.

CHAPTER FOUR: SYSTEMATIC TRENDS OF TRANSFORMATION TEMPERATURES AND CRYSTAL STRUCTURES OF NI-MN-GA-FE-CU ALLOYS

Andrew Armstrong[1,2]*,

Frans Nilsén[2],

Michal Rameš[2],

Ross H. Colman[3],

Petr Veřtát[2],

Tomáš Kmječ [3],

Ladislav Straka[2,3],

Peter Müllner[1],

Oleg Heczko[2]

[1] Micron School of Materials Science and Engineering, Boise State University,

Boise, ID, 83725, USA

[2] Institute of Physics, Czech Academy of Sciences, Na Slovance 1999/2, 182 21

Prague 8, Czech Republic

[3] Faculty of Mathematics and Physics, Charles University, Ke Karlovu 2026/5,

121 16 Prague 2, Czech Republic

Abstract

Here we report a systematic research on effects of Fe and Cu upon properties relevant for the magnetic shape memory effect of Ni-Mn-Ga ferromagnetic shape memory alloys. Fe and Cu were identified as elements with potential synergism to increase the martensite transformation temperature of Ni-Mn-Ga magnetic shape memory (MSM) alloys. Eighteen Ni-Mn-Ga-Fe-Cu alloys with different systematic trends in substituting the ternary elements with Cu and Fe have been investigated. We found a method to describe the effectiveness of Ni, Mn, and Cu upon raising the martensitic transformation temperature, lowering the saturation magnetization, and varying the Curie temperature. We find the martensite transformation temperature most influenced by the Ni content, followed by Mn, with a smaller effect of Cu. The saturation magnetization decreases with similar coefficient for Mn and Cu alloying. The Curie temperature monotonically decreases with Mn, but not Cu. The 10M martensite structure is stable for the composition $Ni_{46.5}Mn_{25+X}Ga_{25-X-Y}Fe_{3.5}Cu_Y$ with X and Y range of $0 – 5.7$, and $0.8 - 3.0$. Used in combination with the *total e/a*, the *elemental e/a ratio* gives some insight into the complex behavior of quinary MSM alloys and is a useful method of analyzing MSM alloys for improved functional properties.

1. Introduction

Magnetic shape memory (MSM) alloys actuate in response to magnetic fields [1]. They convert magnetic field energy into large-strain (up to 12%) high-speed (~1 - 10 ms) reversible deformation with work-output approximately 2.6×10^4 J/m^3 [2]. MSM alloys can expand, contract, and bend in response to magnetic fields [3-5]. The mechanical degrees of freedom of axial strain and bending [6] allows for complex motion, such as for

small constrictions that can be swept through the material in the case of MSM

micropumps [7, 8]. MSM alloys absorb energy in the motion of their twin boundaries and

can be used as dampeners [9, 10] and energy harvesters [11]. In short, MSM alloys

behave akin to metallic muscles activated by magnetic field, morphing to a variety of

geometries, and can operate down to cryogenic temperatures as low as 2 K [12].

Three martensite structures are stable in Ni-Mn-Ga MSM alloys: five-layer

modulated (10M); seven-layer modulated (14M); and non-modulated (NM) [13-17]. The

10M phase exhibits very low twinning stress ($\approx$ 0.1 - 1 MPa) [18], making it efficient for

magnetic actuation. The maximum operating temperature is, however, often the limiting

factor for 10M actuators; aerospace applications, for example require operation up to 373

K [19]. Pagounis *et al.* [20] found the highest austenite start temperature for 10M alloy

(i.e. maximum operating temperature) which was 353 K in $Ni_{50.8}Mn_{28.4}Ga_{20.8}$ alloy. In

this study, we sought to increase the temperature of martensitic transformation (T_M) of the

10M phase through combined Fe and Cu alloying.

One can modify the operational temperature in Ni-Mn-Ga MSM alloy by

alloying, as the T_M is sensitive to elemental composition [21, 22]. For ternary alloys, we

estimate the alloy crystal structure, the T_M, Curie temperature (T_C), and saturation

magnetization (M_S) based upon the *e/a* ratio [23]. The *e/a*-ratio describes the arithmetic

average of the valence electrons surrounding each atom. Given plethora of previous

literature, it is well known that increasing *e/a* increases T_M, but decreases T_C and M_S.

Predictions of the stable phase are based upon the *e/a*-ratio, with 10M structure forming

at *e/a* between 7.62 and 7.68, 14M forming between 7.68 and 7.72, and NM forming

above 7.72 [23-26]. However, the boundaries between these structures are indistinct.

Effects of alloying Ni-Mn-Ga with Fe [19, 27-37], Cu [19, 35, 37-50], Co [19, 29, 30, 37-40, 43, 49, 51-53], and other transition elements [29, 37] have been subject of study. Additions of these elements change crystal structure, T_M, T_C, and M_S. Less explored is the combined effect of alloying elements with potential synergism. Synergistically, Co and Cu, alloyed at 4% into Ni-Mn-Ga allowed for the first magnetically induced reorientation for non-modulated MSM alloy: Co decreased tetragonality, while Cu increased martensite T_M [49], opening a new avenue in the MSM field.

We hypothesized that a synergism exists for alloying Cu and Fe combined into Ni-Mn-Ga for 10M phase. The addition of iron increases T_C [19, 40]. The addition of copper increases T_M, but also may decrease T_C [46]. We sought alloys to look for synergism of Fe and Cu in 10M phase to improve overall functional properties. While we did not find a clear synergism between the elements, we identified systematic trends between alloying elements and thermal and structural properties that differ from the trends of these elements in quaternary alloys (i.e. Ni-Mn-Ga-X, where X is Fe or Cu). Ni-Mn-Ga alloys with two additional elements have been challenging to understand, with the *total e/a* not serving alone as a predictor of behavior. We found a useful predictor to describe some systematic trends, the *elemental e/a*, that when used in combination with *total e/a* ratio can help design of improved functional property MSM alloys.

2. Experimental

2.1 Alloy design

We made eighteen Ni-Mn-Ga-Fe-Cu alloys and varied constituent elements around base system $Ni_{50}Mn_{28}Ga_{22}$. The alloy compositions (in at.%) are reported in Table

1. The alloys were designed to sweep several design constraints predicted to be important: keeping Ni (Mn) near 50 % (28.5%); altering the Fe to Cu ratio (*Fe/Cu*). We swept a broad *total e/a* range, and additionally looked at systems with Mn 25 at%. The alloys approximately follow:

Group 1: Ni 50% | Mn 25% | 1-4% Fe & Cu at 1:1 Fe/Cu reducing Ga
Group 2: Ni 48% | Mn 28-31% | Fe 0-5% + Cu 1% reducing Ga, increasing *Fe/Cu*
Group 3: Ni 46.5% + Fe 3% | Mn 25-29% + Cu 1%, 2%, 3% reducing Ga
Group 4: Ni 49% | Mn 27-29% | Fe 3% & Cu 1-3% reducing Ga, high *e/a*

However, understanding exact group delineation is not necessary to understand the subsequent analysis. The reason for the grouping is mostly for discussion of the different preparation techniques applied for different groups.

2.2 Alloy preparation and measurements

Group 1 and 2 samples were prepared by arc melting pure metals under 4 x 10^{-4} mbar argon atmosphere with an Edmund Bühler MAM-1 arc furnace in a water cooled-copper crucible. Ingots were re-melted three times for homogeneity. Group 1 samples were annealed in an alumina crucible within a tube-furnace under argon gas flow at 1273 K for 72 hours and ordered at 1073 K for 24 hours, then left in the furnace to cool slowly. This treatment resulted in 3% Mn loss. Group 2 samples were annealed instead in argon backfilled quartz ampoules and experienced <0.5% Mn loss.

The arc melting oxidized the Mn causing large loss. We therefore prepared Groups 3 and 4 alloys differently, to reduce overheat and alloy more slowly. We weighed elements into 2 ml alumina crucibles and sealed them in argon-backfilled quartz ampoules. We melted alloys in a box furnace (Clasic) at 1443 K for 48 hours, then

annealed and ordered following above alloying parameters. We checked homogeneity of alloys 7, 15, and 17 by sectioning the ingot into top, middle and bottom samples (A, B, C) and measured elemental composition by X-ray fluorescent spectroscopy with an Eagle III EDAX µProbe (XRF). The measurement error of the XRF was highest for the manganese and gallium compositions which was ±0.5 at%. The chemical segregation of Groups 3 and 4 alloys was at most 0.3%. Given their relatively homogenous nature, we just measured the center section of each ingot for the rest of alloys in these groups. The small variation in Mn concentration was within the typical range for reported for annealed Ni-Mn-Ga alloys [54].

Wire electric discharge machining (ZAP BP) was used for sample cutting. The surfaces of all samples were ground with progressively finer grit SiC papers to 4000 grit for surface analysis to remove kerfs formed during discharge cutting and brass contamination from cutting wire. We determined crystal structures for the alloys with X-ray diffraction (XRD) using a PANalytical X'Pert PRO with Co and Cu tubes equipped with a cooling stage enabling cooling to 250 K.

Saturation field (2.0 T) and low-field (0.01 T) magnetizations as a function of temperature were measured using a vibrating sample magnetometer (Quantum Design PPMS) with temperature rate 4 K/min. The Curie temperature was determined from the inflection point of the low-field magnetization. The M_S was obtained at 10 K from the 2.0 T magnetization. For alloys with T_M greater than T_C, we used differential thermal analysis and differential scanning calorimetry (DTA/DSC), measured using a Setaram Setsys Evolution, in a helium gas flow with a 10 K/min ramp rate in the range 320-1140K on heating and cooling.

The martensitic transformation was identified from the low-field magnetization data up to 400K (i.e. for alloys 4-16), where we reported T_M as the average of the austenite and martensite start temperatures. Above 400 K, the extended high temperature range of the DSC calorimeter allowed better definition of NM structure alloys (i.e. for alloys 1-3, 17 and 18). Here T_M was the average between centers of the endothermic and exothermic peak.

Precise comparison between DTA and PPMS measurements is difficult, as differences arose from the placement of the thermocouple in relation to sample, the sample size, and the size of the sample chamber. These factors led to slightly different lag between the measured sample temperatures vs. measured phenomena, as the heat-transfer conditions were different. We removed this lag from PPMS data by making the T_C coincident on heating and cooling. We also verified on the DSC data that the T_C extracted were consistent on heating and cooling. However, in this case the difference was about 5 K on heating and cooling.

Where Curie transitions were detected in both DSC and low-field magnetization measurements (in case of Alloy 17), the extracted martensitic transformation temperature agreed within 7 K, indicating good compatibility of the techniques and fairly low error. This is similar to the difference of around 5 K as reported in previous work by Chernenko *et al*. [55].

2.3 Element contribution to *e/a*

For *total e/a* calculation, we used Ni, Mn, Ga, Fe, and Cu valence electron contributions of 10, 7, 3, 8, 11 electrons respectively [50]. To find trends amid *e/a* data scatter, we introduced a new parameter, the *elemental e/a contribution*. The parameter

differs from the *total e/a*-ratio. The elemental e/a contribution $X_{element}$ compares the

valence electrons associated with an element constituent to the *total e/a* of the alloy,

separating elemental character from the change in overall *e/a:*

$$X_{element} = \frac{f_{element} \cdot e_{element}}{\Sigma f_i \cdot e_i} \quad ,$$

where $f_{element}$ is atomic fraction of the element, $e_{element}$ is the number of the element's

valence electrons and the denominator is the *total* number of valence electrons per

formula unit, which is just the *total e/a.*

Consider 100 atoms of Ni_2MnGa. Fifty atoms are Ni, which each contribute 10

valence electrons (v.e.). Twenty-five Mn atoms contribute each 7 v.e.; twenty-five Ga

atoms each contributes 3 v.e. In total, the one-hundred atoms have 750 total v.e., of

which Ni, Mn, and Ga contribute 66.7%, 23.3%, and 10.0% to the *total e/a*, i.e. $X_{Ni} =$

0.667, $X_{Mn} = 0.233$, $X_{Ga} = 0.100$. For $Ni_{50}Mn_{28}Ga_{22,}$ $X_{Ni} = 0.656$, $X_{Mn} = 0.257$, $X_{Ga} =$

0.087.

3. Results

The XRD analysis indicated the presence of the common martensite phases (NM,

14M and 10M) and cubic austenite in samples (Table 1). A mixture of multiple phases

was detected for samples in the as-cast state, but after annealing samples became largely

single phase. All the samples were highly textured polycrystals with (100) type

reflections distributed in a small range of Euler angles. Annealing did not broaden the

range. In alloys 7-18 larger grains were detected based on distinct spots in the XRD pole

figures (not shown). This difference can be ascribed to the different manufacturing

methods with different thermal gradients. For these alloys, the material appeared to be

oligo-crystalline rather than polycrystalline.

Results from the PPMS, DTA and XRD measurements were compiled into Table 4-1. The melting temperature was measured in alloys 1-3, 17,18. The melting temperature was between 1363 and 1384 K. The B2'-L2$_1$ ordering temperature was between 973 and 1017 K.

Table 4-1: Composition, magnetic, and thermal properties of alloys: alloy grouping, alloy labeling, chemical compositions, martensitic transformation temperature T_M, Curie temperature T_C, saturation magnetization M_S, *total e/a*, and observed structure at T = 250 K.

Group	Alloy	Composition [at%]					T_M [K]	T_C [K]	2.0T M_s [Am²/Kg] 10K	e/a	Structure 250K
		Ni	Mn	Ga	Fe	Cu					
1	1	50.4	24.8	21.7	1.4	1.7	347	369	58	7.73	NM
	2	50.0	24.7	20.3	2.4	2.7	385	400	69	7.82	NM
	3	49.2	23.7	18	4.3	4.7	523	372	74	7.99	NM
2	4	48.1	27.5	23.6	0	0.9	230	377	84	7.52	A
	5	48.1	30.7	17.8	2.7	0.7	286	385	76	7.79	10M/A
	6	47.4	30.9	16.0	4.9	0.8	336	385	69	7.86	14M
3	7A	46.4	24.9	24.6	3.2	0.9	162	388	90	7.48	A
	7B	46.5	24.7	24.7	3.2	0.9	160	386	85	7.48	A
	7C	46.2	24.9	24.8	3.3	0.9	159	387	86	7.46	A
	8	46.3	26.8	22.8	3.2	0.8	223	380	83	7.54	A
	9	46.2	29.1	20.6	3.3	0.9	290	369	73	7.54	10M
	10	46.7	24.5	23.8	3.2	1.8	158	419	86	7.55	A
	11	46.2	26.8	21.9	3.2	1.9	222	390	83	7.62	A
	12	46.1	28.9	19.8	3.3	1.9	293	378	71	7.70	10M
	13	46.2	24.8	22.7	3.3	3.0	182	417	78	7.63	A
	14	46.0	26.9	20.8	3.2	3.0	247	388	73	7.70	10M/A
	15A	47.0	28.3	18.3	3.3	3.0	323	375	63	7.83	14M
	15B	46.9	28.1	18.8	3.3	3.0	344	373	60	7.81	14M
	15C	46.8	28.1	18.7	3.1	3.3	342	374	59	7.82	14M
4	16	49.1	24.8	21.5	3.7	0.9	307	392	75	7.69	10M
	17A	49.1	27.1	18.7	3.2	2.0	413	385	60	7.84	NM
	17B	49.3	27.0	18.5	3.2	2.0	413	385	53	7.85	NM
	17C	49.1	27.0	18.6	3.3	1.9	414	385	63	7.84	NM
	18	49.3	29.1	15.5	3.3	2.8	564	277	36	8.0	NM

Figure 4-1 shows the measured T_M, T_C, and M_S data from Table 4-1, plotted against *total e/a.* Lines were drawn to compare to the Chernenko [23] ternary system T_M, T_C, and M_S, where the martensitic temperature was determined using DSC [55]. The difference between the two methods is, as previously stated in section 2.2 as around 5-7 K, given sharp transformation behavior.
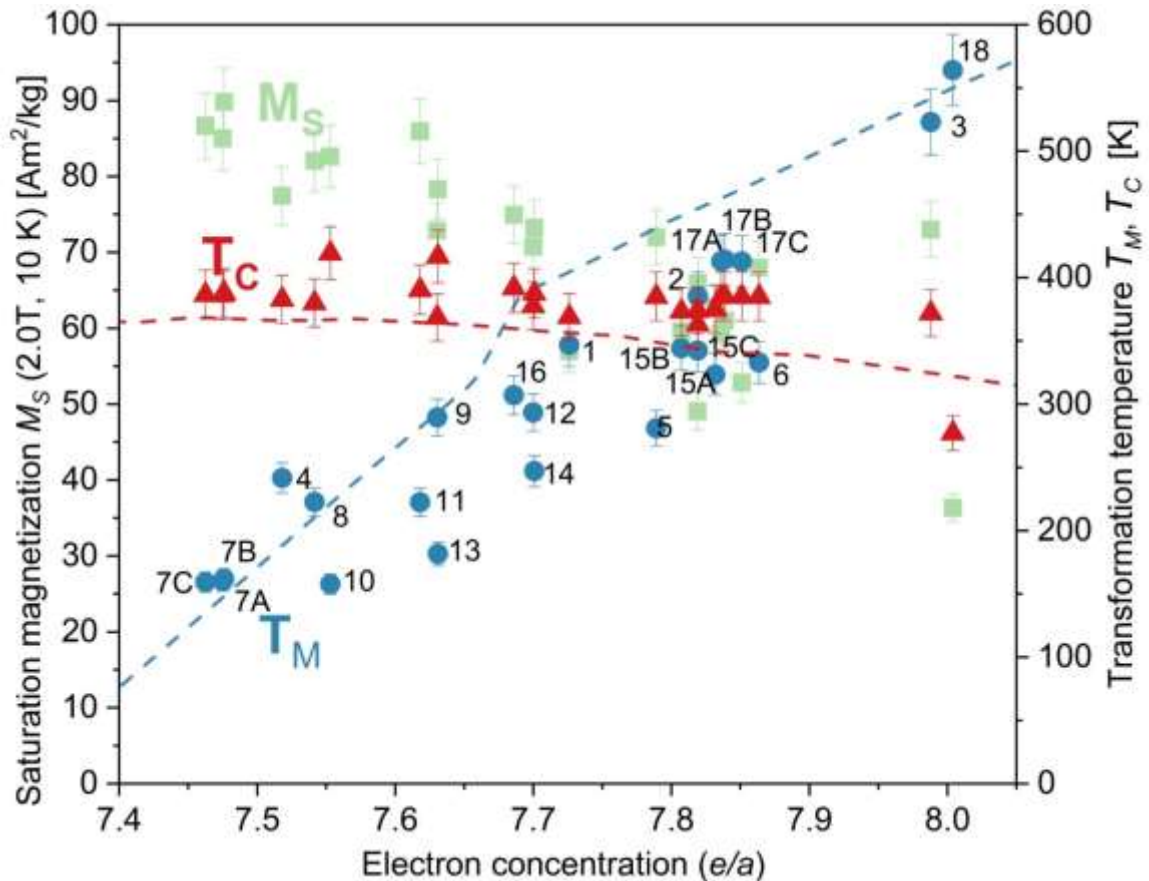
Figure 4-1: **Martensite transformation temperatures and Curie temperatures T_M, T_C, and saturation magnetization M_S as functions of *e/a* in Ni-Mn-Ga-Fe-Cu alloys and previously reported *e/a* trends (dashed lines) for ternary alloys from [23]. T_M, T_C, and M_S values are plotted as blue circles, red triangles, and green squares respectively. The blue dashed line shows the ternary system T_M; the red dashed line shows the ternary system T_C.**

Figure 4-2 shows T_M plotted against elemental contribution to e/a (X_{Ni}) from Equation 1. Here we note these trends: alloys in the upper circled region had NM

structure, while alloys in the lower circled region had 10M/14M structure. NM structure

tended to form with increased X_{Ni} and with high total e/a. Modulated structures formed

with decreased X_{Ni} and lower total e/a. Alloys in Groups 1 and 4 were NM, while Group

2 alloys fell in the lower ellipse region and had modulated structure.
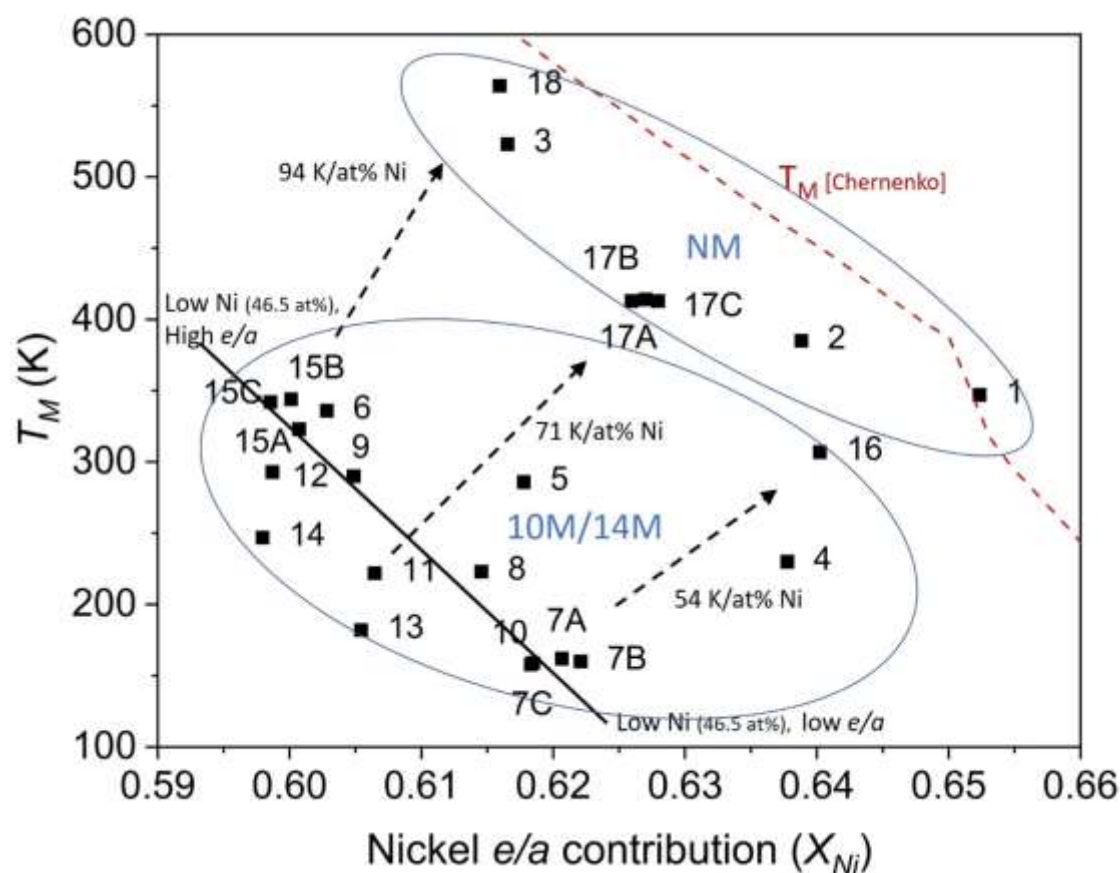
Figure 4-2: **Martensite transformation temperature as a function of X_{Ni}. Alloy labels are from Table 4-1. Alloys in the upper and lower ellipse have the NM and modulated structures. The red dashed line indicates X_{Ni} contribution of Ni-Mn-Ga calculated from [23]. The solid black line marks alloys following Ni$_{46.5}$Mn$_{25+X}$Ga$_{25-X-Y}$Fe$_{3.5}$Cu$_{Y}$. We compared alloys along the black line with alloys in the NM region, which differ in Ni and Ga. The rate of increase between alloys is marked with dashed arrow.**

The solid line indicates T_M behavior for the Group 3 alloys which approximately

followed Ni$_{46.5}$Mn$_{25+X}$Ga$_{25-X-Y}$Fe$_{3.5}$Cu$_Y$ (i.e. Ni and Fe add up to ~50 at%) alloying, and is

the system analyzed further in Figures 4-4, 4-5 and 4-6. Alloy 6 also fell along the solid

line, but had higher Ni concentration than Group 3 alloys, and is not included in the
Group 3 analysis. The red dashed line indicates the T_M versus X_{Ni} for Ni-Mn-Ga, back-
calculated from [23] in which Ni concentration is 50% [23].

The back-calculated values were compared to data from Sozinov *et al.* [21],
which closely follow Ref. [23], but do not indicate the inflection region reported by
Chernenko [23]. The dashed arrows indicate the systematic increase in T_M with
increasing Ni alloying discussed in section 4.2.

In Figure 4-3 we plotted T_M as a function X_{Mn}, and also T_M for Ni-Mn-Ga
calculated from Chernenko [23]. The upper solid line delineates NM from modulated
structure. Alloys with high Ni content (Group 1 and 4 alloys) had high T_M, but were NM
structure with increased Fe and Cu alloying. Alloys with lower Ni content (Group 2 and 3
alloys) were within region marked by ellipse and had modulated structure. In these
alloys, T_M increased with increasing X_{Mn} and maintained modulated structure up to X_{Mn}
about 0.29; X_{Mn} above this was outside the scope of this study.
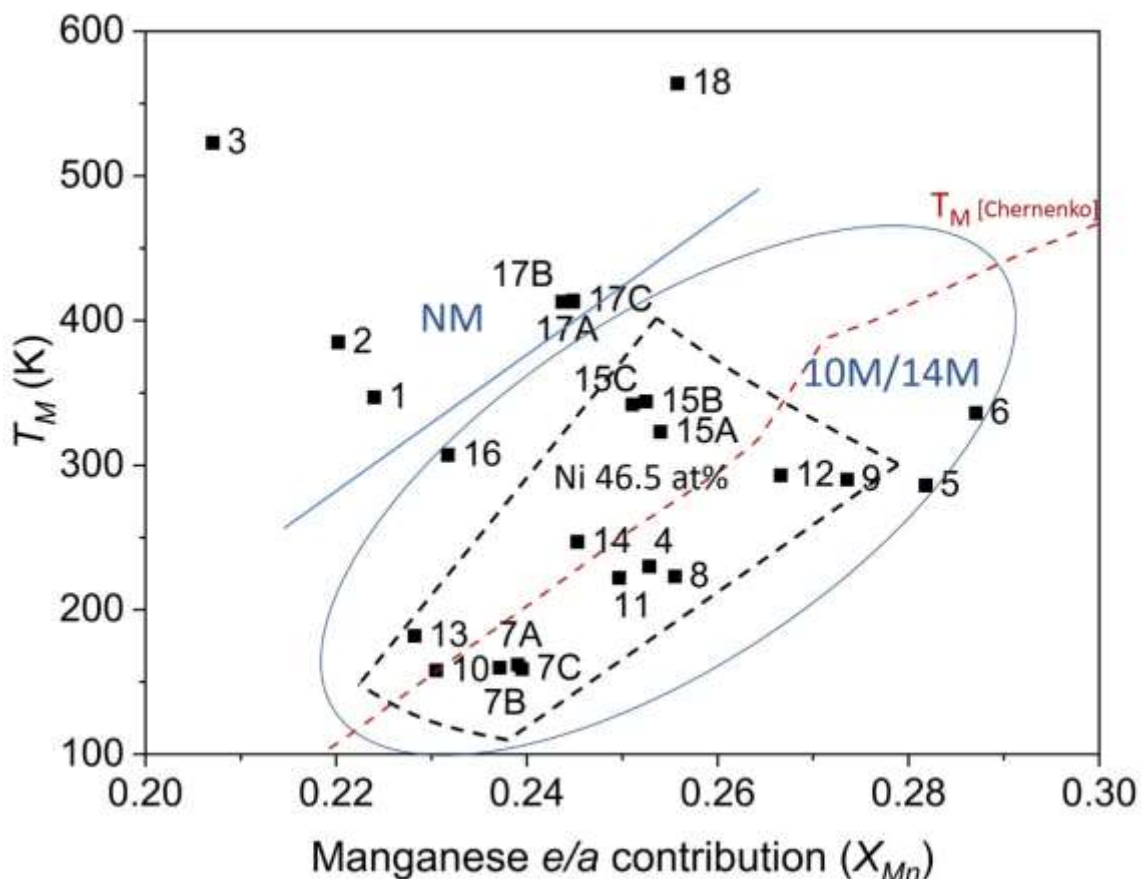
Figure 4-3: **Martensitic transformation temperatures as a function of X_{Mn}. Alloys above the solid line had the NM structure. Alloys within the blue ellipse have modulated structure. The red dashed line indicates X_{Mn} contribution of Ni-Mn-Ga calculated from [23]. The black dashed lines enclose a region where systematic trends are found and further noted in Figure 4-4.**

Figure 4-4 compares in detail T_M of Group 3 alloys against X_{Mn}. T_M increased with

Mn content and T_M followed contours marked in blue solid lines of constant Mn

concentration. We identified contours of constant Cu concentration and marked these as

solid green lines. From the Mn and Cu concentration contours, we isolated Mn and Cu

effects upon T_M from the overall convolution of the effects of the other elements. We

plotted also T_M against X_{Mn}, calculated from [23] as the dashed red line to note the

location and slope of the ternary line vs that for the quinary alloys.
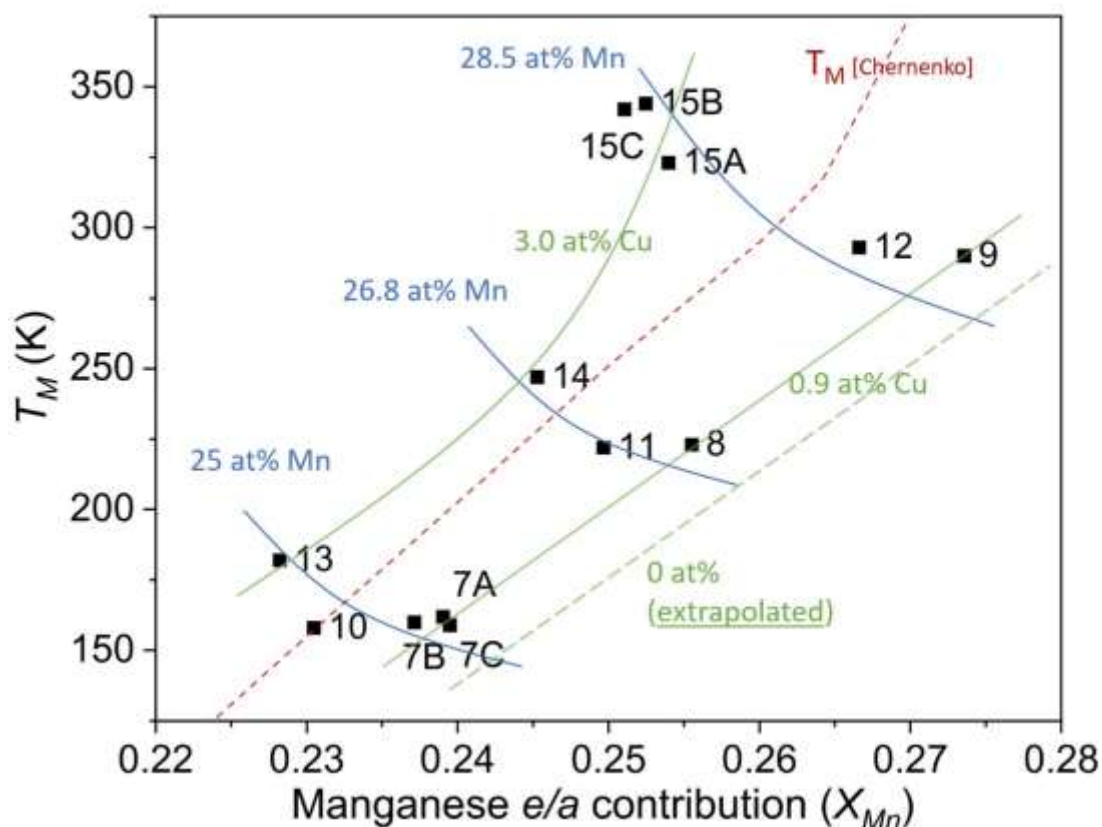
Figure 4-4: **Systematic trends in the Ni$_{46.5}$Mn$_{25+x}$Ga$_{25+x-y}$Fe$_{3.5}$Cu$_y$ system lying within the area bound with a dashed line in Figure 4-3. Contours of constant Mn (Cu) concentration are marked with blue (green) solid lines. The reference X_{Mn} contribution retrieved from Chernenko [23] is plotted in a red dashed line. A zero-copper line extrapolated from the data of this study is marked with a green dashed line. The lines are approximate fits by hand according to the compositions in Table 4-1.**

The dashed region marks Group 3 alloys which had close to 46.5 at% Ni and 3.5 at% Fe and were further analyzed in Figures 4-4, 4-5 and 4-6. Some Group 2 alloys fell within the dashed region of Figure 4-3, but had higher Ni than Group 3 alloys, and had properties in-between high Ni content (Groups 1 and 4) and low Ni content (Group 3) alloys.
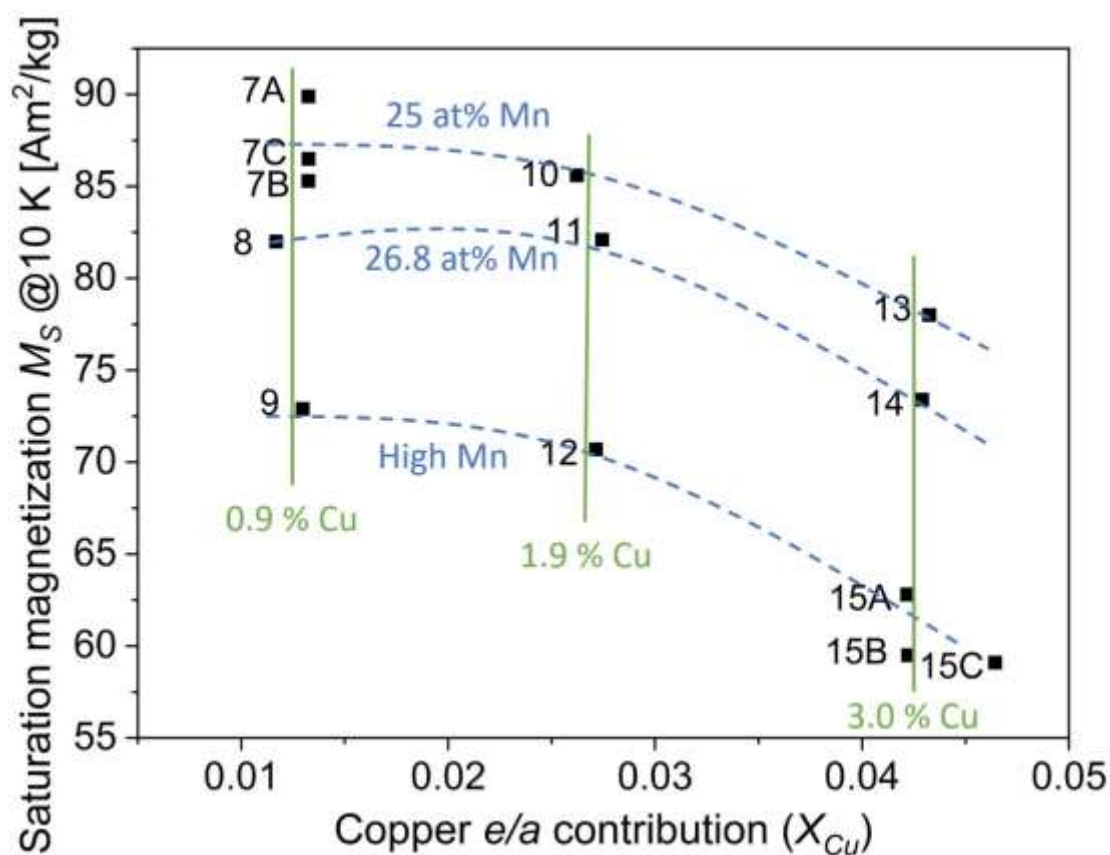
Figure 4-5: **Saturation magnetization plotted against X_{Cu} for the Ni$_{46.5}$Mn$_{25+X}$Ga$_{25+X-Y}$Fe$_{3.5}$Cu$_Y$ system. Green solid line marks alloys with constant Cu concentration. Dashed blue lines indicate contours of constant Mn concentration. The lines are drawn by hand as the best fit.**

Figure 4-5 compares M_S of Group 3 alloys against X_{Cu}. Alloys with similar X_{Cu} were marked along solid green lines of constant Cu concentration. X_{Cu} was from 0.045-0.05, i.e. was quite small, which caused X_{Cu} to align predominantly vertical irrespective of total e/a. The dashed blue lines indicated M_S for Mn content of 25 at% and 26.8 at% and for higher Mn (28.1-29.1 at%). We found systematic contours which show the coefficient of decreased M_S with increased Mn and Cu alloying.

In Figure 4-6, we plotted for Group 3 alloys the Curie temperature against X_{Cu}. Alloys with common Cu concentration aligned in vertical contours and were marked as

green solid lines. The trend in Curie temperature for constant Mn concentration was
drawn in dashed blue lines.
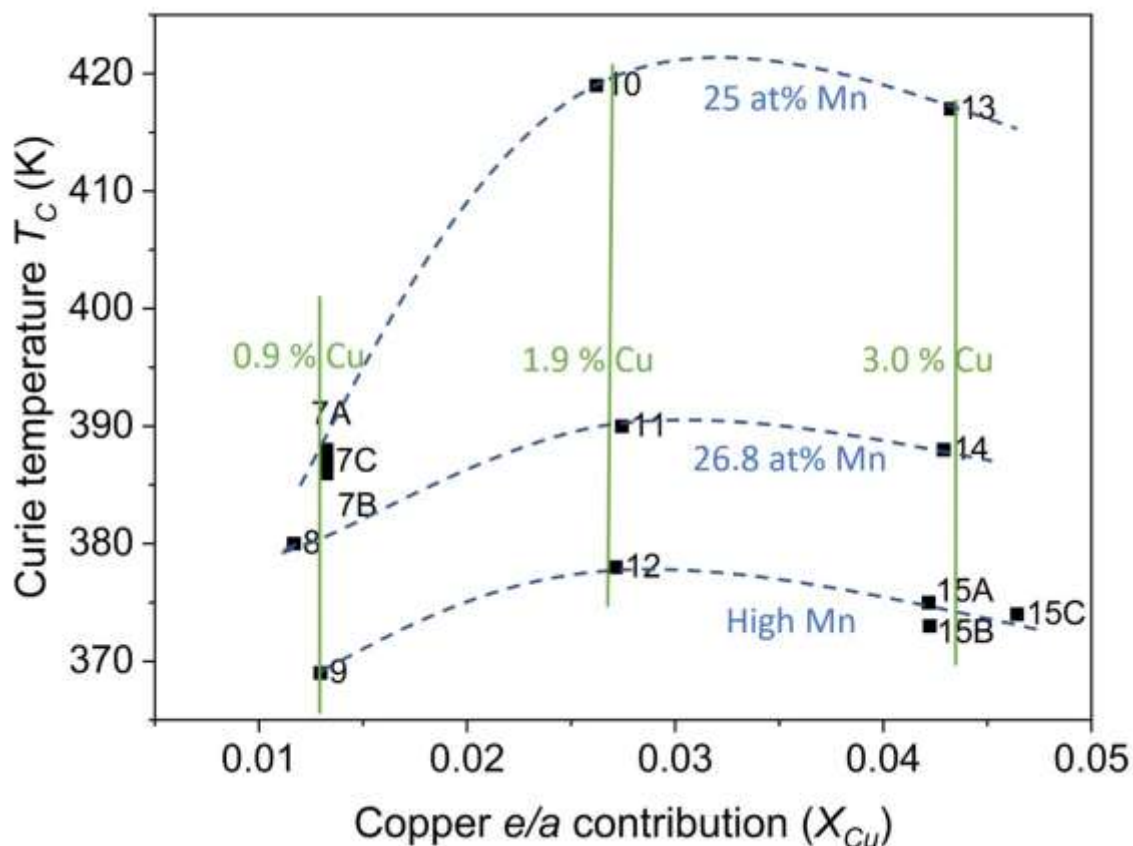
Figure 4-6: Curie temperature plotted against X_{Cu} for the Ni$_{46.5}$Mn$_{25+X}$Ga$_{25-X-Y}$Fe$_{3.5}$Cu$_Y$ system. Solid green (dashed blue) lines indicate contours of constant Cu (Mn) concentration. The lines are best fit drawn by hand.

4. Discussion

4.1 Analysis of total e/a

Compared to the ternary Ni-Mn-Ga system, the *total e/a* diagram (Figure 4-1) shows approximately 100 K scatter in martensitic transformation temperatures for a given *e/a*. The large scatter indicates that the *total e/a* ratio is not effective in predicting transformation temperatures for Ni-Mn-Ga-Fe-Cu. The intersection line reported by

Chernenko [23] turns into a broad intersection range that extends from *total e/a* ~ 7.72 to 7.88 (Figure 4-1).

In ternary Ni-Mn-Ga alloys, increasing *total e/a* above 7.7 results successively in formation of the 14M and NM structure [22]. In quaternary Ni-Mn-Ga alloys singularly alloyed with either Cu or Fe the *e/a* for 10M structure have been as high as 7.82 for alloy $Ni_{50}Mn_{25}Ga_{21}Cu_4$ [56]. In this study, the maximum *total e/a* found for 10M was in Alloy 5, which had 7.79 with $T_M = 286K$. The maximum *e/a* found for 14M alloy was 7.83 in Alloy 15. In all cases, transformation temperatures for Ni-Mn-Ga-Fe-Cu are less than those found for well-annealed ternary alloys, despite having higher *total e/a*. Alloys on upper T_M spread are near to Ni-Mn-Ga compositions (Alloy 4), they have lower nickel and some iron, but little copper. Alloys on the lower T_M band have high Cu, or high Mn and more substantial Fe or Cu, but these trends are neither obvious, nor systematic.

4.2 Effect of nickel on T_M

In Figure 4-2 we look at nickel according to its *elemental e/a*. Ni is second only to Cu in number of valence electrons, and its elemental *e/a* contribution is large. In Figure 4-2, outside of the Group 3 alloys (bottom solid line), Ni appeared the dominant factor in T_M. Alloys with high X_{Ni} and high *total e/a* had NM structure.

To isolate the effect of Ni we compare alloys which vary only by Ni and Ga. Alloy 7 and Alloy 16 have almost equivalent composition, with varying Ni and Ga concentration (Table 4-1). The coefficient of increasing T_M by increasing Ni content is 54 K/at% Ni at Mn 25 at%. The coefficient from increasing Ni content between alloys 11 and 17 is 71 K/ at% Ni at Mn 27 at%. The coefficient from increasing Ni content between alloys 15 and 18 is masked by the Mn increase, but if we assume a dependence of T_M of

30 K/at% Mn (found in subsequent *section 4.3.2*), the coefficient due to the increase of Ni content is 94 K/at% Ni at 28 at%. The rates are noted upon Figure 4-2 as dashed arrows marking the transformation path.

Alloys with high Mn content have a larger Ni coefficient of T_M increase, which causes transformation to 14M structure. Some results suggest Fe acts similarly as Ni, as systematic trends were found for the combined Ni and Fe adding to 50%, with slope parallel to that of the ternary system reported by Chernenko [23], with Mn and Cu varying.

4.3 Group 3 alloys: analysis of manganese and copper on T_M

Alloys in Group 3 approximately follow $Ni_{46.5}Mn_{25+X}Ga_{25-X-Y}Fe_{3.5}Cu_Y$ alloying which is the system indicated in Figure 4-2 as the lower solid line and within Figure 4-3 as the dashed region. In this system with the fixed Ni and Fe content, T_M varies systematically with Cu concentration along contours of constant Mn concentration. Along the blue contours, T_M increases as Cu substitutes for Ga. Along the green contours, Cu remains constant while Mn replaces Ga.

4.3.1 Cu effects on T_M

Referring to Figure 4-4 and comparing to Table 4-1, along the constant 25% Mn concentration contour, alloys 7 and 13 vary by 2% Cu concentration and replaced Ga. The increase of 2% Cu content causes an increase of 20 K in T_M, with a coefficient of 10 K/at% Cu. Along the 26.8% Mn concentration contour, comparing Alloys 8 and 14, T_M increases at 11 K/at% Cu. Along the 28.5% Mn concentration contour, comparing alloys 9 and 15, the Cu effect is obscured by varying Mn content, but if we use a 30 K/at% Mn

dependence (from subsequent section), we find the corrected coefficient to be 9 K/at.% Cu. Thus, despite the shift to the 14M structure, the T_M coefficient remains the same.

Comparing this quinary system to previous results of quaternary alloys, Glavatskyy *et al.* [50] found 10M structure in $Ni_{49.4}Mn_{23.3}Ga_{25.6}Cu_{1.7}$ with $T_M \sim 337$ K. Our closest alloy to this is Alloy 1, which is, however, NM structure. Glavatskyy *et al.* found another 10M alloy at $Ni_{47.3}Mn_{25.5}Ga_{24.5}Cu_{2.7}$ with $T_M \sim 335$ K. The closest composition was our Alloy 10, which likely has 10M martensitic structure owing to low transforming temperature (158K), but was austenitic within measurable range of our XRD set-up.

4.3.2 Mn effects on T_M

Applying the same method to Mn: if we compare alloys 7 and 8 from Table 4-1, which both lie on the 0.9 % Cu concentration contour (Figure 4-4) we find Mn increases T_M by 32 K/at% Mn. We find that, between alloys 8 and 9, the T_M increase is 30 K/at% Mn. Between alloys 13 and 14, the coefficient is 31 K/at% Mn. Along the constant 28.5% Mn concentration contour, replacing Ga with Cu shifts the structure to 14M. Between alloys 14 and 15C, the coefficient increases to 79 K/at% Mn. The increased coefficient seems to be due to the phase transformation. The cause of the structural transformation to 14M might be due to specific Cu elemental effects, or from the extra *total e/a added by Cu*, or both.

4.3.3 Comparison to ternary system and quaternary systems

For Group 3 alloys we found Mn had a larger coefficient than Cu with increased T_M, despite having a lower concentration of valence electrons (i.e. lower *total e/a*). The coefficient is constant in the 10M region, but changes as the material changes structure.

Alloy T_M varies systematically with both Cu and Mn, but with three times greater rate for Mn addition.

The Ni-Mn-Ga-Fe-Cu T_M dependence upon Mn concentration is similar to that from Chernenko who found a slope 37.5 K/at% Mn in the 10M region [23]. Extrapolating the contours of constant Mn concentration to zero Cu concentration, T_M is decreased compared to the ternary system, which might be attributed to adding Fe at Ni expense. Replacing Ni with Fe, though, allows for increased Mn content, which can lead to alloys with reasonably high T_M (Alloy 9). The 10M structure was found in alloys with high Mn with some Fe replacing Ni. This is also seen in Guldbakke *et al.* [34] in $Ni_{45.4}Mn_{29.1}Ga_{21.6}Fe_{3.9}$ with $T_M = 323$ K.

4.4 Effect of Iron on T_M

Iron has a less clear impact on T_M. When we compare Alloys 5 and 6, which vary mostly in Fe and Ga content, but also slightly in Ni content; the 2.2% Fe increases T_M by 50 K for a coefficient of 23 K/at% Fe. However, Ni content also decreased by 0.7%, which, assuming the middle Ni rate of 71 K/at% Ni, would indicate that increasing Fe content actually increased T_M by 73 K/at% Fe. This number may be taken only perfunctorily, as the data set is limited. In Figure 4-4, by extrapolating T_M to zero Cu, when Fe replaces Ni, T_M decreased compared to the ternary system. Obtained data suggest 10M structure may be found systematically when adding Fe at Ni expense.

4.5 Saturation magnetization (M_S)

In Figure 4-1, plotted against the *total e/a* ratio, M_S decreases generally, but not systematically with increasing *e/a*. In Figure 4-5, we plot M_S for Group 3 alloys against X_{Cu}. The alloys group into vertical contours of constant X_{Cu}, with M_S varying

systematically according to Mn concentration. For constant Cu concentration, M_S decreases with increasing Mn. Given a low Cu content, the number of participating valence electrons would be small, such that just chemical composition well approximates the elemental contribution. Nonetheless, the data showed better fit to the electron-weighted *elemental e/a contribution*.

4.5.1 Effects of Mn on M_S

Along the line of fixed 0.9% Cu concentration, comparing alloys 7 and 9 with increasing Mn concentration, M_S decreases at coefficient 2.8 $(Am^2/kg)/at\%$ Mn. Along the line of fixed 3% Cu concentration, comparing alloys 13 and 15, increasing the Mn concentration decreases M_S by 5.1 $(Am^2/kg)/at\%$ Mn.

4.5.1 Effects of Cu on M_S

Given constant 25 at% Mn concentration, comparing alloys 7 and 13, the increase in Cu concentration decreases M_S at 2.8 $(Am^2/kg)/at\%$ Cu. Comparing alloys 9 and 15 with high Mn concentration, the trend is less clear, as the Mn concentration also increases slightly, but, after removing the Mn dependence, we find that increasing Cu concentration decreases M_S at 3.3 $(Am^2/kg)/at\%$ Cu.

Mn alloyed in excess of 25 at% decreased M_S, which can be ascribed to Mn atoms occupying Ga sites and coupling anti-ferromagnetically to Mn on Mn sites, which decreases the overall magnetic moment [57, 58]. Increasing Cu content decreased M_S at slightly less than the Mn coefficient, which indicating that some Cu atoms occupy Mn sites.

4.6 Curie temperature

Plotting against X_{Cu}, T_C systematically decreases with Mn concentration, but does not monotonically vary with the Cu concentration. There is unexpectedly large change in T_C between alloy 7 and alloy 10, which might indicate an effect of low Cu, which we attribute to annealing uncertainty or another unknown effect at low e/a. Between the 25% and 26.8% Mn concentration contours, the coefficient was 3.7 K/at% Mn from alloy 7 to alloy 8, and 14 K/at% Mn between alloys 13 and 14. The coefficient was less for higher Mn concentrations: when comparing 26.8 at% Mn to 28.1-29.1 at% Mn, the coefficient was 4.8 K/at% Mn between alloys 8 and 9, and 9.3 K/at% Mn between alloys 14 and 15. With Ni, Fe, and Mn concentrations held constant, increasing Cu concentration at Ga expense in some cases actually increased T_C, as found when comparing alloys 7 and 10. Adding Fe did not appear to increase T_C temperatures substantially.

4.7 New questions

This phenomenological study evaluated the impact of Cu and Fe on the phase transformation temperatures and structure of quinary Ni-Mn-Ga-Fe-Cu alloys. We found that the elements Fe and Cu have different effects when alloyed together than when alloyed individually in quinary Ni-Mn-Ga-X alloys. Researchers may employ density functional theory calculations to understand such differences.

5. Conclusions

With original intent to create a new, high temperature MSM alloy, we realized a need for new methods to evaluate the broad range of experimental data. We developed a method based on the *individual* contribution of each element to the *total e/a* ratio. Using this *elemental e/a contribution,* we found coefficients which describe alloying of Ni, Mn,

and Cu on T_M, M_S, and T_C. Our experiments indicated that Ni has the largest T_M coefficient, followed by Mn and Cu. Mn additions decreased saturation magnetization at a similar coefficient as Cu alloying. Mn addition systematically decreased the Curie temperature, while Cu had unsystematic effect, even increasing the Curie temperature in cases. Comparison of the slope of the $Ni_{46.5}Fe_{3.5}$ system to ternary system suggest that Fe might act similarly to Ni in the quinary system. The 10M martensite structure is stable for the composition $Ni_{46.5}Mn_{25+X}Ga_{25-X-Y}Fe_{3.5}Cu_Y$ where X and Y range from 0.9 - 4 and from 1 - 3. Using both the *elemental* and *total e/a ratios* gives some insight into the complex behavior of quinary MSM alloys, which can be useful for a consideration of MSM alloys with improved functional properties.

We did not see synergistic effects of Fe and Cu upon the 10M structure, as no compositions showed transformation greater than for the ternary system. Cu did not show the expected effect, in contrast it seems to destabilize the of 10M phase, e.g. it decreases the transformation temperatures.

References

[1]   K. Ullakko, Magnetically controlled shape memory alloys: A new class of actuator materials, Journal of Materials Engineering and Performance 5(3) (1996) 405-409.

[2]   A. Likhachev, A. Sozinov, K. Ullakko, Modeling the strain response, magneto-mechanical cycling under the external stress, work output and energy losses in Ni–Mn–Ga, Mechanics of Materials 38(5-6) (2006) 551-563.

[3]   I. Aaltio, O. Heczko, O. Söderberg, S. Hannula, Magnetically controlled shape memory alloys, Smart Materials, CRC-Press, Boca Raton, USA (2009) 20-1e20.

[4]   S. Murray, M. Marioni, A. Kukla, J. Robinson, R. O'Handley, S. Allen, Large field induced strain in single crystalline Ni–Mn–Ga ferromagnetic shape memory alloy, Journal of Applied Physics 87(9) (2000) 5774-5776.

[5]   A.R. Smith, J. Tellinen, K. Ullakko, Rapid actuation and response of Ni–Mn–Ga to magnetic-field-induced stress, Acta Materialia 80 (2014) 373-379.

[6]   N.J. Kucza, C.L. Patrick, D.C. Dunand, P. Müllner, Magnetic-field-induced bending and straining of Ni–Mn–Ga single crystal beams with high aspect ratios, Acta Materialia 95 (2015) 284-290.

[7]   K. Ullakko, L. Wendell, A. Smith, P. Mullner, G. Hampikian, A magnetic shape memory micropump: contact-free, and compatible with PCR and human DNA profiling, Smart Materials and Structures 21(11) (2012).

[8]   S. Barker, E. Rhoads, P. Lindquist, M. Vreugdenhil, P. Mullner, Magnetic Shape Memory Micropump for Submicroliter Intracranial Drug Delivery in Rats, Journal of Medical Devices-Transactions of the Asme 10(4) (2016).

[9]   I. Aaltio, M. Lahelin, O. Söderberg, O. Heczko, B. Löfgren, Y. Ge, J. Seppälä, S.-P. Hannula, Temperature dependence of the damping properties of Ni–Mn–Ga alloys, Materials Science and Engineering: A 481 (2008) 314-317.

[10]   F. Nilsén, I. Aaltio, S.-P. Hannula, Comparison of magnetic field controlled damping properties of single crystal Ni-Mn-Ga and Ni-Mn-Ga polymer hybrid composite structures, Composites Science and Technology 160 (2018) 138-144.

[11]   J. Feuchtwanger, M.L. Richard, Y.J. Tang, A.E. Berkowitz, R.C. O'Handley, S.M. Allen, Large energy absorption in Ni–Mn–Ga/polymer composites, Journal of applied physics 97(10) (2005) 10M319.

[12]   O. Heczko, V. Kopecký, A. Sozinov, L. Straka, Magnetic shape memory effect at 1.7 K, Applied Physics Letters 103(7) (2013) 072405.

[13]   Y. Noda, S. Shapiro, G. Shirane, Y. Yamada, L. Tanner, Martensitic transformation of a Ni-Al alloy. I. Experimental results and approximate structure of the seven-layered phase, Physical Review B 42(16) (1990) 10397.

[14]   S. Murray, M. Marioni, S. Allen, R. O'handley, T.A. Lograsso, 6% magnetic-field-induced strain by twin-boundary motion in ferromagnetic Ni–Mn–Ga, Applied Physics Letters 77(6) (2000) 886-888.

[15]   A. Sozinov, A.A. Likhachev, N. Lanska, K. Ullakko, Giant magnetic-field-induced strain in NiMnGa seven-layered martensitic phase, Applied Physics Letters 80(10) (2002) 1746-1748.

[16]   C. Jiang, T. Liang, H. Xu, M. Zhang, G. Wu, Superhigh strains by variant reorientation in the nonmodulated ferromagnetic NiMnGa alloys, Applied Physics Letters 81(15) (2002) 2818-2820.

[17]   O. Söderberg, L. Straka, V. Novák, O. Heczko, S.-P. Hannula, V. Lindroos, Tensile/compressive behaviour of non-layered tetragonal Ni52. 8Mn25. 7Ga21. 5 alloy, Materials Science and Engineering: A 386(1-2) (2004) 27-33.

[18]   L. Straka, H. Hänninen, A. Soroka, A. Sozinov, Ni-Mn-Ga single crystals with very low twinning stress, Journal of Physics: Conference Series, IOP Publishing, 2011, p. 012079.

[19]   A. Pérez-Checa, D. Musiienko, A. Saren, A. Soroka, J. Feuchtwanger, A. Sozinov, J. Barandiaran, K. Ullakko, V. Chernenko, Study of the critical parameters for magnetic field-induced strain in high temperature Ni-Mn-Ga-Co-Cu-Fe single crystals, Scripta Materialia 158 (2019) 16-19.

[20]   E. Pagounis, R. Chulist, M. Szczerba, M. Laufenberg, High-temperature magnetic shape memory actuation in a Ni–Mn–Ga single crystal, Scripta Materialia 83 (2014) 29-32.

[21]   A. Sozinov, Low Twinning Stress Ni2Mn(1+X)Ga(1-X) Alloys, ICFSMA, Bilbao, 2009.

[22]   O. Heczko, L. Straka, Compositional dependence of structure, magnetization and magnetic anisotropy in Ni–Mn–Ga magnetic shape memory alloys, Journal of Magnetism and Magnetic Materials 272 (2004) 2045-2046.

[23]   V.A. Chernenko, Compositional instability of β-phase in Ni-Mn-Ga alloys, Scripta Materialia 40(5) (1999) 523-527.

[24]   X. Jin, M. Marioni, D. Bono, S. Allen, R. O'handley, T. Hsu, Empirical mapping of Ni–Mn–Ga properties with composition and valence electron concentration, Journal of applied physics 91(10) (2002) 8222-8224.

[25]   J. Pons, V. Chernenko, R. Santamarta, E. Cesari, Crystal structure of martensitic phases in Ni–Mn–Ga shape memory alloys, Acta Materialia 48(12) (2000) 3027-3038.

[26]   V.A. Chernenko, C. Seguí, E. Cesari, J. Pons, V.V. Kokorin, Sequence of martensitic transformations in Ni-Mn-Ga alloys, Physical Review B 57(5) (1998) 2659-2662.

[27]   D. Soto-Parra, X. Moya, L. Mañosa, A. Planes, H. Flores-Zúñiga, F. Alvarado-Hernández, R. Ochoa-Gamboa, J. Matutes-Aquino, D. Ríos-Jara, Fe and Co selective substitution in Ni2MnGa: Effect of magnetism on relative phase stability, Philosophical Magazine 90(20) (2010) 2771-2792.

[28]   D. Soto, F.A. Hernández, H. Flores-Zúñiga, X. Moya, L. Manosa, A. Planes, S. Aksoy, M. Acet, T. Krenke, Phase diagram of Fe-doped Ni-Mn-Ga ferromagnetic shape-memory alloys, Physical Review B 77(18) (2008) 184103.

[29]   I. Glavatskyy, N. Glavatska, O. Söderberg, S.-P. Hannula, J.-U. Hoffmann, Transformation temperatures and magnetoplasticity of Ni–Mn–Ga alloyed with Si, In, Co or Fe, Scripta materialia 54(11) (2006) 1891-1895.

[30]   R. Fayzullin, V.D. Buchelnikov, S. Taskaev, M. Drobosyuk, V.V. Khovaylo, Experimental Study of Magnetocaloric Effect in Ni-Fe-Mn-Ga and Ni-Co-Mn-Ga Heusler Alloys, Materials Science Forum, Trans Tech Publ, 2013, pp. 456-460.

[31]   V. Khovailo, V. Chernenko, A. Cherechukin, T. Takagi, T. Abe, An efficient control of Curie temperature TC in Ni–Mn–Ga alloys, Journal of magnetism and magnetic materials 272 (2004) 2067-2068.

[32]   S. Yu, S. Yan, S. Kang, X. Tang, J. Qian, J. Chen, G. Wu, Magnetic field-induced martensite–austenite transformation in Fe-substituted NiMnGa ribbons, Scripta Materialia 65(1) (2011) 9-12.

[33]   Z. Liu, M. Zhang, W. Wang, W. Wang, J. Chen, G. Wu, F. Meng, H. Liu, B. Liu, J. Qu, Magnetic properties and martensitic transformation in quaternary Heusler alloy of NiMnFeGa, Journal of Applied Physics 92(9) (2002) 5006-5010.

[34]   J. Guldbakke, M. Chmielus, K. Rolfs, R. Schneider, P. Müllner, A. Raatz, Magnetic, mechanical and fatigue properties of a Ni45. 4Mn29. 1Ga21. 6Fe3. 9 single crystal, Scripta Materialia 62(11) (2010) 875-878.

[35]   R.I. Barabash, O.M. Barabash, D. Popov, G. Shen, C. Park, W. Yang, Multiscale twin hierarchy in NiMnGa shape memory alloys with Fe and Cu, Acta Materialia 87 (2015) 344-349.

[36]   K. Koho, O. Söderberg, N. Lanska, Y. Ge, X. Liu, L. Straka, J. Vimpari, O. Heczko, V. Lindroos, Effect of the chemical composition to martensitic transformation in Ni–Mn–Ga–Fe alloys, Materials Science and Engineering: A 378(1-2) (2004) 384-388.

[37]   S. Guo, Y. Zhang, B. Quan, J. Li, Y. Qi, X. Wang, The effect of doped elements on the martensitic transformation in Ni–Mn–Ga magnetic shape memory alloy, Smart materials and structures 14(5) (2005) S236.

[38]   A. Perez-Checa, J. Feuchtwanger, D. Musiienko, A. Sozinov, J.M. Barandiaran, K. Ullakko, V.A. Chernenko, High temperature Ni45Co5Mn25 (-) xFexGa20Cu5 ferromagnetic shape memory alloys, Scripta Materialia 134 (2017) 119-122.

[39]   A. Pérez-Checa, J. Feuchtwanger, D. Musiienko, A. Sozinov, J.M. Barandiaran, K. Ullakko, V.A. Chernenko, High temperature Ni45Co5Mn25−xFexGa20Cu5 ferromagnetic shape memory alloys, Scripta Materialia 134 (2017) 119-122.

[40]   A. Perez-Checa, J. Feuchtwanger, J. Barandiaran, A. Sozinov, K. Ullakko, V. Chernenko, Ni-Mn-Ga-(Co, Fe, Cu) high temperature ferromagnetic shape memory alloys: Effect of Mn and Ga replacement by Cu, Scripta Materialia 154 (2018) 131-133.

[41]   S. Roy, E. Blackburn, S. Valvidares, M. Fitzsimmons, S.C. Vogel, M. Khan, I. Dubenko, S. Stadler, N. Ali, S. Sinha, Delocalization and hybridization enhance the magnetocaloric effect in Cu-doped Ni 2 MnGa, Physical Review B 79(23) (2009) 235127.

[42]   D.M. Nicholson, K. Odbadrakh, B. Shassere, O. Rios, J. Hodges, G.M. Ludtka, W.D. Porter, A. Sefat, A. Rusanu, G. Brown, Modeling and characterization of the magnetocaloric effect in Ni2MnGa materials, international journal of refrigeration 37 (2014) 289-296.

[43]   M. Zelený, A. Sozinov, L. Straka, T. Björkman, R.M. Nieminen, First-principles study of Co-and Cu-doped Ni 2 MnGa along the tetragonal deformation path, Physical Review B 89(18) (2014) 184103.

[44]   M. Zeleny, A. Sozinov, T. Bjorkmand, L. Straka, R.M. Nieminen, Ab initio study of properties of Co- and Cu- doped Ni-Mn-Ga alloys, Materials Today-Proceedings 2 (2015) 601-604.

[45]   Y. Li, J. Wang, C. Jiang, Study of Ni–Mn–Ga–Cu as single-phase wide-hysteresis shape memory alloys, Materials Science and Engineering: A 528(22-23) (2011) 6907-6911.

[46]   C. Tan, G. Dong, L. Gao, J. Sui, Z. Gao, W. Cai, Microstructure, martensitic transformation and mechanical properties of Ni50Mn30Ga20− xCux ferromagnetic shape memory alloys, Journal of Alloys and Compounds 538 (2012) 1-4.

[47]   I. Aaltio, O. Söderberg, M. Friman, I. Glavatskyy, Y. Ge, N. Glavatska, S. Hannula, Determining the liquidus and ordering temperatures of the ternary NiMn-Ga and quaternary Ni-Mn-Ga-Fe/Cu alloys, European Symposium on Martensitic Transformations, EDP Sciences, 2009, p. 04001.

[48]   M. Rameš, O. Heczko, A. Sozinov, K. Ullakko, L. Straka, Magnetic properties of Ni-Mn-Ga-Co-Cu tetragonal martensites exhibiting magnetic shape memory effect, Scripta Materialia 142 (2018) 61-65.

[49]   A. Sozinov, N. Lanska, A. Soroka, W. Zou, 12% magnetic field-induced strain in Ni-Mn-Ga-based non-modulated martensite, Applied Physics Letters 102(2) (2013).

[50]   I. Glavatskyy, N. Glavatska, A. Dobrinsky, J.U. Hoffmann, O. Söderberg, S.P. Hannula, Crystal structure and high-temperature magnetoplasticity in the new Ni–Mn–Ga–Cu magnetic shape memory alloys, Scripta Materialia 56(7) (2007) 565-568.

[51]   S. Fabbrici, G. Porcari, F. Cugini, M. Solzi, J. Kamarad, Z. Arnold, R. Cabassi, F. Albertini, Co and In doped Ni-Mn-Ga magnetic shape memory alloys: A thorough structural, magnetic and magnetocaloric study, Entropy 16(4) (2014) 2204-2222.

[52] S. Chatterjee, S. Giri, S. De, S. Majumdar, Giant magneto-caloric effect near room temperature in Ni–Mn–Sn–Ga alloys, Journal of Alloys and Compounds 503(2) (2010) 273-276.

[53] D.M. Nicholson, K. Odbadrakh, A. Rusanu, M. Eisenbach, G. Brown, I. Evans, Boyd Mccutchen, First principles approach to the magneto caloric effect: Application toNi2MnGa, Journal of Applied Physics 109(7) (2011) 07A942.

[54] F. Nilsén, I. Aaltio, Y. Ge, T. Lindroos, S.-P. Hannula, Characterization of gas atomized Ni-Mn-Ga powders, Materials Today: Proceedings 2 (2015) S879-S882.

[55] V. Chernenko, E. Cesari, V. Kokorin, I. Vitenko, The development of new ferromagnetic shape memory alloys in Ni-Mn-Ga system, Scripta metallurgica et materialia 33(8) (1995) 1239-1244.

[56] R. Santamarta, J. Muntasell, J. Font, E. Cesari, Thermal stability and microstructure of Ni–Mn–Ga–Cu high temperature shape memory alloys, Journal of Alloys and Compounds 648 (2015) 903-911.

[57] P. Lázpita, J. Barandiarán, J. Gutiérrez, J. Feuchtwanger, V. Chernenko, M. Richard, Magnetic moment and chemical order in off-stoichiometric Ni–Mn–Ga ferromagnetic shape memory alloys, New Journal of Physics 13(3) (2011) 033039.

[58] Enkovaara, J., Heczko, O., Ayuela, A., & Nieminen, R. (2003). Coexistence of ferromagnetic and antiferromagnetic order in Mn-doped Ni2MnGa. Physical Review B, 67(21), 1-4. [212405].

CHAPTER FIVE: EFFECTS OF SURFACE MODIFICATION ON THE FATIGUE

LIFE OF UNCONSTRAINED NI-MN-GA SINGLE CRYSTALS IN A ROTATING

MAGNETIC FIELD

Hu Zhang,[1, 2]

Andrew Armstrong,[2]

Peter Müllner[2]

[1] School of Materials Science and Engineering, University of Science and

Technology of Beijing, Beijing 100083, P R China.

[2] Micron School of Materials Science and Engineering, Boise State University,

Boise, ID 83725, USA.

Abstract

Long-term fatigue life during high-cycle magnetic-mechanical actuation is crucial to the application of Ni-Mn-Ga ferromagnetic shape memory alloys (FSMAs). It has been reported that long fatigue life can be achieved by both reducing surface damage and constraining Ni-Mn-Ga single crystals to exhibit much lower strain than the theoretical limit. In the present study, the fatigue life of Ni-Mn-Ga single crystal samples treated with various surface modifications was investigated in a rotary fatigue testing instrument. The apparatus minimally constrained the samples and allowed for magnetic-field-induced strain (MFIS) close to the theoretical limit. We first treated the samples with electropolishing, which we found created more surface defects than those of the mechanically polished sample. These defects acted as dispersed pinning sites for twin boundaries and nucleated cracks easily due to the localized stress concentration, resulting in reduced fatigue life. We then studied the introduction of residual compressive stresses imparted by micropeening. Although micropeening increased surface roughness, it produced a uniform surface morphology and a finely twinned structure. We argue that the distribution of dislocation pile up was more homogeneous due to the fine twin structure, lowering the crack nucleation rate. Consequently, the fatigue life of unconstrained Ni-Mn-Ga single crystals with large MFIS was significantly improved by the micropeening treatment.

1. Introduction

Since the discovery of magnetic field-induced strain (MFIS) in ferromagnetic shape memory alloys (FSMAs) with strain greater than obtained in magnetostrictive materials, FSMAs have attracted much attention due to their promising application in actuators and sensors [1-4]. At present, off-stoichiometric Ni2MnGa FSMAs have been studied intensively because they exhibit high MFIS up to 12% due to a large magnetic anisotropy constant and high magnetic and martensitic transformation temperatures [5-8]. On the microscopic scale, the MFIS is caused by the magnetic-field-induced reorientation of the twin variant structure, in which the short axis (c) of the martensite close-to-tetragonal crystal lattice aligns with the magnetic field direction [9-11]. Put another way, the MFIS is a magnetoplastic deformation resulting from twin boundary movement driven by magnetostress [12]. Since the FSMAs are required to undergo long-term cycling of MFIS for practical applications, it is crucial to study the magneto-mechanical fatigue property of FSMAs.

The fatigue property is closely related to the nucleation of cracks during high-cycle magnetic-mechanical actuation. If the twin boundary motion is obstructed by interacting twins, stresses concentrate at twin boundaries creating a pile-up of twinning dislocations [13, 14]. Thus, cracks nucleate at twin boundaries due to stress concentration and eventually lead to the fracture of FSMAs. Generally, the twin boundaries can move readily in the crystals with thick twins, and large MFIS can be obtained. But cracks also easily nucleate in such crystals, resulting in a short lifetime [15, 16]. In contrast, twin boundaries cannot move long distances in a sample consisting of many thin twins, since twin boundary movement is strongly hindered by the densely twinned microstructure.

Thus, MFIS is relatively smaller and the stress distribution is more homogeneous than that in a coarse twin microstructure. Researchers have suggested that crystals with thin twin structure are more resistant to crack nucleation and so exhibit a longer fatigue life [13, 17].

On the other hand, it is known that the surface defects could act as dispersed pinning sites which hinder the motion of twin boundaries and cause stress concentrations [18, 19]. Therefore, it has been suggested that the twinning stress can be reduced largely by removing the damaged surface layer, which should improve fatigue life considerably [16, 20]. In addition, macroscopic constraints as an unavoidable component of certain sample holders have also been considered as one of the key factors that affect the MFIS as well as fatigue life [13, 21, 22]. The constraints reduce and even block the movement of twin boundaries, and lead to a remarkable reduction of MFIS [23]. Meanwhile, the fatigue life is shortened in single-domain crystals, because constraints hinder the microstructure from adapting to the internal stress; while a prolonged fatigue life can be achieved in crystals exhibiting self-accommodated multi-domain martensite since the dense twin structure could be stabilized by the constraints [13, 24].

Consequently, it is a challenge to develop such a Ni-Mn-Ga FSMA that shows both large MFIS and long fatigue life. In order to achieve this goal, it is desirable to design a crystal in which twins are fine but do not obstruct each other [16]. In the present work, the effects of surface modifications on the fatigue life of unconstrained Ni-Mn-Ga single crystals have been studied in detail. The fatigue life was diminished significantly following an electropolishing treatment, which caused pitting and surface non-uniformity. Notably, micropeening, a low energy form of shotpeening, gave rise to a fine

twin microstructure, leading to a homogeneous stress distribution. Following

micropeening, fatigue life was improved remarkably while the MFIS remained large.

2. Experimental

A single crystal with nominal composition $Ni_{50}Mn_{28}Ga_{22}$ was grown using the

Bridgman-Stockbarger technique described in detail in Ref. [25]. The growth direction

was parallel to <100>$_{austenite}$, and the size of the initial ingot was 6.3 mm in diameter and

75 mm in length. The crystal structure, orientation, and lattice parameters were

determined with X-ray diffraction along the length of single crystal using a Bruker D8

diffractometer with Cu Kα radiation. The composition along the length of crystal was

investigated using a Hitachi scanning electron microscopy (SEM) with Energy Dispersive

Spectroscopy (EDS, Oxford).

Twenty-five-disc samples with ~1.4 mm thickness were cut from the 10M

portion of crystal along the axial direction using a Princeton Scientific precision wire saw

and divided into five groups with five samples in each group (Table 5-1). After cutting,

all samples were electropolished for 20 s in a solution of ethanol and nitric acid (volume

ratio 2:1) at 12 V. Both sides of all samples were then mechanically polished using a

polishing wheel with progressive grinding steps from 1200 to 4000 grit SiC paper

followed by polishing with water-based diamond suspension from 3 μm to 0.04 μm

(group I). Three groups of samples (II, III, IV) were then electropolished for a second

time with the same electropolishing parameters while another group (II$_{half}$) was only

submerged halfway into the electropolishing solution during this second electropolishing.

Groups III and IV were micropeened with 100 μm SiO_2 particles (Comco) for 8 s under a

nozzle pressure of 25 psi (0.17 MPa) on one side and both sides, respectively. Table 5-1

lists the different groups with different surface treatments. After the surface treatments,

all samples were magnetically trained under a magnetic field of 1 T in order to obtain a

single variant structure.

Table 5-1: **Sample groups with different surface treatments. Each group has five disc samples with ~1.4 mm thickness.**

Group / Surface treatment	I	II	II$_{half}$	III	IV
First electropolishing (volume ratio of ethanol and nitric acid is 2:1, 12 V, 20 s)	√	√	√	√	√
Mechanical polishing (0.04 μm)	√	√	√	√	√
Second electropolishing (volume ratio of ethanol and nitric acid is 2:1, 12 V, 20 s)		√	√ (half sample)	√	√
One-side micropeening (~100 μm powder, 8 s, nozzle pressure: 25 psi)				√	√
Two-side micropeening (~100 μm powder, 8 s, nozzle pressure: 25 psi)					√

A MicroSense Model 10 vibrating sample magnetometer (VSM) was used to

determine the austenite transition temperature (A$_S$) and the switching field of each

sample. The samples were initially loaded with the magnetic field parallel to the sample's

circular face. The samples were fully magnetized in this orientation in a first isothermal

magnetization by increasing the magnetic field up to 1.2 T. Then, the samples were

rotated 90° for the second measurement so that the magnetic field was perpendicular to

the sample face, and then rotated back to the parallel direction for the third measurement.

The switching fields were determined from the second and third measurements of

isothermal magnetizations. The M-H curves were corrected for the demagnetization

effect, i.e., $H_{eff} = H_{ext} - N_d M$, where H_{eff} is the effective field, H_{ext} is external field, and N_d is the demagnetization factor that is determined by the length/diameter ratio [26]. As a result of the demagnetization effect, the slope of the M-H_{eff} curve may be negative.

Rotary fatigue tests were carried out in a custom-made apparatus, in which the samples were oriented such that the $[010]_\text{S}$ was parallel to the axis of rotation and the $[001]_\text{S}$ direction was perpendicular to the axis of rotation. The maximum magnetic field parallel and perpendicular to the sample face was 0.52 T and 0.65 T, respectively. The samples were kept in the sample mount by rubber rings, and were thus nearly free of mounting constraints. Details about the rotary fatigue test were given in Ref. [20].

The microstructure was inspected using a Leica DM6000 microscope with differential interference contrast (DIC). The average surface roughness R_a was determined with an optical profilometer (Veeco, WYKO NT110). A custom-made optical magneto-mechanical device (OMMD) was set up as shown in Figure 5-1(a) in order to record the evolution of twin structure and strain during the rotation of the magnetic field. The sample (1) was attached to the sample holder (2) by double-sided tape. An HD camera (5) recorded the reflection of the sample viewed through a mirror (3) while a sequence-controlled motor rotated the apparatus in the magnetic field (6) of a V3036 electromagnet (Varian Associates). The sample and the camera were rigidly connected and rotated synchronously such that from the sample/camera reference space, the field rotated about the sample. Figure 5-1(b) shows an image of a micropeened IV sample for an example. The dash line denotes the orientation of the rotation axis. By analyzing the variation of the disk based on the images using software (Imagetool), the magnetic-field-induced strain (MFIS) was measured given $\varepsilon = \frac{r - r_{min}}{r_{min}} \times 100\%$. The relative error

$\Delta\varepsilon_{max}/\varepsilon_{max}$ of this method was of the order of 10^{-2}. Furthermore, an open source,

MATLAB based 2D DIC software (Ncorr) [27] was used to analyze the evolutionary

process of localized strain and twin boundary movement during the rotation of the

magnetic field.
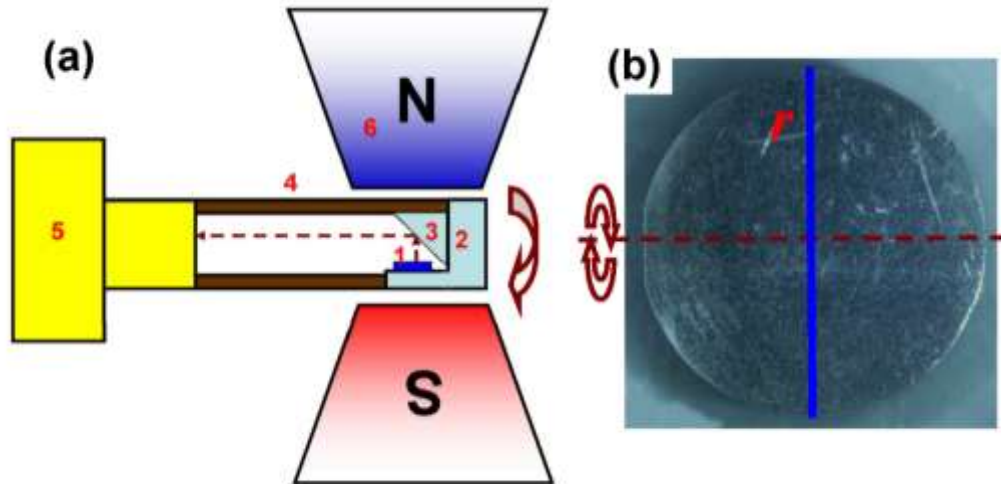
Figure 5-1:   (a) Schematic of the custom-made optical magneto-mechanical device (OMMD) for rotary magnetic-mechanical experiment. The sample (1) was attached to the sample holder (2) by double-sided tape. The tube (4) coupled to the HD camera (5), which recorded the reflection of sample through a mirror (3) while these components were rotated in the magnetic field (6) by a sequence-controlled motor. (b) The image of micropeened IV sample as an example; the dashed line marks the rotation axis and the blue line indicates the diameter which was measured to determine the MFIS; both lines were parallel to <100>.

3. Results

3.1 Magnetic properties of $Ni_{50}Mn_{28}Ga_{22}$ single crystal

The crystal structure was investigated with XRD, and it was found from Figure 5-2 that the sample formed the 10M martensite structure at the seed end and then exhibited 14M martensite after 54 mm. The disc samples were cut from the 10M section of the single crystal. The composition along the axis of the crystal was analyzed by EDS and is shown in Figure 5-2(a). The actual composition of different elements was nearly

consistent with the nominal composition $Ni_{50}Mn_{28}Ga_{22}$. However, the Mn concentration increased while the Ni and Ga contents decreased slightly along the growth direction. The austenite starting temperatures (A_S) of different samples were determined by thermomagnetic curves in a low field (0.025 T), and are also summarized in Figure 5-2(a). The A_S increased gradually along the growth direction. Figure 5-2(b) shows the A_S as a function of Mn concentration. The A_S increased with the increase of Mn concentration, which is consistent with previous reports [28, 29]. In addition, the A_S of all samples was higher than the room temperature of our laboratory (22 °C), suggesting that all samples were in the martensite state during the fatigue experiments.
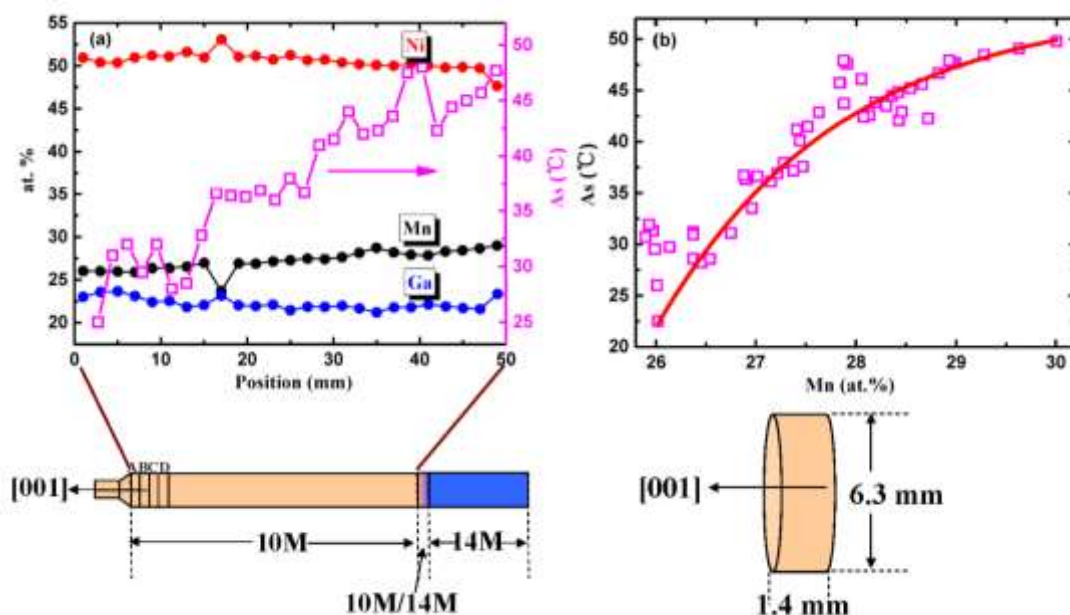
Figure 5-2: **(a) Actual composition and the austenite starting temperatures (A_S) along the axis of the crystal with 10M structure. Twenty-five disc samples with ~1.4 mm thickness were cut from the 10M portion of crystal along the axial direction as shown at the bottom. (b) Austenite starting temperatures A_S as a function of Mn concentration. The red line is a guide for the eyes. The highest temperature 10M alloy was 49 °C.**

The isothermal magnetization was measured to investigate the switching field and Figure 5-3 shows the isothermal magnetization of an I sample with the magnetic field parallel and perpendicular to the sample face respectively.

The magnetization curves show a distinct difference between the different directions, which is due in part to the large difference of demagnetizing fields along different directions [20]. In addition, the effective field H_{eff} decreased due to the switching process because of the sharp increase of M due to the twin switching. Thus, a higher magnetization can be obtained at lower effective field when the easy axis switches to the direction of the magnetic field. The effective switching fields, determined based on the isothermal magnetizations after demagnetization correction, were 0.27 T and 0.10 T for field parallel and perpendicular to the face, respectively, which were lower than the maximum field supplied by our rotary fatigue testing instrument along parallel (0.52 T) and perpendicular (0.65 T) directions [20]. Moreover, the switching fields of all samples were lower than the maximum field of the rotary fatigue testing instrument, implying full realization of periodic, reversible magnetic-field-induced strain (MFIS) of all samples in the testing instrument.
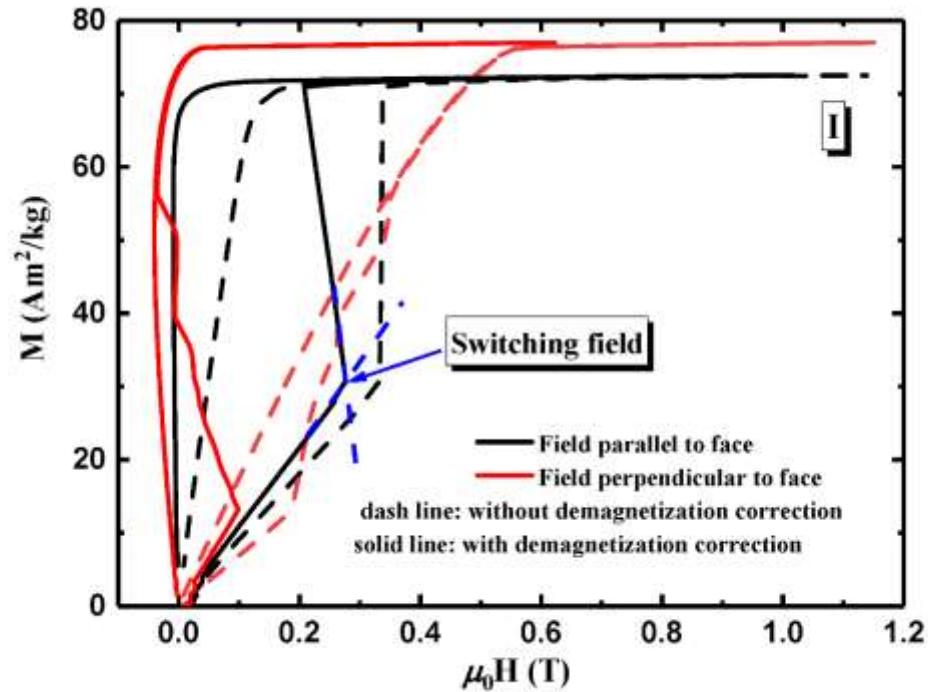
Figure 5-3: **Isothermal magnetizations of I sample (mechanically polished) with field parallel and perpendicular to the sample face before and after demagnetization correction. The switching field is the critical field at which the magnetization jumps. Results are shown with and without demagnetization correction.**

3.2 Effects of electropolishing on fatigue life

Figure 5-4(a) displays the mosaic DIC optical micrograph of the sample with

treatments I (mechanically polished finish) and II (electropolished finish) on each half of

the sample. The half with treatment I had a very smooth surface, while the other half with

treatment II was much rougher with many corrosion pits caused by the electropolishing

(Figure 5-4(b)). Figures 5-4(c) and 5-4(d) show the micrographs taken with an optical

profilometer for each half of the sample. The average surface roughness R_a was 7.99 nm

and 38.74 nm for the half with treatments I and II, respectively. Thus, the

electropolishing treatment increased the surface roughness compared to mechanical

polishing.
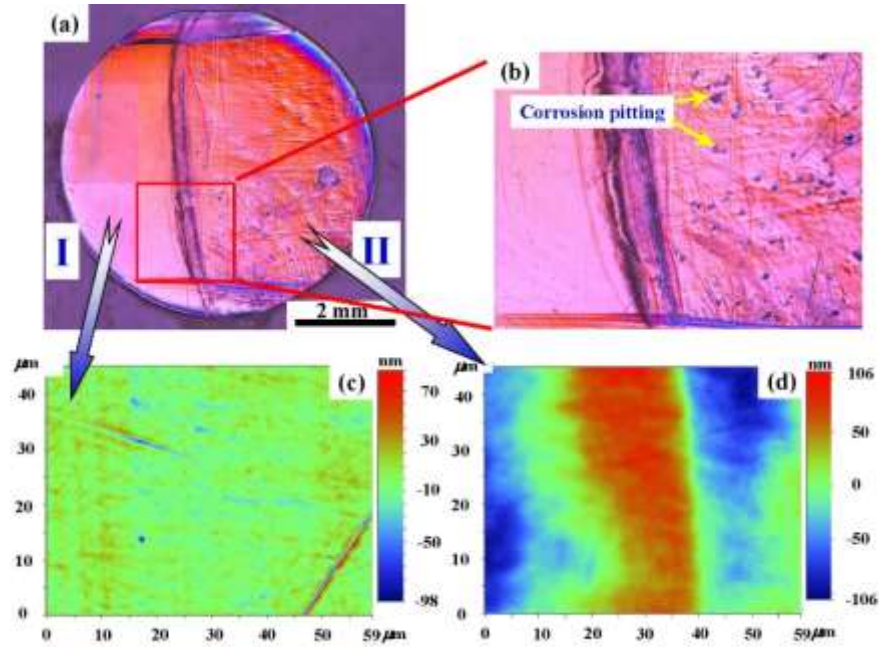
Figure 5-4:   (a) Mosaic DIC optical micrograph of the sample with I (mechanically polished) and II (electropolished) treatments on each half of the sample, and (b) the enlarged image of the square area. The micrographs with an optical profilometer for (c) the half with I treatment and (d) the other half with II treatment, respectively.

Initially, the MFIS was investigated for a I sample and an II sample. Figure 5-5 shows the MFIS as a function of field rotation angle under different magnetic fields for I and II treated samples. At zero degrees of rotation, the magnetic field was perpendicular to the sample face, leading to the orientation of variants along axial direction and the largest MFIS along radial direction. The MFIS varied periodically with the rotation of the magnetic field due to the reorientation of variants, and it increased with increasing magnetic field. The large strain under low fields at the initial angle was artificial, likely caused by pressing the sample into the mounting tape of the holder.
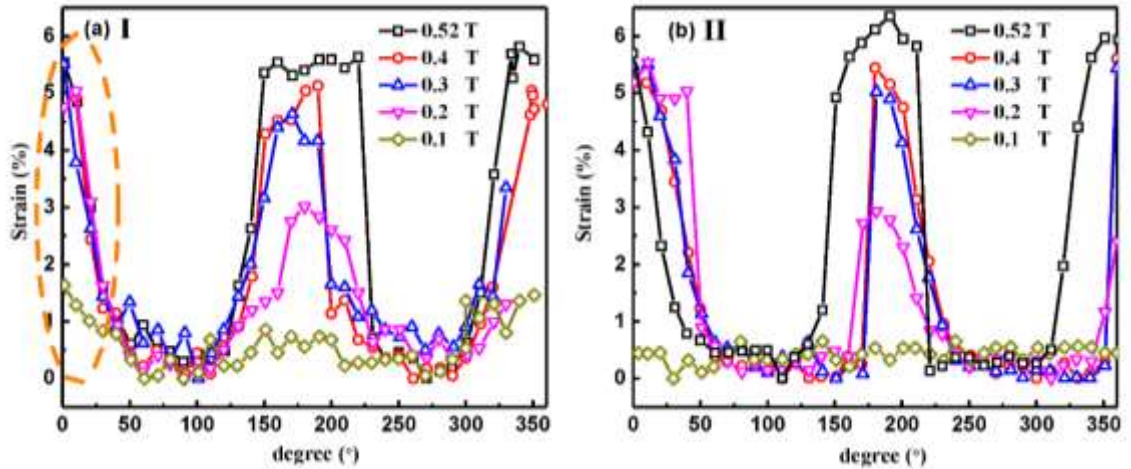
Figure 5-5: **The MFIS as a function of field rotation angle under different magnetic fields for (a) I sample (mechanically polished) and (b) II sample (electropolished). The large strain under low fields at zero angle as shown in the encircled area is artificially caused by the pressing stress during mounting the sample onto the holder.**

Figure 5-6 presents the DIC optical micrograph of the sample with treatment I on one half and treatment II on the other half of the sample after 1,000 cycles of rotary fatigue testing. The half with treatment I kept good integrity (i.e. few cracks are visible). In contrast, the half with II treatment showed large cracks after 1,000 cycles, indicating that the electropolishing treatment diminished the fatigue life. Meanwhile, as shown in Figure 5-6(b), these cracks zigzag back and forth horizontally in <110> directions across the face, consistent with previous studies [20, 24].
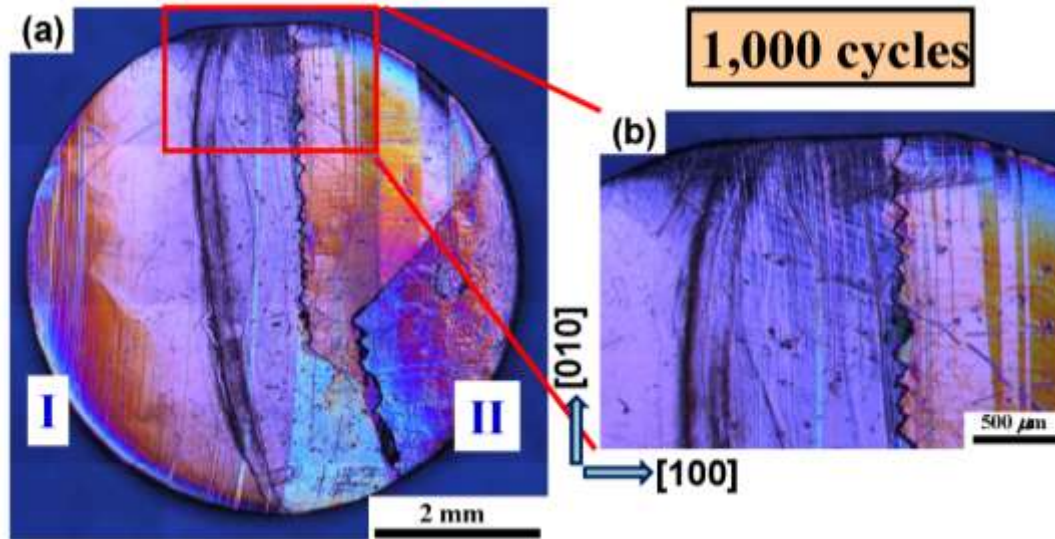
Figure 5-6:   (a) DIC optical micrograph of the sample with I (mechanically polished) and II (electropolished) treatments on each half of the sample after 1000 field cycles of rotary fatigue test, and (b) the enlarged image of the square area.

3.3 Effects of micropeening on fatigue life

Figure 5-7 shows the bulk XRD spectra of II (electropolished finish) and IV (micropeened finish) samples at 100℃. In order to avoid the possible difference induced by the different orientations of tetragonal martensite, the XRD patterns were obtained with the sample in cubic austenite state by heating the samples to 100℃. Both samples showed a diffraction peak (400) of austenite at 63.7°, but the full width at half maximum (FWHM) increased from 0.48° for the non-micropeened sample to 3.20° for the micropeened sample. The micropeening treatment thus introduced strain on the surface of the sample, causing broadening of the diffraction peak.
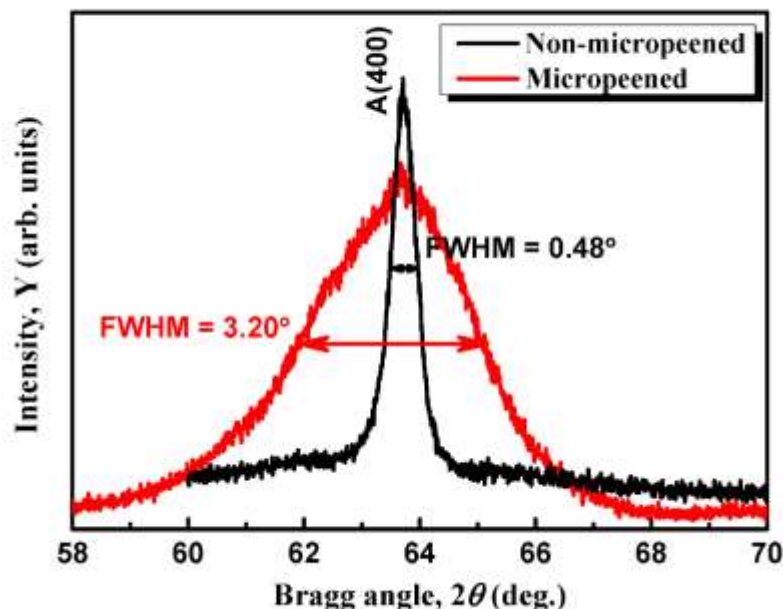
Figure 5-7: Bulk XRD spectra of non-micropeened (II) and micropeened sample (IV) samples at 100℃ around the diffraction peak (400) of austenite at 63.7°.

Figures 5-8(a) and 5-8(b) compare the mosaic DIC optical micrographs of the non-micropeened sample (II) and micropeened sample (IV). The II sample (Figure 5-8(a)) showed a rough surface with corrosion pits which were caused by electropolishing., Twin boundaries were visually apparent on the surface of II sample. In contrast, the IV sample showed a uniform frosted-like surface and the twin boundaries were not visually apparent. The topography images of II and IV samples from the optical profilometer are presented in Figures 5-8(c) and 5-8(d). The II sample showed clear twin boundaries with a surface R_a of 90.18 nm. For the IV sample, no twin boundaries were visible, and the surface R_a was 315.06 nm. Although the R_a was higher after micropeening, the surface morphology was uniform. Figure 5-9 shows the isothermal magnetizations after demagnetization correction for II, III, and IV samples, respectively. There is no distinct difference of the M-H curves between II and III samples. However, the increase in

magnetization due to the reorientation of variants was smooth for the IV sample, and thus twin domain switching occurred over a range of the magnetic field, consistent with fine-twin-controlled MFIS [14].
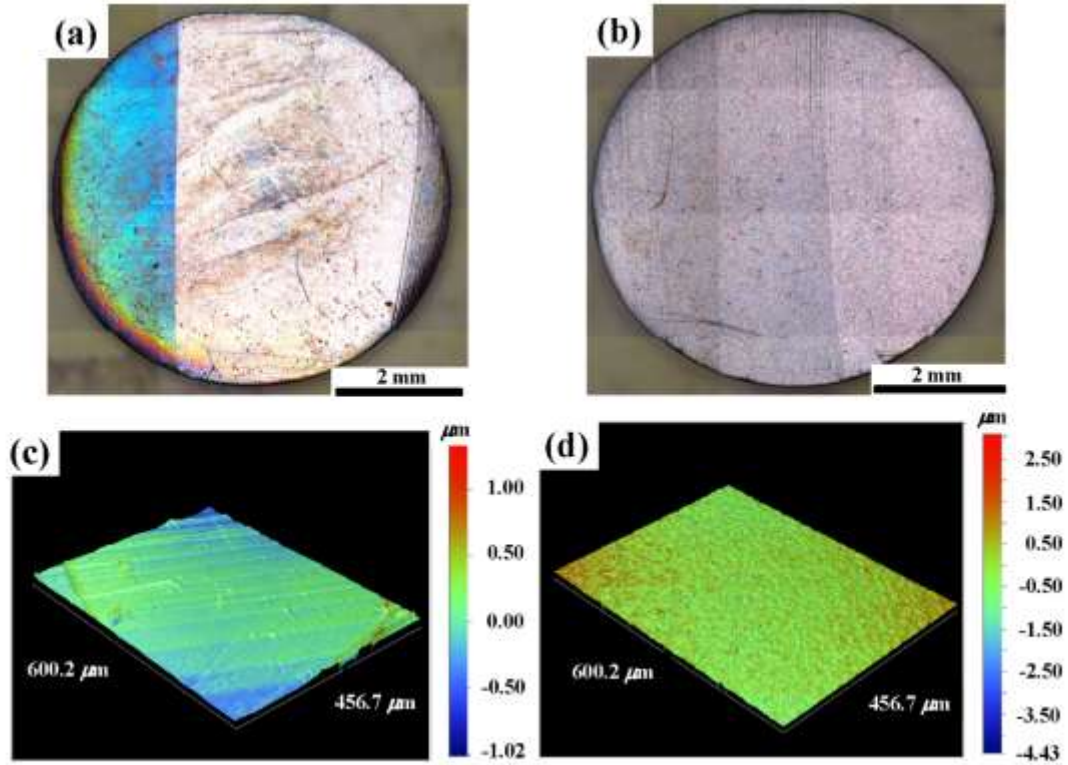
Figure 5-8: **Mosaic DIC optical micrographs of the (a) non-micropeened sample (II) and (b) micropeened sample (IV), and the topography images of (c) II and (d) IV samples with an optical profilometer, respectively.**
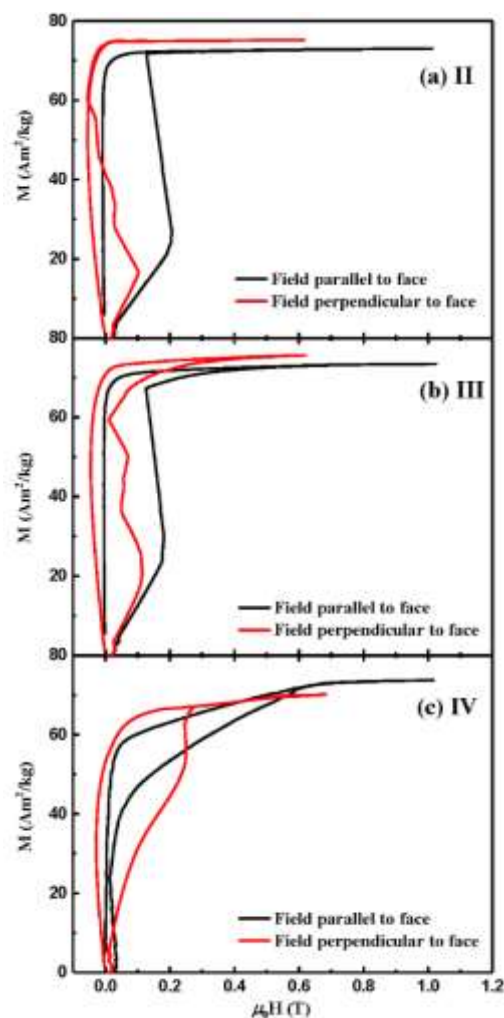
Figure 5-9:   Isothermal magnetizations with demagnetization correction with field parallel and perpendicular to the sample face for (a) II, (b) III, and (c) IV samples, respectively.

Figures 5-10 presents the MFIS as a function of field rotation angle under

different magnetic fields for II, III, and IV samples, respectively. The II sample exhibited

the full MFIS, the strain plateauing at 0.52 T, similar to the results of previous reports

[22, 30]. The MFIS decreased slightly in III and IV samples after the micropeening

treatment and exhibited a less broad plateau. The magnetic field dependence of the

maximum MFIS is plotted in Figure 5-10(d). No samples, regardless of treatment

exhibited MFIS below 0.1 T, indicating that the switching field of all samples was higher

than 0.1 T. The II sample began to exhibit MFIS of ~3.0% under a magnetic field of 0.2

T, while MFIS under 0.2 T was lower in III (about 1%) and IV (below 0.5%) samples,

suggesting a reduction of twin boundary mobility at low field strength. In addition, the

maximum MFIS under 0.52 T was 6.35%, 5.41%, and 4.98% for II, III, and IV samples,

respectively. The micropeening treatment appeared to slightly hamper twin boundary

movement, leading to an increase in switching field as well as a slight reduction in

overall MFIS.
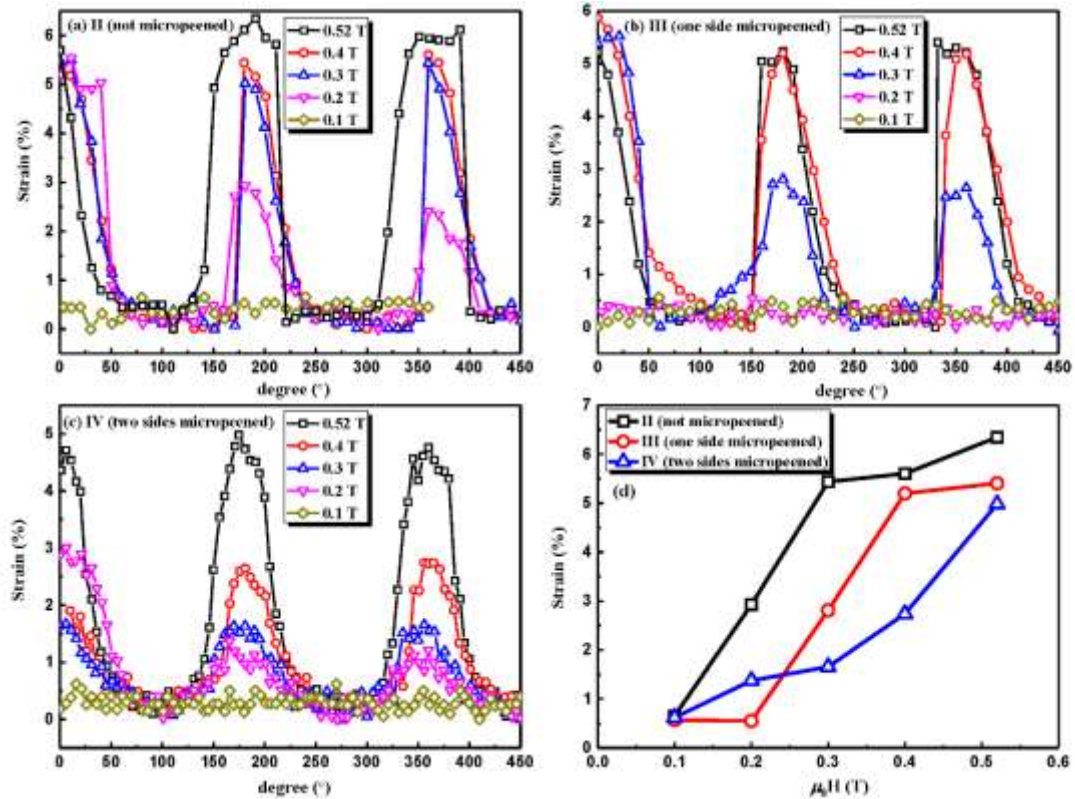
Figure 5-10:   The MFIS as a function of field rotation angle under different magnetic fields for (a) II, (b) III, and (c) IV samples, respectively. (d) Magnetic field dependence of the maximum MFIS.

The mosaic DIC optical micrographs of the II, III, and IV samples after rotary fatigue tests are presented in Figure 5-11. The II sample failed after 1,000 cycles, exhibiting large cracks, consistent with results shown in Figure 5-6.
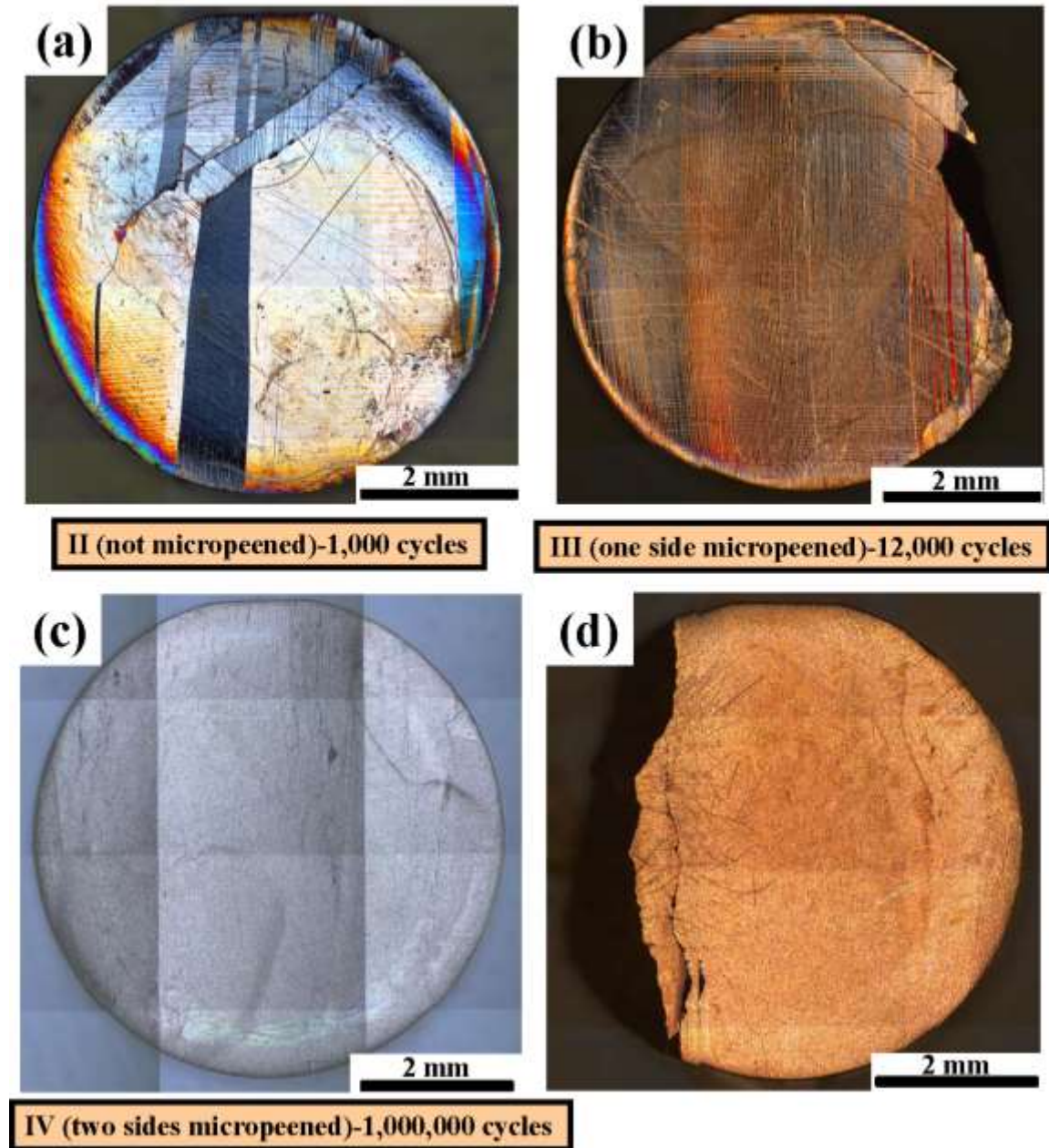
Figure 5-11:   Mosaic DIC optical micrographs of the (a) II sample after 1,000 cycles, (b and d) III sample after 12,000 cycles, and (c) IV sample after 1,000,000 cycles, respectively. (b) non-micropeened side of III sample and (d) micropeened side of III sample.

With the micropeening treatment on one side, the III sample exhibited a much longer fatigue life, but broke into several sections after 12,000 cycles. A fine twin microstructure was visibly apparent on the non-micropeened side of III sample, as shown in Figure 5-11(b), but these twins were not discernable on the micropeened side (Figure 5-11(d)). The IV sample with micropeening on both sides maintained excellent integrity without exhibiting obvious cracks even after 1,000,000 cycles as shown in Figure 5-11(c). The micropeening treatment significantly improved the fatigue life of the FSMA three orders of magnitude.

In order to further study the effect of rotary fatigue test on the microstructure evolution of IV sample, one IV sample before the fatigue test and one following the fatigue test was sectioned in half, and the microstructure of their cross sections was investigated with DIC as shown in Figure 5-12. The IV sample showed a single twin variant microstructure without twin boundaries or any other defects before the fatigue cycling. After 1,000,000 cycles, small cracks along <011> direction appeared, propagating from the circumference.
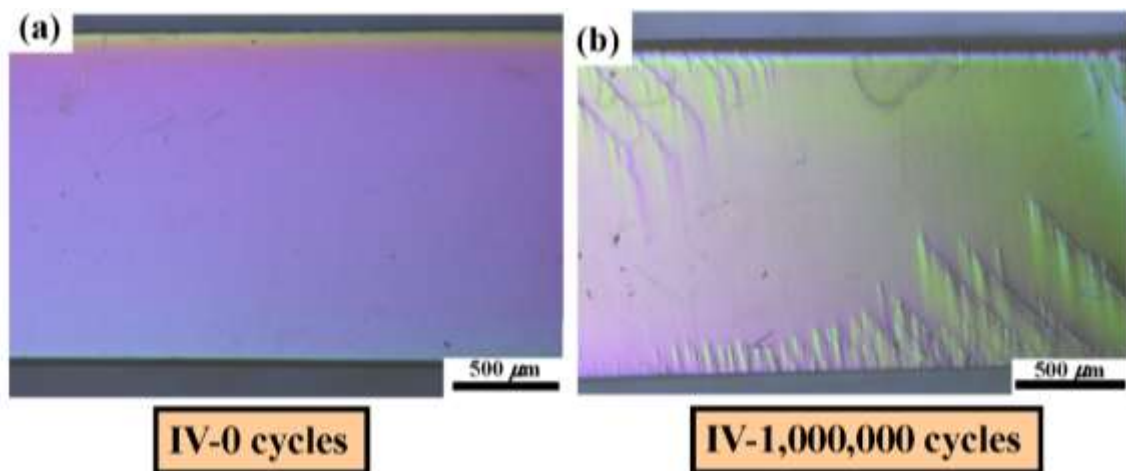
Figure 5-12: Microstructure of the cross sections for IV samples before and after 1,000,000 field cycles of rotary fatigue test.

Figure 5-13 shows the isothermal magnetizations of IV samples after 500,000 and 1,000,000 cycles, respectively. In comparison with the isothermal magnetizations of the sample before cycling in Figure 5-9(c), the M-H curves become much smoother yet demonstrated clear domain switching along the parallel direction after fatigue testing. Moreover, the M-H curves after 500,000 and 1,000,000 cycles fully overlap with each other, revealing that the IV sample almost exactly maintained its magneto mechanical properties.
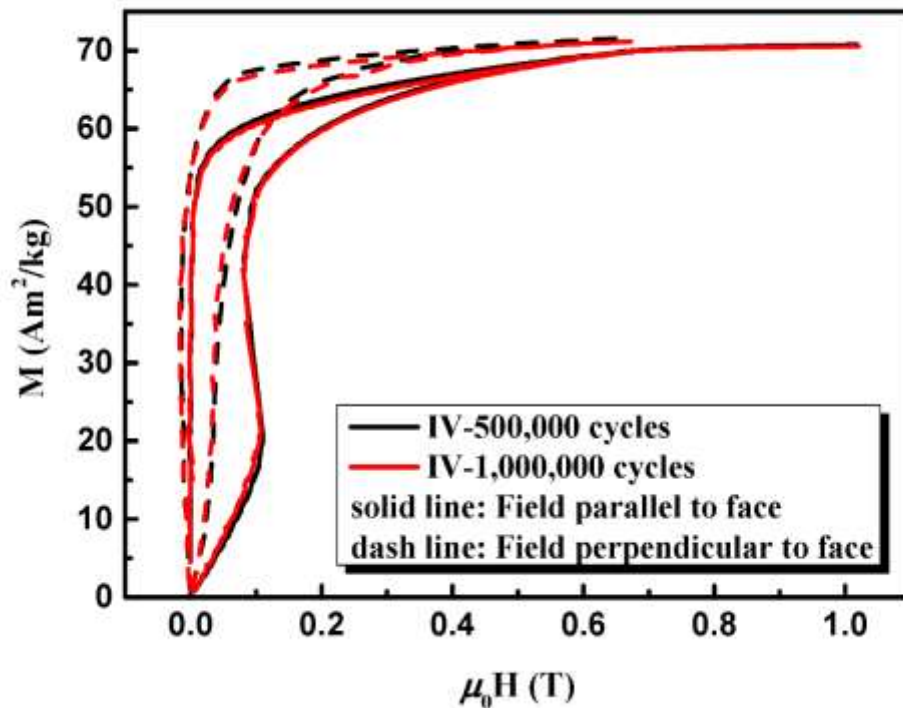
Figure 5-13: Isothermal magnetizations of IV samples with field parallel and perpendicular to the sample face after 500,000 and 1,000,000 cycles, respectively.

The effect of magnetic field cycling on MFIS was evaluated and Figure 5-14(a) presents the MFIS as a function of field rotation angle for IV sample after 1, 100,000, and 1,000,000 cycles, respectively. The MFIS curves remained nearly the same but the

maximum MFIS decreased slightly with the increasing number of cycles. The cycle dependence of the maximum MFIS is plotted in Figure 5-14(b). The maximum strain declined quickly from 4.98% for the first cycle to 4.49% after 100,000 cycles, and then decreased more gradually. Although the MFIS decreased slightly after the magnetic field cycling, the maximum strain remained relatively high at 4.16% under a modest field of 0.52 T after 1,000,000 cycles.
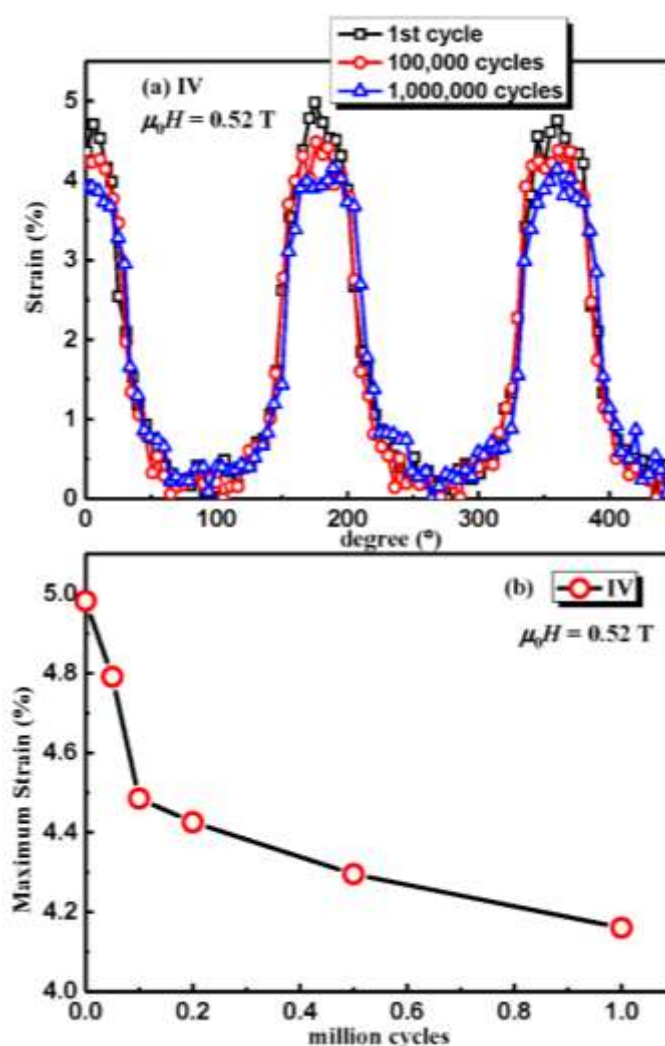
Figure 5-14:   (a) MFIS as a function of field rotation angle under magnetic field of 0.52 T for IV sample after 1, 100,000, and 1,000,000 cycles, respectively. (b) The cycle dependence of the maximum MFIS under 0.52 T for IV sample.

To further investigate the evolutionary process of local strain and twin boundaries during the rotating-field test, a series of DIC images with rotation step of 5° were analyzed with an open source, MATLAB based 2D DIC software Ncorr [27]. Figure 5-15 shows the in-plane Green-Lagrangian strain component σ_{yy} derived from Ncorr for a series of DIC images of micropeened IV sample with an angular resolution of 15° and spatial resolution of 0.008 mm/pixel. The magnetic field was perpendicular to the sample face at 0°, and the rotation axis was along the X axis. Therefore, the twin boundaries moved along the Y axis, and lead to MFIS in this direction. The DIC image at 90° was chosen as the reference image since the short axis (c) was along the Y axis at 90°. The angle was then reduced to 0°. The crystal did not show obvious strain above 45°, but distinct strain appeared immediately following and increased with further rotation, reaching the maximum at 0°.
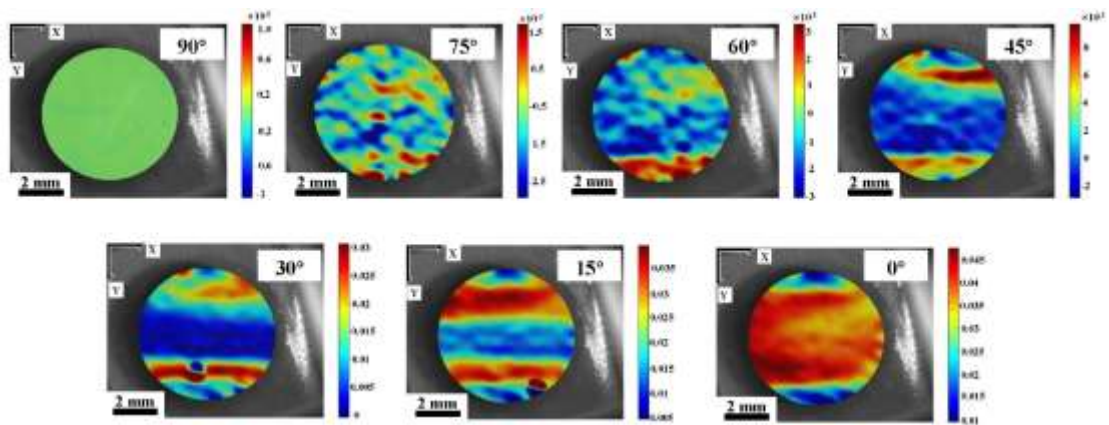
Figure 5-15: In-plane Green-Lagrangian strain component ε_{yy} for a series of DIC images of micropeened IV sample with step of 15° derived from Ncorr. The magnetic field is parallel to the sample surface at 90° and the rotation axis is along X axis. The twin boundaries move along Y axis, and lead to the MFIS in this direction. The DIC image at 90° was chosen as the reference image since the short axis (c) is along Y axis at 90°.

4. Discussion

During magnetic field actuation, twin boundaries move through the crystal driven by magnetostress. If the sample is constrained by the holder, the motion of twin boundaries is restricted at the sample ends if these are adhered to and constrained by the sample holder, which leads to a large reduction of MFIS [23]. Moreover, a stress concentration develops at the sample ends from the increase in magneto-mechanical response, nucleating cracks and eventually causing fracture if the twins are thick [15, 17]. In the present work, the Ni-Mn-Ga single crystal disk was not constrained during the rotating-field testing, and it shows a large MFIS of up to 6.35%, much higher than the (1~2%) in experiments with constrained samples that previously showed good fatigue performance [23].

Surface defects hinder the motion of twin boundaries, leading to stress concentrations and nucleating cracks [16, 19]. Electropolishing has thus been suggested as an effective way to prevent damage accumulation in Ni-Mn-Ga FSMA crystals during high-cycle magnetic-mechanical actuation as it reduces surface defects and decreases twinning stress [13]. In contrast, in our study the electropolishing caused much more damage on the surface compared to mechanically polishing with 0.04 µm water-based diamond suspension as shown in Figure 5-4, and the electropolishing was detrimental to fatigue life. Figure 5-16 shows a schematic illustrating the effects of surface modification on twin boundary mobility. The I sample exhibits a smooth surface with Ra = 7.99 nm after mechanical polishing with 0.04 µm diamond suspension. The twinning stress is low, and the twin boundaries move smoothly through the entire crystal without pinning from surface defects (Figure 5-16(a)) [31]. The twin boundary motion is obstructed by a few

coarsely dispersed internal obstacles and defects (schematically illustrated by the blue

object in the center of Figure 5-16(a)). In comparison, electropolishing creates a rougher

surface with a number of corrosion pits, which act as dispersed pinning sites for twin

boundaries as shown in Figure 5-16(b). Cracks nucleate easily at these pinning sites due

to stress concentration, significantly reducing the fatigue life [20]. In addition, cracks

propagate along 45° with the edges of sample in all surfaces, e.g., the cracks progress zig-

zagging back and forth horizontally in <110> directions on the top surface, and develop

along <011> direction on the cross section. Thus, the cracks preferentially propagate

along the {111} crystal planes, which is in a good agreement with previous studies [20,

24].
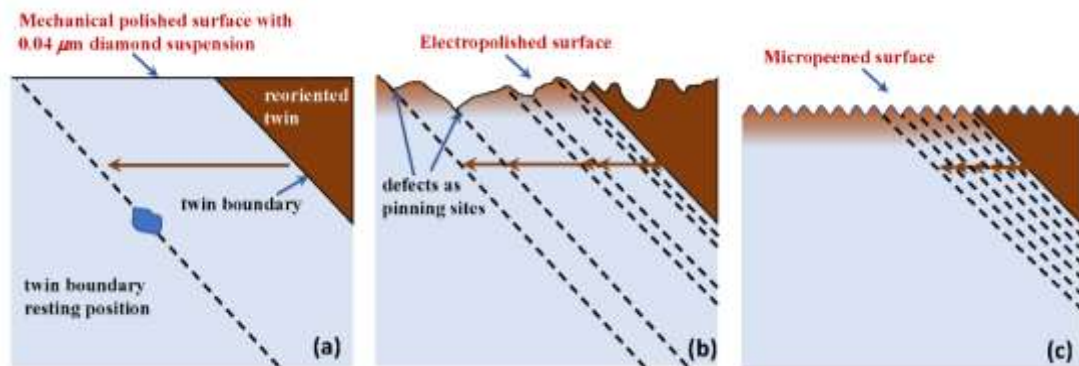
Figure 5-16:   Schematic illustrating the effects of surface modification on the twin boundary mobility. The surface conditions correspond to (a) mechanical polished with 0.04 μm diamond suspension, (b) electropolished, and (c) micropeened surfaces. The dark part is the reoriented twin with preferred orientation relative to the external magnetic field. The solid line indicates the twin boundary and the dash lines correspond to the twin boundary arrests during the rotary magnetic-mechanical experiment. The surface defects act as pinning sites for twin boundaries. The twin boundary motion might be obstructed by a few coarsely dispersed internal obstacles and defects in (a), while it would be mainly hindered due to the pinning effect from surface defects in (b) and (c).

Although the micropeening increases surface roughness, the surface morphology is uniform compared with the electropolished sample (Figure 5-8). The homogeneously distributed defects provide homogeneous pinning sites for twin boundaries, creating numerous small and thin twins as described in Figure 5-16(c). This dense twin microstructure is visible in the non-micropeened side of III sample in Figure 5-11(b). Moreover, since these small twins were decomposed from a well-trained single variant, the orientation of these small twins should be very close, explaining why the twin boundaries cannot be observed clearly using optical methods on the micropeened surface (Figure 5-8(b) and Figure 5-11(c)). Similar to the effect of ineffective training described in Ref. [17], twin boundary mobility is somewhat inhibited in the micropeened crystals with densely twinned microstructure, and the MFIS becomes lower after micropeening. However, while many dislocations pile-up at defects and nucleate cracks in the non-micropeened crystal with coarse twins, in the micropeened sample with a fine twin structure [15] pile-ups of dislocations are small and more homogeneously distributed. Therefore, the fatigue life during the high-cycle magneto-mechanical tests is significantly improved by micropeening.

In electropolished samples with low defect density, twin boundaries typically move through the entire samples [32]. When starting in a single domain crystal, the twinning stress and the switching field are mainly controlled by the nucleation of twin boundaries. Thus, the twinning stress starts out high (above 1 MPa) and quickly drops to below 0.5 MPa, following the nucleation of a twin boundary. This results in an abrupt switching field. In contrast, if twin boundaries are already present, the nucleation energy is irrelevant, and the twinning stress is below 0.5 MPa, and thus switching begins at a

lower magnetic field. Further, the density of twins impacts the twinning stress and stress evolution [33]. For a crystal with only one twin boundary, the twinning stress can be low (0.1 MPa for type II twins) and constant over the entire deformation range covered by twin boundary motion. In contrast, for a crystal with a high density of parallel twin boundaries, the twinning stress begins at about 0.3 MPa and increases monotonically until twin deformation saturates, inhibited by adjacent pinned twin boundaries. The effect of micropeening on the switching field can therefore be explained as in the electropolished state, switching occurs abruptly when a twin boundary is nucleated and then propagates through the sample (Figure 5-9(a)). But in the micropeened state, many twins are present and pinned by the surface defects. The twin boundaries can move partially within the crystal at a very low twinning stress, and thus at a small magnetic field. However, the magnetostress must counter the pinning force of the surface defects introduced by micropeening to complete switching. Therefore, switching starts at a low magnetic field and gradually proceeds with increasing magnetic field to complete at a rather high magnetic field (Figure 5-9(c)).

The evolutionary process of twinning is also evident when comparing the strain maps obtained from Ncorr software (Figure 5-15) with the rotation degree dependence of MFIS shown in Figure 5-10. The regions where the twin boundaries have moved is given by the σ_{yy} contours. The transition between blue (small strain) and red (large strain) implies that twin density is high (Figure 5-11), such that the twin boundaries are not well resolved with the Ncorr strain analysis. The Ncorr software analyzes the strain average over an area larger than the twin width. In areas where the twin boundaries overcome the pinning forces, the σ_{yy} strain component is large. It appears that twin boundaries

overcome pinning forces locally, followed by growth of the strained regions. In addition, the component of magnetic field along the radial direction is greater than that along the axial direction when the angle is above 45°. This indicates why the crystal does not show a strain above 45°, and then distinct strain appears and grows with further rotation, which reaches maximum at 0°. (Figure 5-15 and supplementary video).

5. Conclusions

The effects of surface electropolishing and micropeening treatments on the fatigue life of unconstrained $Ni_{50}Mn_{28}Ga_{22}$ single crystals in a rotating magnetic field were systematically studied. In comparison with the mechanically polished sample with 0.04 μm water-based diamond suspension, electropolishing increases the surface roughness, creating coarsely dispersed pinning sites for twin boundaries. Subsequently, the fatigue life is diminished significantly because the twinning dislocations easily pile up at the pinning sites and then nucleate cracks due to the stress concentration. Conversely, the micropeening treatment produces a uniform surface morphology with a dense distribution of small defects which stabilize a very fine twin structure. The homogeneously distributed surface defects provide homogeneous pinning sites for twin boundaries, which hinder the twin boundary motion, leading to the slight reduction of MFIS. However, large groups of dislocations do not pile up as in the electropolished sample and the stress distribution is more homogeneous due to the fine twin structure in the micropeened sample. The fatigue life is thus remarkably improved by the micropeening treatment. The present work indicates that fatigue life is not only related to the surface defects but also affected by the twin microstructure. Micropeening that produces homogeneous surface

morphology as well as fine twin microstructure appears to be an effective method to improve fatigue life while maintaining a large MFIS.

Acknowledgements

References:

[1]   M. Chmielus, X. X. Zhang, C. Witherspoon, D. C. Dunand, P. Müllner, Giant magnetic-field-induced strains in polycrystalline Ni-Mn-Ga foams, Nat. Mater. 8 (2009) 863.

[2]   D. C. Dunand, P. Müllner, Size effects on magnetic actuation in Ni-Mn-Ga shape-memory alloys, Adv. Mater. 23 (2011) 216.

[3]   I. Suorsa, J. Tellinen, E. Pagounis, I. Aaltio, K. Ullakko, Applications of magnetic shape memory alloys, Proceedings of the 8th International Conference on Actuators, Bremen, Germany, 10-20 June 2002, p. 158.

[4]   P. Müllner, V. A. Chernenko, G. Kostorz, Stress-induced twin rearrangement resulting in change of magnetization in a Ni-Mn-Ga ferromagnetic martensite, Scr. Mater. 49 (2003) 129.

[5]   K. Ullakko, J. K. Huang, C. Kantner, R. C. O'Handley, V. V. Kokorin, Large magnetic-field-induced strains in Ni_2MnGa single crystals, Appl. Phys. Lett. 69 (1996) 1966.

[6]   A. Sozinov, A. A. Likhachev, N. Lanska, K. Ullakko, Giant magnetic-field-induced strain in NiMnGa seven-layered martensitic phase, Appl. Phys. Lett. 80 (2002) 1746.

[7]   J. M. Guldbakke, M. Chmielus, K. Rolfs, R. Schneider, P. Müllner, A. Raatz, Magnetic, mechanical and fatigue properties of a $Ni_{45.4}Mn_{29.1}Ga_{21.6}Fe_{3.9}$ single crystal, Scr. Mater. 62 (2010) 875.

[8]   A. Sozinov, N. Lanska, A. Soroka, W. Zou, 12% magnetic field-induced strain in Ni-Mn-Ga-based non-modulated martensite, Appl. Phys. Lett. 102 (2013) 021902.

[9]   R. C. O'Handley and S. M. Allen, Shape memory alloys, magnetically activated ferromagnetic shape-memory materials, *Encyclopedia of Smart Materials*, ed M. Schwartz (New York: Wiley) 2002, p. 936.

[10]   O. Söderberg, Y. Ge, A. Sozinov, S.-P. Hannula, V. K. Lindroos, *Handbook of Magnetic Materials*. ed J. Buschow (Amsterdam: Elsevier) 2006, p. 1.

[11]   I. Aaltio, O. Heczko, O. Söderberg, S.-P. Hannula, *Smart Materials*, ed M. Schwartz (CRC Press, Boca Raton, FL) 2009, p. 20.

[12]   P. Müllner, V. A. Chernenko, M. Wollgarten, G. Kostorz, Large cyclic deformation of a Ni-Mn-Ga shape memory alloy induced by magnetic fields, J. Appl. Phys. 92 (2002) 6708.

[13]   M. Chmielus, P. Müllner, Effects of surface pinning, locking, and adaption of twins on the performance of magnetic shape-memory alloys, Mater. Sci. Forum 684 (2011) 177.

[14]   P. Müllner, G. Kostorz, Microstructure of magnetic shape-memory alloys: between magnetoelasticity and magnetoplasticity, Mater. Sci. Forum 583 (2008) 43.

[15]P. Müllner, V. A. Chernenko, D. Mukherji, G. Kostorz, Cyclic magnetic-field-induced deformation and magneto-mechanical fatigue of Ni-Mn-Ga ferromagnetic martensites, Mater. Res. Soc. Symp. Proc. 785 (2004) 415.

[16]   M. Chmielus, C. Witherspoon, K. Ullakko, P. Müllner, R. Schneider, Effects of surface damage on twinning stress and the stability of twin microstructures of magnetic shape memory alloys, Acta Mater. 59 (2011) 2948.

[17]   M. Chmielus, V. A. Chernenko, W. B. Knowlton, G. Kostorz, P. Müllner, Training, constraints, and high-cycle magneto-mechanical properties of Ni-Mn-Ga magnetic shape-memory alloys, Eur. Phys. J. Special Topics 158 (2008) 79.

[18]   L. Straka, O. Heczko, H. Hänninen, Activation of magnetic shape memory effect in Ni-Mn-Ga alloys by mechanical and magnetic treatment, Acta Mater. 56 (2008) 5492.

[19]   M. Chmielus, K. Rolfs, R. Wimpory, W. Reimers, P. Müllner, R. Schneider, Effects of surface roughness and training on the twinning stress of Ni-Mn-Ga single crystals, Acta Mater. 58 (2010) 3952.

[20]   T. Lawrence, P. Lindquist, K. Ullakko, P. Müllner, Fatigue life and fracture mechanics of unconstrained Ni-Mn-Ga single crystals in a rotating magnetic field, Mater. Sci. Eng. A 654 (2016) 221.

[21]   C. P. Henry, D. Bono, J. Feuchtwanger, S. M. Allen, R. C. O'Handley, as field-induced actuation of single crystal Ni-Mn-Ga, J. Appl. Phys. 91 (2002) 7810.

[22]   P. Müllner, V. A. Chernenko, G. Kostorz, Large cyclic magnetic-field-induced deformation in orthorhombic (14M) Ni-Mn-Ga martensite, J. Appl. Phys. 95 (2004) 1531.

[23]   M. Chmielus, I. Glavatskyy, J.-U. Hoffmann, V. A. Chernenko, R. Schneider, P. Müllner, Influence of constraints and twinning stress on magnetic field-induced strain of magnetic shape-memory alloys, Scr. Mater. 64 (2011) 888.

[24]   I. Aaltio, A. Soroka, Y. Ge, O. Söderberg, S. P. Hannula, High-cycle fatigue of 10M Ni-Mn-Ga magnetic shape memory alloy in reversed mechanical loading, Smart Mater. Struct. 19 (2010) 075014.

[25]   D. Kellis, A. Smith, K. Ullakko, P. Müllner, Oriented single crystals of Ni-Mn-Ga with very low switching field, J. Cryst. Growth 359 (2012) 64.

[26]   D. X. Chen, J. A. Brug, Demagnetizing factors for cylinders, IEEE T. Magn. 27 (1991) 3601.

[27]   J. Blaber, B. Adair, A. Antoniou, Ncorr: open-source 2D digital image correlation matlab software, Exp. Mech. 55 (2015) 1105.

[28]   V. A. Chernenko, E. Cesari, V. V. Kokorin, I. N. Vitenko, The development of new ferromagnetic shape memory alloys in Ni-Mn-Ga system, Scr. Met. Materi. 33 (1995) 1239.

[29]   S. K. Wu, S. T. Yang, Effect of composition on transformation temperatures of Ni-Mn-Ga shape memory alloys, Mater. Lett. 57 (2003) 4291.

[30]   P. Müllner, V. A. Chernenko, G. Kostorz, Large magnetic-field-induced deformation and magneto-mechanical fatigue of ferromagnetic Ni-Mn-Ga martensites, Mater. Sci. Eng. A 387 (2004) 965.

[31]   I. Aaltio, X. W. Liu, M. Valden, K. Lahtonen, O. Söderberg, Y. Ge, S. P. Hannula, Nanoscale surface properties of a Ni-Mn-Ga 10M magnetic shape memory alloy, J. Alloy. Compd. 577 (2013) S367.

[32] I. Aaltio, O. Söderberg, Y. L. Ge, S. P. Hannula, Twin boundary nucleation and motion in Ni-Mn-Ga magnetic shape memory material with a low twinning stress, Scr. Mater. 62 (2010) 9.

[33]   L. Straka, N. Lanska, K. Ullakko, A. Sozinov, Twin microstructure dependent mechanical response in Ni-Mn-Ga single crystals, Appl. Phys. Lett. 96 (2010) 131903.

CHAPTER SIX: TRAVELING SURFACE UNDULATION ON A NI-MN-GA SINGLE

CRYSTAL ELEMENT.

Andrew Armstrong[1],

Bibek Karki[1],

Aaron Smith[2],

Peter Müllner[1]

[1]Boise State University, Boise, ID 83725, USA

[2]Shaw Mountain Technology LLC, Nampa, ID 83687, USA

Abstract

Active materials couple a stimulus (electrical, magnetic, thermal) with a mechanical response. Typical materials such as piezoelectrics strain as bulk materials to the stimuli. Here we consider an undulation created by the *heterogeneous* strain within a magnetic shape memory alloy (MSM) transducer. We study the mechanical response of an MSM element vs. two surface treatments: a *polished* state with minimal surface stresses, and a *micropeened* state with compressive surface stress. The polished element had a sharp-featured, faceted shrinkage shape. The micropeened element had a smooth shrinkage shape, forming an additional hump. Both microstructures had the same macroscopic motion: a twin packet that nucleates and moves down the element. The packet is a single twin, in the case of the polished sample. The packet is a twinned lamellar, in the case of the micropeened element. The twinned lamellar approximates the single thick twin while allowing additional degrees of freedom. The dense twin microstructure smoothed the magnetic field pattern. The micropeened element deformed differently than the polished sample, deforming equally as a hump and a depression. The peak-to-peak undulation stroke for both states was about 30 μm.

1. Introduction

Classically, active materials strain uniformly to the stimuli. Piezoelectric elements, for example, actuate by electrical impulses which uniformly strain the transducer about 0.1% [1]. The coordination of many transducer elements enables large strokes as well as complex and precise motion such as that found for ultrasonic traveling wave motors and piezowalk actuators [1, 2]. Here we evaluate an actuator which strains heterogeneously within a magnetic shape memory alloy (MSM) transducer. A locally

strained region causes a depression on the transducer surface. The depression moves along the transducer surface with the rotation of a magnetic field. While appearing to propagate, the depression is a quasi-equilibrium structure created by the magnetic field.

Reversible plastic deformation of MSM alloys by magnetic field has been known since 1996 [3]. MSM materials act as metallic muscles, capable of longitudinal strain, shrinkage [4, 5], bending [6, 7], and localized constriction [8] in magnetic fields. In MSM alloys, crystallographic twinning accommodates the deformation [9]. For the most commonly used Ni-Mn-Ga compositions which have a 10M crystal structure, the maximum magnetic-field-induced strain is 7% [10]. High magneto-crystalline anisotropy [11], combined with highly mobile twin boundaries [12], enable the magnetic-field-driven motion of twin boundaries and present the two conditions necessary for magnetic-field-induced strain (MFIS).

An optimal MSM element would have strain close to the theoretical limit in addition to good fatigue life. Elements that have demonstrated good fatigue life have a dense twin microstructure [13]. Here the twin boundaries are mobile but move only short distances, retarded by interacting twins and surface constraints. Modification to the sample's surface by surface hardening, surface damage [14], roughness [15], and coatings [16] can constrain the sample surface and lead to a fine twin microstructure [14]. Rigid edge constraints also affect the mechanical response.

MSM elements that have been treated via our recently reported surface hardening technique, micropeening, are capable of 5% MFIS while also having a fatigue life greater than 10^6 cycles as a result of the dense twin microstructure [13]. Crack nucleation on the surface is hindered by the residual compressive stress of the micropeening. The treatment

smoothed the mechanical response of the element. Rather than deforming sharply as a twinning plateau, the strain increases smoothly with magnetostress. The effects of a similar tailor-made fine twin structure on a sample has been studied for push-pull actuators actuated with a uniform magnetic field [17]. Here we study the effect of micropeening upon an element locally actuated in a heterogeneous magnetic field, in the manner of an MSM micropump [4, 5, 18, 19]. The rotation of a magnetic field underneath an MSM element causes a local deformation to move across the element's top surface. An MSM micropump uses this moving cavity to pump small amounts of fluid at a relatively high pressure of 10 bar [19]. The stress state within the element is a combination of magnetostress, external stress, and surface constraints. Surface constraints can be created by surface treatments and external forces, including fixturing and the Maxwell force which attracts the ferromagnetic element to the magnet. The actuation mechanism of the MSM element is thus complex.

In this study, we measure the mechanical response of an MSM element with stress-free, polished surfaces. We then micropeened the element surfaces to induce a dense twin microstructure, and study the mechanical response of the MSM element. Comparing the mechanical response to the magnetic simulation of the transducer for the two surface treatments, we propose a model to describe the microstructural changes which lead to the mechanical response.

2. Experimental

A $Ni_{50}Mn_{28.5}Ga_{21.5}$ single crystal grown in a modified Bridgeman furnace according to Kellis et. al was used in this study [20]. The structure was 10M martensite which is typical for MSM actuators. The martensite to austenitic transition temperature

(i.e. the upper limit for MSM functionality) was 315K. We cut elements along {100}

ground them to a parallelism of 10 μm with a Struers Accustop. We polished sequentially

to a final polish using a 0.3 μm aluminum oxide slurry. The switching field of an element

directly adjacent to the studied element was 40 mT for Type II twins and 210 mT for

Type I twins [21].

The element was mounted onto a 0.25 mm thick glass coverslip with double-sided

3M scotch tape 0.1 mm thick. The tape allowed for localized strain while holding the

sample in place. We transferred the MSM element from one test to another on the slide to

avoid modifying the twin microstructure by handling the element. We initially trained the

element on the slide by turning it 20 times between a parallel and perpendicular

orientation within a homogeneous 1.5 T magnetic field and removed the element from the

electromagnet with the magnetic field parallel to the sample's long axis. This established

a single variant structure where the c axis was oriented parallel to the long axis of the

element.

2.1 Laser measurement stage

We built a custom non-contact laser measurement stage. The stage included a

rotating permanent magnet which cycled the magnetic field. Figure 6-1 shows the three

types of tests conducted with the laser measurement system. Components in red were

active during the measurement. Components in blue were active between measurements.

Figure 6-1a is a diagram of the scan of the magnetic field envelope which was recorded

without an MSM element on the stage. A transverse hall probe measured the vertical

component of the magnetic field as it scanned across the stage surface at 0.5 mm/s, while

the magnet rotated at a constant velocity of 2.5 Hz. Figure 6-1b shows the surface

profilometry scan, where the stage moves across the laser as a function of the magnetic

field angle (α). In Figure 6-1c, the magnet rotated at 2.5 Hz while the laser measured the

elevation variation in the center of the MSM element.
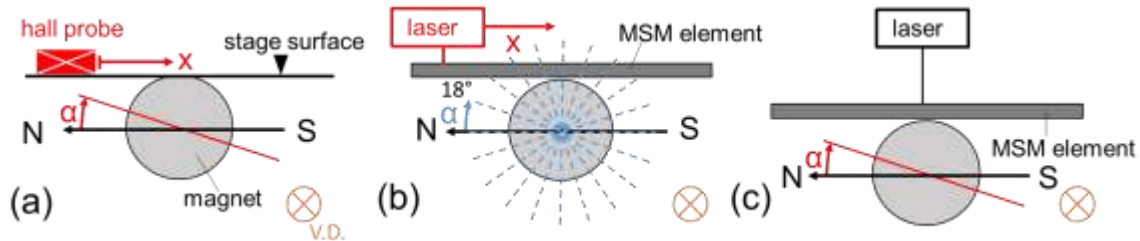
Figure 6-1: **Diagram of the laser measurements. Components in red were active during each test and components in blue were active between tests. The orange cross indicates the view direction (V.D). In (a) the hall probe scanned the magnetic field along the stage. In (b) the magnet rotated in 18° increments and a laser measured the surface profile at each increment. In (c) the magnet rotated at 2.5 Hz and the laser measured the element surface undulation.**

Figure 6-2 is a diagram of the custom non-contact laser measurement stage. A

stepper motor rotated a diametrically magnetized cylindrical N52 magnet behind the

MSM element. The element surface was measured with a laser (Keyence LK-HO52)

which was fixed to an optical table. The motor, magnet, and MSM element were drawn

across the laser beam by a linear stage (Thorlabs PT1-Z8). Figure 6-2b shows a

magnified view of the system sliced orthogonal to the stage. The MSM element mount

attached to the stage and was clamped by a polycarbonate top plate. The plate had a 0.5

mm wide slot to allow the laser beam to reach the element surface. The pressure bearing

beams of the top plate were only 0.5 mm thick. Thus, while constraining, the pressure

beams flexed slightly under the clamping load. The top plate was compressed onto the

element using nylon screws (not shown). At $\alpha = 0°$, the magnetic north was parallel to the

MSM element and pointed to the left. Rotating the permanent magnet clockwise from $\alpha =$

0° caused the magnet's north pole to turn away from the stage.
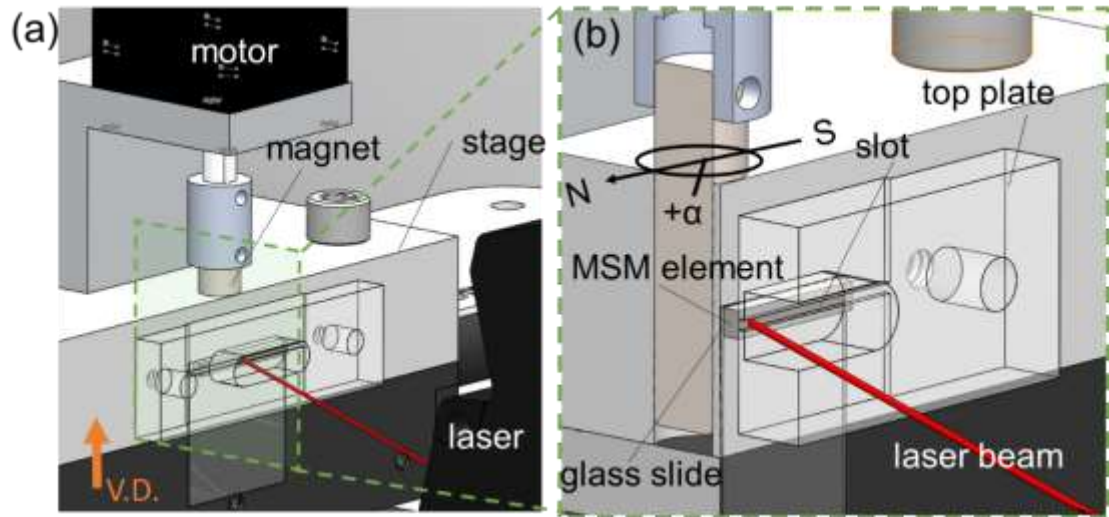
Figure 6-2: **Drawing of the laser measurement system. The motor spun a diametrically magnetized cylindrical magnet behind the MSM element. The laser measured the element surface. A linear stage moved the laser. The green dashed box in (a) shows the region magnified in (b). The MSM element was taped to a thin glass slide which mounted onto the stage. We held the MSM element down with a polycarbonate top plate which had a window for the laser beam. The orange arrow indicates the view direction corresponding to the test schematic. The coordinate system centered upon the magnet is indicated in (b). The laser beam in (b) is in reality much smaller than indicated in the figure.**

2.2 Optical microscopy test block

      We built an apparatus to view the twin microstructure under a Leica DM6000

optical microscope. In Figure 6-3a, an N52 magnet was turned by a gearhead micromotor

equipped with an optical encoder (Namiki SBL07). We placed the element upon the

block and fixed the glass slide from the top with mounting putty. Using the convention

defined for the laser experiments, we positioned the magnet at 18° intervals (3(b)). We

imaged the active region (ROI), boxed in red, using the microscope's default image

stitching software. We imaged 20 magnetic field positions (i.e. a full revolution of the

magnet). Local contrast was enhanced using the CLAHE process of the FIJI image

processor to improve the contrast between twins.
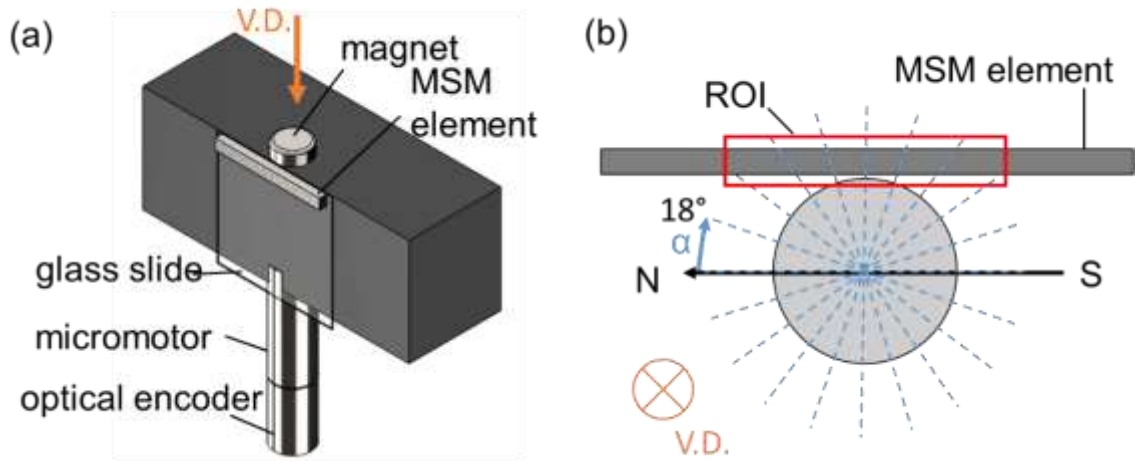
Figure 6-3: **Drawing and diagram of the microscopy block. (a) The micromotor rotated the magnet to angle *α a*nd a micrograph of the twin microstructure of the element side was taken. (b) The magnet rotated in increments of 18° between micrographs. The red box marks the region of interest of the MSM element which actuated.**

2.3 Micropeening

After recording laser measurements and optical tests on the polished element, we removed the element from the supporting glass slide and removed the tape residue with acetone. The element was micropeened according to the procedure discussed in Zhang *et al.* [13] In brief: the element was heated to 80° C, thereby transforming it to austenite. The element was micropeened for 8 seconds at 1.75 bar with 50 μm glass beads. The element was micropeened on its top and bottom surfaces. When cooled back to martensite, the MSM element was again taped to the glass slide. The unoriented twin microstructure resulting from the phase transformation was uniformly oriented using an electromagnet. After conducting the laser and optical tests on the micropeened element, we cast the element in cyanoacrylate, then polished the top surface to reveal the twin microstructure with 0.3 µm alumina slurry. During this polishing process, we removed about 5 µm of material.

3. Computer Simulation

We used a 2D magnetostatic finite element analysis software (FEMM) to simulate the interaction of the twin microstructure and the magnetic field. In our model, the 10M martensite MSM element contains two orthogonal crystallographic directions whose lattice parameters are *a* and *c*. We use relative permeability values of (2, 40) along the (*a, c*) axis to model the material anisotropy [22]. In FEMM, we could simulate either anisotropic material properties, or a BH curve, not both. Using the anisotropy linear approximation can extend the magnetization past the material's saturation magnetization leading to large overestimates of flux density. Thus the simulations were instructive but only approximate.

The simulated element was the same size as used in experiments. The gap between the magnet and the MSM element was 0.5 mm. The location of the twin was approximated from the micrographs. For the polished sample, we measured a twin thickness of 1.4 mm and the twin was centered at 1.4 mm left ($\alpha = 54°$) and right $\alpha =$ 144°) of the center of the MSM element. The dense twin microstructure was simulated as a lamellar of 25 μm plates. In the region corresponding to the thick twin variant, three out of four plates have the *c* axis oriented vertically. In the region of the parent variant, three out of four plates have the *c* axis oriented horizontally. The simulated twin bilayer was 100 μm, about 5 times thicker than measured experimentally for the micropeened twin structure. We chose this density because of the limited computing power available in this study.

4. Results:

4.1 Measurement of the magnetic field

Figure 6-4 gives the vertical component of the magnetic field along the stage. At

±10 mm from the center of the stage, the magnetic field was about 50 mT. At the center

of the stage on the surface, the field was nearly 600 mT. The blue dashed lines drawn at

±200 mT indicate the estimated region of sufficient magnetic field to move boundaries of

type I twins. The measurement was only an estimate, as induced magnetization is a

function of the twin microstructure and also the horizontal component of the magnetic

field, which biases the *c-axis* horizontally.
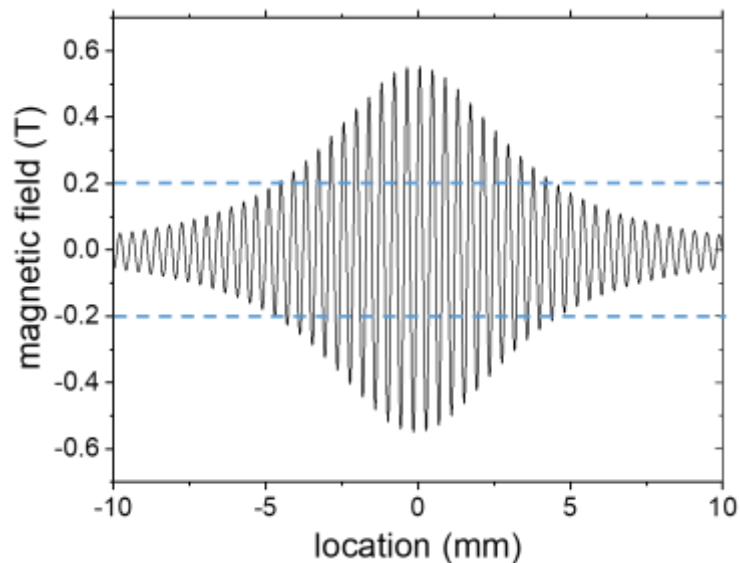
Figure 6-4: **Measurement of the magnetic field along the stage. The profile was obtained by rotating the magnet while advancing the stage. The blue dashed lines show the estimated switching field for actuation by the type I twinning mechanism.**

4.2 Laser measurements

Figure 6-5 shows surface profiles for the polished (a) and micropeened (b)

element measured by the laser. The black profiles are the experimental data of the

element measured without the magnetic field (we removed the magnet and compressed

the element.) The red profiles are experimental data of the surface profile taken at $\alpha =$

90°. To obtain the blue line, we subtracted the baseline from the $\alpha = 90°$ profile.

Localized horizontal extension and contraction prevented full alignment with the baseline

profile, resulting in noise. We smoothed data with a Butterworth filter in MATLAB

(green top profile) using a cutoff wavenumber of 0.5 mm^{-1} and an order parameter of $n =$

3. The deformation of the polished element was approximately an asymmetrical, faceted,

triangular valley. The micropeened element had a smoother, more symmetrical

depression and formed an additional hump on the leading edge. Comparing the baseline

profiles, the micropeened element had greater curvature along the length of the element.
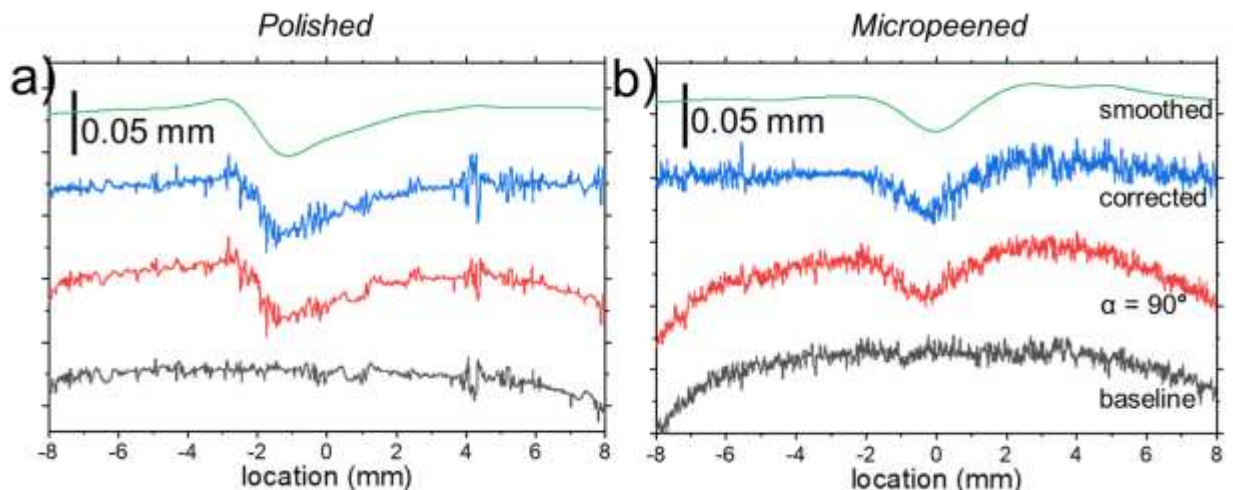
Figure 6-5: **Elevation profiles at locations along the MSM element for the two different surface treatments. The bottom profile (black) was the baseline scan of the element without a magnetic field. The red scan was taken at $\alpha = 90°$. The blue scan is the difference between baseline and $\alpha = 90°$ scan. The blue scan was filtered in MATLAB with a Butterworth filter. The green scan is the filtered output (a) Polished element surface profile. (b) Micropeened element surface profile.**

4.2.1 Surface profiles

The profiles taken at the different fields were plotted together in Figure 6-6 to

give an actuation envelope. The polished element, Figure 6-6a, at $\alpha = 0°$, had a nearly

symmetrical depression centered at $x = +2.7$ mm. At $\alpha = 18°$ a depression formed at $x = \pm2.7$ mm. The newly formed depression deepened and moved to the right as the magnet rotated. The left slope of depression (1) was steep and nearly constant from $\alpha = 54°$ to $\alpha = 90°$. At $\alpha = 90°$, the element rose slightly (2) behind the trailing edge of the depression. The slope had a distinct disinclination (3) on the right slope of depression. For the profiles from $\alpha = 36°$ to $\alpha = 90°$, the right shoulder of the depression (4) was pinned at +2.2 mm. The profile became nearly symmetrical with further rotation. The north pole and south poles actuate identically, given the similarity of $\alpha = 0°$ and $180°$ profiles in a) and c). In Figure 6-6b, but there is a noticeable difference in depth, nearly 5 µm, between $0°$ and $180°$. The effect could be due to a slight training effect, or some source of hysteresis in the system. See Supp. Figure 6-1 for the full range of scans of the polished sample.

For the micropeened sample, the field rotated clockwise (Figure 6-6b) and counterclockwise (Figure 6-6c). In Figure 6-6b, at $\alpha = 0°$, the depression center was at ±3.0 mm. With rotation of the magnet, the depression deepened, and a hump grew correspondingly. At $\alpha = 90°$, the hump was 18 µm above the baseline, and the depression was 18 µm deep. While the hump was asymmetrical about the origin, being much larger on the right, the depth of the depression was almost symmetrical about the origin. In Figure 6-6c, the magnet rotated counterclockwise. The strain amplitude was slightly greater for the clockwise actuation, while the width of the strain envelope was the same for both treatments and directions, from -5 to +7mm. The slope noted in Figure 6-6 was steepest for the polished sample and less steep for the micropeened sample actuated by a magnetic field rotating clockwise. The micropeened sample actuated by a magnetic field

rotating counterclockwise had the least steep slope. See Supp. Figure 6-2 for the full

range of scans of the micropeened sample.
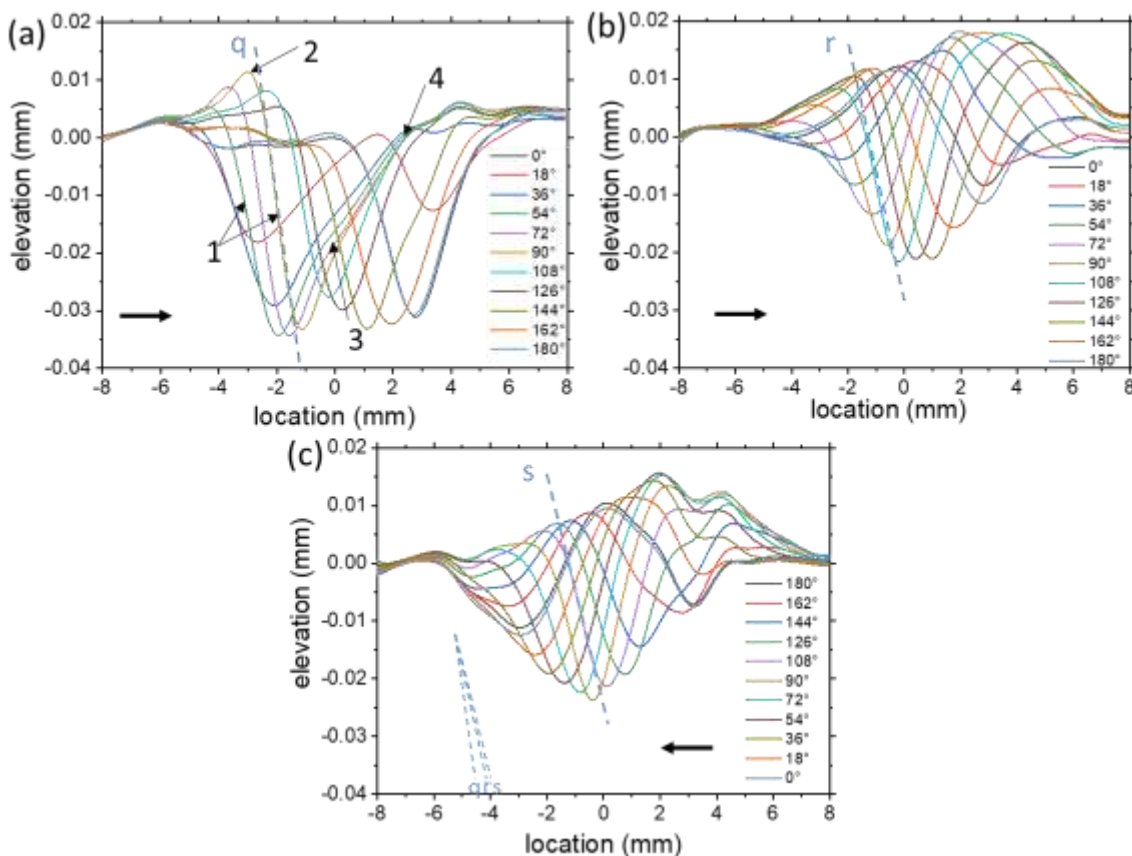
Figure 6-6:   MATLAB filtered profiles taken during half a magnet revolution. (a) The profile of the polished sample as magnet rotated clockwise. The numbers point to behaviors discussed previously in text. (b) The profile of the micropeened sample as the magnet rotated clockwise. (c) The sample micropeened and the magnet rotated counterclockwise. The labeled arrows denote twin behaviors further discussed in the text. The blue dashed lines indicate the slope of the left side of shrinkage. The slopes are compared in the bottom left of (c). q has a comparatively greater slope than r, or s

4.2.2 Elevation variation in the center of the MSM element

Figure 6-7 shows surface elevation at the center of the element as the magnet

rotated underneath at 2.5 Hz. We captured a snapshot of the twin boundary movement in

time. The polished sample transformed quickly when elevating (1) and slowly when

depressing (2). The peaks (3) and valleys (4) transition at roughly the same rate, which is

evident by the equidistant peak and valley widths. The micropeened element had a

broader peak and narrower trough when actuated clockwise which indicates a propensity

for the element to remain elevated in the top position, in a hump. Rotated

counterclockwise, the transition rate was slow in the depression and fast in the hump.

Black arrows (5) point to slight shoulders on the downward transition, found for both

surface treatments. The position and width of the shoulder is located at slightly different

positions of the transition for different surface treatments and actuation direction.
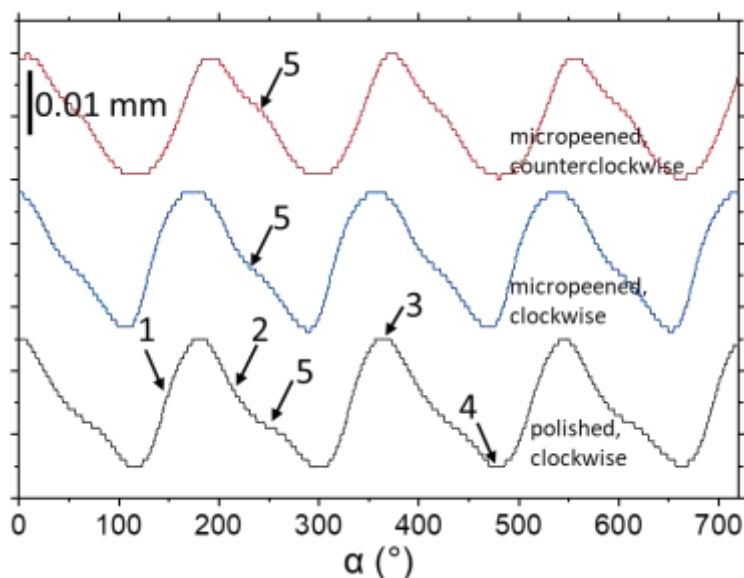
Figure 6-7: **Laser measurement at the center of the element as the magnetic field rotated. In black, the polished sample as the magnetic field rotated clockwise. In blue, the micropeened sample as the magnet rotated clockwise. In red, the micropeened sample as the magnet rotated counterclockwise. The arrow on each curve points to a transition further discussed.**

4.3 Microscopy

Figure 6-8a shows a side profile of the twin microstructure for the polished

sample taken at $\alpha = 54°$. The polished sample had a thick twin, and the dashed lines mark

the twin boundaries. A few thin twins nucleated leading the thick twin's movement.

Figure 6-8c shows the top surface of the polished sample taken at $\alpha = 0°$, and several thin

twins are visible which create the actuated region. The width of the twin double layer (i.e.

containing both twin and parent) is indicated by the white bar. The width of the bilayers

varied from about 10 to 150 μm at this angle.
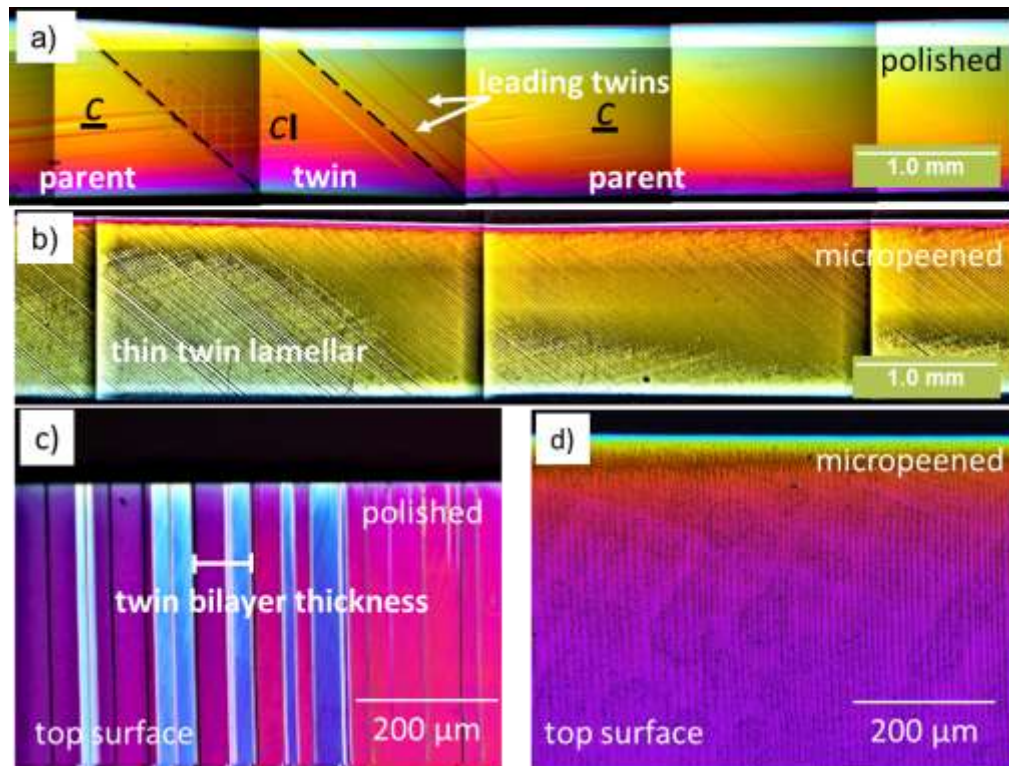
Figure 6-8: **Micrographs taken of the twin microstructure for the sample polished and micropeened. (a) At $\alpha = 54°$ the sample has a thick twin in the parent matrix, as viewed from the side. The c- axis direction is noted for the parent and twin variant. Thinner twins lead the motion of the primary thick twin. (b) At $\alpha = 90°$, the twin microstructure of the micropeened sample, viewed from the side. (c) Viewed from the top, the twin structure for the polished sample. Twins show up as contrast between variants. The purple/red tones are the parent matrix, and the blue the twin variant. The twin bilayer is the distance of the two twin variants, shown for the polished sample. (d) The fine twin microstructure as viewed from the top.**

Figure 6-8b is the microstructure for the micropeened element having a dense

twin microstructure, captured at $\alpha = 90°$. While the element had actuated, the mechanism

of actuation was unclear as it was masked within the dense twin microstructure. Figures

6-8c and 6-8d show a top view of the polished (c) and the micropeened (d) elements at α = 90° with coarse and dense twin microstructures. For the micropeened element, the double-layer width was 10 µm, measured after polishing down the surface to view the twins.

4.3.1 Microscopy of polished element

Figure 6-9 shows a sequence of micrographs for the polished element (a) and the element after micropeening (b). We highlighted the position of the twin boundaries which appear steep, but are in reality 45° but scaled 10X in the vertical direction. At α = 18°, the c axis was horizontal throughout the element. At 54°, an approximately 1.0 mm thick twin had nucleated and grown. This thick twin created an inclined facet on the top surface, which forms the left slope of the depression. The right slope of the depression had a few thin twins separating regions of parent variant. At α = 90°, the twin had thickened to ~1.5 mm and moved to the right along the element. At 136°, the depression was composed of thick twins and numerous thin twins. At 180°, the depression contained only thin twins and was more symmetrical. Further rotation of the magnetic field removed all twins. The motion repeated nearly identically when actuated by the S. pole. We direct the reader to Supp. Figure 6-3 for the full sequence.
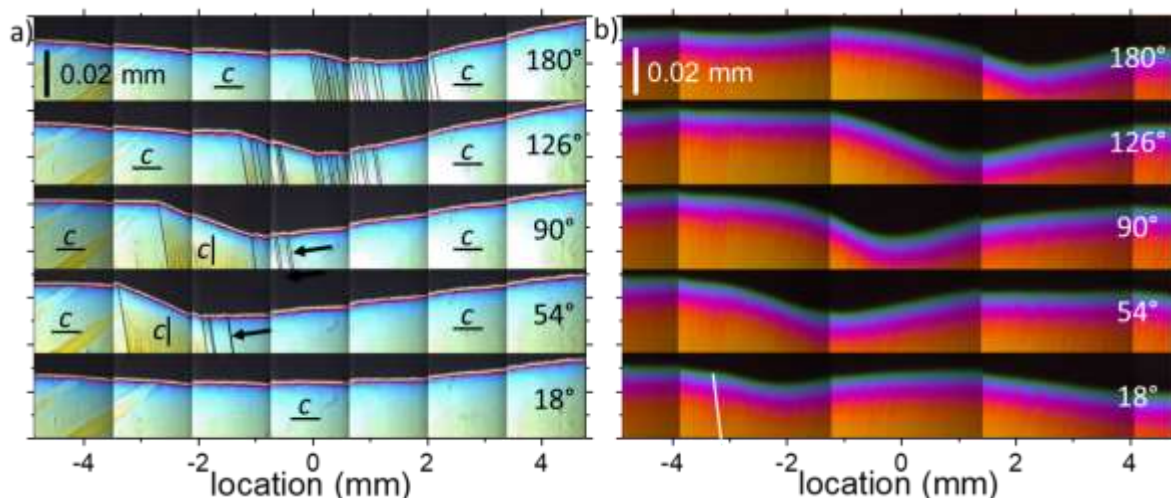
Figure 6-9: A sequence of micrographs taken for the polished sample as the magnetic field rotated clockwise. The micrographs were stretched 10X in the vertical direction, making the twin boundary appear much steeper than the 45° in reality. Reading from bottom to top: At 18°, the region is a nearly single variant of the parent matrix. At 54° the twin nucleated and expanded, creating the left slope of shrinkage. At 90° the twin slightly thickened and moved along the element. At 136°, the primary twin broke apart into thinner twins and moved along the element. At 180°, the primary twin further thinned into multiple finer twins and moved along the element. The arrows point to leading twins which create the right slope of shrinkage. (b) the sequence for the micropeened sample. The twin lamellar is oriented along the white line in the bottom micrograph.

In Figure 6-9b, the micropeened element has a smoother deformation which continues further along the element. The deformation follows that given by the laser scans, a shrinkage which resembles a smoothened form of the polished sample shrinkage. Suppl. Figures 6-4 and 6-5 show snapshots of the moving surface undulation in the micropeened sample.

<u>4.3.2 Microscopy of micropeened element.</u>

To determine the deformation mechanism of the fine twin microstructure, we plotted a contrast profile viewing the side at the center of the element as the depression moved past. Figure 6-10 shows micrographs taken at $\alpha = 90°$, $108°$, and $126°$ and the white line which the contrast was plotted along. In the contrast profile, the maximum thickness of the darker twin variant occurred at $\alpha = 90°$. Here the thickness of the dark

variants averaged 5 μm measured at full-width half max (FWHM). At $\alpha = 108°$, the dark

variants decreased to a thickness of 3 μm FWHM, then disappeared at $\alpha = 126°$. After

rotating the magnet back and forth many times, we determined that the twin

microstructure orientation did not change with rotation direction. The orientation was

locked by the initial training procedure in the electromagnet.
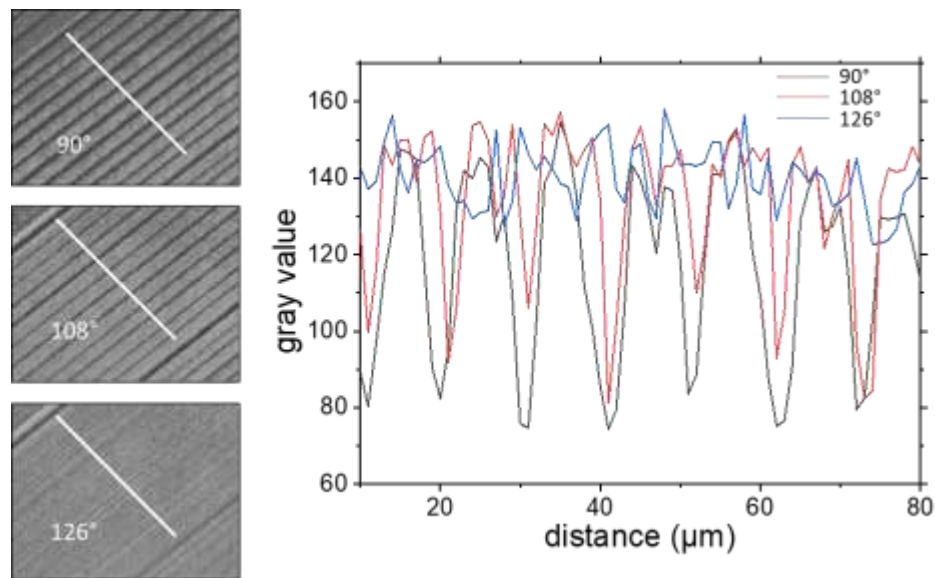
Figure 6-10:   For the sample micropeened, we used an image analysis software to analyze the bellows mechanism of the twin microstructure. The contrast of the twin variant was maximum at $\alpha = 90°$. With the rotation of the field, the dark twin variant gradually thins and disappears after 126°.

4.4 Simulation results

Figure 6-11 shows a simulation of the magnetic field for the polished and

micropeened element with a thick twin (twin lamellar) on the left (a) and the right (b) of

the element centroid, at positions and a magnetic field similar to that that found

experimentally. The black bars indicate the orientation of the c axis in the model. We did

not model the material's dimensional change, as it was small compared to the bulk

dimension. At $\alpha = 54°$, magnetic field lines entered the twin vertically and were mirrored

across the right twin boundary. No flux lines exited across the left boundary of the twin

or through the twin into the air above. The right half of the twin had high flux density

(800 mT) while the top left corner had much lower flux density (100 mT). Moving the

left twin boundary 1 mm farther left in the model (not shown) only slightly increased flux

in the twin, the flux still concentrating at the right twin boundary. In Figure 6-11c at $\alpha =$

126°, the twin centroid was 1.4 mm right of the element center. Here less flux entered the

twin, and the entering field diverged across both boundaries. To exit the left twin

boundary, the field circled back to mirror across the twin boundary into the parent

variant.
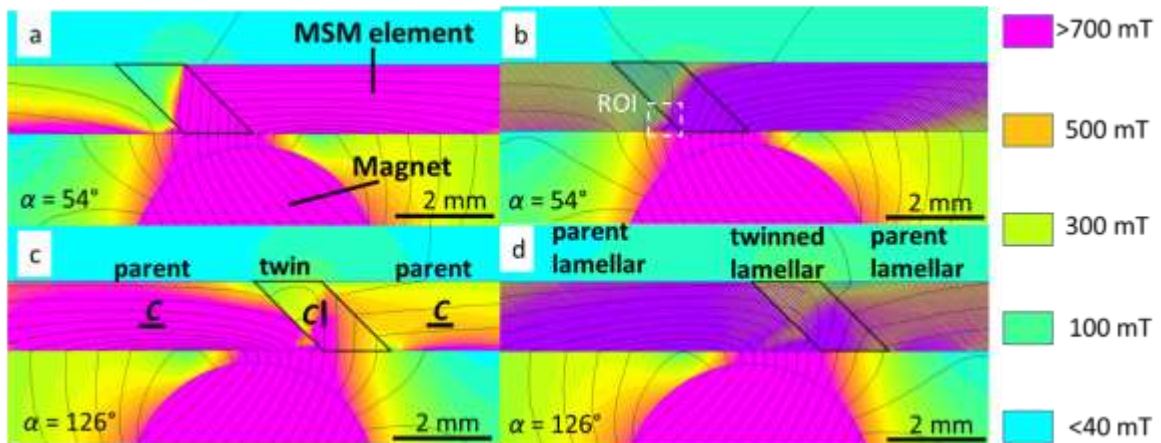
**Figure 6-11:   FEMM Simulation of the magnetic circuit for the polished sample.
We modeled a 1.4 mm thick twin. The c – axis indicated the orientation of the easy
axis of magnetization for the twin and parent matrix. At $\alpha = 54°$ the twin is to the
left of the center of the magnet. In (a) the field enters vertically and is reflected
across the right twin boundary. (b) The twinned lamellar enters less vertically and is
less reflected. The interface is smoother. The white dashed box shows the ROI in
Figure 12. At $\alpha = 126°$, the twin is to the right of the center of the magnet. In (c), the
twin polished sample diverged magnetic flux across both twin boundaries and
magnetized weakly. In (d) the twinned lamellar had some divergence but
magnetized more strongly.**

Figure 6-11b shows a simulation at $\alpha = 54°$ of the micropeened sample. Twin

domains deflected flux lines to maintain symmetry across the right twin boundary and

horizontal in the parent variant. At interfaces between the twinned lamellar and parent

lamellar, the field lines experienced a more abrupt mirroring, similar to the coarse twin

boundary of Figure 6-11a. Figure 6-12 shows a magnified view of the inset marked with

a dashed box in Figure 6-11b. In the parent lamellar variants, twins with vertical c

magnetized, but the flux tapered off up along the twin. The twinned lamellar had slightly

higher overall flux density than the parent variant.
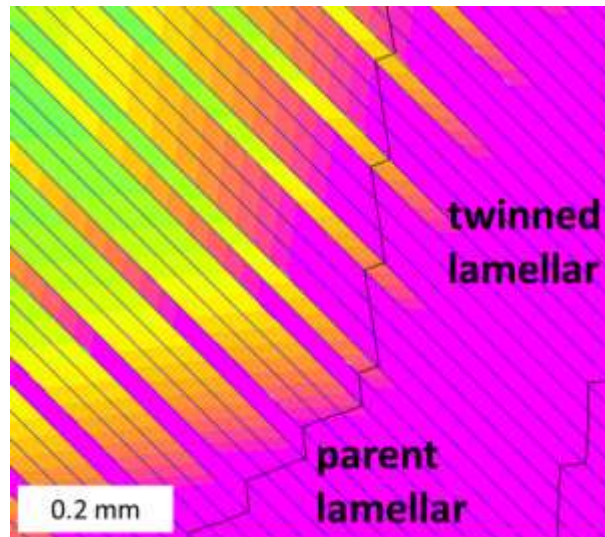
Figure 6-12:   Simulated flux schematic for the ROI defined in Figure 6-11 of the micropeened twin microstructure. The parent lamellar was modeled as a repetition of three horizontal c plates and one vertical c plate. The twinned lamellar was modeled as a pattern of three vertical c plates and one horizontal c plate. The field lines were deflected slightly by the plates within the microstructure, and defected largely at the interface between parent and twinned lamellar.

5. Discussion and conclusions

We discuss the mechanical response of the polished and micropeened MSM

elements in the context of the laser measurements, micrographs, and existing literature.

The constraints between the optical and the laser measurements differ by the clamping

mechanics. MSM alloys respond sensitively to constraints such as fixtures [23]. The

constraints cause the differences in the geometry of the undulation. In the laser

measurements, the element was clamped down, while for micrographs it was

unconstrained from the top. This difference was not expected to cause such a large impact upon the mechanical behavior, and so was not accounted for in the design of the study. The impact of the top constraint is significant and should be addressed in future studies.

5.1 Polished sample actuation

Figure 6-13 is a schematic of the twin-microstructure for the polished sample. The constant slope (1) in Figure 6-6A is the slope between the primary twin and the parent surface. The twin forms the facet. An upward slope preceding the left twin boundary (2) in Figure 6-6A might be explained partly by the element surface being forced away from the stage as the twin thickens, kinking up and away from the bottom. The transition (3) in Figure 6- 6A on the right slope from steep near the center to shallower slope on the right suggests thin twins that kink the surface. These twins are highlighted in Figure 6-9. These twins kink the surface back.
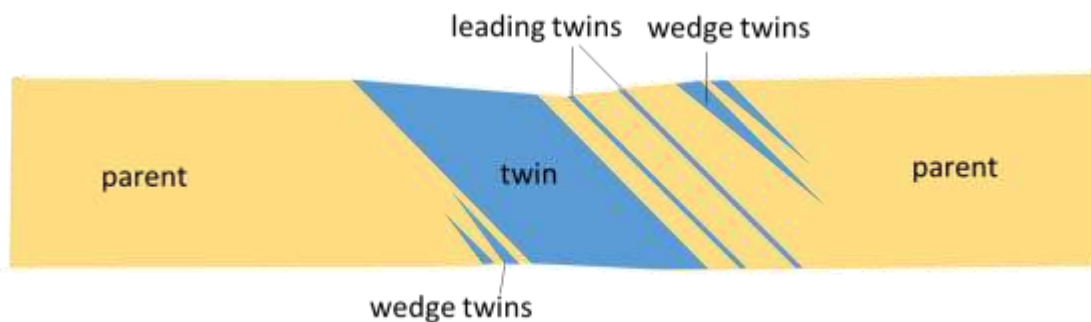
Figure 6-13:   Interpretation of twin structures found in the actuation of the polished sample. Wedge twins adjacent to the primary twin's left boundary formed to reduce interface surface stresses near the bottom. Leading twins recover the shrinkage back to the parent twin. Wedge twins interface between the actuated region and parent on the top, while also pinning the shoulders of right shrinkage slope.

The shoulder (4) is at a fixed position from $\alpha = 36°$ to $\alpha = 108°$. This shoulder is likely formed by an obstacle that traps twin boundaries. In the micrographs, we find a

100 μm thick twin at a location close to that of the shoulder, and also several wedge-like twins. The wedge tapering is fine, similar to that presented in Ref. [7]. The taper angle is exaggerated in Figure 6-13. Wedge-like twins create curvature, as found in connecting the left parent bottom with the primary twin (Figure 6-13). Wedge twins act as obstacles and reduce the mobility of twin boundaries [14, 15]. The micrographs of the polished element show no definitive shoulder, which is perhaps caused by the constraints of clamping the sample.

5.2 Micropeened sample actuation

The micropeened sample has a fine twin microstructure with twins thinner than those in the polished sample. Surface defects pin the twin boundaries [14, 16, 24] such that the twin boundaries cannot move over large distances. The cyclic magnetic field causes a periodic back and forth motion of the twin boundaries. As a result, twins widen and shrink with a phase shift, locally similar to the motion of a bellow. Figure 6-10 shows how the twins gradually expand and contract. This expansion and contraction of fine twins has also been described by Straka *et al.* [25].
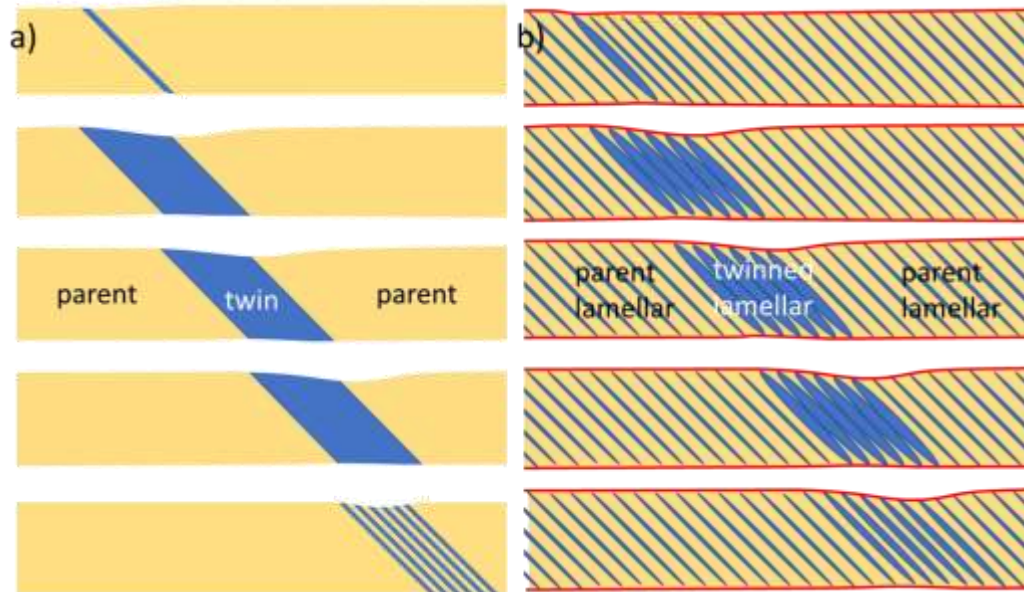
Figure 6-14: Translational movement of the twinned region in the sample for the different surface treatments. The parent variant is orange and the twin variant is blue. Red lines mark the stressed surface layer of the micropeened element. (a) The polished element had a single twin variant that nucleates and thickens, then moves along the element, then broke apart. (b) The micropeened element had a twinned lamellar which nucleated, moved down the element, then transformed into parent lamellar.

As the twin boundaries move back and forth, they slightly bend as shown in the Supp. Figure 6-6. This bending stems from the elastic interaction of twinning dislocations (disconnections) typical for materials with a high degree of defects such as present in micropeened elements [26].

The very fine twin microstructure of the micropeened element results in a smoother, more symmetrical depression than that of the polished element. A major difference in the deformation mode is the formation of a large hump in the center of the element with the micropeened surface. The hump is not due to the kinking for the polished sample, as the bottom surface of the micropeened element shows only a slight depression of ~2 μm (shown in Supp. Figure 6-4).

We speculate that the hump forms as an elastic response to the strain at the element surface. The damaged surface layer of the micropeened hardens the surface against strain. The magnetic field is sufficiently strong to move twin boundaries in the center of the element, but not at the surface. The material strains against this surface and deforms the surface layer elastically. Upon polishing, we find something resembling a fine type II twin structure [27] in the element center (shown in Supp. Figure 6-7).

5.3 Model of twin boundary motion in polished and micropeened samples.

Comparison of the micrographs, surface profiles, and the central variation yields a model of the twin architecture and the twinning mechanism of the formation and migration of the depression (Figure 6-14). For the polished sample, a twin nucleates then thickens by the motion of the right twin boundary. The twin domain then migrates to the right by the simultaneous motion of both twin boundaries. Eventually the leading (i.e. right) twin boundary stops where the magnetic field is insufficient for activating its motion. The trailing twin boundary reaches the leading twin boundary and the two combine, which causes the twin to collapse and the depression to disappear. This mechanism was reported in 2012 [28].

The micropeened MSM element has a finely twinned microstructure as shown in Figure 6-14b. The twins with c perpendicular to the long axis of the MSM element (blue in Figure 6-14) are thin and make up a small volume fraction of the MSM element. Thus, the MSM element is short and wide. When a magnetic pole points to a particular area, the blue twins in that area expand. Consequently, the fraction of blue twins is large in that area and this area becomes thin and long, thus it forms a depression. When the magnetic pole moves away from that particular area, the twin boundaries retract, the blue twins

become thin, and the MSM element widens. As the magnetic pole moves along the MSM element, the blue twins first thicken and then thin and the area with thick blue twins propagates along the MSM element. The propagation of the package of thick twins resembles the motion of a wave package, albeit it is a quasi-static motion, entirely controlled by the position of the magnetic pole.

Since the twins are pinned at the surface for the micropeened MSM element, some orange area remains present at any given time. Thus, the output strain is slightly less for the micropeened sample compared to the polished sample, which turns fully blue in the depression area. This reduced depression results in a slightly shallower depression for the micropeened MSM element as shown with the dashed lines in Figure 6-6 highlighting the maximum slopes for each case. The actuation is less because the magnetostress is insufficient to cause complete twin boundary motion. Higher magnetostress would cause the twin matrix to strain further and become more similar to the strain seen for the coarse twin.

The transition marked as (5) in Figure 6-7 is the transition between the thickening of the twin and the translational motion of the twin. We determined this by comparing Figures 6-6, 6-7, and 6-9. The elevation variation in the center of the micropeened MSM element was strikingly similar to that of the polished MSM element, suggesting the mechanism must be very similar. In Figure 6-14(b) we show a diagram of a packet of thin twins moving along the parent lamellar. The slight difference in the position of the transition (5) points to differences in the thin twin packet thickness. The clockwise twin packet was wide, similar to that for the thick twin packet. The counterclockwise twin packet was thinner. This provides the basis of the difference between the actuation

envelopes of the clockwise and counterclockwise rotation directions. The clockwise rotation has a wide twin packet, resulting in large actuation, while the counterclockwise rotation has a thinner twin packet and deforms less.

5.4 Magnetic interaction with the twin structures.

Magnetic flux creates the magnetostress, which causes twin boundary motion. The driving magnetic field is created by the same mechanism: the rotating diametrically magnetized permanent magnet. The flux pattern, however, depends upon the interaction of the magnetic field with the twin microstructure due to the high magnetic anisotropy between the two variants. We modeled the difference between the flux pattern for the coarse twin microstructure and the fine twin microstructure.

We find the flux pattern is similar for both twin microstructures. Twin boundaries within the element refract the magnetic field as lenses according to their volume fraction of each variant [29]. Thus, a fine twin packet which is near full strain (fully blue according to Figure 6-14), reflects flux approximately similar to a thick twin packet, as seen by comparing Figures 6-11a and 6-11c. The flux pattern is smoother, as the fine twin packet is not fully transformed to the blue variant, Figure 6-14b.

The induced magnetic field pattern strongly depends on the orientation of the magnetic field relative to the twin boundaries. The highest flux condition occurs when the flux can enter the parent variant vertically, then be directed orthogonally by the twin boundary. The lowest flux conditions occur when the magnetic field angle is parallel or orthogonal to the twin boundaries.

5.5 Application of localized actuation to an MSM device: the MSM micropump

The MSM micropump is a simple extension of this actuation mechanism. We put a plate on top of the MSM element, with inlet and outlet holes centered at ±3 mm from the element center. Rotation of the permanent magnet causes a depression to form under the inlet, then translation of the depression to the outlet, then the dissolution of the depression under the outlet, transferring the fluid. As shown by Chmielus *et al.* [14], coarse twins are stochastic, snapping from one stable position to the next, which causes the material to flow in serrated fashion. The rapid, stochastic snapping of the material causes in micropumps unstable fluid flow, resulting in serrations to the output flow rate, seen for example in Barker *et al.* and Saren *et al.* [5, 19].

A smooth, controlled shrinkage is advantageous to the performance of the MSM pump. Smooth, controlled actuation gives flow stability and repeatability. Repeatable behavior allows for better sealing. The addition of the hump in Figure 6-6b, 6-6c, improves the seal against the top plate, resulting in a higher head pressure. The oriented dense-twin microstructure gives good fatigue life for the pump element.

The flowrate reported for the MSM micropump has a strong resemblance to the central elevation variation of the MSM element. In Figure 6-15, we report the flowrate results of a previous study [30] for a similarly sized MSM micropump made from a micropeened element. The flowrate has nearly identical features to the temporal elevation variation, to include even the shoulder marked by the arrow. At the element center, the MSM element experiences the maximum depression depth (Figure 6-6(b), 6-6(c)). The results indicate that this depth determines the MSM pump flowrate.
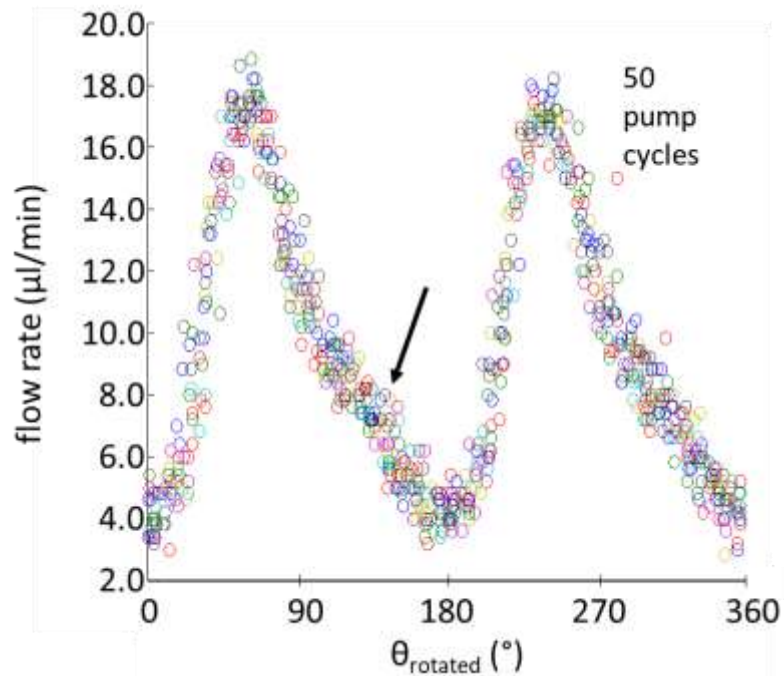
Figure 6-15: Fifty MSM micropump cycles were superimposed, detailed, and adapted with permission from [29]. $\theta_{rotated}$ refers to elapsed angle, and is a temporal unit not based upon field orientation, unlike α in this study, which is a spatial coordinate of magnet field angle. Used as a micropump, the flowrate shows a similar modulation to that of the central elevation variation of the element in Figure 6-7. The black arrow shows a transition point also marked in Figure 6-7 as (5). We interpret the point as being the transition between twinned lamellar thickening and twinned lamellar motion down the element.

The hump between the newly forming and old disappearing depressions occurring in the micropeened sample has ramifications to the MSM micropump performance. Whereas a shrinkage acts as a "negative displacement" mechanism and draws fluid in by creating a vacuum, the hump acts more akin to the traditional peristaltic motion of larger pumps which drives the fluid forward. Knowing the geometry of the shrinkage in each "step" of a cycle is important to understanding the behavior seen in MSM micropumps. The asymmetry of the surface profiles clearly explains the asymmetry seen between forward and reverse flow found in MSM micropumps [18, 19].

6. Summary and Conclusion:

We compared profilometries and optical experiments to analyze MSM elements actuated in the manner of an MSM micropump. We studied the effects of two different surface treatments on a single MSM element: polished and micropeened. The polished element had a sharp-featured, faceted shrinkage shape. The micropeened element had a smooth shrinkage shape, forming an additional hump at the shoulders of the shrinkage. Both microstructures had the same macroscopic motion: a twin packet that nucleates and moves along the element. The motion mechanism differed on the microscale. The packet is a single twin in the case of the polished sample and is a twinned lamellar in the case of the micropeened element. The twinned lamellar approximates the single thick twin while allowing additional bending. The dense twin microstructure smoothed the magnetic flux. The micropeened element deformed differently than the polished sample, exhibiting a slight hump. Knowledge of these surface undulations, which give the actuator behavior, is a prerequisite to building high pressure, high repeatability MSM micropumps.

References

[1] T. Hemsel, J. Wallaschek, Survey of the present state of the art of piezoelectric linear motors, Ultrasonics 38(1-8) (2000) 37-40.

[2] Y. Ting, L.C. Chen, C.C. Li, J.L. Huang, Traveling-wave piezoelectric linear motor part I: The stator design, Ieee Transactions on Ultrasonics Ferroelectrics and Frequency Control 54(4) (2007) 847-853.

[3] K. Ullakko, J.K. Huang, C. Kantner, R.C. Ohandley, V.V. Kokorin, Large magnetic-field-induced strains in Ni2MnGa single crystals, Applied Physics Letters 69(13) (1996) 1966-1968.

[4] K. Ullakko, L. Wendell, A. Smith, P. Müllner, G. Hampikian, A magnetic shape memory micropump: contact-free, and compatible with PCR and human DNA profiling, Smart Materials and Structures 21(11) (2012) 115020.

[5] S. Barker, E. Rhoads, P. Lindquist, M. Vreugdenhil, P. Mullner, Magnetic Shape Memory Micropump for Submicroliter Intracranial Drug Delivery in Rats, Journal of Medical Devices-Transactions of the Asme 10(4) (2016).

[6] N.J. Kucza, C.L. Patrick, D.C. Dunand, P. Müllner, Magnetic-field-induced bending and straining of Ni–Mn–Ga single crystal beams with high aspect ratios, Acta Materialia 95 (2015) 284-290.

[7] R. Chulist, L. Straka, H. Seiner, A. Sozinov, N. Schell, T. Tokarski, Branching of {110) twin boundaries in five-layered Ni-Mn-Ga bent single crystals, Materials & Design 171 (2019).

[8] A. Smith, J. Tellinen, P. Mullner, K. Ullakko, Controlling twin variant configuration in a constrained Ni-Mn-Ga sample using local magnetic fields, Scripta Materialia 77 (2014) 68-70.

[9] K. Ullakko, Magnetically controlled shape memory alloys: A new class of actuator materials, Journal of Materials Engineering and Performance 5(3) (1996) 405-409.

[10] E. Pagounis, R. Chulist, M. Szczerba, M. Laufenberg, High-temperature magnetic shape memory actuation in a Ni–Mn–Ga single crystal, Scripta Materialia 83 (2014) 29-32.

[11] L. Straka, O. Heczko, Magnetic anisotropy in Ni–Mn–Ga martensites, Journal of Applied Physics 93(10) (2003) 8636-8638.

[12] L. Straka, A. Soroka, H. Seiner, H. Hanninen, A. Sozinov, Temperature dependence of twinning stress of Type I and Type II twins in 10M modulated Ni-Mn-Ga martensite, Scripta Materialia 67(1) (2012) 25-28.

[13] H. Zhang, A. Armstrong, P. Mullner, Effects of surface modifications on the fatigue life of unconstrained Ni-Mn-Ga single crystals in a rotating magnetic field, Acta Materialia 155 (2018) 175-186.

[14] M. Chmielus, C. Witherspoon, K. Ullakko, P. Mullner, R. Schneider, Effects of surface damage on twinning stress and the stability of twin microstructures of magnetic shape memory alloys, Acta Materialia 59(8) (2011) 2948-2956.

[15] M. Chmielus, K. Rolfs, R. Wimpory, W. Reimers, P. Mullner, R. Schneider, Effects of surface roughness and training on the twinning stress of Ni-Mn-Ga single crystals, Acta Materialia 58(11) (2010) 3952-3962.

[16] K. Ullakko, M. Chmielus, P. Mullnr, Stabilizing a fine twin structure in Ni-Mn-Ga samples by coatings and ion implantation, Scripta Materialia 94 (2015) 40-43.

[17] L. Straka, H. Hänninen, A. Soroka, Y. Ezer, Enhanced Fatigue Behavior of Ni-Mn-Ga Magnetic Shape Memory Alloys with Tailor-made Fine Twin microstructure, 13th International Conference on New Actuators, Bremen, Germany, 2012.

[18] A.R. Smith, A. Saren, J. Jarvinen, K. Ullakko, Characterization of a high-resolution solid-state micropump that can be integrated into microfluidic systems, Microfluidics and Nanofluidics 18(5-6) (2015) 1255-1263.

[19] A. Saren, A.R. Smith, K. Ullakko, Integratable magnetic shape memory micropump for high-pressure, precision microfluidic applications, Microfluidics and Nanofluidics 22(4) (2018).

[20] D. Kellis, A. Smith, K. Ullakko, P. Mullner, Oriented single crystals of Ni-Mn-Ga with very low switching field, Journal of Crystal Growth 359 (2012) 64-68.

[21] D. Musiienko, e. al., Universality of temperature dependence of twinning stress in Ni-Mn-Ga 10M martensite and effect of crystal quality, Acta Materialia, submitted, 2020, pp. 235-238.

[22] I. Suorsa, E. Pagounis, K. Ullakko, Position dependent inductance based on magnetic shape memory materials, Sensors and Actuators a-Physical 121(1) (2005) 136-141.

[23] M. Chmielus, I. Glavatskyy, J.U. Hoffmann, V.A. Chernenko, R. Schneider, P. Mullner, Influence of constraints and twinning stress on magnetic field-induced strain of magnetic shape-memory alloys, Scripta Materialia 64(9) (2011) 888-891.

[24] M. Chmielus, P. Müllner, Effects of Surface Pinning, Locking and Adaption of Twins on the Performance of Magnetic Shape-Memory Alloys, Trans Tech Publ, pp. 177-201.

[25] L. Straka, N. Lanska, K. Ullakko, A. Sozinov, Twin microstructure dependent mechanical response in Ni-Mn-Ga single crystals, Applied Physics Letters 96(13) (2010).

[26] P. Müllner, G. Kostorz, Microstructure of Magnetic Shape-Memory Alloys: Between Magnetoelasticity and Magnetoplasticity, Materials Science Forum 583 (2008) 43-65.

[27] O. Heczko, L. Straka, H. Seiner, Different microstructures of mobile twin boundaries in 10 M modulated Ni-Mn-Ga martensite, Acta Materialia 61(2) (2013) 622-631.

[28]   Boise State University, https://www.boisestate.edu/coen-mml/research/. 2020).

[29]   T. Schiepp, *A Simulation Method for Design and Development of Magnetic Shape Memory Actuators*, University of Gloucestershire, 2015.

[30]   *A. Armstrong* , B. Johnston, P. Lindquist, A. Smith, P. Müllner, Analysis of individual cycle deformation in Ni-Mn-Ga micropumps, Proceedings of the international conference ACTUATOR'18, Bremen, Germany, 2018, pp. 235-238.

CHAPTER SEVEN: A MOTIONLESS ACTUATION SYSTEM FOR MAGNETIC

SHAPE MEMORY DEVICES

Andrew Armstrong[1],

Kevin Finn[1,2],

Anthony Hobza[1],

Paul Lindquist[1],

Nader Rafla[2],

Peter Müllner[1]

[1]Micron School of Materials Science and Engineering, Boise State University, Boise, ID,

USA

[2]Department of Electrical and Computer Engineering, Boise State University, Boise, ID,

USA

Abstract

Ni-Mn-Ga is a Magnetic Shape Memory (MSM) alloy that changes shape in response to a variable magnetic field. We can intentionally manipulate the shape of the material to function as an actuator, and the material can thus replace complicated small electromechanical systems. In previous work, a very simple and precise solid-state micropump was developed, but a mechanical rotation was required to translate the position of the magnetic field. This mechanical rotation defeats the purpose of the motionless solid-state device. Here we present a solid-state electromagnetic driver to linearly progress the position of the applied magnetic field and the associated shrinkage. The generated magnetic field was focused at either of two pole pieces, providing a mechanism for moving the localized shrinkage in the MSM element. We confirmed that our driver has sufficient strength to actuate the MSM element using optical microscopy. We validated the whole design by comparing results obtained with finite element analysis with the experimentally measured flux density. This drive system serves as a possible replacement to the mechanical rotation of the magnetic field by using a multi-pole electromagnet that sweeps the magnetic field across the MSM micropump element, solid-state switching the current to each pole piece in the multi-pole electromagnet.

1. Introduction

In microfluidics and drug infusion, Magnetic Shape Memory (MSM) micropumps [1] are a new type of peristaltic pump that show pressure performance up to 150 kPa, a pumped volume of 110 nL per pulse and a repeatability of 1% [2]. They are actuated by sweeping a magnetic field along the MSM element, causing the MSM element to shape change near the position of maximum magnetic field to form a minute pocket in the

element that captures a small quantity of fluid and transfers it from inlet to outlet as the magnetic field is swept across [3,4]. This is similar to how positive displacement pumps work or how mammals swallow.

The first MSM micropump for use in Polymerase Chain Reaction (PCR) analysis was reported by Ullakko *et al*. [1]. Research continued and another MSM micropump of similar design was built and characterized by Smith *et al.* [2]. This pump delivered high pressure with high volumetric precision in a compact size. Recently, Barker *et al*. [5] researched pumping teterodotoxin and ketamine via in-vivo infusions to intracranial regions of Lister hooded rats with an MSM micropump at a rate of 0.33 µl/min. With Barker's pump, the MSM element itself measured only about 1 mm x 2 mm x 10 mm, but the entire pump measured more than 50 mm along its longest dimension. The electromotor and permanent magnet required to drive the magnetic field through the MSM element actually determine the device size.

In this work, a Solid-State Drive System (SSDS) comprising a ferromagnetic yoke, a series of conductive coils, and a current-control circuit was constructed and coupled to an MSM element. This actuation system offers the potential advantages of a motionless driver, minimization of stray magnetic fields, significant device miniaturization, and, because a micromotor is no longer needed, substantial reductions in manufacturing costs. In this embodiment, the design and shape of the supporting yoke or housing determine the shape and size of the device instead of the motor and permanent magnet.

This study evaluates the feasibility of a solid-state micropump driver that creates the pumping action with carefully designed electromagnets and multiple pole pieces,

controlled by electronic switching circuits as opposed to rotating motors. The idea of a rotating magnetic field was proposed previously [1], and localized electromagnetic actuation of MSM materials has been researched [6, 7], but a method of driving these fields with electromagnets and multiple pole pieces needs further study.

2. Materials and Methods

2.1 Working principles

An MSM micropump presented in [1, 2, 5] is operated by rotating a small diametrically polarized permanent magnet perpendicular to the surface of an MSM element. When the magnetic flux exceeds the twinning stress, a small pocket (shrinkage) in the pump element forms. The region of shrinkage sweeps along the element with the magnetic flux lines as the magnet rotates. Figure 7-1 shows a Finite Element Method Magnetics (FEMM 4.2) simulation of the magnetic flux lines in an MSM element with a shrinkage. The formation of the shrinkage is caused by magnetic-field-induced crystallographic twinning [4] and is described by Ullakko [1].

In the magnetic simulation, a diametrically magnetized neodymium iron boron magnet generates flux lines perpendicular to the element face in a shrinkage region and parallel flux lines in the remainder of the MSM element. "Perpendicular" and "parallel" describe the approximate direction with respect to the long edge of the MSM element. This simulation depicts the magnetic field creating the shrinkage. When actuated by rotating the magnet clockwise, the magnetic field sweeps clockwise, and the shrinkage moves with the flux lines from left to right. This phenomenon has been used to capture a precise volume of liquid at a pump inlet and transport the liquid to a pump outlet [1].
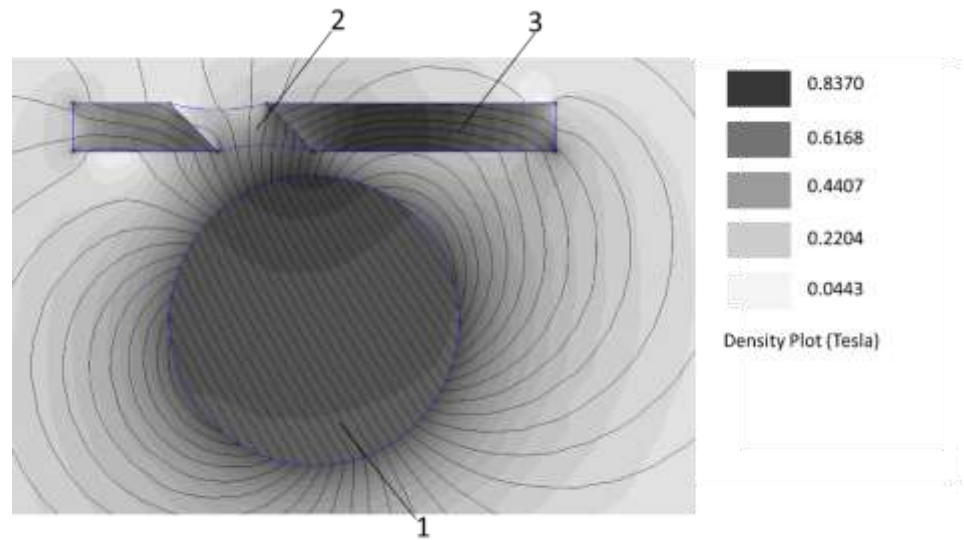
Figure 7-1: Cross-sectional view of magnetic flux present in permanent-magnet-actuated micropumps. The flux lines were calculated with FEMM software. As flux lines from the permanent magnet (1) permeate the MSM element (3), the easy axis of magnetization of the MSM material aligns with the flux lines. This causes a shrinkage (2) in the MSM element where the flux lines are predominantly perpendicular to the length of the element. For clarity, the shrinkage region is shown as a single crystallographic twin, a simplification of the densely twinned state of the shrinkage [2].

A localized shrinkage can also be generated by the magnetic field of a small electromagnet [7]. Here, we demonstrate an assembly of solenoids, iron yoke, and pole pieces which create shrinkages at different positions in the MSM element. The drive is an example of a magnetic circuit, which is analogous to an electric circuit: coils induce magnetic flux; ferromagnetic materials such as iron and nickel manganese gallium (Ni-Mn-Ga) act as magnetic flux conductors; air gaps and other sections with low magnetic permeability act as reluctance gaps and, thus, as magnetic resistors, which resist magnetization and decrease the total magnitude of magnetic flux.

Figure 7-2 illustrates the functional components of this type of drive. A series of electrically conductive coils (1) generate magnetic flux within a ferromagnetic core (2). Magnetic flux concentrates axially within a pole piece (3) and across the working gap,

and normal to an MSM element (4); the concentrated flux induces crystallographic twinning which causes a localized shrinkage. The flux path continues horizontally along the MSM element back to the ferromagnetic yoke (5) and returns into the ferromagnetic core.
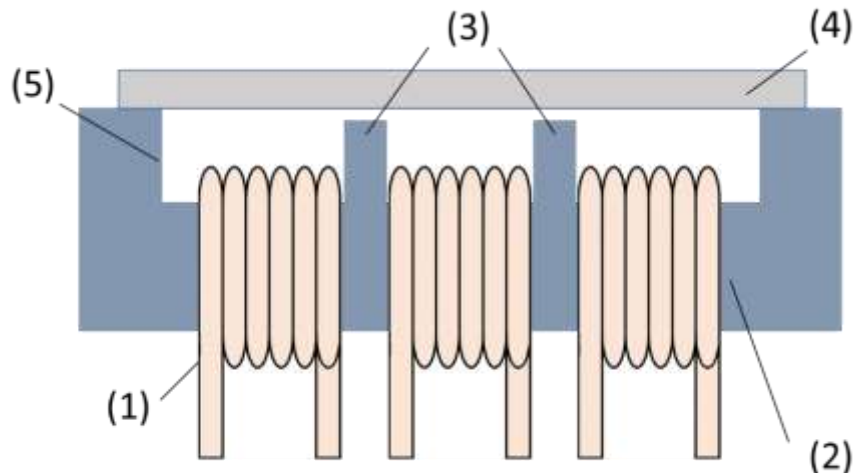
Figure 7-2: **Components of the drive design consisting of a number of electrical coils (1) wrapped around a ferromagnetic core (2) with ferromagnetic pole pieces (3) separating the coils.**

This is analogous to Kirchhoff's current law for electric circuits: just as the sum of electric currents into a node must be zero, the sum of fluxes into a magnetic circuit node must also be zero. By orienting magnetic field sources (the coils) such that they produce flux in opposing directions, their field lines compress at the pole pieces and the flux can be controlled and amplified, as shown in Figure 7-3.

If two adjacent coils are energized with opposing current, the pole between these coils is active and the other pole is passive since the reluctance of the ferromagnetic core is less than that of the air gap above the passive pole. Activating the left and center coils with opposite polarity generates a magnetic flux that concentrates predominantly in the left pole. Activating the center and right coils with opposite polarity generates a flux

which concentrates primarily in the right pole. Figure 7-3 shows schematically the

shrinkage formed in MSM material in response to the activation of the left pole (3a) and

that in response to the activation of the right pole (3b).
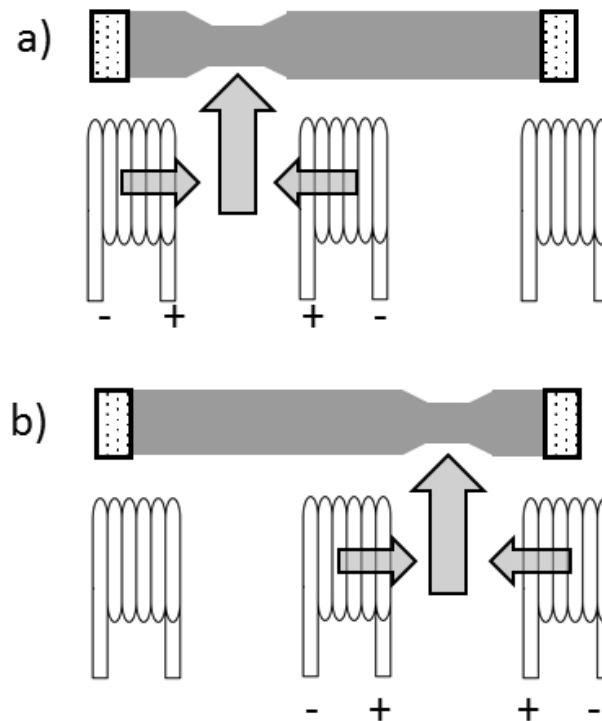
Figure 7-3:   Graphic representation of the MSM element response to the magnetic fields of the SSDS. a) Direct current pulses simultaneously in opposition through the left and center electromagnets, causing a shrinkage above the left pole piece. b) The center coil's polarity is reversed, the left coil turns off, and the right coil is energized. A shrinkage is now formed above the right pole piece.

2.2 Device construction

The device presented in Figure 7-4a was machined from magnetically soft iron

rod (Ward's Science). Each coil consisted of 80 turns of 30 AWG (0.254 mm bare

conductor diameter) heavy-insulation copper magnet wire (1), which were wound around

a ferromagnetic core (2). Pole pieces (3) protruded from between the coils and served to

direct magnetic flux across the air gap, which was adjusted to 3mm thickness to

accommodate a hall probe. The device had slotted legs (5) for adjustment of the air gap

distance between poles (3) and yoke (4). Stainless steel machine bolts (6) affixed the

elements together.
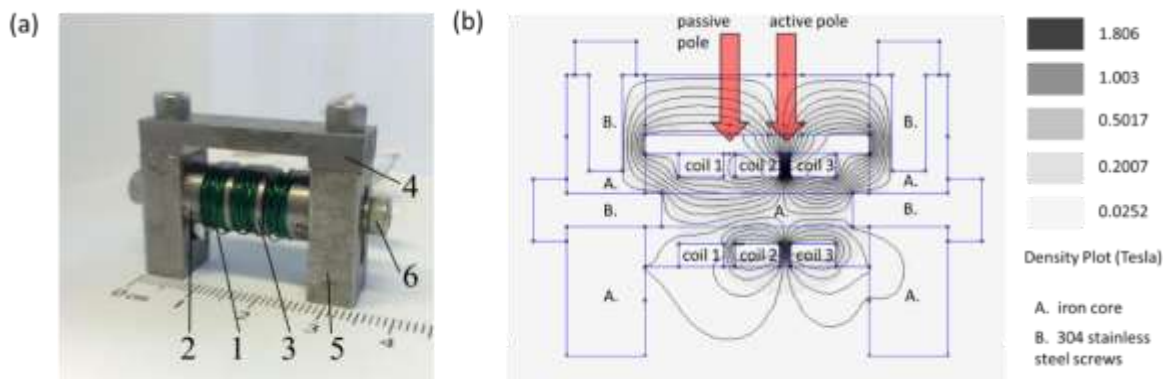
Figure 7-4:   **a) Photograph of the constructed actuator (the scale numbers indicate centimeters). It consists of five components: (1) copper conductive coils, (2) ferromagnetic core piece, (3) ferromagnetic pole pieces, (4) an upper ferromagnetic yoke, (5) ferromagnetic legs slotted for adjustment, and (6) attachment hardware; b) FEMM simulation of constructed SSDS with the right pole active, energized with 10 A through coil 2 and 3. The shading and spacing of flux lines indicates flux intensity: lines are spaced tightly in high magnetic flux regions and remotely for regions of low flux intensity. Dark regions correspond to areas of high flux density.**

Figure 7-4b shows results from a FEMM simulation of the SSDS's magnetic

performance. In this scenario, the right pole is engaged with 10 A, concentrating

magnetic flux across the working gap to the upper ferromagnetic element. The flux

density in the passive pole is significantly lower.

2.3 Finite element analysis

We used FEMM software in parallel with experimental testing to analyze the

ferromagnetic core and coil assembly. The software allowed modification of the current,

the number of turns per coil, the geometry of the assembly, and the choice of construction

materials. Figure 7-4b represented one 10 mm-thick slice of the device and included the

same primary features as the physical system: each leg piece measured 7 mm by 20 mm;

the core piece had a length of 20 mm, pole sections had a diameter of 10 mm, and the

reduced sections had a diameter of 6 mm; three 80-turn 30 AWG copper magnet wire

coils were wound around the core; two 9-mm-long, 3-mm-diameter 304 stainless steel

screws attached the leg pieces to the core. Above the coils and poles was either a 34-mm

pure iron yoke piece (held in place with the same stainless steel screws that attach the

legs to the core) or a 27-mm Ni-Mn-Ga element; a 1.55-mm air gap separated the pole

tops from the bottom surface of the iron or Ni-Mn-Ga piece. In the model, pure iron was

magnetically isotropic and had a maximum relative magnetic permeability of 14872

(FEA; FEMM 4.2). We used published values for the relative magnetic permeability of

Ni-Mn-Ga as 40 in its axis of easy magnetization and 2 in a direction perpendicular to the

axis of easy magnetization [8]. The complex twinning in the shrinkage region was not

modeled in detail. Rather, we assumed two twin boundaries with a single twin domain in

between. Such a twin microstructure creates a double kink [3,4]. Creating a smooth

shrinkage requires the coordinated formation of a large number of fine twins [1,2].

Further study of this can be found in Smith *et al.* [7] and Schiepp *et al.* [9]. FEMM

simulations were performed alongside physical experiments to deepen understanding of

the drive behavior and to predict the effects of modifying drive geometry, coil current,

number of turns per coil, and choice of construction materials.

2.4 Electrical characteristics

With a semiconductor switching circuit, controlled by a microcontroller (Arduino

Uno, Rev. 3), we manipulated the current and its polarity in the coils. Figure 7-5

illustrates the circuit schematic as modeled (LTspice XVII). Power was supplied by a

1500 W direct current power supply (Ametek Sorensen XG60-25). When thyristor A and

transistor A were on and thyristor B and transistor B were off, the left and center coils were energized, activating the left pole. When thyristor B and transistor B were on and thyristor A and transistor A were off, the right and center coils were energized activating the right pole. Table 7-1 gives the electrical characteristics of the three coils.
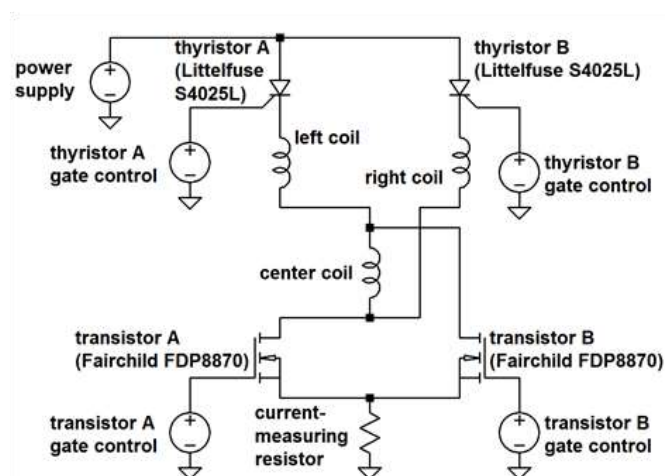
Figure 7-5: **Schematic of semiconductor switching circuit to control polarity of current through center coil.**

Table 7-1: **Electrical characteristics of coils.**

	Inductance (µH)	Resistance (Ω)
Left coil	293.9	1.517
Center coil	277.1	1.505
Right coil	286.7	1.441

2.5 Measurement methods

An air gap of 1.55 mm was introduced between the active pole and the upper yoke for insertion of a Hall probe (Lake Shore rigid transverse Hall probe) connected to a Gaussmeter with analog output (Lake Shore 450 Gaussmeter). The coil current was calculated using Ohm's law from the potential difference across a 50 W 0.1 Ω shunt

resistor, measured with an integrated oscilloscope (Digilent Analog Discovery 2). We connected the oscilloscope probe measuring the shunt resistor voltage to channel 1 of the oscilloscope, and the Gaussmeter's analog output to its channel 2. This allowed us to simultaneously view and record the values for the current and flux density.

2.6 MSM element production and processing

A $Ni_{51}Mn_{24.4}Ga_{24.6}$ single crystal was grown with a modified Bridgman furnace [10]. A 27.0 mm by 2.9 mm by 1.0 mm MSM element was cut from this crystal with faces parallel to $\{100\}_c$, electropolished in $-20°$ C 2:1 ethanol to 14M nitric acid solution at 12 V to remove surface stresses, polished to a 1 µm finish, and subjected to a uniform 0.8 T magnetic field parallel to the long axis of the element, placing it in a compressed state with the easy axis of magnetization parallel to the long dimension. The MSM element was too long for the sample chamber of our DMS Model 10 vibrating sample magnetometer, so to determine the magnetic switching field (magnetic field at which the material undergoes a shape-change response) of the MSM element, we measured the switching field of neighboring sections of the Ni-Mn-Ga single crystal from which the element was cut; these sections showed a switching field of 150 mT. The prepared MSM element was then coupled to the drive in place of the ferromagnetic yoke.

2.7 Coupling of MSM element to solid-state drive system

Figure 7-6 shows the MSM element coupled to the solid-state drive system. Adhesive tape (1) secured either one end or both ends of the MSM element (2) to the legs of the drive, depending upon the test being performed. Fixing a single end of the MSM element to the drive allowed linear expansion of the MSM element to accommodate a twinned region (shrinkage). Fixing both ends of the MSM element with adhesive tape

would keep the shrinkage in the MSM element and simply transfer its position. Various

spacers were placed between the MSM element and the pole pieces, the distances ranging

from 1.55 mm to 0 mm.
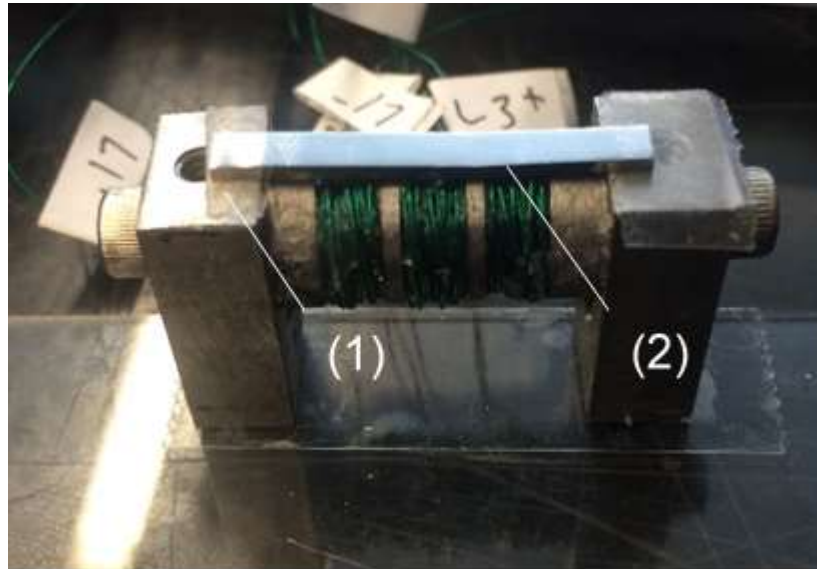
Figure 7-6:   Photograph of solid-state drive apparatus with mounted MSM element (2), which was attached to the left and right iron legs with adhesive tape (1).

2.8 Optical characterization of MSM actuation

We imaged the MSM element with a Leica DM6000 microscope equipped for

differential interference contrast at 5X magnification using the power mosaic function.

Before and after pulsing magnetic flux with the solid-state drive system, we captured

images of the entire MSM element. For selected experiments, we recorded the

appearance of shrinkages during pulse actuation with a high-speed video camera

(Edgertronic SC1) at 1849 frames per second, i.e. one frame per 541 µs.

3. Results and discussion

3.1 Pulse duration for maximum magnetic field

The magnetic pulse shape, strength, and duration were a function of the

inductance of the coils, the current supplied, the switching speed of the semiconductor

devices, and the rise time of the current source. A short magnetic pulse duration was

desired to minimize power consumption and to minimize resistive heating in the coils,

which would cause an undesirable phase transformation in the MSM element. To find the

minimum pulse duration required, we generated pulses of different durations and

observed the waveforms on the oscilloscope. The recorded magnetic field pulses are

plotted in Figure 7-7. The corresponding peak magnetic fields at the active pole piece are

listed in Table 7-2. Pulses of 2 ms or longer produced the maximum possible magnetic

field, but additional time was allowed for the material to respond to the field. Smith *et al*.

(2014) [11] reported extremely fast MSM response times of 2.8 µs, but bulk shrinkage

creation times have not yet been fully characterized, and an additional 1 ms - for a total

actuation time of 3 ms - was utilized to give ample time for the formation of a shrinkage.
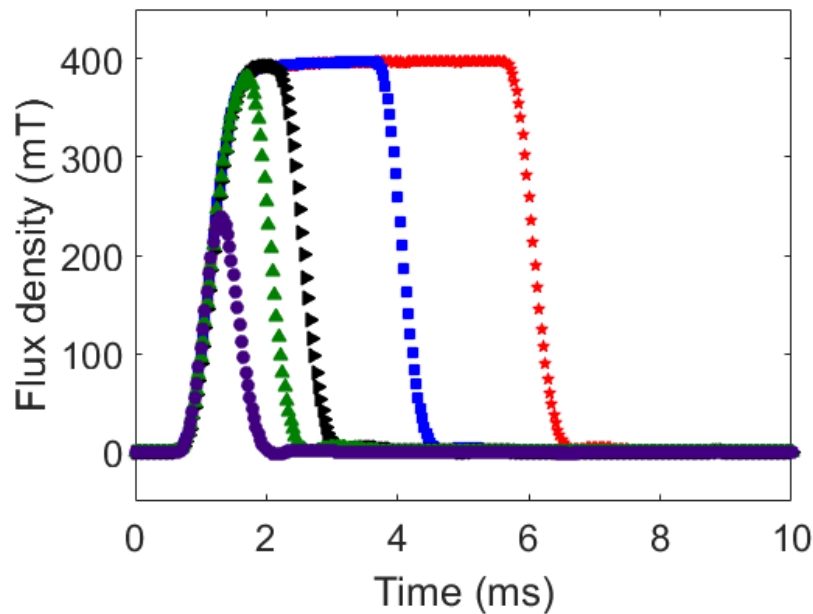
Figure 7-7:   **Magnetic field at the active pole achieved with current pulses of various durations. We incrementally decreased the duration of the pulse from a maximum of 5 ms down to 0.5 ms. The symbols represent the following pulse times: red stars 5 ms; blue squares 3 ms; black right-pointing triangles 1.5 ms; green up-pointing triangles 1 ms; purple circles 0.5 ms. We chose a 3 ms pulse duration to allow ample time for the material to respond to the applied magnetic field.**

Table 7-2:   **Peak magnetic field at active pole measured for each pulse duration.**

Pulse duration	Peak field
0.5 ms	250 mT
1 ms	382 mT
1.5 ms	393 mT
3 ms	397 mT
5 ms	397 mT

Fourier analysis of the chosen pulse duration indicated that the principle flux intensity was at frequencies below 333 Hz, with weaker, though still significant, harmonics near 500 Hz and 800 Hz. The pole piece saturated with flux uniformly at frequencies up to 450 Hz, but above 450 Hz flux did not fully saturate the pole piece and traveled predominantly in the material's outer layer, the skin depth decreases with increasing frequency. For example, at 1000 Hz, the skin depth was about 0.2 mm, such that most of the flux traveled in only 0.4 mm of the pole piece's cross section. To generate flux with the full cross-sectional area of the pole, current pulses greater than 1.5 ms were therefore utilized for experimental testing.

3.2 Drive performance

To characterize the generated flux density as a function of input current, we operated the power supply as a voltage source and increased its voltage from 4 V, the minimum voltage needed to operate the semiconductor devices, to 25 V and measured the corresponding current and flux density with the Hall probe positioned in the air gap. These results were compared to FEMM simulation results. Figure7- 8 shows both the experimental and simulated results for system flux density versus current. The calculated

magnetic flux densities were evaluated at three positions, directly at the pole pieces

(black circles), halfway between pole pieces and iron yoke (red triangles), and at the

surface of the iron yoke (blue stars). The experimental results appear to most approximate

an average value in the air gap before magnetic saturation.
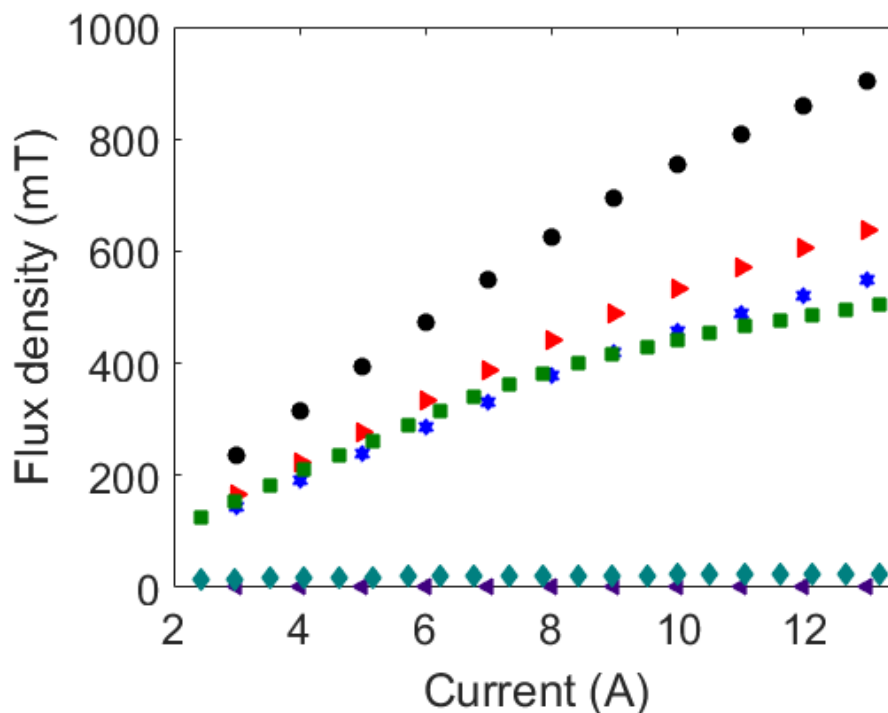
Figure 7-8: **Simulated and experimental results for magnetic flux density vs. current at the active and passive poles. To account for uncertainty regarding the position of the Hall sensor within the Hall probe, flux density was calculated at several locations within the 1.55 mm gap separating the pole from the upper ferromagnetic element: the pole surface (0 mm from pole, black circles); a point in the middle of the air gap (0.78mm from pole, red right-pointing triangles); and at the bottom surface of the iron yoke (1.55 mm from pole, blue stars); the other symbols represent simulated flux density in the air gap above the passive pole (purple left-pointing triangles) and experimental results above the active pole (green squares) and above the passive pole (cyan diamonds).**

The simulated model represents an ideal construction with no reluctance gaps

between magnetic circuit component interfaces. The simulated flux densities in the

middle of the air gap and near the pole piece were higher than experimentally measured

flux densities. The values near the surface of the yoke coincided well with the measured values, suggesting the Hall sensor within the probe rests near the upper surface. For the modeled and measured values, the magnetic flux density increased linearly with current up to about 7 A. At current above 7 A, the slope of the flux density versus current line decreased. Both experimental and simulated results demonstrate that this is due to magnetic saturation of core, yoke, and pole pieces, as the circuit components were operating within the ohmic region, displaying a linear voltage-current relationship.

3.3 Temperature testing

In the martensitic MSM element, phase transformation from martensite to austenite [12] began at 306 K and the apparatus needed to stay below this transformation temperature during operation. We operated the device with 3 ms, 10 A pulses and measured each of the three coils, both transistors, and both thyristors with a K-type thermocouple. The center coil was the component that reached the highest temperature. We operated the device for one hour with 10 A pulses with a 0.3% duty cycle (3 ms on, 997 ms off); which was sufficient to keep the temperature of the center coil below 303 K. At pulses of lower current, it was possible to shorten the off-time and operate the device at a higher duty cycle without exceeding a temperature of 303 K in the center coil. Given this, we were able to consistently operate the device and keep our MSM element in its martensitic phase.

4. Actuation of an MSM element

The MSM element was subjected to magnetic pulses of various strengths with spacers of various thicknesses. With a 1.55 mm glass slide, which is the spacing represented by the green squares in Figure 7-8, no level of current created enough flux

density to actuate the MSM element. The spacer was then removed and a 0.5 mm glass slide was inserted. Subsequently, a single 3 ms pulse of 10 A transformed the region above and caused the desired shrinkage. At 5 A, three pulses of 3 ms were required to completely transform a region corresponding to the width of a pole piece. At pulses below 3 A no shrinkage formed.

When both element ends were fixed with adhesive tape, a 10 A pulse at one pole consistently formed a new twinned section at the expense of the other. An example is presented in the differential interference contrast micrographs of Figure 7-9. However, with only one end constrained, using 10 A pulses, two different outcomes occurred: sometimes a new section formed at the expense of the former, as in Figure 7-9, and sometimes a second section of shrinkage appeared without removal of the first shrinkage, as in Figure 7-10.

5 mm
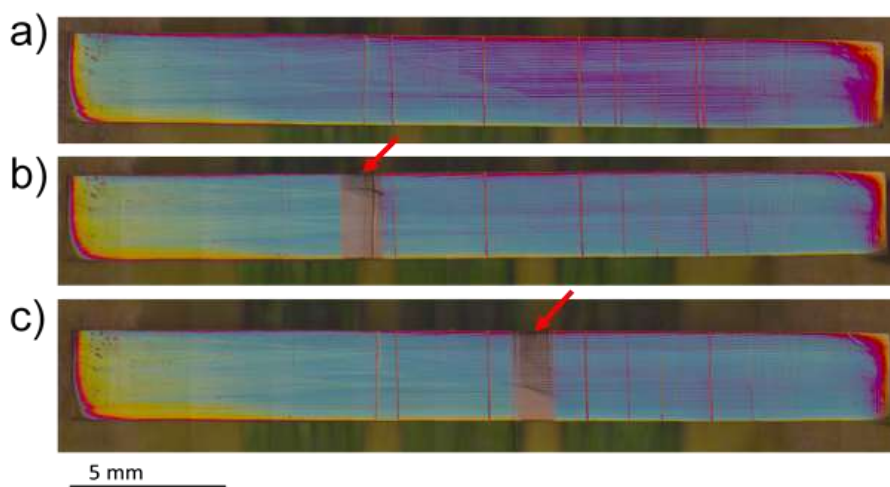
Figure 7-9:   Differential interference contrast optical microscopy images taken before (a) and after two subsequent current pulses (b) and (c), looking down on the setup in Figure 7-6. The MSM element was initially fully compressed (a) with both ends fixed with adhesive tape. Horizontal blue and purple striations indicate compound twins. After activation of the left pole, a shrinkage developed above the activated pole (b). The right pole was then activated which caused a new shrinkage above the right pole while the shrinkage above the left pole disappeared (c). Print readers should view the online version of color contrast.

This suggests that the energy required to overcome the twinning stress is on a similar order of magnitude as the energy needed to overcome the mass inertia of further elongating the element [13].
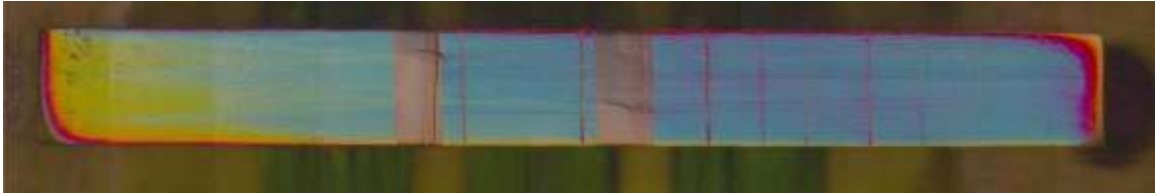
Figure 7-10:   Formation of a twinned region over each pole with only one end constrained.

As MSM actuation occurs with a response time of a few microseconds [7], initial visual observations were inconclusive as to whether the shrinkage moved to a new location, as required for actuation in MSM micropumps [1], or instead diminished as another region formed. We therefore analyzed the response with a high-speed video camera. Figure 7-11 shows a sequence of frames taken before, during, and after pulsing the device's left pole where the mounted MSM element already contained a twinned region above the right pole. Figure 7-11a shows the element before pulsing with the twinned region above the right pole visible as a bright white reflection. A 3 ms pulse was generated at the left pole; Figure 7-11b shows the first frame after the start of the pulse. An absolute zero time was not established between the camera and drive system, and we defined this first frame as time 0 ms. The formation of a new twinned region was faintly visible above the left pole (indicated with an arrow), and the old twinned region was still present above the right pole. Figure 7-11c, 0.541 ms after the start of the pulse, more clearly shows the new twinned region; in this frame, the left pole magnetically attracted the MSM element, causing the element to buckle slightly. The old twinned region was still visible above the right pole, though it appeared narrower than before. Figure 7-11d

shows the element after the left pole pulse had finished. The element was again straight and the newly created twinned region was clearly visible above the left pole. Parts of the previous shrinkage remain which is a result from a slight kinking of the element. The rise time of the magnetic pulse was on the order of 1 ms. Thus, the camera allowed identification of the switching onset in relation to the rise of the magnetic pulse. However, the response time of MSM actuation is on the order of a few microseconds [7]. Thus, more experiments with better time resolution are needed to conclusively characterize the formation mechanism of the new shrinkage over the left pole. When the poles are separated by 4 mm, it appears energetically unfavorable for a twin band to move from one pole position to the other pole position. If the poles were situated closer, twin band movement might be more energetically favorable.

While our element displayed a relatively low switching field (150 mT) in VSM testing, recent research showed that switching fields can be as low as 30 mT if type II twins are present [14]. For MSM elements with consistent small switching fields, the required current in our device would be below 1 A. With small currents, power consumption and heat production are small and switching frequencies could be increased.
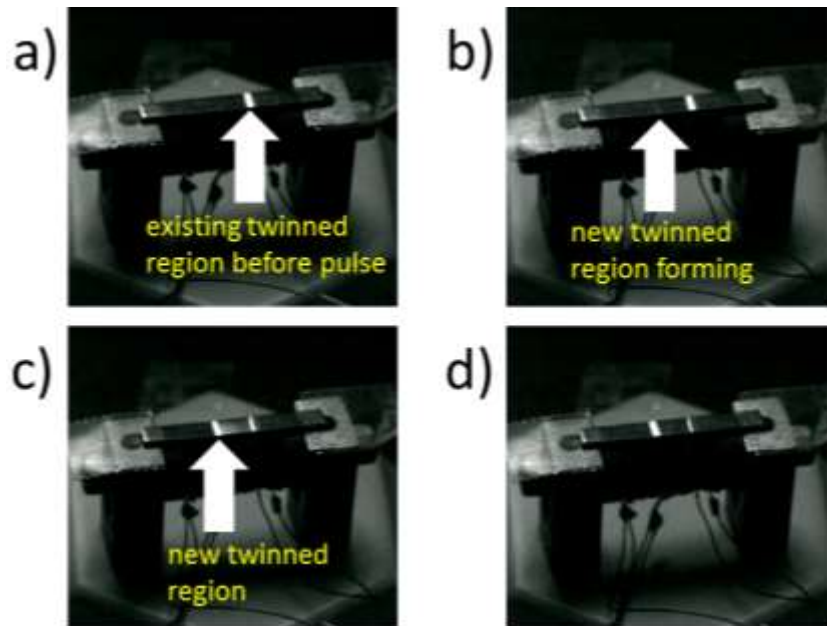
Figure 7-11: A sequence of frames showing device actuating an MSM element. The video from which these images come was filmed at 1849 frames per second, i.e. one frame was captured approximately every 541 µs. We tested with a pulse duration of 3 ms. Some frames were omitted; the presented images were taken at (a) prior to the pulse (b) 0 ms after start of pulse, (c) 0.541 ms after start of pulse, and (d) 4.3289 ms after start of pulse (pulse has finished).

5. Conclusion

A motionless drive system was built and characterized for localized MSM actuation of Ni-Mn-Ga to be used in creating a drive system for a motionless MSM micropump. Our electrical circuit and ferromagnetic drive assembly produced localized magnetic fields comparable to those of Nd-Fe-B permanent magnets and can be used for the actuation of an MSM element, and as such has the potential to replace the existing driving mechanism of the MSM micropump. At present, large currents are required, but design improvements and magnetic circuit optimization will enable the use of smaller currents. Further development is necessary to translate the discrete creation and destruction of twin variant regions demonstrated in this work to the continuous fluid transfer mechanism of the micropump.

Acknowledgements

References

[1]   Ullakko K, Wendell L, Smith A, Müllner P and Hampikian G 2012 *Smart Mater. Struct.* 21 115020

[2]   Smith A R, Saren A, Jarvinen J and Ullakko K 2015 *Microfluidics Nanofluidics* 18 1255

[3]   Heczko O 2014 *Mater. Sci. Technol*. 30 1559

[4]   Ullakko K, Huang J K, Kantner C, Ohandley R C and Kokorin V V 1996 *Appl. Phys. Lett.* 69 1966

[5]   Barker S, Rhoads E, Lindquist P, Vreugdenhil M and Müllner P 2016 ASME *J. Med. Devices* 10 041009

[6]   Faran E and Shilo D 2011 *J. Mech. Phys. Solids* 59 975

[7]   Smith A, Tellinen J, Müllner P and Ullakko K 2014 *Scr. Mater.* 77 68

[8]   Suorsa I, Pagounis E and Ullakko K 2005 *Sensors Actuators A* 121 136

[9]   Schiepp T, Maier M, Pagounis E, Schlüter A and Laufenverg M *2014 IEEE Trans. Magn.* 50 989

[10]   Kellis D, Smith A, Ullakko K and Müllner P 2012 *J. Cryst. Growth* 359 64

[11]   Smith A R, Tellinen J and Ullakko K 2014 *Acta Mater*. 80 373

[12]   Otsuka K and Wayman C M 1998 *Shape Memory Materials* (Cambridge: Cambridge University Press)

[13]   Faran E and Shilo D 2013 *J. Mech. Phys. Solids* 61 726

[14]   Straka L, Heczko O, Seiner H and Sozinov A 2011 *Acta Mater*. 59 7450

CHAPTER EIGHT: ACTUATING A MAGNETIC SHAPE MEMORY ELEMENT LOCALLY WITH A SET OF COILS

Andrew Armstrong[1],

Peter Müllner[1]

[1]Micron School of Materials Science and Engineering, Boise State University,

Boise, ID, USA

Abstract

We consider the local actuation of a magnetic shape memory (MSM) element as used in the MSM micropump. We present differences between an electromagnetic drive system and a system which uses a rotating permanent magnet. For the magnetic field energy of the permanent magnet system, the element takes in significant stray field. In a particular case, energy reduction was 12.7 mJ. For an electromagnetic drive with identical size of the MSM element, the total magnetic field energy created by the system was 2.28 mJ. Attempts to experimentally nucleate twins in an MSM element by energizing an electromagnetic drive system failed even though the local magnetic field exceeded the magnetic switching field. The energy variation is an order of magnitude smaller for the EM system, and does not generate the necessary driving force. In previous work, we assumed that the so-called magnetic switching field presents a sufficient requirement to nucleate a twin and, thus, to locally actuate an MSM element. Here, we show that the total magnetic field energy available to the MSM element presents another requirement.

1. Introduction:

Magnetic Shape Memory (MSM) alloys are functional materials with advantages for application in microactuators, strain sensors [1], energy harvesters [2, 3], and micropumps [4-6]. MSM alloys exhibit large stroke and short actuation time. Essentially, the material operates as a metallic muscle, controlled by the variation of a magnetic field. Ni-Mn-Ga exhibits a martensite phase with highly mobile twin boundaries. Upon application of mechanical stress or a magnetic field, the twin domains reorient and enable high magnetic-field-induced strain (MFIS).

In a uniform magnetic field, the MSM element deforms by extending and contracting uniformly in the bulk [7]. A localized magnetic field causes a localized shrinkage in the MSM element [4], and rotating the localized field moves the shrinkage through the MSM element [8]. The motion of the shrinkage along the element can be used to build a pump in a similar manner to the esophageal contractions that mammals use to swallow food [4].

In previous work, the rotating magnetic field has been provided by the rotation of a diametrically magnetized permanent magnet, where a micromotor spun the magnet. Micromotors are costly and still quite large in comparison to an MSM sample and have moving parts prone to fatigue. In lieu of actuating the shrinkage with a rotating magnet, researchers applied a local magnetic field with a miniaturize electromagnet [9]. To move the localized magnetic field, Smith *et al.* physically repositioned the poles of the electromagnet. The authors found that a locally twinned region formed at the magnetic pole tips. In [10], we created a motionless magnetic driver in a device with multiple magnetic poles arranged in a row. We energized individual poles with a strong magnetic field by passing current in opposite direction through two coils. Changing the polarity of the coils energized other poles and moved the magnetic field. The shrinkage formed on the MSM element near the pole tips. However, the spacing between poles was too coarse to move the deformed region.

Here we present an electromagnetic drive system with two rows of magnetic poles, similar to linear motor yokes, which are staggered across the MSM element. Each pole can be energized individually and sequentially to approximate a moving vertical

field along the MSM element. In Chapter 6, we showed that the mechanism of the MSM micropump is a moving thick twin.

We use magnetic modeling to study the possibility of moving a thick twin with a staggered pole device. We looked to FEA simulation to show us material models such that allow further understanding of the effect of the MSM switching effect upon the pulsed magnetic fields. We compare the simulations to that of the permanent magnet driven system.

2. Experiments

2.1 Device design

We machined the magnetic yokes shown in Figure 8-1 out of a 3.0 mm thick plate of Fe-Co (Vacoflux 50). The material is magnetically soft and supports 2.3 T at saturation [11]. The yoke was composed of a top and bottom yoke which interfaced via a friction fit. The bottom yoke had three poles and the top yoke had four poles. The bottom yoke slid into the top yoke. The two yokes had poles juxtaposed to each other. In Figure 8-1a, the yokes are separated by an air gap. The poles (P1-P7) were magnetized by the bottom coils, B1-B4, and the top coils T1-T5. Figure 8-1a shows the flux pattern when P1 and P2 are actuated with magnetic flux flowing upward.

Each side of the yoke had an inner row of poles and an outer row of poles. The outer poles were simply for coil containment when winding. Upon actuation, the magnetic circuit guided the vast majority of magnetic flux through the inner poles. The inner width of the yoke was 20 mm, designed to accommodate an MSM element. The edges were deburred by sandblasting such that coils could be wound directly onto the yokes. The coil wire had a polyamide coated and a diameter of 0.13 mm (36 AWG).

Figure 8-1b shows the yokes with only five coils, while for the experiments, we added

four coils outside of the outermost poles in each row. Each coil in the system had 200

turns. We wound the coils on a machinist lathe.
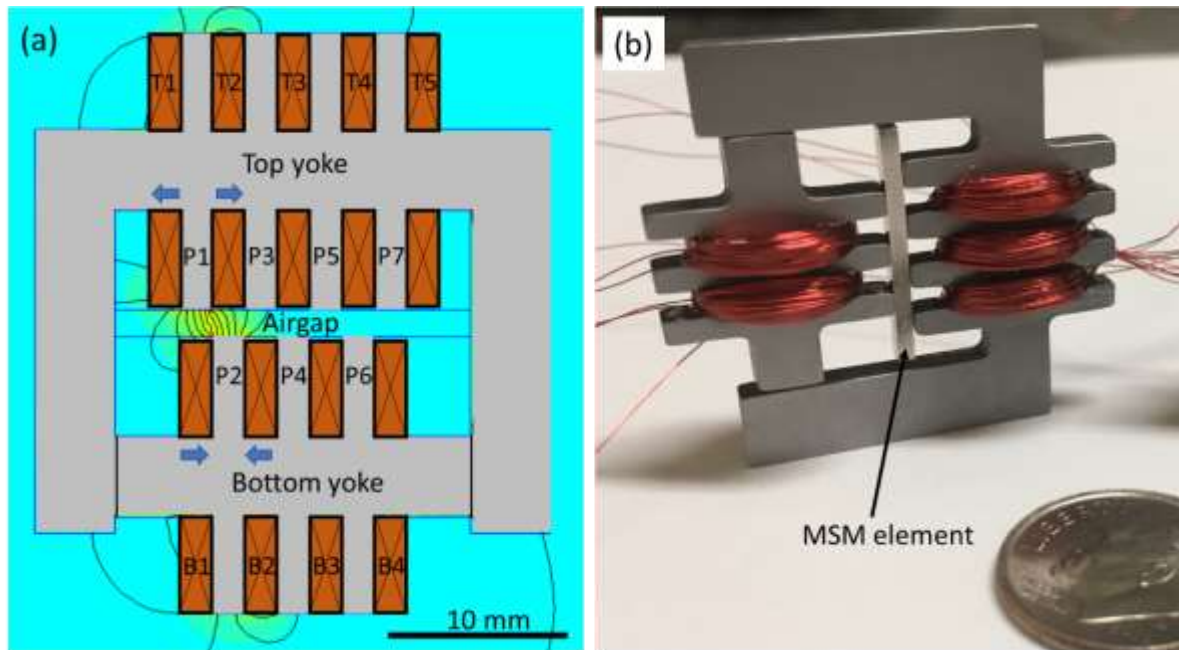
**Figure 8-1:   Design of the electromagnetic drive device: (a) schematic of the Fe-Co
yoke geometry, pole geometry, and coil geometry. The bottom yoke contains the
bottom poles P2, P4, and P6 and slides between the tines of the top yoke. The bottom
and top yokes had poles that were staggered relative to each other. Figure (b)
depicts the device before winding the outermost coils, such that the interface
between the top and bottom yoke is depicted.**

2.2 Magnetic circuits and magnetic field propagation

To create and move the vertical magnetic field patterns, we sequentially energized

circuits. In Figure 8-1a, for example, coils B1 and B2 were energized in opposition

thereby creating a North pole to form at P2. Coils T1 and T2 were opposed and with

polarity opposite to the B1 and B2 coils. P1, therefore, becomes a South pole. The

magnetic field flew from the North pole (P2) to the South pole (P1) across the air gap.

We identified five circuits that deem suitable to induce and advance a strong vertical magnetic field. The mechanism we considered advanced the field by one pole pitch, though the mechanism could have been extended in either direction. We numbered the circuit according to the sequence. The circuits were described by the energized, opposed electrical coil pair (B2, B3) and the pole direction they cause at the airgap (N or S). The circuits were:

1. (B2, B3) N, (T2, T3) S

2. (B2, B3) N, (T2, T4) S

3. (B2, B3) N, (T3, T4) S

4. (B2, B4) N, (T3, T4) S

5. (B3, B4) N, (T3, T4) S which begins the next elementary sequence.

2.3 Magnetic measurements

We measured the device induction in the air gap as a function of coil current. The gap was 1.4 mm which corresponded to the thickness of the MSM element used in this study. We energized each circuit using an Arduino microcontroller, which controlled an 8 channel 5V optocoupled relay board (Sunfounder). We applied 10 ms pulses which appeared rectangular in the oscilloscope. We recorded the magnetic field with a Hirst GM08 gaussmeter with a transverse Hall probe with a 1.5 mm wide Hall sensor. The measured Hall sensor location is indicated by the red box in Figure 8-2. For the measured circuits 1, 2, 3, the hall probe was at locations H1, H2, and H3 respectively.

We characterized circuits 1, 2, 3 by measuring magnetic field and current at 1V increments. We powered the circuit with a BK Precision 30V, 5A power supply and

measured the current with a shunt resistor. We recorded measurements with a Diligent

Analog Discovery 2 oscilloscope.
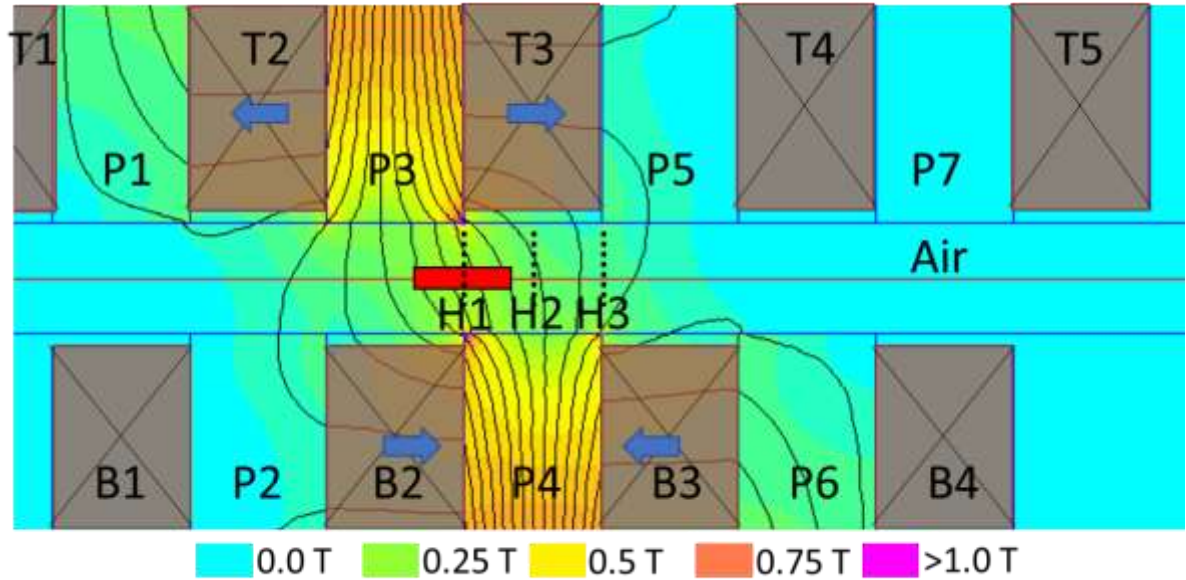
Figure 8-2: Schematic of the poles (P1-P7), the bottom yoke poles (B1-B4), and the top yoke coils (T1-T5). The flux density was measured in the center of the air gap, at location H1, for sequence 1. The hall probe (the red box) recorded data at positions H2 and H3 for the pulsing sequences measured experimentally.

2.4 Actuation with MSM element

We used a single crystal MSM element which was manufactured at Boise State

University [12] The MSM element measured 1.4 mm x 2.0 mm x 20 mm. The faces were

cut parallel to {100} crystallographic planes. The element was electropolished in a 1:3

14M Nitric acid in ethanol solution. The element was compressed along the 20 mm

dimension such that the crystallographic c-axes, which coincides with the direction of

easy magnetization, was all aligned in the horizontal direction (Parent variant) throughout

the entire element. The sample faces were mechanically ground then finely polished

using 0.3 µm diamond suspension for optical analysis. A twin domain, where the c-axis

was aligned along the short dimension of the element, was mechanically induced into a

portion of the element with calipers such that the volume fraction of the twin was approximately 15% following Ref. [9]. The sample was then fixed in this configuration to a glass coverslip with double-sided tape. We actuated the MSM element with circuits described in section 2.2 and 2.3 with an electrical current of 1 A on each coil.

2.5 Optical microscopy

We inserted the MSM element into the drive system. The entire system was placed on the stage of an optical microscope with polarized illumination. We then applied the circuits described in 2.2 on the MSM element. We performed video analysis and still micrography to measure the twin boundary motion at the shrinkage.

3. Finite element analysis

The experiment was simulated by magnetic finite element analysis (FEA: FEMM 4.2). In the parent variant, we used relative permeability of $\mu_r = 2$ in the vertical direction and 40 in the horizontal direction [13]. The twin was the opposite and had its axis of easy magnetization in the vertical direction ($\mu_r = 40$). In all FEA simulations, we used an energization current of 1A/coil, producing field in the coil in the direction indicated by arrows.

In this model, the magnetic permeability was assumed to be constant and not depend upon the field strength. Simulation of the dynamical response of the material is not straightforward. Provided a sufficiently strong magnetic field, the material switches to become twinned. Once the twin is formed, the twin becomes a low-reluctance "short" in the magnetic circuit. The position of the "short" dictates the shape of the resultant circuit. We accounted for the dynamic variation of the magnetic structure by simulating instances before and after the switching event.

3.1 Simulated cases

We first simulated the magnetic field patterns without any MSM element for the circuits described in section 2.2. We then compared experimental and simulated values to determine the validity of our FEMM simulations.

Second, we simulated the device coupled to an MSM element, fully compressed, with the *c*-axis oriented horizontally. The device thus magnetized the MSM sample along the hard magnetization axis. We simulated pulse sequences 1- 5 described in section 2.2. The simulations thus showed the magnetic field available to cause the switching effect in an unswitched element.

We then modeled the magnetic field with a twin in the element. The twin had *c* vertical and provided a path for the flux short through the MSM element. However, we were only guessing the position of the twin. We modeled the twin at different locations, determining the magnetic flux pattern and interaction of the twin with the activated poles.

Finally, we modeled the magnetic field of a permanent magnet drive system. The simulations allow for comparison of the magnetic field energy between the permanent magnet system and the staggered pole electromagnetic system.

3.2 Magnetic field energy

We used FEMM to analyze the magnetic field energy in the system (with and without the MSM element). The magnetic field energy of the permanent magnet is large and varies slightly with the configuration of the MSM element. The stray field interacts with the MSM element to lower the stray field energy. FEMM integrates the magnetic energy (MFE) of the defined region as $W_m = \int_0^B H dB$ [14].

We evaluated the MFE of two areas. The region of interest (ROI) was the region where the volume occupied by the MSM element. In some simulations, we simulated the drive without the MSM element, and the material within the ROI was air. The second area was the entire system. We approximated the total system energy within the system by evaluating a cylindrical volume with 60 mm diameter and zero-flux density boundary condition on the circumference. This cylindrical volume was centered on the drive system.

We then modeled the MFE in the MSM element for the staggered pole circuit. We introduced a 2.0 mm thick twin into the element. For each pulse sequence (1-5), we moved the twin along the element and recorded the MFE of the MSM element at each position. The twin was moved in increments of 0.5 mm along the element. We then evaluated the system and ROI MFE energies to make direct comparison between the energetics of the electromagnetic drive and that of the permanent magnet drive systems.

4. Results

4.1 Device measurements

Figure 8-3 shows the experimental results of the flux generated in the air gap by activation of circuit 1 (gray), circuit 2 (green), and circuit 3 (blue). We recorded the system's total current during each measurement and divided it by the number of energized coils to determine the current per coil. The magnetization was quite similar for circuits 1, 2, and 3. The red curve shows the activation of only P4 by coils B2 and B3 alone. In the red curve, the magnetic induction began to saturate at a lower field in the airgap than for the other circuits, which have two energized poles.
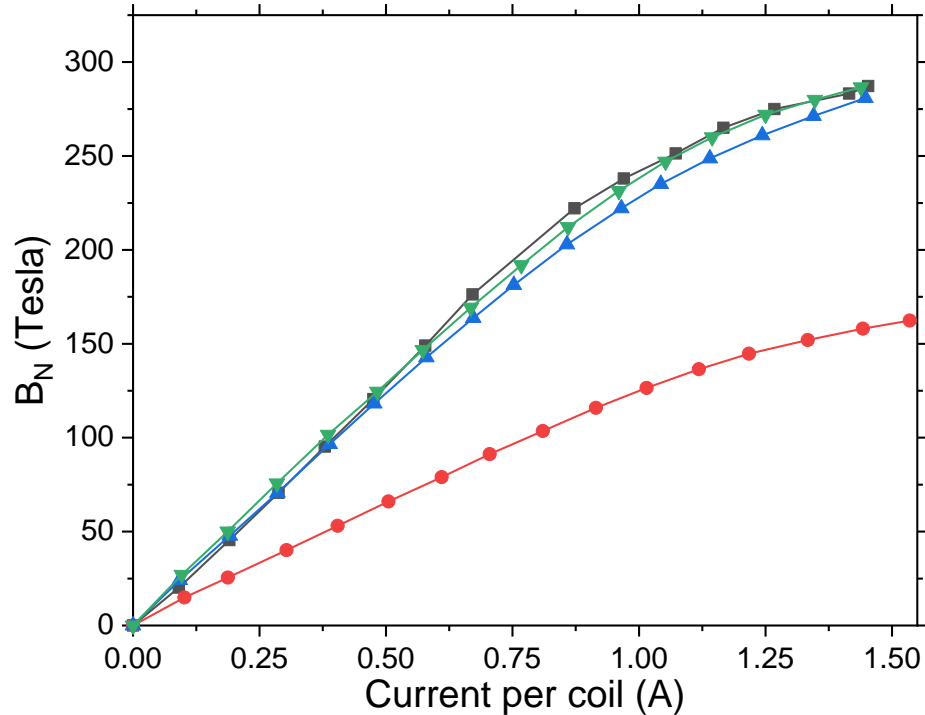
Figure 8-3: **Experimental data of the magnetic induction in the air gap as a function of the applied current. In gray, the results of pulse sequence 1, measured at Hall sensor location H1. In green, the energized sequence 2 measured at H2. The blue pulse sequence 3, measured at H3. The red data shows activation of just P4 pole by coils B2 and B3, at H2.**

4.2 MSM actuation

No motion of twin boundaries was observed for the pulsing sequence. Before and after pulsing, the twin boundary geometries were identical. Slight motion appeared to be due to Maxwell forces at the poles which attracted the MSM element.

4.3 FEA simulation

4.3.1 Airgap simulation.

The magnetic induction in the airgap was approximately 250 mT at 1 A on each coil, which correlated well to the experimental measurements of Figure 8-3.

4.3.2 Parent variant

Figure 4 shows the elementary sequence of circuits which we use to advance the vertical flux along the single variant MSM element. In Figure 4a, circuit 1 activated poles P4 and P3. In (b), circuit 2 activated P4 and also P3 and P5. In (c), circuit 3 activated P4 and P5. In (d) circuit 4 activated P4 and P6 on the bottom yoke, and P5 on the top. The circuit number following section 2.2 is noted in the bottom right of each frame in Figure 4.

When activated with circuit 1 (Figure 8-4a), poles P3 and P4 were saturated and directed magnetic flux between them. A significant portion of the flux generated by the individual poles leaked back through adjacent poles P2 and P6, rather than continuing to the other side of the MSM element. When activated with circuit 2 (Figure 8-4b), the vertical field in the MSM element was broad, and some flux lines circled back to adjacent poles. Activated with circuit 3 (Figure 8-4c), the field pattern was symmetrical to that of circuit 1. Pole 2 leaked slightly more induction than pole 3. Activated by circuit 4 (Figure 8-4d), the pattern was symmetrical to circuit 2, advanced by half a pole pitch.
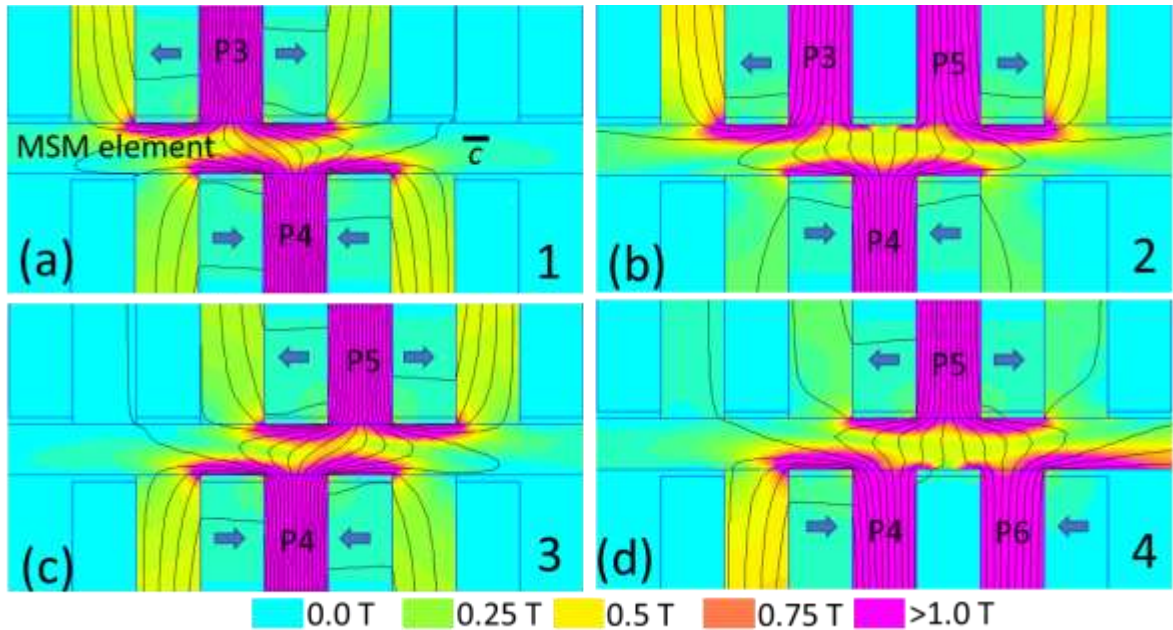
Figure 8-4: FEMM simulation of the pulsing sequence which we use approximate a moving vertical field. The simulation shows the fields induced in a single variant MSM element with the c-axis oriented horizontally. (a) shows circuits 1-4 as defined in section 2.2.

Figure 8-5 shows the line profiles for the circuits which complete the switching pattern in the parent variant. The line position is shown in Figure 8-2 as the red horizontal line. The peak field takes either of two values. Circuits 1, 3, and 5 have narrower peaks, and lower peak maximum with about 0.3 T. Circuits 2 and 4 have broader peaks, and a peak maximum of about 0.47 T. The broadening of the peaks is because three poles conduct the flux. The vertical field moves 6.0 mm from peak to peak which gives the stroke of the elementary sequence.
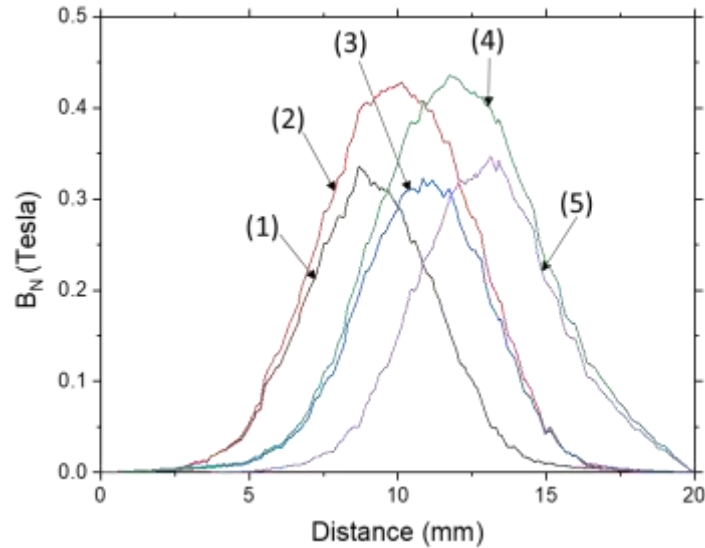
Figure 8-5: **Profiles of the induction of the single variant element for circuits 1-5.**

4.3.3 MSM element with a twin

The switching of the material had a large effect on induction [15]. Figure 8-6 shows the induction along the red line in air, the parent variant, and the parent variant with a twin, activated by circuit 1. In air, the peak of the flux was 251 mT. For the material unswitched in the parent variant, the peak maximum was 334 mT. When switched, i.e. with a twin in the MSM element, the field in the twin exceeds 1.4 T. The induction values for the twin were higher than the material's magnetic saturation of about 600 mT [16].
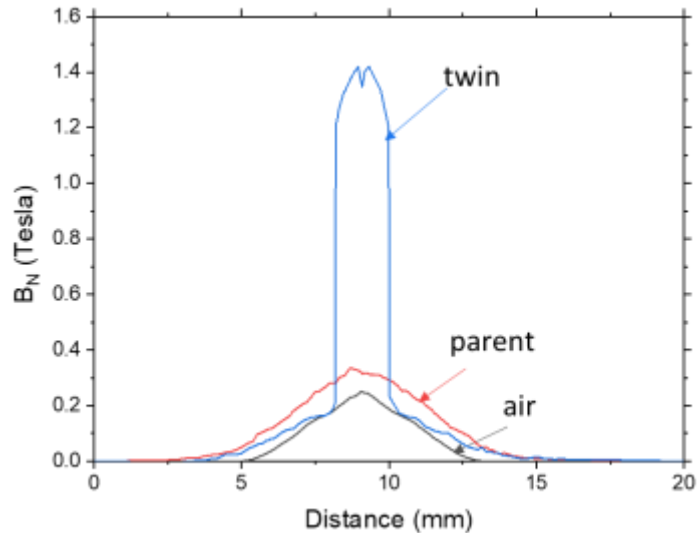
Figure 8-6: **The twin has induction much greater than that for the parent variant, or air. The profiles show the profile along the center of the simulations presented in Figure 8-2, Figure 8-4(a), and Figure 8-7(a).**

Figure 8-7 shows simulation results with a twin at three different locations, namely between poles P3 and P4 (Figure 8-7a), between poles P4 and P5 (Figures 8-7b and 7c) and between poles P5 and P6 (Figure 8-7d). In the first situation, poles P3 and P4 were energized (*i.e.* circuit 1), in the other three cases poles P4 and P5 were energized (*i.e.* circuit 3). In Figure 8-7(a), the twin was evenly saturated across its width. The broad, symmetric peak of the twin in Figure 8-6 corresponds to the even saturation at the sample center, across the twin.

In Figure 8-7(b), the magnetic flux entered the twin vertically, then was mirrored across the twin boundary, to be horizontal in the element, before it exited the MSM element and entered P5. The right twin boundary was highly magnetized, while the left twin boundary was almost void of magnetic flux.

In Figure 8-7(c), the flux narrowly constricted at a location defined by the connection of the right side of P4 and the left side of P5. With the advancement of the mechanism, in (d), the situation was the opposite of (b), with the left twin boundary

redirecting substantial magnetic flux and the right boundary in a region of low induction.

In a next step (not shown here), we energized poles P5 and P6 with the twin at the

position as in Figure 8-7d. The resulting magnetic flux pattern was identical to that

shown in Figure 8-7a but displaced by one pole pitch to the right.
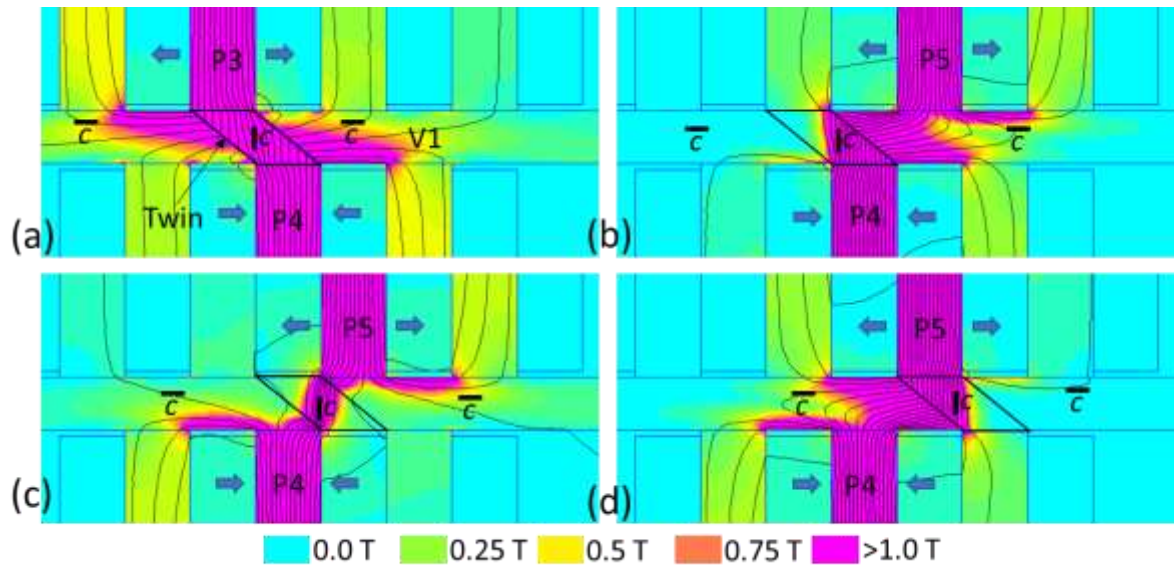
Figure 8-7: **FEMM simulations of circuit 1 for (a) and circuit 3 for (b-d). The location of the twin affected the magnetic flux pattern. In (a), we placed a twin between P3 and P4 using circuit 1. In (b), with circuit 3 activated, we simulated the fields which would be incident on the twin still at the location of (a). We then moved the twin further along the element in (c) and (d). In (c) magnetic flux was locally concentrated in a strong vertical magnetic field. In (d), magnetic flux reflected strongly across the left twin boundary, in a pattern symmetrical to that of (b).**

Figure 8-8 shows profiles (a) through (d) corresponding to the simulation

scenarios of Figure 8-7. For profile (e), the twin was in the position as in (d), but the

circuit 5 was energized. For this situation, the magnetic flux pattern was nearly identical

to that of Figure 8-7a, though it was advanced by a pole pitch. The induction calculated

by FEMM was higher than possible for the MSM sample, which has a saturation

magnetization of about 600 mT [16]. The deviation was due to FEMM's linear

approximation of the anisotropic magnetic permeability.
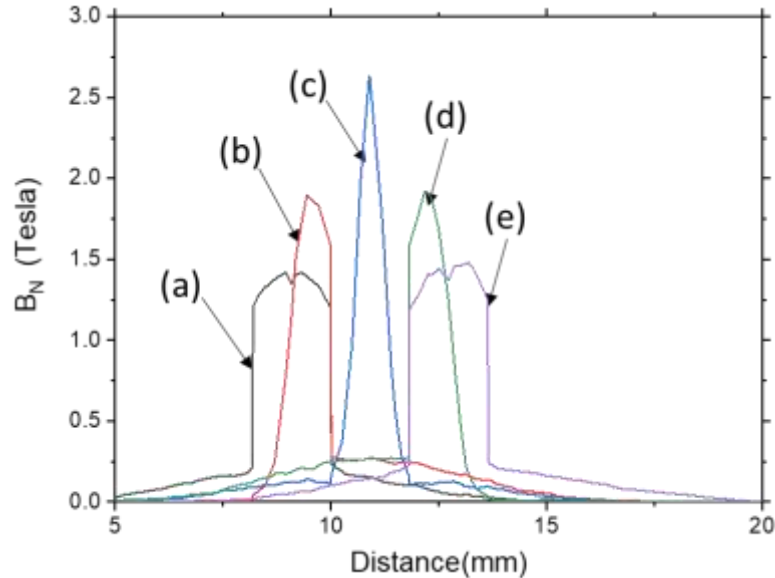
Figure 8-8: **Simulation of the flux density along the MSM element including a twin region. The twin region moved along the element corresponding to the (a) –(d) sequences in Figure 8-7. (e) profile shows the simulation of the (d) twin boundary position, using circuit 5.**

<u>4.3.4 Simulation of magnetic field energies</u>

Figure 8-9 shows the MFE for each magnetic circuit (1-5) as a function of twin positions. The units of MFE was recorded in mJ/mm, which gives the energy for each mm depth of our two-dimensional (planar) simulation. We initially recorded the MFE for the parent variant MSM element without any twin, which is represented in Figure 8-9 as dashed horizontal lines with the same as the active circuit.

Circuits 2 and 4 had higher MFE than 1, 3, or 5. The deviation in energy between the single variant (dashed line) and the energy minima, was the energy variation available to nucleate the twin. The energy reduction of circuit 2 compared to the single variant condition (dashed line), had a maximum of 0.12 mJ/mm at 9 mm. The local minima at 9 mm was distinct. The energy variation between adjacent positions, was steep on the left side of the minima, yet shallow on the right side. The energy configurations for circuit 4 is nearly symmetrical to that of circuit 2.
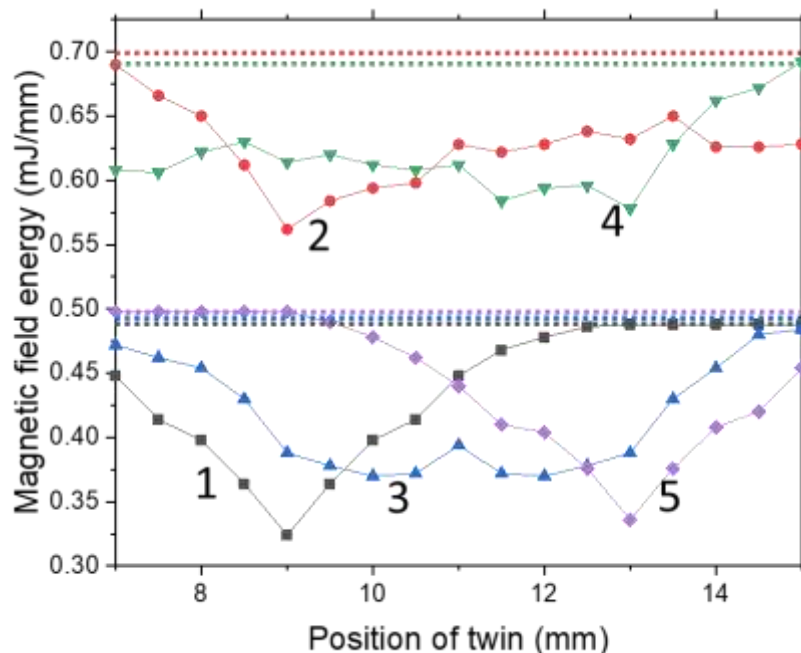
Figure 8-9: **System energy at configurations of a 2.0 mm wide twin moving through the studied circuits (1-5). The dotted lines correspond to the circuit by color and give the energy of the single variant condition.**

Circuits 1, 3, and 5 had lower MFE for the single variant condition. The MFE for the three circuits was about 0.49 mJ/mm. The energy variation of circuit 1, was 0.155 mJ/mm, slightly greater than that of circuit 2. Circuit 1 had a clear and distinct energy minimum compared to circuit 2.

Circuit 3 had similar single variant MFE to circuits 1 and 5. The circuit does not have a distinct minimum, though. The profile takes two shallow troughs separated by a slight peak which arose at the connection of the troughs. We interpret this behavior as the twin is relatively stable from about 9 mm to 13 mm, but has little preference for position. Figure 8-10 shows results of simulation of the permanent magnet drive system (PM). In (a), the magnet was surrounded by air. The system energy was found within the 60 mm boundary condition. The element energy was found within the dashed black box indicated in (a). (b) shows simulation now with a parent region in the dashed box. The

magnetic stray field, which previously entered the air-gap in (a) was directed horizontally to the ends of the parent variant and back down to the permanent magnet. In (c), the region was a single variant, which has the *c* axis oriented vertically (i.e. perpendicular to the axis of the MSM element). The magnetic anisotropy directed magnetic flux up, causing a large magnetic stray field, similar to the magnetic flux distribution in the airgap. In (d), we introduced a twin which split the element in half. The parent variant (with *c* horizontal) was on the left and the twin (with *c* vertical) was on the right. Flux concentrates in the parent variant, and only weakly magnetizes the twin. In (e), the situation was reversed. Here the twin magnetized strongly underneath the twin boundary, and in the parent variant, mirrored across the twin boundary. In (f) we simulated a twin within two parent variants. Similarly, to (e), magnetic flux concentrated underneath the twin boundary. The parent variant on the left directed flux horizontally. Minimal stray field was present above the element in (b) and (c).
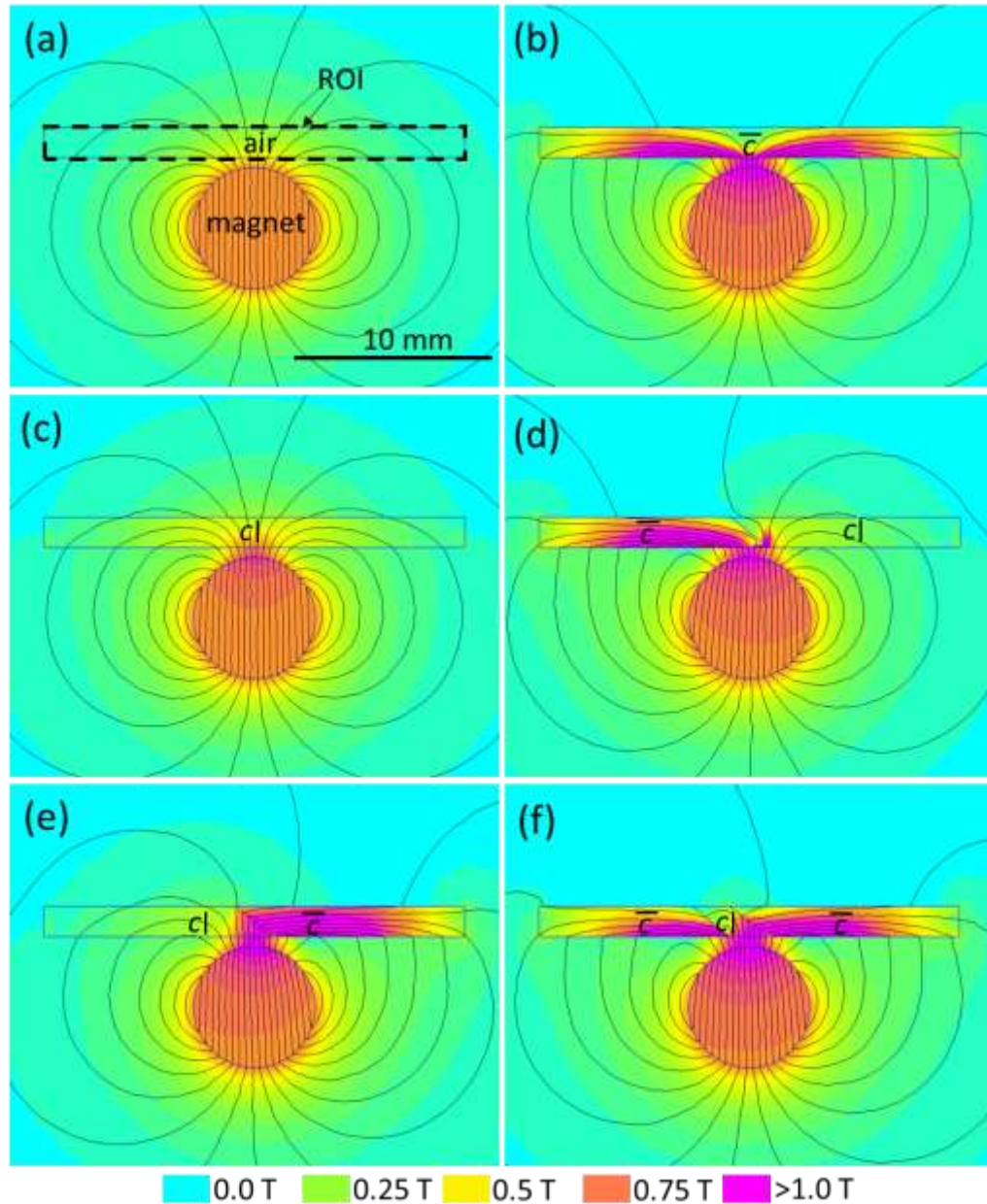
Figure 8-10:   FEM simulation of the magnetic flux pattern of the permanent magnet drive system. In (a) the cylindrical magnet generated a magnetic dipole field in air. In (b), the boxed region was defined as the parent variant with the c-axis oriented horizontally. Figure (c) shows the boxed region defined as a single variant of twin with the c axis oriented vertically. In (d), we defined a twin boundary in the center which separated the twin and parent into equal volumes. The left volume we defined as the parent (c horizontal), and the right as the twin (c vertical). In (e), a twin boundary again separates equal twin volumes, however, the twin was defined on the left and the parent on the right. In (f), we insert two twin boundaries with a twin in between, at the center of the parent variant. The energy within the dashed box is highest in air, and lowest with two twin boundaries.

Figure 8-11 shows a comparison of the magnetic energies of the permanent magnet drive and the staggered pole electromagnetic (EM) drive. The horizontal axis indicates the simulation. (a) gives the energies corresponding to Figure 8-10a. The black circle is the system energy. The upside-down triangles show the magnetic field energy in the magnet (gray) and the stray field (blue). The red square indicates the magnetic field in the boxed region, which in this simulation was air. The red squares are read by the right axis, which shows finer energy variations. Thus, for (a) the system energy was 13.62 mJ/mm, the MFE in the permanent magnet was 7.08 mJ/mm, and the MFE for the stray field was 6.54 mJ/mm. The MFE in the ROI was 0.61 mJ/mm. In (b) the air region was changed to the parent variant, and the MFE for the system and ROI defined. The system and ROI energy are decreases relative to (a). In (c) the parent variant was changed to the twin variant, and shows switching of the entire element. The system and ROI energy were greater than for the parent variant, but less than for the air. In (c -d) we considered a twin boundary which split the volume of the ROI equally into twin and parent. With the parent on the right (d), the system energy is in-between that of the single variant parent or twin. The ROI energy is about the same as for the parent. With the parent on the left, the system energy was slightly decreased, and the ROI energy decreasing more substantially. In (e), with a single thick twin in the center of two parent variants, the system energy and the ROI energy is the lowest for the permanent magnet drive system.

Figure 8-11 shows the MFE for three simulations of the electromagnetic (EM) system for activation of circuit 1. With an airgap separating the top and bottom yokes, the total system MFE was 0.43 mJ/mm. The MFE in the airgap region was 0.14 mJ/mm. With a parent variant MSM element inserted, the system's MFE energy increased to 0.75

mJ/mm. The MFE of the MSM element was 0.49 mJ/mm. With a twin connecting poles P4 and P3, as in Figure 8-7a, the systems energy was slightly lower, and the energy of the MSM element decreased compared to the parent variant, at 0.33 mJ/mm. The system MFE of the electromagnetic drive was almost an of magnitude less than that for the permanent magnet driven system.
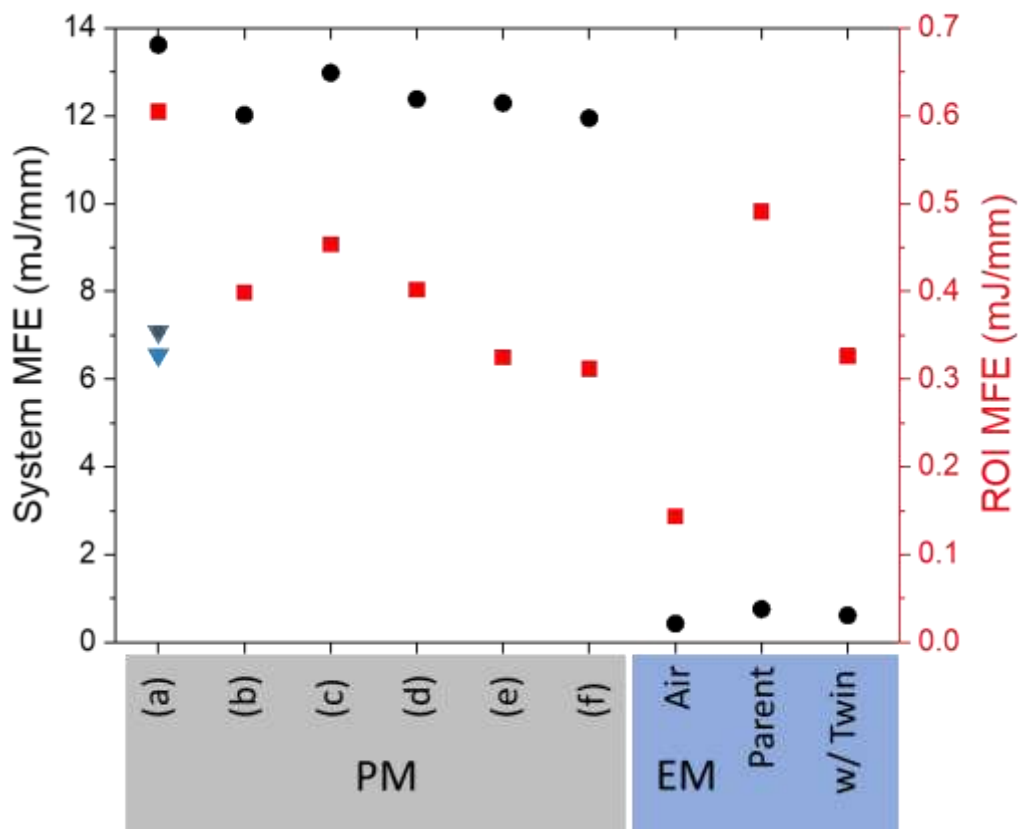
Figure 8-11: Comparison of the magnetic field energies for the configurations of the PM drive in Figure 8-10, compared our EM system. The black circles show the magnetic field energy of the system. In red squares show the magnetic field energy of the region boxed in (a) and reads according to the right axis. The triangles show the magnetic field energy in the magnet (black triangle) and in the stray field, blue triangle for simulation of the permanent magnet in air, Figure 8-10a. (a – f) show the energy for the permanent magnet drive configurations. The air, parent, and w/twin are the energies for the staggered pole yoke system using circuit 1.

5. Discussion

We find a discrepancy between the actuator properties of the permanent magnet drive and the electromagnetic drive. The permanent magnet drive system creates a twin in the material, and then translates the twin along the MSM element (Chapter 6). The electromagnetic drive system does not readily generate the twin nor move the twin boundaries. For the permanent magnet system (Figure 6-5), the vertical magnetic field which first caused deformation was about 200 mT. Our electromagnetic drive here generates a 300 mT magnetic field in the airgap. Our previous device in Chapter 7 required a field measured in the airgap of 500 mT to nucleate a twin, which is more than three times more than the switching field of 150 mT measured along the short direction in a vibrating sample magnetometer. Thus, the local magnetic switching field is perhaps three times the global magnetic switching field

We calculate the MFE in FEMM. The method disregards the contributions of the anisotropy energy and the Zeeman energy. Significant sections of our element exhibit magnetic saturation which causes additional significant error to the MFE.

In Figure 8-11a, the energy of the permanent magnet and the stray field without an MSM element is 13.6 mJ/mm. The permanent magnet in a PM drive is 12.7 mm long. The multiplication of these two numbers gives an MFE of 172 mJ for the system. The minimum required length of the magnetic is unknown, however if only as wide as the element (2.0 mm), the MFE would be 27.2 mJ. The energy needed to cause a shrinkage to form and move through the element has been experimentally measured by Smith *et al.* as 0.77 mJ by difference in energy of a motor before and after coupling to the MSM element [6]. In Figure 8-11, by taking either the parent single variant, or the twin within the

parents, the stray field is reduced by about 1 mJ/mm. Multiplying by the length of the magnet, the MSM element captures potentially between 2.0-12.7 mJ from the magnet's stray field. This is perhaps not the only energy given to the MSM element, which can draw also anisotropy energy.

For the EM drive system, the MSM element can draw energy proportional to its reluctance. The maximum system energy is 0.76 mJ/mm, which, translates for our physical device, which has a yoke depth of only 3 mm, to a maximum output of 2.28 mJ.

The variation of the stray field energy for just the MSM element is actually greater in the electromagnetic drive system. A permanent magnet acts as constant source of magnetic flux, analogous to a current source in electronics. In contrast, the electromagnetic coils act as a generators of flux potential, analogous to a voltage driving a current according to the circuit's resistance. The flux induced by the coils is a function of the reluctance of the circuit. When the reluctance is decreased, *e.g.* by insertion of the MSM element, the magnetic flux across the entire system increases. The different behaviors can be seen in Figure 8-11. When the MSM element is added to the magnetic circuit of the permanent magnet drive, the total system energy decreases. The electromagnetic drive system has initially a low system energy, as the airgap causes a large reluctance gap, and reduces generated flux in the system. When the MSM element is inserted, the system energy increases by 79%.

Our device has a relatively high physical pole density. However, this does not necessarily translate to the creation of a high density of stable twin positions. In Figure 8-9, only circuits 1 and 5 have distinct energy minima. Circuits 2 and 4 have low energy variations, and energy minima are at the same position as for circuits 1 and 5 (i.e. no

motion of the minima). Circuit 3 exhibits a shallow depression which is composed of two shallow troughs. The slight peak between the troughs indicates that a twin at this position is a bit unstable. The local minima observed do not account for the anisotropy energy, which together with the Zeeman energies affects the total system energy configuration which drives the deformation. Calculation of all energies is however quite challenging.

The energies of a single domain MSM element in the field of a permanent magnetic (Figure 8-10b) and the energy of an MSM element with a small twin (Figure 8-10f) are almost identical. The creation of the twin reduces the magnetic stray field energy by only 0.07 mJ/mm. This indicates that other energy contributions play a significant role, such as the magnetocrystalline anisotropy energy. Further analysis of this situation is required, which is beyond the scope of this study.

6. Conclusion

We exposed an MSM element to localized magnetic fields in two ways: (1) with a permanent magnet, (2) with sets of electrical coils and yokes. The magnetic field strength at the position of the MSM element was similar for the two cases and larger than the magnetic switching field. For the permanent magnet, the magnetic field nucleated twins, not so for the electromagnetic drive system. We attribute this variation (1) to the high energy carried in the stray field of the permanent magnet, and (2) to the coils generating a magnetic flux potential where the actual magnetic flux depends on the reluctance of the magnetic circuit. More detailed studies are required to develop a quantitative understanding of the localized switching of MSM elements in heterogeneous magnetic fields.

Acknowledgments:

References

[1]   I. Suorsa, J. Tellinen, K. Ullakko, E. Pagounis, Voltage generation induced by mechanical straining in magnetic shape memory materials, Journal of Applied Physics 95(12) (2004) 8054-8058.

[2]   P. Lindquist, T. Hobza, C. Patrick, P. Müllner, Efficiency of Energy Harvesting in Ni–Mn–Ga Shape Memory Alloys, Shape Memory and Superelasticity 4(1) (2018) 93-101.

[3]   I. Karaman, B. Basaran, H.E. Karaca, A.I. Karsilayan, Y.I. Chumlyakov, Energy harvesting using martensite variant reorientation mechanism in a NiMnGa magnetic shape memory alloy, Applied Physics Letters 90(17) (2007).

[4]   K. Ullakko, L. Wendell, A. Smith, P. Mullner, G. Hampikian, A magnetic shape memory micropump: contact-free, and compatible with PCR and human DNA profiling, Smart Materials and Structures 21(11) (2012).

[5]   A. Saren, A.R. Smith, K. Ullakko, Integratable magnetic shape memory micropump for high-pressure, precision microfluidic applications, Microfluidics and Nanofluidics 22(4) (2018).

[6]   A.R. Smith, A. Saren, J. Jarvinen, K. Ullakko, Characterization of a high-resolution solid-state micropump that can be integrated into microfluidic systems, Microfluidics and Nanofluidics 18(5-6) (2015) 1255-1263.

[7]   K. Ullakko, Magnetically controlled shape memory alloys: A new class of actuator materials, Journal of Materials Engineering and Performance 5(3) (1996) 405-409.

[8]   Boise State University, https://www.boisestate.edu/coen-mml/research/. 2020).

[9]   A. Smith, J. Tellinen, P. Mullner, K. Ullakko, Controlling twin variant configuration in a constrained Ni-Mn-Ga sample using local magnetic fields, Scripta Materialia 77 (2014) 68-70.

[10] A. Armstrong, K. Finn, A. Hobza, P. Lindquist, N. Rafla, P. Mullner, A motionless actuation system for magnetic shape memory devices, Smart Materials and Structures 26(10) (2017).

[11] D. Jiles, Introduction to magnetism and magnetic materials, CRC press2015.

[12] D. Kellis, A. Smith, K. Ullakko, P. Mullner, Oriented single crystals of Ni-Mn-Ga with very low switching field, Journal of Crystal Growth 359 (2012) 64-68.

[13] I. Suorsa, E. Pagounis, K. Ullakko, Position dependent inductance based on magnetic shape memory materials, Sensors and Actuators a-Physical 121(1) (2005) 136-141.

[14] D. Meeker, Finite Element Method Magnetics--Version 4.0 User's Manual, (2006).

[15] I. Suorsa, E. Pagounis, K. Ullakko, Magnetization dependence on strain in the Ni-Mn-Ga magnetic shape memory material, Applied Physics Letters 84(23) (2004) 4658-4660.

[16] T. Schiepp, M. Maier, E. Pagounis, A. Schluter, M. Laufenberg, FEM-Simulation of Magnetic Shape Memory Actuators, Ieee Transactions on Magnetics 50(2) (2014).

CHAPTER NINE: SUMMATIVE DISCUSSION, CONCLUSIONS AND FUTURE WORK

This dissertation addresses problems encountered in MSM devices. In Chapter 4, we study a material system to develop strategies for increasing the operating temperatures of the material. In the end, we do not manage to increase the operating temperature for the Ni-Mn-Ga-Fe-Cu alloy system compared to Ni-Mn-Ga system. We however develop a criterion for identifying compositions with the 10M phase for Ni-Mn-Ga-Fe-Cu 10M phase of Ni-Mn-Ga-Fe-Cu. We find that the overall *e/a* is not alone a good predictor of transformation temperatures for this quinary alloy. We define a new parameter: the elemental *e/a* ratio. With this parameter, we separate the effects of each element on the phase transformation temperature. The elemental *e/a* is a phenomenological parameter and did not consider the underlying physics. To evaluate the fundamental parameters of element occupancy, *ab initio* DFT calculations might be considered [91, 92]. However, we find certain trends which can guide alloying strategies. Alloying of Ni-Mn-Ga to improve actuator operating temperatures is an ongoing project conducted by groups around the world. While the proposed parameter has only been applied to the Ni-Mn-Ga-Fe-Cu system, we invite other researchers to also uses this parameter in the evaluation and design of their alloys. For example, Perez-Checa *et al*. study the effects of the Ni-Mn-Ga-Fe-Co-Cu alloys [93-95]. Sozinov *et al.* [96] reported on a 14M martensite which

shows Type II twins, in Ni-Mn-Ga-Fe. The results of this study inform future work towards modifying the transformation temperatures of Ni-Mn-Ga based MSM alloys.

Micropeening, in Chapter 5 substantially improves the functional properties of MSMA. The process was first pioneered by Adaptamat Ltd. Here we present a focused study on the effect of micropeening on magnetic switching and fatigue (Chapter Five) and localized actuation (Chapter 6).

As reported in other studies [80] the fine twin lamellar has a greater twinning stress than that of a Type II twin boundary. Low twinning stress corresponds to high efficiency in MSM actuators; thus the Type II twin boundary seems desirable. However, actuators based on the type II twin boundary do not exist yet because no method of stabilizing a single mobile type II twin boundary has been found to date. Practically, as an actuator, a single twin boundary motion is stochastic and results in quick fracture of the actuator due to the concentration of magnetostresses upon defects [71]. But compared to a type I twin boundary, the micropeened element exhibits lower twinning stress up to about 3% strain. This is the region that can be actuated at high efficiencies with long fatigue life.

The cause of the initial high mobility we propose to be due to the high twin boundary density. The twin boundaries interact with the stressed surface layer in such a way that preserves many disconnections. These disconnections respond readily to a subtle variation in the magnetic field or mechanical stress. Such stored disconnections lead to magnetoelastic properties as opposed to magnetoplastic properties [40, 97]. Veligatla *et al*. further suggested that increased twin density introduce magnetoelastic defects, which leads to hardening [98]. The increased magnetoelasticity causes more elastic

deformations, such as the curvature of the micropeened element compared to that of the polished element, in Figure 6-5b.

If the fine twin lamellar consists of a mixture of type I and type II twins (we currently do not know the twin boundary type in the lamellar), this may be the source of the initial high mobility. The twin boundaries spanning an element can be composed of sections of type I and type II twins [99]. It might be possible that a fine twin structure may take a lamellar of fine twins with mixed twin types. Such an element might have superior functional properties. For example, twinning stress would be lower than type I twins as we determined in [61]. At the beginning of deformation, highly mobile type II twin boundaries would move first at a low stress. With increasing strain, type II twin boundaries encounter other twins and get blocked, resulting in hardening. The effect of temperature upon the material might be between that of Type I twins ($T_A - 0.04$ MPa/K) [60], and that of Type II twins, which have nearly zero temperature dependencies [66, 100]. A mixed type, fine twin microstructure might be both mobile and have a greater operating temperature range.

Applying the micropeening process to the actuator in Chapter 6, we find that the increased magnetoelasiticy has substantial effects on the mechanical behavior of the MSM element transducer. The micropeening treatment causes the material to exhibit a deformation with a "hump" and a shrinkage. The hump we explain as another magnetoelastic effect. Whereas a shrinkage acts as a "negative displacement" mechanism and draws the fluid in by creating a vacuum, the hump acts more akin to the traditional peristaltic motion of larger pumps which drives the fluid forward. The hump further creates a strong seal between subsequent shrinkages that prevents backflow. This

explains the high pressures generated by micropeened element micropumps [26], which exceeds the head pressure of commercially available micropumps by at least one order of magnitude, for most technologies even two or three orders of magnitude [84-86].

The surface treatment causes other effects. For example, the magnetoelastic behavior is predictable, smooth, and repeatable. Magnetoplastic behavior is very sensitive to changes in history from actuation cycle to actuation cycle when not subject to a restoring force [15]. Likewise, the magnetoelasticity makes the shape of the deformation per cycle repeatable, shown for example in the highly repeatable flow rate profile in Figure 6.15. At $\alpha = 90°$ in Figure 6-6b the peak maximum of the hump was $+18$ µm and the bottom minimum was -18 µm. Therefore, while fine twin microstructure is associated with lower MFIS, we find that the volume of the shrinkage in the micropeened and polished states are similar.

Magnetoelasticity enhances the precision of the MSM micropump. In the polished element in Figure 6-6a, the shrinkage ends its stroke at $\alpha = 0°$. At $+18$ deg, the topology has two shallow shrinkages. At $36°$, the right shrinkage vanishes. The fluid which would be in the shrinkage, in the case of the MSM micropump, would thus be pushed out slowly over a $36°$ angle range. In the micropeened element, Figure 6.6b, it is a bit hard to predict shrinkage shape, as the constraints are different. We can however assume due to high magnetoelasticity, a rigid top plate might "push down" the hump such that the shrinkage volume increases. In the actuation envelope for the micropeened sample, it is similarly difficult to delineate where one shrinkage ends and another begins. However, taking again the shrinkage at $0°$, the shrinkage is mostly transitioned out by $90°$. The system flows from state to state smoothly. Correspondingly, the micropeened element has a

flowrate that continually oscillates, as found in Figure 6-15. In the micropump of Saren *et al.* [26], the flowrate stochastic spikes up to about 65 µL/min, which indicates the quick collapse of the shrinkage. We find the micropeening gives the pump a smooth, softly oscillating flow rate. The magnetoelasticity tends to move the material as almost a ripple down the element, which suggests the possibility of finely controlling the flowrate by controlling the motor. By applying a variable motor speed in inverse relation to the flow rate at a constant speed, the flowrate of the MSM element could be made constant. Pumped slowly, such that the shrinkage moves slowly, we can stop it at a defined position.

The source of the asymmetry of the device is the asymmetrical interaction of the magnetic field with the twin boundaries. The magnetic field prefers to take orthogonal orientations across a twin boundary. The rotating magnetic field interacts with a fixed plane set by the twin boundary orientation. We find that this fixed twin boundary plane does not change upon the reversal of the magnet rotation direction. The asymmetrical response of the surface topology in Figure 6-8 is thus due in part to the twin plane orientation. The amplitude depends upon the magnet's direction of rotation. Rotated clockwise, against the twin boundaries, the response has a relatively larger amplitude than rotated "with" the twin boundaries. Thus, we find an additional parameter upon the system which controls the behavior of the actuator. *The twin plane orientation* largely affects the response for devices actuated by heterogeneous magnetic fields.

In Chapter 7, we propose a method of using opposed stationary coils to cause the MSM element to switch in a manner akin to an MSM micropump. The purpose of this device is to switch a vertical magnetic field between two locations of the element and

thereby nucleate and move a twin. The switching process includes the removal of the twin above one pole and the formation of a new twin on the other pole. The twin does not however move from one pole to the other. The device, thus, would not be predicted to advance a twin along an MSM element. The mechanism is not suitable to replace the micromotor based drive system for the micropump. However, the mechanism may be used for a valve where the formation of a shrinkage opens a channel for fluid flow.

We come to perhaps the most difficult puzzle to solve. In the first EM drive, we are only able to generate and switch the twin at a magnetic field of 500 mT (measured in the airgap), which is much higher than the switching field for the MSM element of 150 mT (measured in the uniform field of a vibrating sample magnetometer). The effect is not explained by the nature of the constraints or the high demagnetization factor expected for the Ni-Mn-Ga element in the magnetic circuit. This difficulty stands in stark contrast to the deformation driven by the permanent magnet, which is very smooth, easy to rotate, and has high efficiency of coupling the magnet rotation into deformation [24].

In Chapter 8, we compare the magnetic field energy (MFE) of two systems: an EM drive with two juxtaposed rows of magnetic poles, with a permanent magnet (PM) driven system, which is the system known to effectively create the motion of MSM micropumps. In the comparison of the magnetic field energies between the two systems, the PM supplies a large amount of magnetic field energy available for the MSM to convert into twin nucleation and motion. The MFE of the PM system is about 2.0 - 12.7 mJ.

The maximum MFE energy generated in the EM system is only 2.28 mJ. In the EM system, the MFE is proportional to the reluctance of the circuit. Therefore, the MFE

increases when we insert the MSM element. In contrast, for the PM system, the MSM element can convert the large static MFE supplied by the PM into twin nucleation and motion.

The challenge with the EM drive is to increase the total magnetic energy in the system. We may add this energy with a biasing permanent magnet. Future computer simulations may address the PM system's other energies to discover the hitherto unknown effect of the anisotropy saturation behavior in locally actuated MSM devices. The simulation should also approximate the saturation behavior to fully simulate the twinning phenomena in MSM elements.

To move twins with a local magnetic field generated by an electromagnet, Smith *et al.* [89] imposed a rigid end constraint that locked in a twin volume fraction. Pulsed with a high field generator, the element switched at the pole and concentrated the distributed twins into one dense area of twins. A question for simulation would be whether the magnetic field generated by a permanent magnet stabilizes the twins by biasing the system to have a high MFE.

APPENDIX A

Micropeening

In this appendix section, we consider the micropeening apparatus. Micropeening causes a layer of plastic deformation upon the Ni-Mn-Ga element surface, which stabilizes a fine twin microstructure with twin boundaries of relatively high mobility, as shown in Chapter 5 and Chapter 6.

We micropeen at quite low energies compared to the industrial shotpeening processes. The equipment is quite simple, a motorized stage combined with a small air eraser device that accelerates the media. The air eraser atomizes a hopper of the media, then accelerates the particle stream through the nozzle. We use a pneumatic valve to open and close the input air. We control pressure supplied to the air eraser by a regulator.

We then use a linear stage controlled by a stepper motor to draw the element through the air stream. We heat a Peltier module to transform the element into austenite before conducting the peening. We measured the temperature of the stage using a National Instruments-TC01. We used magnets to hold the sample to the Peltier stage and stay below the material's Curie temperature. A similar process has been reported before as hot shot peening [80].

We first look into the components of the device. Then we characterize the shot stream geometry. We look into the geometry of the surface layer by using optical profilometry. We give data of roughness changes during the peening process, which are non-linear, and similar irrespective of phase peened in (martensite vs austenite). We briefly characterize the fine twin lamellar, and some associated magneto-mechanical properties. Finally, we include a shortened version of the machine's standard operating procedures..

Equipment

The micropeening was conducted inside of a sandblasting cabinet. The control systems were located outside of the cabinet. The components are shown in Figure A-1. Process air entered the system, and was controlled by a pressure regulator. The regulated air was switched on and off by the solenoid valve. The Arduino and motor controller (Sparkfun, Easy-Driver) were located in the electronics housing. A 12V power supply powered the electronics and motor. A variable DC power supply powered the Peltier module (indicated in Figure A-2).

Figure A-1:   The micropeening apparatus is located within a sandblasting cabinet.
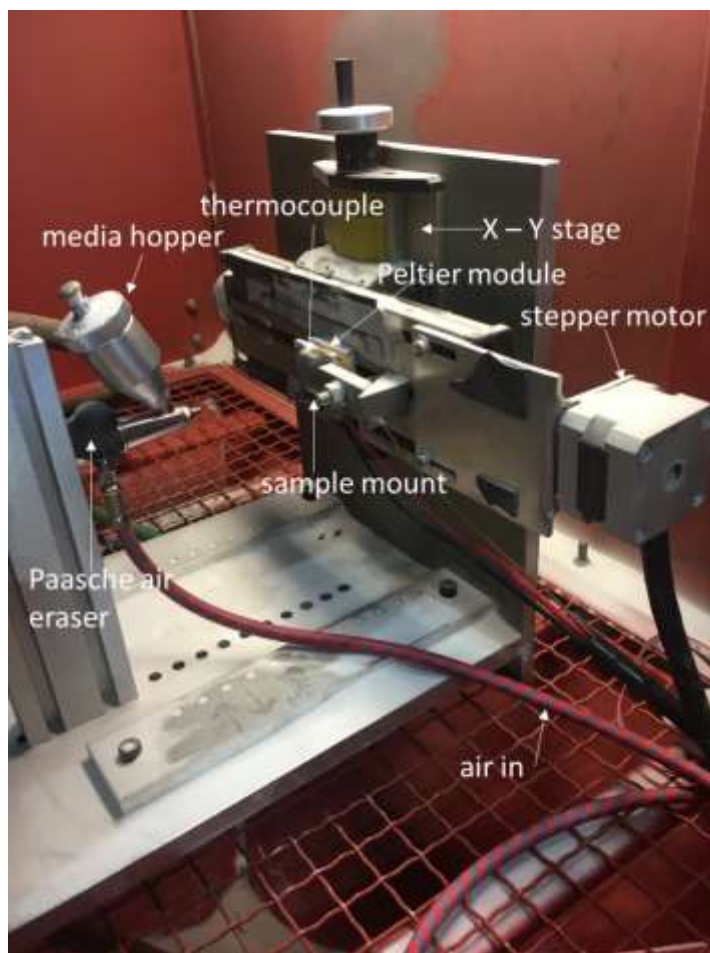
Figure A-2: **The micropeening apparatus inside of the cabinet. A stepper motor draws the MSM element across an atomized stream of glass spheres which bombard the element surface. A Peltier module heats the MSM element into the Austenite stage for micropeening.**

Within the chamber, the air eraser (Paasche) was positioned perpendicular to the

MSM element. The manual button on the air eraser was permanently fixtured in the

depressed position. We used several different glass media in the initial characterization.

We eventually settled upon Precision Micro-Abrasive Powder - 50 Micron Glass Beads

from Comco Inc. The media was loaded into the hopper. The thermocouple measured the

temperature of the sample mount generated by heat of the Peltier module. The Peltier

module was sandwiched between two aluminum plates. Work-holding magnets were

glued to the outer aluminum plate. A thermocouple was glued to the top aluminum plate.
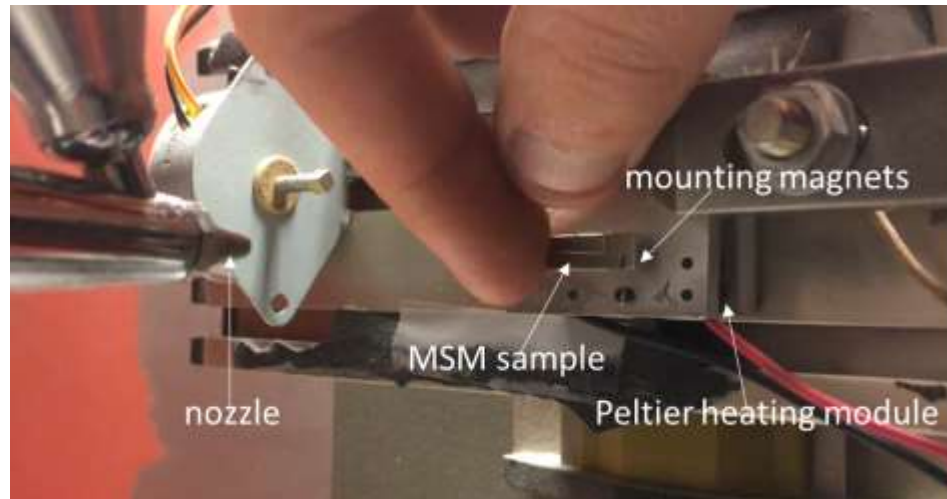
Figure A-3:   **Close up view of the peening components. The MSM sample is attached to the heating stage by magnets.**

The MSM element was centered on the mounting magnets (Figure A-3) The stage was moved such that the mount started outside of the incident stream and passed fully through the stream driven at constant velocity. In this way, we measured the incident time by dividing the stream diameter (characterized in Figure A-4) by the velocity of the stage, which is driven by a stepper motor. The speed of the motor was adjusted by altering the stepping parameters.

Characterization

We characterized the deformation upon test strips of aluminum foil, then bombarded them at varying pressure, duration, and distance between the nozzle and MSM element. We measured the impacted area with a microscope and default image stitching software. We converted the files to grayscale in Image J and measured a profile of the contrast. The heavily damaged areas showed up as dark, while the undamaged showed as white. We found that the width of the stream did not vary more than about 1 mm from 20 psi to 100 psi. The apparatus minimum pressure was 10 psi. The red dashed line in Figure A-4 indicates the approximate width of the stream of 12 mm. This was

sufficient for our purposes and we used 5 cm as the distance between the MSM element and nozzle in the future tests.
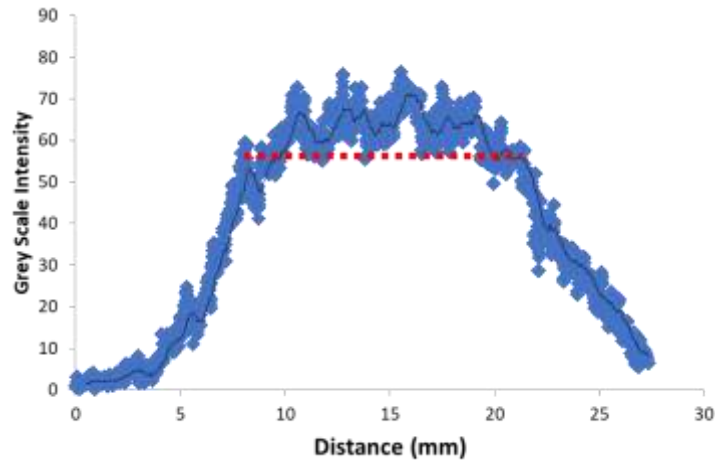
Figure A-4: **At 5 mm distance between nozzle and sample, the surface roughness took a plateau of about 12 mm width. The jagged nature of the plateau is related to the contrast errors in the default microscope stitching software.**

We then looked at the effects of the pressure upon the layer of surface damage on the MSM sample surface. Figure A-5 shows a sample that was micropeened on the right side at about 15 psi and masked on the left side with tape. The peening pressure is just at the onset of deformation.

Figure A-5: **Optical micrograph of a sample at the masking following 15psi peening for 10-second duration. The surface scratches appear to be deeper than the damaged layer.**

Figure A-6 shows the peened region surface structure following when treated at 50 psi for 8 sec.
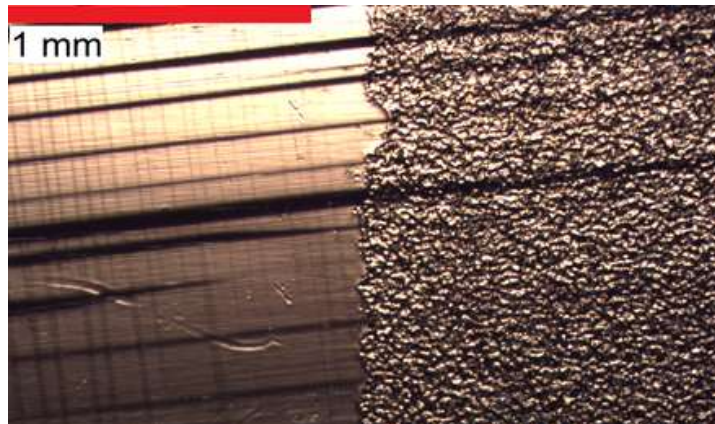
Figure A-6:   The contrast between an Austenite peened region at 50 psi compared to a non-peened region. When cooled to martensite, in the peened region, smaller twin boundaries and surface imperfections are not visible while larger twins are visible.

Figure A-7 shows the structure at 20 psi for an 8.0 second duration treatment.
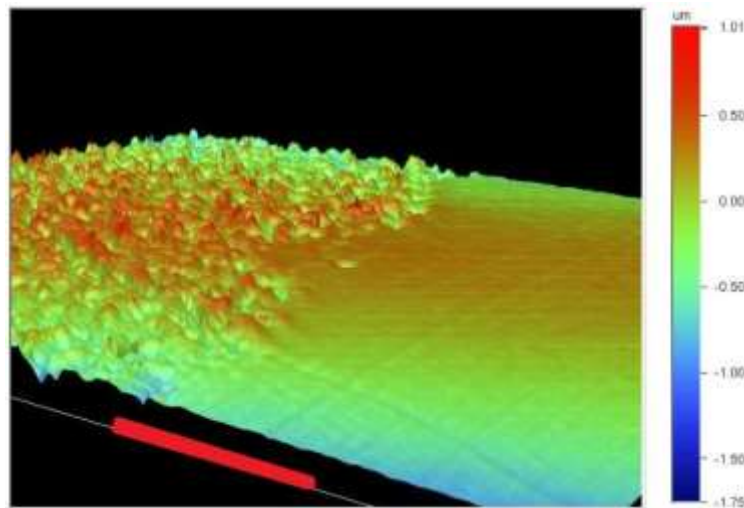
Figure A-7:   Martensite-peened region at 20 psi contrasted with a non-peened region. Image produced with a WYCO optical profilometer. The non-peened region was masked with tape to maintain its structure.

Figure A-8 shows the surface after peening at 30 psi for a duration of 10 seconds.
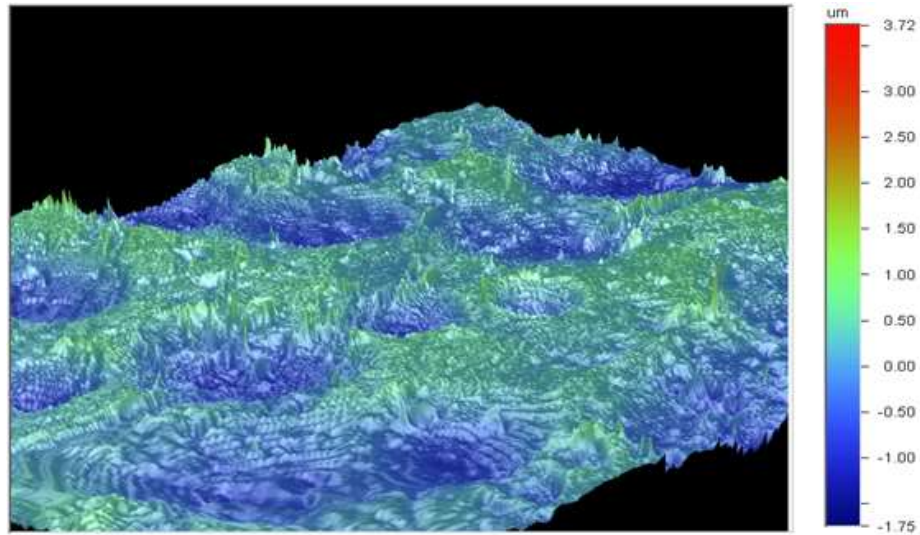
Figure A-8:   Optical profilometer image at 50x of a micro-peened sample treated at 30 psi.

Figure A-9 shows the evolution in average surface roughness with increasing pressure for the samples micropeened in martensite (orange) and austenite (blue). The evolution of roughness takes a step function, where initially no plastic damage occurs. At pressures greater than 15 psi, the peening media begins to deform the surface. Between 15-30 psi, the roughness increases with increasing damage. Above 30 psi, the element surface does not accrue further roughness, but may accrue further damage by increased depth of the damaged layer.

Figure A-10 shows a switching field curve for a 10M sample which was micropeened at 15 psi (black) and 30 psi (red). The 15 psi treatment caused deformation by a Type 1 twin. After removing damage and treating at 30 psi the element takes a different and smooth deformation response.
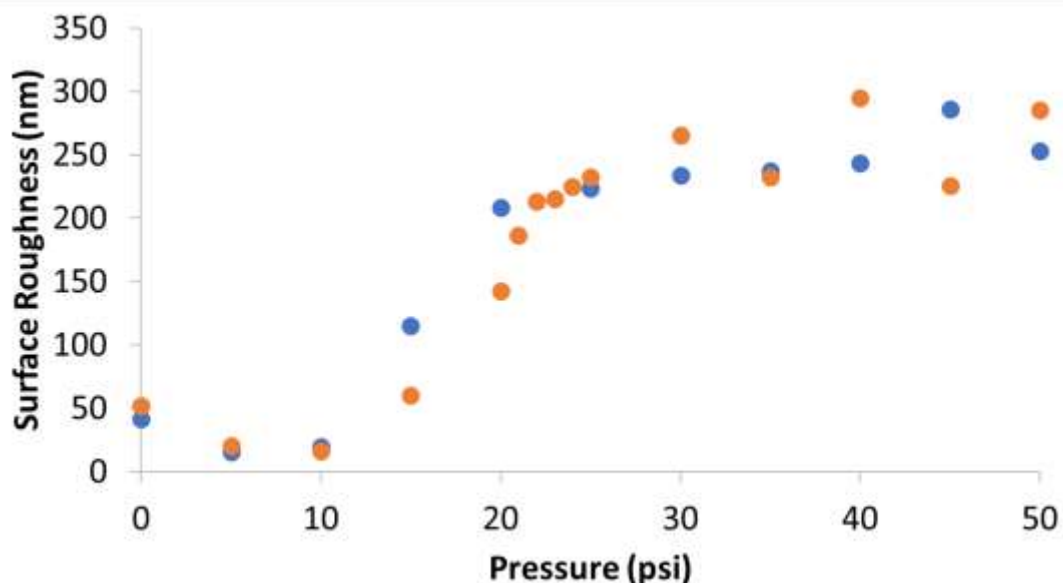
Figure A-9: Evolution in roughness with increased peening pressure for martensite samples (orange), and austenite peened samples (blue). Both phases show an inflection point where roughness rapidly evolves and then flattens with increased pressure. While increased peening pressure may cause greater surface damage, the surface roughness saturates.
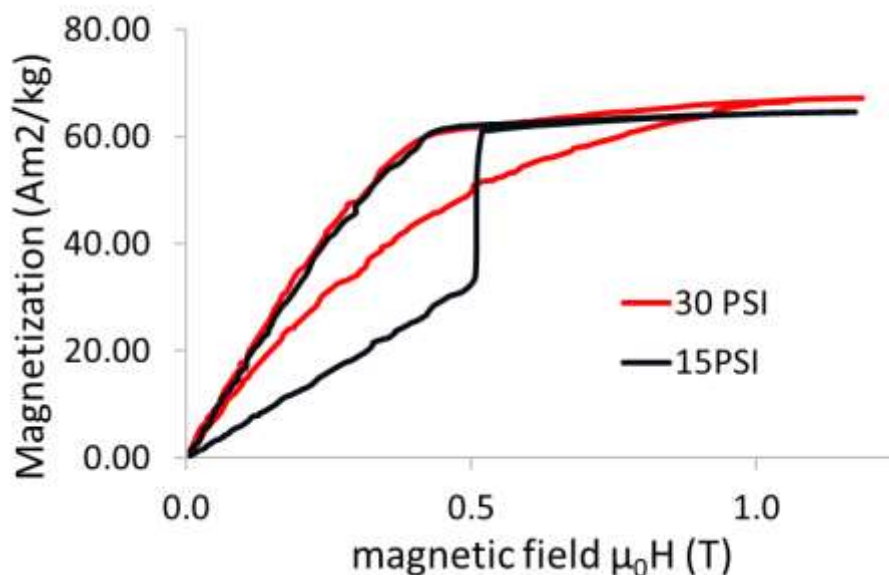
Figure A-10: The change to magnetomechanical behavior due to the micropeeining process. The 10M sample was micropeened at 15 psi, which gave a large switching field of about 0.5T. The switching of the sample micropeened at 30 psi was a gradual response, rather than an abrupt switching field.

Figure A-11: The fine twin lamellar structure that is caused by the micropeening surface treatment process. This is taken on the top view after cycling the element 500,000 times in MSM pump manner and following polishing to reveal the twin density.

In Figure A-11, we show the twin structure which evolved after 500,000 cycles in a MSM pump. The micropeened surface was polished away to show the twin lamellar structure.

Standard operating procedure

<u>Setup</u>

a.   Turn on the air. This is located inside HML 103, by the top left corner of the main doors.

b.   The green handle controls the air. When it is parallel with the pipe, air is flowing. If it is perpendicular, the air is off.

c.   Turn on the power. The powerstrip is located on the back of the micropeening station.

d.   Plug in Thermocouple and Arduino USBs. Arduino USB is a black cable; Thermocouple plugs into USB-TC01 Temperature Input Device.

e.   Launch TC01 Program: CD Drive > TC01 Launcher (blue icon) > Temperature

Logger > Select 'Type K' and '°C'.

f.   Launch Arduino IDE: Tools > Board > Arduino Uno

Open "MicropeeningMainDriver.ino", which is modified from Sparkfun's Easy

Driver demo file.

g.   If needed, the step number in the for loops of the StepForwardDefaulet() function

and the ReverseStepDefault() function can be changed to help center the magnetic

mount, or to alter the amount of time the element is passed through the stream of

glass beads. A good target is a treatment time of $t = 8$ seconds, calculated as the

treated diameter (12mm) divided by the motor speed, given the 1.0 mm pitch

leadscrews of the Proxxon stage.

h.   If needed, change to desired pressure by twisting black knob, however it is best to

not adjust unless changing parameters.

<u>Dry run</u>

a.   Turn on black power supply to supply heat to the magnetic mount. Refer

to the TC01 program to ensure that the temperature change is being read.

b.   Load acorn/hopper with 50μm glass beads.

c.   In the Arduino IDE: Tools > Serial Monitor. Input '1' or '2' to make a

pass. Motor should move and glass bead stream should be visible.

d.   Turn off black power supply.

<u>Run</u>

a.   Use beaker to fill hopper with glass beads every fourth pass.

b.   Place element on magnetic mount, and latch door shut.

c.   Turn on black power supply, and allow element to reach ≅ 80℃. The

element should be in austenite, but should not exceed its Curie

temperature.

d.   Once desired temperature has been reached, make a pass by entering '1' or

'2' into the Arduino Serial Monitor. The temperature drops a few degrees

during while the glass beads impact the sample.
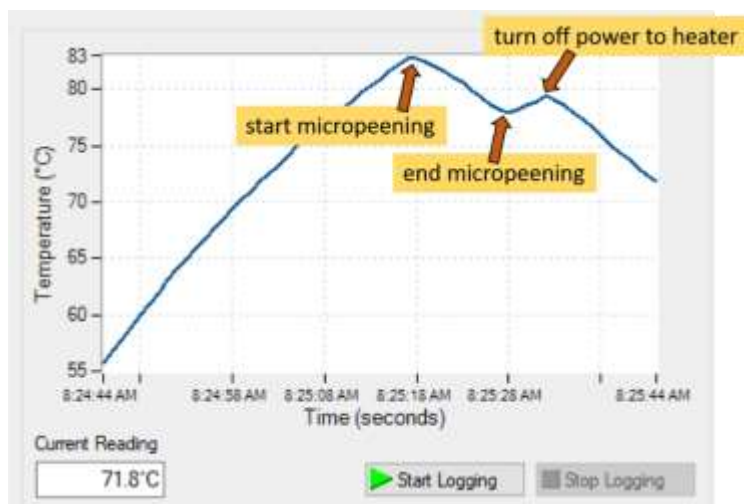
Figure A-12: The air stream incident upon the MSM sample causes slight cooling effect upon the sample. Such decrease should be considered in the targeted process temperature.

e.   Turn off black power supply once pass has finished. Allow element to

cool, remove from the magnetic mount, flip, and repeat on the other side.

f.   Refill hopper every four passes.

Shut down

a.   Turn off power strip

b.   Turn off air (inside HML 103)

c.   Eject TC01 properly and unplug both USBs

d.   Cabinet light off.

REFERENCES

[1]   J.J. Rhyne, S. Foner, E.J. McNiff, R. Doclo, Rare Earth Metal Single Crystals. I. High- Field Properties of Dy, Er, Ho, Tb, and Gd, Journal of Applied Physics 39(2) (1968) 892-893.

[2]   H.H. Liebermann, C.D. Graham, Plastic and magnetoplastic deformation of Dy single crystals, Acta Metallurgica 25(7) (1977) 715-720.

[3]   P.J. Webster, K.R.A. Ziebeck, S.L. Town, M.S. Peak, Magnetic Order And Phase-Transformation In Ni2mnga, Philosophical Magazine B-Physics of Condensed Matter Statistical Mechanics Electronic Optical and Magnetic Properties 49(3) (1984) 295-310.

[4]   V.A. Chernenko, V.V. Kokorin, A.N. Vasilev, Y.I. Savchenko, The Behavior Of The Elastic-Constants At The Transformation Between The Modulated Phases In Ni2mnga, Phase Transitions 43(1-4) (1993) 187-191.

[5]   I.K. Zasimchuk, V.V. Kokorin, V.V. Martynov, A.V. Tkachenko, V.A. Chernenko, Crystal-Structure Of Martensite In Ni2mnga Geislers Alloy, Fizika Metallov I Metallovedenie (6) (1990) 110-114.

[6]   V.V. Kokorin, V.A. Chernenko, V.I. Valkov, S.M. Konoplyuk, E.A. Khapalyuk, Magnetic transformation in Ni2MnGa compounds, Fizika Tverdogo Tela 37(12) (1995) 3718-3722.

[7]   A.N. Vasilev, V.V. Kokorin, Y.I. Savchenko, V.A. Chernenko, Magnetoelastic Properties Of The Ni2mnga Single-Crystal, Zhurnal Eksperimentalnoi I Teoreticheskoi Fiziki 98(4) (1990) 1437-1441.

[8]   V.V. Kokorin, V.V. Martynov, V.A. Chernenko, Stress - Induced Martensitic Transformations In Ni2mnga, Scripta Metallurgica Et Materialia 26(2) (1992) 175-177.

[9]   A.N. Vasilev, A. Kaiper, V.V. Kokorin, V.A. Chernenko, T. Takagi, J. Tani, Structural Phase-Transitions Induced In Ni2mnga By Low-Temperature Uniaxial Compression, Jetp Letters 58(4) (1993) 306-309.

[10]   K. Ullakko, J.K. Huang, C. Kantner, R.C. Ohandley, V.V. Kokorin, Large magnetic-field-induced strains in Ni2MnGa single crystals, Applied Physics Letters 69(13) (1996) 1966-1968.

[11]   E. Pagounis, A. Laptev, J. Jungwirth, M. Laufenberg, M. Fonin, Magnetomechanical properties of a high-temperature Ni-Mn-Ga magnetic shape memory actuator material, Scripta Materialia 88 (2014) 17-20.

[12]   S.J. Murray, M. Marioni, S.M. Allen, R.C. O'Handley, T.A. Lograsso, 6% magnetic-field-induced strain by twin-boundary motion in ferromagnetic Ni-Mn-Ga, Applied Physics Letters 77(6) (2000) 886-888.

[13]   A. Sozinov, A.A. Likhachev, N. Lanska, K. Ullakko, Giant magnetic-field-induced strain in NiMnGa seven-layered martensitic phase, Applied Physics Letters 80(10) (2002) 1746-1748.

[14]   V.A. Chernenko, V.A. L'Vov, S.P. Zagorodnyuk, T. Takagi, Ferromagnetism of thermoelastic martensites: Theory and experiment, Physical Review B 67(6) (2003) 6.

[15]   P. Mullner, V.A. Chernenko, G. Kostorz, Large cyclic magnetic-field-induced deformation in orthorhombic (14M) Ni-Mn-Ga martensite, Journal of Applied Physics 95(3) (2004) 1531-1536.

[16]   A. Sozinov, N. Lanska, A. Soroka, W. Zou, 12% magnetic field-induced strain in Ni-Mn-Ga-based non-modulated martensite, Applied Physics Letters 102(2) (2013).

[17]   P. Mullner, V.A. Chernenko, M. Wollgarten, G. Kostorz, Large cyclic deformation of a Ni-Mn-Ga shape memory alloy induced by magnetic fields, Journal of Applied Physics 92(11) (2002) 6708-6713.

[18]   A. Sozinov, A.A. Likhachev, N. Lanska, K. Ullakko, V.K. Lindroos, 10% magnetic-field-induced strain in Ni-Mn-Ga seven-layered martensite, Journal De Physique Iv 112 (2003) 955-958.

[19]   I. Suorsa, J. Tellinen, K. Ullakko, E. Pagounis, Voltage generation induced by mechanical straining in magnetic shape memory materials, Journal of Applied Physics 95(12) (2004) 8054-8058.

[20]   P. Mullner, V.A. Chernenko, G. Kostorz, Stress-induced twin rearrangement resulting in change of magnetization in a Ni-Mn-Ga ferromagnetic martensite, Scripta Materialia 49(2) (2003) 129-133.

[21]   I. Suorsa, E. Pagounis, K. Ullakko, Position dependent inductance based on magnetic shape memory materials, Sensors and Actuators a-Physical 121(1) (2005) 136-141.

[22]   I. Karaman, B. Basaran, H.E. Karaca, A.I. Karsilayan, Y.I. Chumlyakov, Energy harvesting using martensite variant reorientation mechanism in a NiMnGa magnetic shape memory alloy, Applied Physics Letters 90(17) (2007).

[23]   K. Ullakko, L. Wendell, A. Smith, P. Mullner, G. Hampikian, A magnetic shape memory micropump: contact-free, and compatible with PCR and human DNA profiling, Smart Materials and Structures 21(11) (2012).

[24]   A.R. Smith, A. Saren, J. Jarvinen, K. Ullakko, Characterization of a high-resolution solid-state micropump that can be integrated into microfluidic systems, Microfluidics and Nanofluidics 18(5-6) (2015) 1255-1263.

[25]   S. Barker, E. Rhoads, P. Lindquist, M. Vreugdenhil, P. Mullner, Magnetic Shape Memory Micropump for Submicroliter Intracranial Drug Delivery in Rats, Journal of Medical Devices-Transactions of the Asme 10(4) (2016).

[26]   A. Saren, A.R. Smith, K. Ullakko, Integratable magnetic shape memory micropump for high-pressure, precision microfluidic applications, Microfluidics and Nanofluidics 22(4) (2018).

[27]   E. Pagounis, R. Chulist, M. Szczerba, M. Laufenberg, High-temperature magnetic shape memory actuation in a Ni–Mn–Ga single crystal, Scripta Materialia 83 (2014) 29-32.

[28]   J.P. Joule, XVII. On the effects of magnetism upon the dimensions of iron and steel bars, The London, Edinburgh, and Dublin Philosophical Magazine and Journal of Science 30(199) (1847) 76-87.

[29]   D.M. Addington, D.L. Schodek, Smart materials and new technologies: for the architecture and design professions, Routledge2005.

[30]   T. Duerig, A. Pelton, D. Stockel, An overview of nitinol medical applications, Materials Science and Engineering a-Structural Materials Properties Microstructure and Processing 273 (1999) 149-160.

[31]   J.M. Jani, M. Leary, A. Subic, M.A. Gibson, A review of shape memory alloy research, applications and opportunities, Materials & Design 56 (2014) 1078-1113.

[32]   A. Ölander, An electrochemical investigation of solid cadmium-gold alloys, Journal of the American Chemical Society 54(10) (1932) 3819-3833.

[33]   L.C. Chang, T.A. Read, Behavior of the elastic properties of AuCd, Trans Met Soc AIME 191 (1951) 47.

[34]   G.V. Kurdyumov, L.G. Khandros, On the thermoelastic equilibrium on martensitic transformations, pp. 211-214.

[35]   G.B. Kauffman, I. Mayo, The story of nitinol: the serendipitous discovery of the memory metal and its applications, The chemical educator 2(2) (1997) 1-21.

[36]   F.E. Wang, W.J. Buehler, S.J. Pickart, Crystal Structure and a Unique``Martensitic''Transition of TiNi, Journal of Applied Physics 36(10) (1965) 3232-3239.

[37]   W.J. Buehler, J.V. Gilfrich, R.C. Wiley, Effect of low- temperature phase changes on the mechanical properties of alloys near composition TiNi, Journal of applied physics 34(5) (1963) 1475-1477.

[38] https://commons.wikimedia.org/wiki/File:NiTi_structure_transformation.jpg

[39] A.R. Pelton, Nitinol fatigue: a review of microstructures and mechanisms, Journal of Materials Engineering and Performance 20(4-5) (2011) 613-617.

[40] P. Müllner, G. Kostorz, Microstructure of Magnetic Shape-Memory Alloys: Between Magnetoelasticity and Magnetoplasticity, Materials Science Forum 583 (2008) 43-65.

[41] E. Faran, D. Shilo, The kinetic relation for twin wall motion in NiMnGa, Journal of the Mechanics and Physics of Solids 59(5) (2011) 975-987.

[42] E. Faran, D. Shilo, The kinetic relation for twin wall motion in NiMnGa-part 2, Journal of the Mechanics and Physics of Solids 61(3) (2013) 726-741.

[43] A.R. Smith, J. Tellinen, K. Ullakko, Rapid actuation and response of Ni-Mn-Ga to magnetic-field-induced stress, Acta Materialia 80 (2014) 373-379.

[44] W.D. Callister Jr, D.G. Rethwisch, Fundamentals of materials science and engineering: an integrated approach, John Wiley & Sons2012.

[45] D. Jiles, Introduction to magnetism and magnetic materials, CRC press2015.

[46] O. Heczko, L. Straka, N. Lanska, K. Ullakko, J. Enkovaara, Temperature dependence of magnetic anisotropy in Ni-Mn-Ga alloys exhibiting giant field-induced strain, Journal of Applied Physics 91(10) (2002) 8228-8230.

[47] D. Meeker, Finite element method magnetics, FEMM 4 (2010) 32.

[48] H.C. Lovatt, P.A. Watterson, Energy stored in permanent magnets, IEEE Transactions on Magnetics 35(1) (1999) 505-507.

[49] P. Campbell, Comments on "Energy stored in permanent magnets", IEEE Transactions on Magnetics 36(1) (2000) 401-403.

[50] F. Heusler, Über magnetische manganlegierungen, Verhandlungen der Deutschen Physikalischen Gesellschaft 5 (1903) 219.

[51]   P. Lázpita, J. Barandiarán, J. Gutiérrez, J. Feuchtwanger, V. Chernenko, M. Richard, Magnetic moment and chemical order in off-stoichiometric Ni–Mn–Ga ferromagnetic shape memory alloys, New Journal of Physics 13(3) (2011) 033039.

[52]   S.K. Wu, S.T. Yang, Effect of composition on transformation temperatures of Ni–Mn–Ga shape memory alloys, Materials Letters 57(26-27) (2003) 4291-4296.

[53]   R. Niemann, U.K. Rößler, M.E. Gruner, O. Heczko, L. Schultz, S. Fähler, The role of adaptive martensite in magnetic shape memory alloys, Advanced Engineering Materials 14(8) (2012) 562-581.

[54]   Z. Li, N. Xu, Y. Zhang, C. Esling, J.-M. Raulot, X. Zhao, L. Zuo, Composition-dependent ground state of martensite in Ni–Mn–Ga alloys, Acta Materialia 61(10) (2013) 3858-3865.

[55]   J. Pons, V.A. Chernenko, R. Santamarta, E. Cesari, Crystal structure of martensitic phases in Ni-Mn-Ga shape memory alloys, Acta Materialia 48(12) (2000) 3027-3038.

[56]   M. Zeleny, L. Straka, A. Sozinov, O. Heczko, Transformation Paths from Cubic to Low-Symmetry Structures in Heusler Ni2MnGa Compound, Scientific Reports 8 (2018).

[57]   V.A. Chernenko, Compositional instability of β-phase in Ni-Mn-Ga alloys, Scripta Materialia 40(5) (1999) 523-527.

[58]   A. Sozinov, Low Twinning Stress Ni2Mn(1+X)Ga(1-X) Alloys, ICFSMA, Bilbao, 2009.

[59]   O. Heczko, Magnetic shape memory effect and highly mobile twin boundaries, Materials Science and Technology 30(13A) (2014) 1559-1578.

[60]   L. Straka, A. Soroka, H. Seiner, H. Hanninen, A. Sozinov, Temperature dependence of twinning stress of Type I and Type II twins in 10M modulated Ni-Mn-Ga martensite, Scripta Materialia 67(1) (2012) 25-28.

[61]   D. Musiienko, F. Nilsén, A. Armstrong, M. Rameš, R.H. Colman, P. Müllner, O. Heczko, L. Straka, Universality of Temperature Dependence of Twinning Stress in Ni-Mn-Ga 10M Martensite and Effect of Crystal Quality, Available at SSRN 3606816.

[62]   O. Heczko, L. Straka, Temperature dependence and temperature limits of magnetic shape memory effect, Journal of Applied Physics 94(11) (2003) 7139-7143.

[63]   O. Heczko, K. Ullakko, Effect of temperature on magnetic properties of Ni-Mn-Ga magnetic shape memory (MSM) alloys, Ieee Transactions on Magnetics 37(4) (2001) 2672-2674.

[64]   A. Sozinov, N. Lanska, A. Soroka, L. Straka, Highly mobile type II twin boundary in Ni-Mn-Ga five-layered martensite, Applied Physics Letters 99(12) (2011).

[65]   D. Kellis, A. Smith, K. Ullakko, P. Mullner, Oriented single crystals of Ni-Mn-Ga with very low switching field, Journal of Crystal Growth 359 (2012) 64-68.

[66]   O. Heczko, V. Kopecký, A. Sozinov, L. Straka, Magnetic shape memory effect at 1.7 K, Applied Physics Letters 103(7) (2013) 072405.

[67]   O. Heczko, L. Straka, I. Aaltio, S.P. Hannula, Strain and concurrent magnetization changes in magnetic shape memory Ni–Mn–Ga single crystals – experiment and model, Materials Science and Engineering: A 481-482 (2008) 283-287.

[68]   O. Heczko, L. Straka, S.-P. Hannula, Stress dependence of magnetic shape memory effect and its model, Materials Science and Engineering: A 438-440 (2006) 1003-1006.

[69]   M. Chmielus, V.A. Chernenko, W.B. Knowlton, G. Kostorz, P. Mullner, Training, constraints, and high-cycle magneto-mechanical properties of Ni-Mn-Ga magnetic shape-memory alloys, European Physical Journal-Special Topics 158 (2008) 79-85.

[70]   O. Heczko, Understanding Motion of Twin Boundary-A Key to Magnetic Shape
        Memory Effect, Ieee Transactions on Magnetics 50(11) (2014).

[71]   P. Müllner, V.A. Chernenko, D. Mukherji, G. Kostorz, Cyclic magnetic-field-
        induced deformation and magneto-mechanical fatigue of Ni-Mn-Ga
        ferromagnetic martensites, MRS Online Proceedings Library Archive 785 (2003).

[72]   L. Straka, N. Lanska, K. Ullakko, A. Sozinov, Twin microstructure dependent
        mechanical response in Ni-Mn-Ga single crystals, Applied Physics Letters 96(13)
        (2010).

[73]   N.J. Kucza, C.L. Patrick, D.C. Dunand, P. Müllner, Magnetic-field-induced
        bending and straining of Ni–Mn–Ga single crystal beams with high aspect ratios,
        Acta Materialia 95 (2015) 284-290.

[74]   H.D. Chopra, C. Bailly, M. Wuttig, Domain structures in bent In-22.5 at.%Tl
        polydomain crystals, Acta Materialia 44(2) (1996) 747-751.

[75]   I. Aaltio, A. Soroka, Y. Ge, O. Soderberg, S.P. Hannula, High-cycle fatigue of
        10M Ni-Mn-Ga magnetic shape memory alloy in reversed mechanical loading,
        Smart Materials & Structures 19(7) (2010).

[76]   L. Straka, H. Hänninen, A. Soroka, Y. Ezer, Enhanced Fatigue Behavior of Ni-
        Mn-Ga Magnetic Shape Memory Alloys with Tailor-made Fine Twin
        Microstructure, 13th International Conference on New Actuators, Bremen,
        Germany, 2012.

[77]   T. Lawrence, P. Lindquist, K. Ullakko, P. Mullner, Fatigue life and fracture
        mechanics of unconstrained Ni-Mn-Ga single crystals in a rotating magnetic field,
        Materials Science and Engineering a-Structural Materials Properties
        Microstructure and Processing 654 (2016) 221-227.

[78]   M. Chmielus, K. Rolfs, R. Wimpory, W. Reimers, P. Mullner, R. Schneider,
        Effects of surface roughness and training on the twinning stress of Ni-Mn-Ga
        single crystals, Acta Materialia 58(11) (2010) 3952-3962.

[79]   M. Chmielus, C. Witherspoon, K. Ullakko, P. Mullner, R. Schneider, Effects of surface damage on twinning stress and the stability of twin microstructures of magnetic shape memory alloys, Acta Materialia 59(8) (2011) 2948-2956.

[80]   A. Tech, Y. Ezer, A. Soroka, L. Straka, Method of producing magnetic shape memory alloy elements and the use thereof, Adaptamat, USA, 2012.

[81]   K. Ullakko, M. Chmielus, P. Müllner, Stabilizing a fine twin structure in Ni–Mn–Ga samples by coatings and ion implantation, Scripta Materialia 94 (2015) 40-43.

[82]   D. Musiienko, A.R. Smith, A. Saren, K. Ullakko, Stabilization of a fine twin structure in Ni-Mn-Ga by a diamond-like carbon coating, Scripta Materialia 106 (2015) 9-12.

[83]   M. Chmielus, P. Müllner, Effects of Surface Pinning, Locking and Adaption of Twins on the Performance of Magnetic Shape-Memory Alloys, Trans Tech Publ, pp. 177-201.

[84]   M.W. Ashraf, S. Tayyaba, N. Afzulpurkar, Micro Electromechanical Systems (MEMS) Based Microfluidic Devices for Biomedical Applications, International Journal of Molecular Sciences 12(6) (2011) 3648-3704.

[85]   A. Nisar, N. AftuIpurkar, B. Mahaisavariya, A. Tuantranont, MEMS-based micropumps in drug delivery and biomedical applications, Sensors and Actuators B-Chemical 130(2) (2008) 917-942.

[86]   P. Woias, Micropumps - past, progress and future prospects, Sensors and Actuators B-Chemical 105(1) (2005) 28-38.

[87]   R.K. Sivamani, B. Stoeber, G.C. Wu, H. Zhai, D. Liepmann, H. Maibach, Clinical microneedle injection of methyl nicotinate: stratum corneum penetration, Skin Research and Technology 11(2) (2005) 152-156.

[88]   J. Gupta, S.S. Park, B. Bondy, E.I. Felner, M.R. Prausnitz, Infusion pressure and pain during microneedle injection into skin of human subjects, Biomaterials 32(28) (2011) 6823-6831.

[89]   A. Smith, J. Tellinen, P. Mullner, K. Ullakko, Controlling twin variant configuration in a constrained Ni-Mn-Ga sample using local magnetic fields, Scripta Materialia 77 (2014) 68-70.

[90]   P. Mullner, A. Armstrong, K. Finn, N. Rafla, Electrically driven magnetic shape memory apparatus and method, Google Patents, 2020.

[91]   M. Zeleny, A. Sozinov, T. Bjorkmand, L. Straka, R.M. Nieminen, Ab initio study of properties of Co- and Cu- doped Ni-Mn-Ga alloys, Materials Today-Proceedings 2 (2015) 601-604.

[92]   M. Zelený, A. Sozinov, L. Straka, T. Björkman, R.M. Nieminen, First-principles study of Co-and Cu-doped Ni 2 MnGa along the tetragonal deformation path, Physical Review B 89(18) (2014) 184103.

[93]   A. Pérez-Checa, D. Musiienko, A. Saren, A. Soroka, J. Feuchtwanger, A. Sozinov, J. Barandiaran, K. Ullakko, V. Chernenko, Study of the critical parameters for magnetic field-induced strain in high temperature Ni-Mn-Ga-Co-Cu-Fe single crystals, Scripta Materialia 158 (2019) 16-19.

[94]   A. Perez-Checa, J. Feuchtwanger, J. Barandiaran, A. Sozinov, K. Ullakko, V. Chernenko, Ni-Mn-Ga-(Co, Fe, Cu) high temperature ferromagnetic shape memory alloys: Effect of Mn and Ga replacement by Cu, Scripta Materialia 154 (2018) 131-133.

[95]   A. Pérez-Checa, J. Feuchtwanger, D. Musiienko, A. Sozinov, J.M. Barandiaran, K. Ullakko, V.A. Chernenko, High temperature Ni45Co5Mn25−xFexGa20Cu5 ferromagnetic shape memory alloys, Scripta Materialia 134 (2017) 119-122.

[96]   A. Sozinov, D. Musiienko, A. Saren, P. Vertat, L. Straka, O. Heczko, M. Zeleny, R. Chulist, K. Ullakko, Highly mobile twin boundaries in seven-layer modulated Ni-Mn-Ga-Fe martensite, Scripta Materialia 178 (2020) 62-66.

[97]   L. Straka, H. Hanninen, N. Lanska, A. Sozinov, Twin interaction and large magnetoelasticity in Ni-Mn-Ga single crystals, Journal of Applied Physics 109(6) (2011).

[98]   M. Veligatla, C.J. Garcia-Cervera, P. Müllner, Magnetic domain-twin boundary interactions in Ni-Mn-Ga, Acta Materialia (2020).

[99]   R. Chulist, L. Straka, H. Seiner, A. Sozinov, N. Schell, T. Tokarski, Branching of {110) twin boundaries in five-layered Ni-Mn-Ga bent single crystals, Materials & Design 171 (2019).

[100] P. Mullner, Twinning stress of type I and type II deformation twins, Acta Materialia 176 (2019) 211-219.